



# Kent Academic Repository

**Sun, Duo (2012) *Flame stability and burner condition monitoring through optical sensing and digital imaging*. Doctor of Philosophy (PhD) thesis, University of Kent.**

## Downloaded from

<https://kar.kent.ac.uk/86491/> The University of Kent's Academic Repository KAR

## The version of record is available from

<https://doi.org/10.22024/UniKent/01.02.86491>

## This document version

UNSPECIFIED

## DOI for this version

## Licence for this version

CC BY-NC-ND (Attribution-NonCommercial-NoDerivatives)

## Additional information

This thesis has been digitised by EThOS, the British Library digitisation service, for purposes of preservation and dissemination. It was uploaded to KAR on 09 February 2021 in order to hold its content and record within University of Kent systems. It is available Open Access using a Creative Commons Attribution, Non-commercial, No Derivatives (<https://creativecommons.org/licenses/by-nc-nd/4.0/>) licence so that the thesis and its author, can benefit from opportunities for increased readership and citation. This was done in line with University of Kent policies (<https://www.kent.ac.uk/is/strategy/docs/Kent%20Open%20Access%20policy.pdf>). If y...

## Versions of research works

### Versions of Record

If this version is the version of record, it is the same as the published version available on the publisher's web site. Cite as the published version.

### Author Accepted Manuscripts

If this document is identified as the Author Accepted Manuscript it is the version after peer review but before type setting, copy editing or publisher branding. Cite as Surname, Initial. (Year) 'Title of article'. To be published in *Title of Journal*, Volume and issue numbers [peer-reviewed accepted version]. Available at: DOI or URL (Accessed: date).

## Enquiries

If you have questions about this document contact [ResearchSupport@kent.ac.uk](mailto:ResearchSupport@kent.ac.uk). Please include the URL of the record in KAR. If you believe that your, or a third party's rights have been compromised through this document please see our [Take Down policy](https://www.kent.ac.uk/guides/kar-the-kent-academic-repository#policies) (available from <https://www.kent.ac.uk/guides/kar-the-kent-academic-repository#policies>).

**FLAME STABILITY AND BURNER CONDITION  
MONITORING THROUGH OPTICAL SENSING AND  
DIGITAL IMAGING**

A Thesis Submitted to The University of Kent  
For The Degree of Doctor of Philosophy  
In Electronic Engineering

By

**DUO SUN BEng MSc**

**November 2012**

## Abstract

This thesis describes the design, implementation and experimental evaluation of a prototype instrumentation system for flame stability and burner condition monitoring on fossil-fuel-fired furnaces.

A review of methodologies and technologies for the monitoring of flame stability and burner condition is given, together with the discussions of existing problems and technical requirements in their applications. A technical strategy, incorporating optical sensing, digital imaging, digital signal/image processing and soft computing techniques, is proposed. Based on this strategy, a prototype flame imaging system is developed. The system consists of a rigid optical probe, an optical-beam-splitting unit, an embedded photodetector and signal-processing board, a digital camera, and a mini-motherboard with associated application software. Detailed system design, implementation, calibration and evaluation are reported.

A number of flame characteristic parameters are extracted from flame images and radiation signals. Power spectral density, oscillation frequency, and a proposed universal flame stability index are used for the assessment of flame stability. Kernel-based soft computing techniques are employed for burner condition monitoring. Specifically, kernel principal components analysis is used for the detection of abnormal conditions in a combustion process, whilst support vector machines are used for the prediction of  $\text{NO}_x$  emission and the identification of flame state.

Extensive experimental work was conducted on a  $9\text{MW}_{\text{th}}$  heavy-oil-fired combustion test facility to evaluate the performance of the prototype system and developed algorithms. Further tests were carried out on a  $660\text{MW}_{\text{th}}$  heavy-oil-fired boiler to investigate the cause of the boiler vibration from a flame stability point of view. Results obtained from the tests are presented and discussed.

## Acknowledgements

The author wishes to express grateful thanks to the following:

### University of Kent

*Dr G. Lu* My first supervisor, whose advice, encouragement, and contributions made it possible for me to complete this work.

*Professor Y. Yan* My second supervisor for his advice, support and encouragement, which allowed the project to progress at all times.

### Zhejiang University

*Professor H. Zhou* Who provided the 9MW<sub>th</sub> Combustion Test Facility at Zhejiang University, Hangzhou, P. R. China.

Dongfang Boiler Group Co., Ltd., in particular, staff and technicians for their technical advice and assistance during industrial trials on the 660MW<sub>th</sub> boiler in Saudi Arabia.

The Engineering and Physical Sciences Research Council, who provided the research grants for the project.

A number of academic staff, technicians and colleagues at the University of Kent, in particular, Mr C. Birch, Mr T. Brazier, Mr Md. M. Hossain, Dr C. Xu, Dr X. Qian, Dr X. Li, Dr J. Krabicka, who made various contributions to the project.

Special thanks to the friends I've known here who kept me going, Tian Qiu, Jiaqing Shao, Zhiguang Geng, Lu Bai, Huilin Zhu, Yiqing Liang, Karl Harmer, David Hobson.

This thesis is dedicated to my parents and my wife Lingjun Gao, for their encouragement, help and support throughout the project.

# Content

<b>Abstract .....</b>	<b>i</b>
<b>Acknowledgements .....</b>	<b>ii</b>
<b>Content.....</b>	<b>iii</b>
<b>List of Tables.....</b>	<b>viii</b>
<b>List of Figures .....</b>	<b>ix</b>
<b>Nomenclature.....</b>	<b>xiv</b>
<b>Chapter 1 Requirements for Flame Stability and Burner Condition</b>	
<b>Monitoring .....</b>	<b>1</b>
1.1 Introduction.....	1
1.2 Importance of Flame Stability Monitoring and its Technical Requirements.....	2
1.3 Importance of Burner Condition Monitoring and its Technical Requirements .....	3
1.4 Objectives of the Research Programme .....	6
1.5 Major Technical Challenges .....	7
1.6 Thesis Outline .....	8
<b>Chapter 2 Review of Techniques for Flame Stability and Burner</b>	
<b>Condition Monitoring .....</b>	<b>9</b>
2.1 Introduction.....	9
2.2 Flame Monitoring .....	10
2.2.1 Laser-Based Imaging .....	10
2.2.2 Passive Imaging .....	11
2.2.2.1 Chemiluminescence Imaging.....	12
2.2.2.2 Imaging-Based Pyrometry .....	13
2.2.2.3 Broadband Imaging.....	15
2.2.3 Photodetectors.....	16
2.3 Flame Stability Monitoring.....	17

2.4 Burner Condition Monitoring .....	18
2.4.1 Abnormal Condition Detection in a Combustion Process .....	18
2.4.2 NO <sub>x</sub> Prediction .....	20
2.4.3 Flame State Identification .....	21
2.5 Summary .....	22

## **Chapter 3 Theory of Flame Stability and Burner Condition**

<b>Monitoring .....</b>	<b>24</b>
3.1 Introduction .....	24
3.2 Image Processing and Spectral Analysis Techniques for Flame Stability Monitoring .....	25
3.2.1 Standard Deviation of Flame Parameters .....	25
3.2.2 Power Spectral Analysis and Oscillation Frequency .....	25
3.2.3 Universal Flame Stability Index .....	27
3.2.3.1 Conversion of Colour Space from RGB to HSI .....	27
3.2.3.2 Extraction of Image Features .....	29
3.2.3.3 Data Fusion .....	30
3.3 Soft Computing Techniques for Burner Condition Monitoring .....	32
3.3.1 Flame Characteristics Used for KPCA and SVM Models .....	32
3.3.1.1 Characteristics of Flame Radiation Signals .....	32
3.3.1.2 Characteristics of Flame Images .....	34
3.3.2 KPCA for Abnormal Condition Detection in a Combustion Process .....	34
3.3.2.1 Kernel Principal Component Analysis .....	35
3.3.2.2 Hotelling's T <sup>2</sup> Statistic and Q Statistic .....	38
3.3.2.3 Work Flow of KPCA .....	39
3.3.3 SVM for Flame State Identification and NO <sub>x</sub> Prediction .....	42
3.3.3.1 Support Vector Classification .....	42
3.3.3.2 Support Vector Regression .....	44
3.3.3.3 Work Flow of SVM .....	45
3.4 Measurement of Soot Temperature, Emissivity and Concentration in Soot-Laden Flames .....	47
3.5 Summary .....	50

<b>Chapter 4 System Description .....</b>	<b>51</b>
4.1 Introduction .....	51
4.2 System Design and Implementation .....	52
4.2.1 Photodetector Subsystem .....	53
4.2.1.1 Photodiodes .....	55
4.2.1.2 Amplifier Unit .....	55
4.2.1.3 Signal Conditioning Unit .....	56
4.2.1.4 Digital Signal Microcontroller Unit .....	58
4.2.2 Imaging Subsystem .....	60
4.2.2.1 Optical Probe .....	60
4.2.2.2 Digital Camera .....	61
4.2.2.3 Optical Lens .....	62
4.2.3 Computing Subsystem .....	62
4.2.3.1 Mini-Motherboard .....	62
4.2.3.2 Software .....	63
4.3 Evaluation of Photodetector Subsystem .....	66
4.3.1 System Characteristics .....	66
4.3.2 Evaluation of Oscillation Frequency Measurement .....	67
4.4 Evaluation of Imaging Subsystem .....	69
4.4.1 System Characteristics .....	69
4.4.1.1 Sensor Dark Current .....	70
4.4.1.2 Exposure Time .....	72
4.4.1.3 Master Gain .....	74
4.4.1.4 Gain Boost .....	76
4.4.1.5 R/G/B Gains .....	76
4.4.2 Calibration of Temperature Measurement .....	78
4.4.3 Evaluation of Temperature Measurement .....	82
4.5 Summary .....	83
<b>Chapter 5 Tests on a 9MW<sub>th</sub> Heavy-Oil-Fired Combustion Test</b>	
<b>Facility .....</b>	<b>84</b>
5.1 Introduction .....	84

5.2 Experimental Conditions.....	85
5.2.1 Combustion Test Facility and System Installation .....	85
5.2.2 Properties of Heavy Oil.....	87
5.2.3 Test Programme and Measured Flame Parameters.....	88
5.3 Results of Flame Stability Monitoring.....	90
5.3.1 Different Swirl Vane Angles of Tertiary Air .....	90
5.3.2 Different Swirl Vane Positions of Secondary Air.....	96
5.3.3 Different Ratios of Primary Air to Total Air .....	101
5.3.4 Different Ratios and Nozzle Positions of Overfire Air.....	106
5.3.4.1 Flame Stability .....	108
5.3.4.2 Soot Temperature, Emissivity and Concentration .....	110
5.3.5 Correlation between Flame Stability and NO <sub>x</sub> Emission.....	114
5.4 Results of Burner Condition Monitoring .....	116
5.4.1 Detection of Abnormal Conditions in a Combustion Process Using KPCA.....	116
5.4.2 Flame State Identification and NO <sub>x</sub> Prediction Using SVM.....	123
5.4.2.1 Flame State Identification .....	124
5.4.2.2 NO <sub>x</sub> Prediction .....	128
5.5 Summary .....	132
<b>Chapter 6 Tests on a 660MW<sub>th</sub> Heavy-Oil-Fired Boiler.....</b>	<b>133</b>
6.1 Introduction.....	133
6.2 Thermo-Acoustic Combustion Instability.....	134
6.2.1 Theory of Thermo-Acoustic Instability .....	134
6.2.2 Acoustic Characteristics of the Tested Boiler.....	135
6.3 Experimental Conditions.....	137
6.3.1 Boiler Structure and System Installation .....	137
6.3.2 Test Programme .....	138
6.4 Results and Discussions .....	139
6.4.1 Impact of Nozzle Rotation .....	139
6.4.1.1 Flame Stability Index and Oscillation Frequency.....	141
6.4.1.2 Flame Temperature .....	146
6.4.2 Impact of Boiler Load .....	148
6.4.2.1 Flame Stability Index and Oscillation Frequency.....	148

6.4.2.2 Flame Temperature .....	152
6.5 Summary .....	152
<b>Chapter 7 Conclusions and Recommendations for Future Work.....</b>	<b>154</b>
7.1 Introduction.....	154
7.2 Conclusions.....	154
7.2.1 Instrumentation System.....	154
7.2.2 Tests on the 9MW <sub>th</sub> Combustion Test Facility .....	156
7.2.2.1 Flame Stability .....	156
7.2.2.2 Burner Condition Monitoring .....	157
7.2.3 Tests on the 660MW <sub>th</sub> Boiler .....	158
7.3 Recommendations for Future Work.....	159
<b>References.....</b>	<b>162</b>
<b>Appendix 1: Schematic and PCB Layout of the Embedded     Photodetector and Signal-Processing Board .....</b>	<b>172</b>
<b>Appendix 2: Program for dsPIC Microcontroller Configuration.....</b>	<b>175</b>
<b>Appendix 3: Program for Computation of Oscillation Frequency.....</b>	<b>185</b>
<b>Appendix 4: Program for Computation of Flame Stability Index .....</b>	<b>188</b>
<b>Appendix 5: Program for Computation of Temperature.....</b>	<b>194</b>
<b>Appendix 6: Program for of Abnormal Condition Detection in a     Combustion Process Using KPCA.....</b>	<b>200</b>
<b>Appendix 7: Program for Flame State Identification Using SVM .....</b>	<b>204</b>
<b>Appendix 8: Program for NO<sub>x</sub> Emission Prediction Using SVM.....</b>	<b>207</b>
<b>Publications and Dissemination .....</b>	<b>210</b>

## List of Tables

Table 3.1 Frequency ranges of wavelet subspace .....	33
Table 4.1 Specifications of the photodiodes .....	55
Table 4.2 Specifications of the digital signal microcontroller (dsPIC33FJ256GP710)..	60
Table 4.3 Specifications of the camera (UI-1640SE-C) .....	61
Table 4.4 Specifications of the mini-motherboard (PICO820).....	63
Table 4.5 Specifications of the blackbody furnace (Landcal R1500T) .....	70
Table 4.6 Averaged grey-level intensity of offset caused by dark current of camera sensor .....	72
Table 5.1 Specifications of the heavy oil tested.....	87
Table 5.2 Summary of the test programme on the 9MW <sub>th</sub> combustion test facility .....	89
Table 6.1 Summary of the test programme on the 660MW <sub>th</sub> boiler .....	139

## List of Figures

Figure 2.1 Schematic diagram of a PLIF system .....	11
Figure 2.2 Sensing arrangement of a chemiluminescence imaging system.....	12
Figure 2.3 Sensing arrangement of a multi-colour imaging-based pyrometric system ..	14
Figure 2.4 Schematic diagram of a broadband imaging system .....	15
Figure 2.5 Schematic diagram of a flame detector .....	16
Figure 3.1 Measurement procedure of the universal flame stability index.....	27
Figure 3.2 HSI colour space.....	29
Figure 3.3 Flow chart of KPCA-based combustion process monitoring .....	41
Figure 3.4 Key idea of SVM in a two-class problem.....	43
Figure 4.1 Block diagram of the flame monitoring system .....	53
Figure 4.2 Physical implementation of the flame monitoring system .....	53
Figure 4.3 Block diagram of the embedded photodetector and signal-processing board	54
Figure 4.4 Physical implementation of the embedded photodetector and signal- processing board .....	54
Figure 4.5 Schematic diagram of the photodiode amplifier unit .....	56
Figure 4.6 Schematic diagram of the signal conditioning unit .....	57
Figure 4.7 Simulated frequency response of the second-order Sallen-Key low pass filter using TINA .....	57
Figure 4.8 Flow chart of oscillation frequency measurement.....	59
Figure 4.9 Screenshot of the graphical user interface .....	64
Figure 4.10 Flow chart of measurement procedure of computing subsystem .....	65
Figure 4.11 Variation of gain with the wiper position of the digital potentiometer .....	67
Figure 4.12 A typical example of the signal captured and its corresponding power spectral density .....	68
Figure 4.13 Comparison between the measured and reference frequencies .....	69
Figure 4.14 Distribution of a single red dark frame image.....	72
Figure 4.15 Relationship between the averaged grey-levels of blackbody images and camera exposure time for camera R, G and B channels.....	73
Figure 4.16 Variations of pixel value with master gain setting .....	75
Figure 4.17 Variations of actual gain coefficient with master gain setting .....	75
Figure 4.18 Pixel values for various R gain settings.....	77

Figure 4.19 Pixel values for various G gain settings .....	77
Figure 4.20 Pixel values for various B gain settings.....	78
Figure 4.21 Experimental setup of the temperature calibration using blackbody furnace .....	80
Figure 4.22 Blackbody images captured for different temperatures settings under the same camera exposure time .....	80
Figure 4.23 Variation of instrument factor with grey-level ratio.....	81
Figure 4.24 Relationship between the grey-level intensities of R component and blackbody temperature .....	81
Figure 4.25 Comparison between the measured and reference temperatures.....	83
Figure 5.1 The 9MW <sub>th</sub> heavy-oil-fired combustion test facility .....	86
Figure 5.2 Schematic diagram of the combustion test facility and the installation location of the flame imaging system.....	86
Figure 5.3 Flame images taken for different swirl vane angles of tertiary air.....	91
Figure 5.4 Variations of stability index with the swirl vane angle of tertiary air .....	93
Figure 5.5 Variations of power spectral density estimates of flame radiation signal in visible band with the swirl vane angle of tertiary air .....	93
Figure 5.6 Variations of power spectral density estimates of flame radiation signal in infrared band with the swirl vane angle of tertiary air.....	94
Figure 5.7 Variations of oscillation frequency with the swirl vane angle of tertiary air	94
Figure 5.8 Variations of average temperature with the swirl vane angle of tertiary air	95
Figure 5.9 Variations of NO <sub>x</sub> emission with the swirl vane angle of tertiary air.....	95
Figure 5.10 Flame images taken for different swirl vane positions of secondary air .....	96
Figure 5.11 Variations of flame stability index with the ratio of primary air to total air	98
Figure 5.12 Variations of power spectral density estimates of flame radiation signals in visible band with the ratio of primary air to total air.....	98
Figure 5.13 Variations of power spectral density estimates of flame radiation signals in infrared band with the ratio of primary air to total air.....	99
Figure 5.14 Variations of oscillation frequency with the ratio of primary air to total air .....	99
Figure 5.15 Variations of average temperature with the swirl vane position of secondary air .....	100

Figure 5.16 Variations of $\text{NO}_x$ emission with the swirl vane position of secondary air .....	100
Figure 5.17 Flame images taken for different ratios of primary air to total air .....	102
Figure 5.18 Variations of flame stability index with the ratio of primary air to total air .....	103
Figure 5.19 Variations of power spectral density estimates of flame radiation signals in visible band with the ratio of primary air to total air .....	103
Figure 5.20 Variations of power spectral density estimates of flame radiation signals in infrared band with the ratio of primary air to total air .....	104
Figure 5.21 Variations of oscillation frequency with the ratio of primary air to total air .....	104
Figure 5.22 Variation of average temperature with the ratio of primary air to total air	105
Figure 5.23 Variations of $\text{NO}_x$ emission with the ratio of primary air to total air .....	105
Figure 5.24 Flame images taken for different ratios of overfire air for different nozzle positions .....	107
Figure 5.25 Variations of stability index with ratio and position of overfire air .....	108
Figure 5.26 Variations of power spectral density estimates of flame radiation signal in visible band with the ratio of overfire air (OFA2) .....	109
Figure 5.27 Variations of power spectral density estimates of flame radiation signal in infrared band with the ratio of overfire air (OFA2) .....	109
Figure 5.28 Variations of oscillation frequency with ratio and position of overfire air	110
Figure 5.29 Averaged image of the heavy oil flame and the corresponding distributions of soot temperature, emissivity and concentration .....	112
Figure 5.30 Variations of average temperature with the ratios and nozzle positions of overfire air .....	112
Figure 5.31 Variations of $\text{NO}_x$ emission with the ratios and nozzle positions of overfire air .....	113
Figure 5.32 Variations of average emissivity with the ratios and nozzle positions of overfire air .....	113
Figure 5.33 Variations of $KL$ factor with the ratios and nozzle positions of overfire air .....	114
Figure 5.34 Variations of $\text{NO}_x$ emission with measured flame stability index .....	115

Figure 5.35 Variations of NO <sub>x</sub> emission with the measured oscillation frequency in visible band.....	115
Figure 5.36 Variations of NO <sub>x</sub> emission with the measured oscillation frequency in infrared band.....	116
Figure 5.37 Monitoring charts of non-OFA combustion process.....	120
Figure 5.38 Monitoring charts of OFA combustion process.....	122
Figure 5.39 Variation of false warning rate with training data size.....	123
Figure 5.40 Architecture of the neural network for flame state identification.....	125
Figure 5.41 Variations of the success rate of classification of training data with training set size.....	126
Figure 5.42 Variations of the success rate of classification of testing data with training set size.....	126
Figure 5.43 Success rate of classification of testing data in one hundred trials (training set size 80%).....	127
Figure 5.44 Success rate of classification of testing data in one hundred trials (training set size 10%).....	127
Figure 5.45 Performance of SVM and NN for NO <sub>x</sub> prediction (training data).....	129
Figure 5.46 Performance of SVM and NN for NO <sub>x</sub> prediction (test data).....	130
Figure 5.47 Comparison between predicted and measured NO <sub>x</sub> emissions.....	131
Figure 6.1 Feedback loop responsible for thermo-acoustic instability.....	134
Figure 6.2 Spectrum of the combustion acoustic signal obtained at boiler load 300MW <sub>th</sub> (non-vibration).....	136
Figure 6.3 Spectrum of the combustion acoustic signal obtained at boiler load 340MW <sub>th</sub> (vibration).....	136
Figure 6.4 Schematic diagram of longitudinal-section of the 660MW <sub>th</sub> boiler.....	137
Figure 6.5 Flame imaging system and its installation.....	138
Figure 6.6 Front view of the burner and the nozzle.....	140
Figure 6.7 Flame images taken at burner FB1.....	140
Figure 6.8 Flame images taken at burner RB1.....	140
Figure 6.9 Comparison of flame stability indices before and after nozzle rotation.....	141
Figure 6.10 Comparison of oscillation frequencies of whole flame before and after nozzle rotation.....	142
Figure 6.11 Location of measurement points of flame oscillation frequency.....	143

Figure 6.12 Comparison of oscillation frequencies in different flame areas before and after nozzle rotation at burner FB1 .....	144
Figure 6.13 Comparison of oscillation frequencies in different flame areas before and after nozzle rotation at burner RB1 .....	145
Figure 6.14 Averaged flame images and the corresponding temperature distributions at burner FB1 .....	146
Figure 6.15 Temperature histogram of the flame at burner FB1 .....	147
Figure 6.16 Comparison of average flame temperature before and after nozzle rotation .....	148
Figure 6.17 Flame images taken under different boiler loads at burner RB1 .....	149
Figure 6.18 Variation of flame stability index with boiler load.....	150
Figure 6.19 Variation of oscillation frequency of whole flame with boiler load.....	150
Figure 6.20 Variations of oscillation frequencies of different flame regions with boiler load .....	151
Figure 6.21 Variation of average temperature with boiler load .....	152

## Nomenclature

$\gamma$	Empirical parameter in Hottel and Broughton's emissivity equation
$\delta$	Stability index of a flame
$\varepsilon_{\lambda_R}(T)$	Emissivity of soot particles in a flame at wavelength $\lambda_R$ for temperature $T$
$\lambda$	Light wavelength
$\lambda_R$	Peak wavelength within the spectral range of the red channel
$\lambda_G$	Peak wavelength within the spectral range of the green channel
$\mu_x$	Mean of variable $x$
$\sigma_x$	Standard deviation of variable $x$
$A$	Instrument constant
$A_I$	Luminous area of a flame determined by the I channel of an HSI image
$B$	Blue channel of a RGB image
$B_f$	Brightness of a flame
$c_T$	Speed of sound at temperature $T$
$c_0$	Speed of sound at temperature 273°K
$C_2$	Second Planck's constant
$C_H$	Contrast of the hue channel of an HSI colour image
$C_I$	Contrast of the intensity channel of an HSI colour image
$C_S$	Contrast of the saturation channel of an HSI colour image
$D$	Geometric dimension of a combustion chamber
$E_b$	Energy contained in wavelet subspace $b$
$f_i$	$i^{\text{th}}$ frequency component of a flame radiation signal
$F$	Oscillation frequency of a flame
$F_a$	Acoustic frequency of a combustion chamber
$F_{p,N-p,\alpha}$	$F$ -distribution with $p$ and $N$ degrees of freedom with significance level of $100(1 - \alpha)\%$
$G(\lambda_R, T)$	Grey-level intensity of the R channel of a RGB image at temperature $T$
$G(\lambda_G, T)$	Grey-level intensity of the G channel of a RGB image at temperature $T$
$G_b(\lambda_R, T)$	Grey-level intensity of the R image of a blackbody for temperature $T$
$G$	Green channel of a RGB colour image
$H$	Hue channel of an HSI colour image

$I$	Intensity channel of an HSI colour image
$KL$	$KL$ factor
$M(\lambda_R, T)$	Monochromatic emissive power of a non-blackbody at $\lambda_R$ for temperature $T$
$M_b(\lambda_R, T)$	Monochromatic emissive power of a blackbody at $\lambda_R$ for temperature $T$
$M_H$	Mean value of the hue channel of an HSI colour image
$M_I$	Mean value of the intensity channel of an HSI colour image
$M_S$	Mean value of the saturation channel of an HSI colour image
$P(f)$	Power spectral density of a flame radiation signal
$Q$	Q statistic
$R$	Red channel of a RGB image
$R_f$	Luminous region of a flame
$s_i$	$i^{\text{th}}$ sample point of a flame radiation signal
$\bar{s}$	DC component of a flame radiation signal
$\tilde{s}$	AC component of a flame radiation signal
$s_{ske}$	Skewness of a flame radiation signal
$s_{kur}$	Kurtosis of a flame radiation signal
$S$	Saturation channel of an HSI colour image
$S_{\lambda_R}$	Spectral sensitivity of the imaging system at wavelength $\lambda_R$
$S_{\lambda_G}$	Spectral sensitivity of the imaging system at wavelength $\lambda_G$
$S(f)$	Fourier transform of a flame radiation signal
$T$	Temperature
$T^2$	Hotelling's $T^2$ statistic
$U_f$	Non-uniformity of a flame
$x_i$	$i^{\text{th}}$ reading of variable $x$

ADC	Analogue-to-Digital Converter
ANN	Artificial Neural Network
BCURA	British Coal Utilisation Research Association
BF2RA	Biomass and Fossil Fuels Research Alliance
CCD	Charge-Coupled Device
CEMS	Continuous Emission Monitoring System
CFD	Computational Fluid Dynamics

CMOS	Complementary Metal–Oxide–Semiconductor
CTF	Combustion Test Facility
DMA	Direct Memory Access
DSP	Digital Signal Processing
dsPIC	Digital Signal Microcontroller
EPSB	Embedded Photodetector and Signal-Processing Board
EPSRC	Engineering and Physical Sciences Research Council
FFT	Fast Fourier Transform
GUI	Graphical User Interface
HSI	Hue, Saturation, Intensity
KPCA	Kernel Principal Component Analysis
ICA	Independent Component Analysis
IR	Infrared
LII	Laser Induced Incandescence
MSE	Mean Squared Error
MSPC	Multivariate Statistical Process Control
OFA	Overfire Air
PA	Primary Air
PCA	Principal Component Analysis
PCB	Printed Circuit Board
PLIF	Planar Laser Induced Fluorescence
PLS	Partial Least Square
PSD	Power Spectral Density
RBF	Radial Basis Function
RGB	Red, Green, Blue
SA	Secondary Air
SVM	Support Vector Machine
TSB	Technology Strategy Board
TA	Tertiary Air
UV	Ultraviolet
VIS	Visible

# Chapter 1

## Requirements for Flame Stability and Burner Condition Monitoring

### 1.1 Introduction

Fossil-fuel-fired furnaces are widely used in many industries to generate electric power by combusting various fuels such as gas, oil and coal. In such combustion processes, optimal operating conditions are required to achieve increased combustion efficiency and reduced pollution emissions. A flame is the central reaction zone of a combustion process. The characteristics of a flame, such as size, shape, brightness, colour, oscillation frequency and temperature, contain valuable information on the quality and performance of the combustion process. However, conventional instruments available in combustion industries are capable of measuring only global variables such as air/fuel flow rate and flue gas composition (e.g., CO, NO<sub>x</sub>, SO<sub>2</sub> and O<sub>2</sub>), providing very limited description of the process taking place inside the combustion chamber. A more precise diagnosis and control requires richer sensorial information directly captured from flame. Therefore, the development of techniques suitable for the online characterisation and monitoring of industrial flames is receiving a growing attention and significant research efforts.

At the University of Kent, the Instrumentation, Control and Embedded Systems Research Group, supported by the external funding bodies including EPSRC, TSB, EU, BCURA and BF2RA, has been conducting pioneering work in the use of digital imaging technique for two-dimensional (2-D) and three-dimensional (3-D) flame monitoring and characterisation over the past fifteen years. Several prototype systems have been developed [1-6], and substantial trials of the systems have been undertaken on laboratory test rigs [7-9] and industrial-scale combustion test facilities operated by RWE npower, E.ON and Doosan Babcock [10-14].

The author joined the Group in December 2008 for undertaking an EPSRC funded project (EP/F061307/1) with the aim of developing a methodology for flame stability and burner condition monitoring. This thesis reports the work which has been done during the course of the project.

## **1.2 Importance of Flame Stability Monitoring and its Technical Requirements**

Unstable flames are a recognised problem in fossil-fuel-fired combustion processes, particularly where low quality fuel, fuel blends and co-firing of biomass with fossil fuels are applied. An unstable flame can result in many combustion problems such as low combustion efficiency, high NO<sub>x</sub> emissions, and unburnt carbon in ash [15, 16]. It may also cause a non-uniform thermal distribution in the flue gas, and increase the wall thermal stress and vibration of the furnace [16]. The stability of a flame should therefore be monitored and maintained continuously for the improved overall performance of the furnace. However, flame monitoring techniques currently available to the power generation industry can provide only basic information such as flame presence or absence for a furnace safety purpose. They cannot give qualitative or quantitative information on the stability of the flame. This situation motivated the present work.

The requirements for a flame stability monitoring system have been identified as follows. General requirements, which have been suggested for a basic flame failure detector (flame eye) by previous research work [17], include a fast response, sensitivity to the supervised flame alone, tolerance to the heat and dirt conditions, and minimal maintenance. In addition to these general requirements, an advanced flame stability monitoring system should be capable of providing direct, temporal and spatial measurement, which is essential to observe the dynamic nature of a flame. Moreover, the system should be capable of giving the assessment of flame stability in general cases without ad-hoc adaptation. It is envisaged that optical sensing and digital imaging techniques would meet the requirements.

### **1.3 Importance of Burner Condition Monitoring and its Technical Requirements**

The ultimate aim of developing flame monitoring techniques suitable for industrial applications is to achieve the reliable control of a combustion process for improved combustion efficiency and reduced pollutant emissions. The primary obstacle in the development of advanced combustion control is thought to lie in the lack of effective and reliable means for the monitoring of the combustion process, including flame and burner conditions.

The recent advances in the flame monitoring techniques make it possible to measure quantitatively flame parameters (such as flame temperature and length) which can be directly used for the control of a combustion process. One of the aspects that present work focuses on is the measurement of flame temperature. The flame temperature, generally referring to the temperature of solid particles such as soot and fly-ash in the flame field, plays a key role in every part of the combustion process such as ignition, burnout and the formation of pollutant emissions [18]. However, the flame temperature measurements in plants generally use physical probes such as thermocouple and gas-sampling probe, which are intrusive and give only a single-point gas temperature measurement. Therefore, more advanced approaches, which are non-intrusive and capable of providing 2-D flame temperature distribution on an online basis, are desirable.

On the other hand, although significant research efforts have been devoted to determine the flame characteristics through a variety of sensing and signal/image processing techniques, how to interpret and convert these characteristics into physically meaningful information like temperature for practical control use is still a challenging objective for combustion engineers and researchers. Therefore, in addition to measuring a range of flame characteristic parameters such as 2-D temperature distribution, oscillation frequency, etc., the present research programme attempts to develop a methodology which uses the flame characteristic parameters as the “signature” of a particular combustion state, so as to monitor burner conditions with the aim to (1) detect abnormal

conditions in a combustion process, (2) predict  $\text{NO}_x$  emissions, and (3) identify flame state.

- **Detection of abnormal combustion conditions:** The detection of abnormal conditions in a process is also known as fault detection. In a power generation plant, boilers are required to operate under optimum conditions to maintain satisfactory combustion performance. Abnormal conditions caused by drifts or faults in the boiler would result in not only a low combustion efficiency and high pollutant emissions but also an enormous impact on the health of the system [19]. The recent trend of using a variety of fuels, including low quality coals, coal blends, and co-firing biomass and coal, has further deteriorated this issue. Therefore, a reliable fault detection technique is highly desirable for the optimised operation and control of a combustion process. However, as mentioned, the supervisions of a combustion process in power plant are currently realized based on the information obtained using conventional instruments, which measure mainly global variables such as air/fuel flow rate and flue gas composition, providing very limited description of the flame, which is regarded as the central reaction zone of a combustion process. On the other hand, individual flames in a multi-burner system (such as a boiler) may behave very differently from that estimated from global variables. Consequently, the drift or malfunction of an individual burner can go unnoticed until they become serious.
- **Prediction of  $\text{NO}_x$  emissions:**  $\text{NO}_x$  is a known precursor to the formation of pollutant ozone and acid rain, which has a significant impact on air quality, human health, and climate change [20].  $\text{NO}_x$  emanated from fossil fuel combustion processes contributes as much as 80% to the total  $\text{NO}_x$  emissions in the air. With the increasingly strict environmental rules on the  $\text{NO}_x$  pollution, the control of  $\text{NO}_x$  emissions has become a world-wide concern as the utilization of fossil fuels continues a major means of power generation. The reliable, on-line monitoring of  $\text{NO}_x$  emissions is essential to meet those rules. However, traditional  $\text{NO}_x$  measurement techniques (e.g., continuous emission monitoring systems) have a number of disadvantages such as slow system response, requirements for frequent system calibration, and high system and maintenance cost [21]. The predication of

NO<sub>x</sub> emissions from flame would provide a complementary technique to traditional measurement techniques for NO<sub>x</sub> monitoring. It should be noted that although there are other pollution emissions such as SO<sub>2</sub> from power plants, NO<sub>x</sub> is emphasized in the present work. This is because compared with other pollution emissions, NO<sub>x</sub> is much more expensive and difficult to remove.

- **Identification of flame state:** The reliable identification of flame state plays an important role in achieving the robust control of a combustion process. The behaviour of a flame is dependent on burner conditions such as air-to-fuel ratio and furnace load, and can be reflected via its representative characteristics such as geometrical size, temperature, and oscillation frequency. By treating these representative characteristics as the “signature” of a specific flame state, the burner condition can be directly or indirectly identified by classifying the state of flame into one of states which are previously characterized under known burner conditions.

The information provided by the solutions to the above-mentioned issues can be used either by an operator to manually regulate the combustion process, or by a control system to automatically adjust the combustion process. For example, the indication of the occurrence of abnormal combustion events can be used to inform operators the change of combustion condition and hence immediate actions can be taken. The predicted NO<sub>x</sub> emissions can be used directly for a control system to drive a control. The identified flame state can be used indirectly to drive a control if it is linked with a meaningful combustion parameter of practical relevance such as equivalence ratio.

Soft computing techniques, such as statistical methods and heuristics, have been gaining momentum as a viable complementary technique to conventional hardware sensors, and they are widely accepted as a technology offering an effective way to tackle complex and ill-defined problems. In the present work, it was hoped that suitable soft computing techniques can be developed to handle noisy, non-linear optical sensorial information captured from a flame and achieve the reliable monitoring of burner conditions. The technical requirements for soft computing techniques include less demanding for the size of training set, good generalization ability, less prone to overtraining, and fast system response.

## 1.4 Objectives of the Research Programme

The research programme aims to develop a methodology for the monitoring of flame stability and burner condition on fossil-fuel-fired furnaces. The objectives of the research programme are as follows:

- To define the state of the art in the field. The existing flame monitoring techniques, especially visualization methods, will be reviewed to identify suitable flame sensing methods for flame stability and burner condition monitoring on industrial furnaces.
- To design and implement a prototype instrumentation system for flame stability and burner condition monitoring. Optical sensing and digital imaging techniques will be adopted to acquire flame radiation signals and images. Embedded system techniques will be employed for on-line data processing to ensure the robustness, compactness and fast response of the system.
- To develop novel algorithms for quantifying flame stability and indicating burner condition. Advanced computing algorithms will be developed to process the obtained flame data for assessing flame stability and burner condition. A range of flame characteristics will be quantified, such as flame stability, geometrical/luminous parameters, temperature distribution, and oscillation frequency. Dedicated software will be developed using object-orientated techniques and visual C++.
- To evaluate the system through extensive experiments on industrial-scale combustion test facilities. The performance of the system, including its sensitivity to the variations in combustion conditions, the effectiveness of the computing algorithms, will be evaluated.

In addition to the monitoring of flame stability and burner condition, it was hoped that the system would be multifunctional and capable of measuring other important parameters of the flame, such as temperature, emissivity and concentration of soot particles in soot-laden flames. It was also hoped that the system would demonstrate if the methodology developed is effective on a full-scale furnace in a power plant.

## 1.5 Major Technical Challenges

The development of the methodology for flame stability and burner condition monitoring faces many technological challenges. The main challenges have been identified as follows:

- **Multiple parameters:** Due to the high complexity of a flame, the reliable monitoring of the flame stability and burner condition demands the concurrent measurement and analysis of multiple parameters that characterize the flame from different aspects (e.g., dynamic, temporal, and spatial). The sensing techniques required for the measurement of these parameters may differ significantly from each other, which poses challenges in the design of the system. For example, the measurement of flame oscillation frequency over different wavelength bands requires multiple photodiodes, while the measurement of flame temperature distribution needs an imaging sensor such a CCD/CMOS camera.
- **Fast system response:** The system should be capable of processing a large amount of data (1-D radiation signals, 2-D images) on an online basis and giving a fast response to rapid variations in the characteristics of the flame.
- **Variable operational conditions:** A furnace may operate under a wide range of conditions such as different fuel supplies, furnace loads, air/fuel flow rates and burner configurations. The system should thus have a self-adjusting ability and be capable of providing valid measurements in a wide range of operation conditions.
- **Quantitative assessment of flame stability:** There is a lack of means for quantitative assessment of flame stability. Effective approaches should be developed to process flame sensorial data and evaluate the stability of the flame.
- **Hostile environment:** The electronic and optical components of the system should be protected from excessive heat radiation from the furnace. The optical lens should be kept clean under dusty and smoky conditions.
- **Acceptable cost:** An industrial boiler in a power plant is generally a multi-burner system, which would require multiple flame monitoring systems for each of the burners. Therefore, the cost of a single system to be developed should be acceptable, which to some extent limits the selection of system components and the design of the system.

## 1.6 Thesis Outline

The contributions of this thesis to the state of the art include (1) the development of a multifunctional flame monitoring system, which incorporates optical sensing and digital imaging techniques and is capable of measuring a number of flame characteristics simultaneously (such as oscillation frequency, temperature distribution, geometrical and luminous parameters), (2) the proposal of a universal flame stability index for quantitative assessment of flame stability, (3) the use of KPCA method (kernel principal component analysis) with flame characteristics for detecting abnormal events in a combustion process, and (4) the use of SVM method (support vector machine) with flame characteristics for predicting  $\text{NO}_x$  emissions and identifying flame state.

The thesis is organized in seven chapters as follows:

- Chapter 1 introduces the importance of flame stability and burner condition monitoring, covers the technical requirements, and outlines the proposed research programme and objectives.
- Chapter 2 reviews the existing techniques that could be potentially used for flame stability and burner condition monitoring.
- Chapter 3 presents the theory of image processing and spectral analysis techniques for flame stability assessment, and the theory of soft computing techniques for burner condition monitoring.
- Chapter 4 gives the detailed descriptions of the design, implementation and evaluation of the multifunctional flame monitoring instrumentation system.
- Chapter 5 presents and discusses the experimental results obtained from a  $9\text{MW}_{\text{th}}$  heavy-oil-fired combustion test facility.
- Chapter 6 presents and discusses the experimental results obtained from a  $660\text{MW}_{\text{th}}$  heavy-oil-fired boiler.
- Chapter 7 draws conclusions from the work that has been presented and provides suggestions for future work.

## Chapter 2

# Review of Techniques for Flame Stability and Burner Condition Monitoring

### 2.1 Introduction

A complete literature review was conducted to examine all existing techniques that might be used for flame stability and burner condition monitoring at a combustion system. The state-of-the-art in the field of study is defined following the analysis and digestion of all relevant references and materials in the field. The literature survey not only was useful to acquire necessary background knowledge that might contribute to this work but also assisted in demonstrating a clear contribution of this work to the state of the art.

The study of flame has a long history and involves different areas from fundamental laboratory studies to industrial applications. Significant efforts have been being devoted to study the chemical mechanisms and structure properties of flames, experimentally or theoretically. In addition, with the improved understanding of combustion and progress of computing science, mathematical modelling of flames, also known as CFD (Computational Fluid Dynamics), forms another important branch of flame studies. The researches in these areas are useful in understanding the fundamentals of flames and in simulating combustion processes. They are, however, beyond the scope of the research programme and therefore excluded from this review. In addition, 3-D flame imaging techniques are also excluded in this review, due to the complexity of their system set up, which would be considered to be impractical for uses in industrial boilers.

This chapter is organized as follows. Firstly, the chapter reviews the existing flame monitoring techniques, especially visualization methods, which could potentially be used for the flame stability and burner condition monitoring, including laser-based

imaging techniques, chemiluminescence imaging, imaging-based pyrometry, and broadband imaging. Photo detectors are also included due to their wide availability in power plants as essential flame failure detectors. The basic principle, advantages and disadvantages of each technique are described in each case. A comprehensive survey about the flame monitoring and characterisation techniques was previously conducted by Lu [22]. A recent survey about the diagnostic strategies for the monitoring and control of practical flames was given by Ballester et al. [19]. These two surveys constitute the key references of some of techniques described in this part of the review.

Secondly, the chapter reviews the work that has been reported about the flame stability and burner condition monitoring. Being different from the review of flame monitoring techniques, this part of review mainly focuses on the methods/algorithms of data processing and analysing.

## **2.2 Flame Monitoring**

### **2.2.1 Laser-Based Imaging**

A variety of laser-based imaging techniques have been developed for the study of flames, such as PLIF (Planar Laser Induced Fluorescence) [23-26], LII (Laser Induced Incandescence) [27, 28], Rayleigh Scattering [28], Mie Scattering [29], Raman Scattering, Schlieren Photography [30], Shadowgraphy [27], Interferometry [31], and Particle Imaging Velocimetry [32]. Among these techniques, PLIF is the most common one due to its superior ability to study the fundamentals of flame, such as its propagation, temperature, heat release pattern and rate [33]. The basic principle of PLIF involves using a laser sheet of a particular wavelength to excite an atomic or molecular species of interest within the flame from a lower energy state, most often the ground state, to an upper excited state. When the excited atoms or molecules decay back to a lower energy level, they emit spontaneously photons. The spontaneous emission is known as fluorescence, and its intensity can be related to the density of the species of interest. For certain molecules, such as OH and CH, they have been found that with an

appropriate selection of excitation and detection scheme, the fluorescence signal is directly proportional to the concentration of the species [34]. Figure 2.1 shows a typical sensing arrangement of OH PLIF.

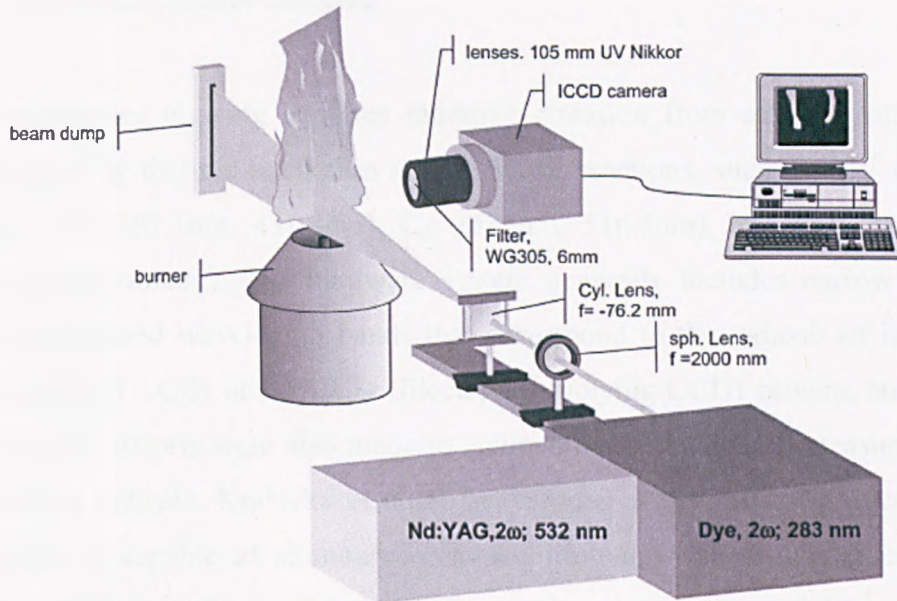


Figure 2.1 Schematic diagram of a PLIF system (Cessou et al. [26])

Laser-based techniques have been proven extremely useful in understanding the fundamentals and mechanisms of combustion processes including flames [33, 35, 36]. However, practical reasons (e.g., the complexity and high cost of the system set up, the requirement of highly-skilled personnel for the operation, and particularly the need for optical accesses for laser excitation and imaging) still pose significant challenges in applying these techniques for routine operations in industrial furnaces such as boilers [19].

### 2.2.2 Passive Imaging

Unlike laser-based imaging techniques, passive imaging techniques avoid the need for external illumination or seeding. They record the radiation naturally emitted by the flame and thus appear to be the feasible methods for industrial applications. According to the radiation band recorded, passive imaging techniques can be further classified into

following categories: chemiluminescence imaging, imaging-based pyrometry, and broadband imaging.

### 2.2.2.1 Chemiluminescence Imaging

Chemiluminescence imaging captures radiative emission from electronically excited species formed by thermal excitation and chemical reactions, such as  $\text{OH}^*$  (282.9nm, 308.9nm),  $\text{CH}^*$  (387.1nm, 431.4nm),  $\text{C}_2^*$  (513nm, 516.5nm), and  $\text{CO}_2^*$  (continuous spectrum 350nm-600nm). The hardware system generally includes narrow bandpass filters at the selected wavelength bands that correspond to the radicals of interest, an ICCD (Intensified CCD) or EMCCD (Electro-Multiplying CCD) camera, and a frame grabber [37-39]. Efforts were also made to achieve the simultaneous measurements of multiple flame radicals. Krabicka et al. [6] developed a chemiluminescence imaging system which is capable of simultaneously acquiring four chemiluminescent images ( $\text{OH}^*$ ,  $\text{CN}^*$ ,  $\text{CH}^*$ ,  $\text{C}_2^*$ ). Figure 2.2 shows the sensing arrangement of the system. The system uses a dedicated optical splitting unit which divides the light of the flame into four identical beams. Each beam is passed through a narrow bandpass optical filter in order to block all light other than that corresponding to the spectral range of a particular flame radical, before being captured by an EMCCD camera.

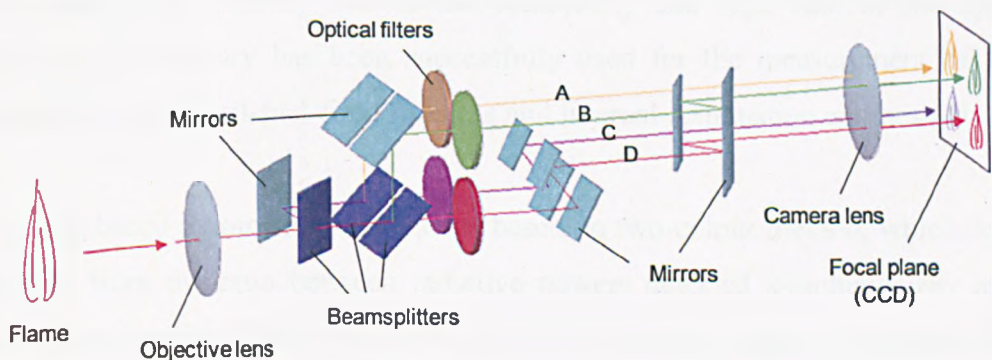


Figure 2.2 Sensing arrangement of a chemiluminescence imaging system

(Krabicka et al. [6])

The magnitude of a chemiluminescence signal is related to the concentration of the corresponding excited species. Due to this property, chemiluminescence imaging has been widely used to determine the location of flame reaction zone and to infer the heat release pattern and rate. Chemiluminescence, however, is mainly originated in thin reaction zones, and thus the technique is commonly used in the study of gaseous flames. The problem with a flame fired with liquid or solid fuels (e.g., heavy oil, coal, and biomass) is that the very intense blackbody emission of soot particles would exceed by far and blur the actual chemiluminescence signal [40]. Therefore, chemiluminescence imaging technique is not selected as the sensing method for flame stability and burner condition monitoring in the present work.

#### **2.2.2.2 Imaging-Based Pyrometry**

The techniques for the measurement of flame temperature can be intrusive or non-intrusive. The intrusive techniques, which mainly include thermocouples and gas-sampling probes, are widely used in plants. They are simple and low cost, but give only a single-point gas temperature measurement. Non-intrusive techniques operate on optical principles, including active laser-based methods (such as laser-induced fluorescence and laser scattering), and passive imaging-based pyrometric technique. While laser-based optical methods are commonly used in laboratories but unsuitable for routine operation in industry due to the complexity and high cost of the system, imaging-based pyrometry has been successfully used for the measurement of flame temperature in both fossil-fuel-fired furnaces and internal combustion engines [41, 42].

The imaging-based pyrometric technique is based on two-colour method, which derives temperature from the ratio between radiative powers detected simultaneously at two different wavelengths. The two-colour method is mainly used for measuring the temperature of a flame whose radiation bands are dominated by black-body emission. The main advantage of the two-colour method is that it does not require the pre-knowledge of the flame emissivity (to be more accurate, the emissivity of soot particles contained in the flame) [41].

Berry et al. [43] used a monochrome CCD camera with two near infrared filters in combination with neutral density filters to measure the temperature of laminar jet diffusion flames under atmospheric and elevated pressures. Huang et al. [1] adopted a single CCD camera with optical filters mounted on a rotatable holder to acquire alternatively the radiation images at two different wavelengths to measure the temperature of a coal flame in a 500kW model furnace. Lu et al. [44] constructed an imaging system for the on-line measurement of temperature distribution and soot concentration of pulverized coal flames. The system incorporates a monochrome CCD camera with a beam-splitting unit and two bandpass filters centred at 650nm and 700nm with bandwidth of 10nm to capture the flame images at two wavelengths. In addition, attempts were also made to develop multi-colour pyrometric techniques [11, 45, 46]. Lu et al. [11] designed a three-colour imaging-based pyrometric system for measuring the temperature profiling of a pulverized coal flame. Figure 2.3 shows the sensing arrangement of the system. A dedicated beam-splitting unit is used to split the light into three identical beams. These beams are filtered by three different bandpass filters centred at 550nm, 632nm and 700nm, respectively, and then projected onto a CCD panel.

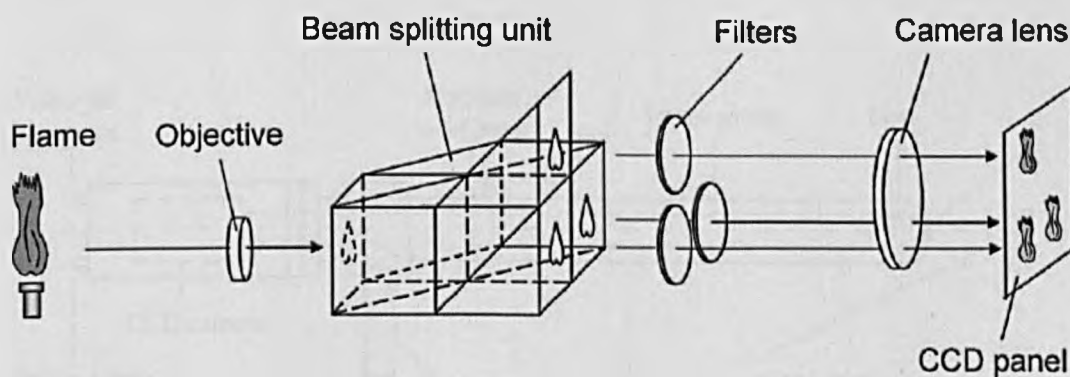


Figure 2.3 Sensing arrangement of a multi-colour imaging-based pyrometric system

(Lu et al. [11])

### 2.2.2.3 Broadband Imaging

Broadband imaging systems have been widely used as a compulsory flame supervision tool in many industrial furnaces for an observation purpose. In comparison with chemiluminescence and pyrometric imaging systems, the hardware of broadband imaging system is relatively simple and cost-effective. The system can be just a monochromatic or colour CCD/CMOS camera with a suitable optical lens, no need for any beam-splitting unit or narrow bandpass filter. The system response of a broadband imaging system corresponds to a certain band width rather than a specific wavelength, which poses difficulties in explaining the data. The interpretation of the obtained non-filtered images is generally from the subjective analysis of boiler operators based on their experience. Significant efforts have been devoted to convert the raw non-filtered images into meaningful, usable information through image processing techniques (e.g., multivariate image analysis [47, 48] and colour characterization [49]), and pattern recognition techniques (e.g., median threshold clustering [50] and neural network [51, 52]). Figure 2.4 shows a typical schematic diagram of a broadband imaging system [53]. The system consists of a lens, an image guide, and a colour CCD Camera. The image guide is fixed in the centre of a stainless steel pipe that is inserted into the water-wall of the furnace. The optics of the system is kept cool and clean by purging compressed air.

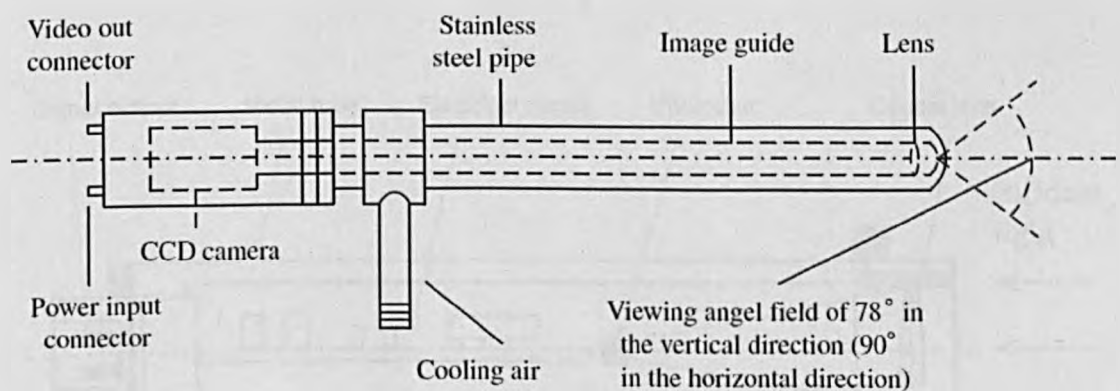


Figure 2.4 Schematic diagram of a broadband imaging system (Jiang et al. [53])

### 2.2.3 Photodetectors

Photodetectors are widely used in industrial furnaces for flame extinction detection [17]. Undetected flame extinction in a furnace can be followed by explosive re-ignition of the unburnt fuel that has continued to be admitted into the furnace. The explosive re-ignition could damage equipment and pose a safety hazard to anyone in vicinity. For a safety purpose, industrial boilers equip every individual burner with a flame detector, which is mainly based on photodetector and installed at the sight-tube of the burner. Such a device can, however, only detect flame “on” or “off”. Figure 2.5 shows a schematic of a flame detector, which mainly consists of an optical lens, a photocell and an associated electrical circuit [22].

The photodetector technique can also be used for advanced flame monitoring, such as for studying the power spectral density and characteristic frequency of flames [54], and for fuel tracking [55, 56]. In the sense of system installation and maintenance, photodetectors can be a good choice for the flame stability and burner condition monitoring in industrial environments. However, photodetector has its intrinsic disadvantages. First, the received raw radiation signal is an one-dimensional signal, and thus the information provided is limited. Second, the field of view of a photodetector is generally narrow, about  $5^{\circ}\sim 10^{\circ}$ , so only a small region of flame can be viewed.

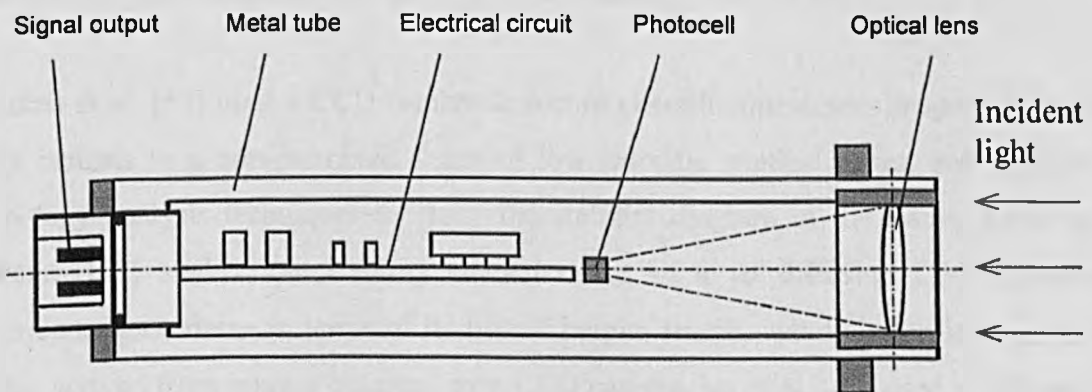


Figure 2.5 Schematic diagram of a flame detector (Lu [22])

## 2.3 Flame Stability Monitoring

Before reviewing the reported work about flame stability monitoring, one concept that should be clarified is flame stability limits [57]. A spatially stable flame requires a balance between the velocity of flame (i.e., the rate of burning) and the velocity of the air-fuel mixture fed. If it is not possible to match these two velocities, the flame will either blow off or flash back. The flame blow-off and flashback limits are known as flame stability limits. The flame stability limits are usually indicated in a flame stability diagram, which is generally represented using axis coordinates of two key controllable parameters [58], such as heat input rate and equivalence ratio [59], air stream velocity and fuel stream velocity [60], and Wobbe fuel flow rate and air flow rate [61]. Many research efforts were made to investigate the flame stability limits and diagram. However, the flame stability limits and diagram generally correspond to a specific fuel and burner and give only the range of the controllable parameters within which the flame blow-off and flashback can be avoided for a safety purpose, rather than quantitative information on the stability of the flame. Therefore, the studies of flame stability limits are not covered in the present study.

Unlike the well-defined flame stability limits, there is no widely accepted concept for flame stability monitoring. Although a variety of flame monitoring techniques (as described in Section 2.2) have been developed to study flames, only very limited work have been reported to use these techniques for studying flame stability.

Paubel et al. [58] used a CCD camera to record chemiluminescence images of excited CH radicals in a non-premixed flame of low calorific residual gases, and employed topology analysis techniques to study the stability diagram of the flame. Kiran and Mshira [62] studied the stability characteristics of a jet diffusion LPG (liquefied petroleum gas) flame in terms of its lift-off height, length, and emission levels, which were derived from images obtained by a CCD camera. Ng et al. [63] used a high-speed camera at 500 frames per second to study the flame dynamics in a gas turbine combustor. It was found that the frequency spectrum of the mean pixel image intensity of the flame is in good agreement with the acoustic spectrum of the combustor.

Wojcik et al. [15] adopted an optical fibre probe with a photodetector to capture flame radiation for detecting flame instability in a pulverized coal-fired furnace. The optical fibre probe observed the pulverized coal flame in different zones, and transmitted the light of flame to the photodetector, where the optical signal is transformed into an electrical signal. Continuous and discrete wavelet transforms were employed to analyse the frequency structure of radiation signal. It was found that the high frequency components of both stable and unstable combustion signals are of comparable levels. The differences exist at scales corresponding to low-frequency components, which are contained mostly in signal corresponding to unstable combustion flame.

## **2.4 Burner Condition Monitoring**

This section reviews the soft computing techniques that have been used for the detection of abnormal conditions in a combustion process, the prediction of NO<sub>x</sub> emissions and the identification of flame state.

### **2.4.1 Abnormal Condition Detection in a Combustion Process**

Traditional statistical process control techniques, which are used to detect the occurrence of abnormal conditions in a process, adopt univariate control charts such as Shewhart, CUSUM (Cumulative Sum control chart) and EWMA (Exponentially Weighted Moving Average chart) to monitor separately key process variables [64]. A problem with these techniques is that they chart only a small number of process variables and examine them one at a time. These techniques are inadequate for most modern process industries. A more reliable diagnosis of an abnormal occurrence requires the simultaneous analysis of various process variables, which could be hundreds or thousands and would demand an enormous amount of data processing and system response time. One promising approach is through MSPC (Multivariate Statistical Process Control).

The MSPC techniques are based on the premise that virtually all dynamic processes have a unique noise or variation signature. Changes in these signatures may indicate that a significant change in the process, process equipment, or sensor will occur or has occurred. The MSPC techniques uses statistical modelling [65] to reduce the information collected from process variables, which can be hundreds or more. The widely used MSPC techniques include PCA (Principal Component Analysis), ICA (Independent Component Analysis) and PLS (Partial Least Square) [66-70]. Among these methods, the PCA is the most popular one due to its capability of effectively dealing with high-dimensional, noisy and highly-correlated data by projecting the data onto a lower dimensional subspace which contains the most variance of the original data [71].

The most extensive applications of the PCA-based process monitoring have been found in the manufacturing industry for product quality control [72]. Efforts have also been devoted to combustion process monitoring. Zhao et al. [73] proposed a fault detection and diagnosis framework for early fault detection and diagnosis of an MSW (Municipal Solid Waste) incinerator to improve the safety and continuity of production by using PCA. Tavares et al. [74] also reported the application of the PCA and PLS for the continuous process control of an MSW moving grate-type incinerator. The monitoring, fault detection and diagnosis of the process were achieved based on the information extracted from historical data. However, in the above-mentioned cases, the supervisions of the combustion process are realized through the measurements of global variables such as air/fuel flow rates, steam pressure and flue gas compositions, which provide the limited representation of the process inside the furnace. Previous research has suggested that the reliable identification of anomalous or off-design operation in a combustion system can be achieved by analysing the sensorial information of the flame [19]. On the other hand, the characteristics of individual flames in a multi-burner system may behave very differently from that estimated from global variables, and consequently, the drift or malfunction of an individual burner can go unnoticed until the problem becomes serious [19]. Furthermore, the PCA-based process monitoring techniques as mentioned above rely on the assumption that the process data are linear. They may not perform well in a nonlinear case.

## 2.4.2 NO<sub>x</sub> Prediction

With the increasingly stringent standards regarding the NO<sub>x</sub> emissions, the control of NO<sub>x</sub> emissions for reduced environmental impact has become a world-wide concern. Great efforts have been made to develop methodologies to understand the mechanism of the production of NO<sub>x</sub> and minimize its emissions from electrical power generation. The measurement of NO<sub>x</sub> emissions is traditionally achieved by using conventional hardware emission sensors or analysers, known as CEMS (Continuous Emission Monitoring Systems). However, the CEMS have many disadvantages such as high capital cost, drifts in measurements due to humidity and ambient temperature, long measurement time, and frequent calibration requirements [21].

Artificial neural networks (ANNs), as a viable complementary technique to conventional hardware sensors, have been used to predict pollutant emissions from fossil-fuel-fired combustion processes [21, 75-79]. Ikonen et al. [21] reported a distributed neuro-fuzzy processor for the prediction of flue gas emissions in a power plant, where the flue gas oxygen, estimates of residence time and primary air stoichiometry were used as the inputs to the model. Li et al. [75] adopted neural networks and genetic algorithms to predict NO<sub>x</sub> emission in a 500 MW<sub>e</sub> coal-fired power plant, where the speed of the coal conveyor belt, O<sub>2</sub> at the sides of the furnace and tilting position of burners were used as the model inputs. Shakil et al. [76] used a dynamic neural network to predict NO<sub>x</sub> and O<sub>2</sub> emissions from a water tube boiler fired by natural gas. The inputs of the neural network included the temperatures of superheater tubes and riser tubes, air-to-fuel ratio, mass air flow rate, and mass mixed gas flow rate.

Efforts were also made to correlate the flame optical sensorial information with the NO<sub>x</sub> emissions by using ANNs. Wang et al. [51] applied a back-propagation neural network to estimate NO<sub>x</sub> emissions from a pulverized coal boiler. A set of parameters derived from flame images (average and deviation of temperature, ignition distance) were used as the inputs of the network. Hernández et al. [80] related flame image with NO<sub>x</sub> emissions by using a SOFM (Self Organising Feature Maps) neural network. Instead of

extracting features, the whole flame image was treated as a data set and taken as the inputs of the network.

### **2.4.3 Flame State Identification**

The ANNs have also been used as a classifier for identifying flame state. Allen et al. [81] demonstrated successfully an imaging and neural network based combustion control system on a laboratory liquid-fuelled spray flame facility. The full image of the chemiluminescence radiation from excited intermediate radical OH within the flame zone was used as the input of the neural network for classifying different combustion states. Tao et al. [25] adapted the ANN and fuzzy logic into a vision-guided system for the closed loop control of air and fuel flow rates of stationary luminous flames. Flame brightness and length were used as inputs of the ANN to identify the combustion process states. Lu et al. [52] also reported notably good results from a four layers feed-forward ANN to predict the flame states. The inputs of the neural network include five parameters (i.e., length, luminous region and its centroid, brightness and luminous uniformity) extracted from flame images, which were captured by a ½ inch monochromatic CCD camera fitted with a short bandpass filter. Bae et al. [82] used a neural network to distinguish flame on/off conditions from the analysis of luminosity distributions.

## 2.5 Summary

This chapter has reviewed firstly the existing flame monitoring techniques, including laser-based techniques, chemiluminescence imaging, imaging-based pyrometry, broadband imaging and photo-detector, and secondly the work that have been reported on flame stability and burner condition monitoring.

As can be seen from the cited work (Section 2.3), although a variety of flame monitoring techniques have been developed, very limited work has focused on flame stability monitoring. The main challenges of developing flame stability monitoring technique suitable for practical uses reside in two aspects. First, there is no widely accepted method for assessing the flame stability. No matter what kind of flame sensorial data are available, PLIF images, chemiluminescent radiation maps, pyrometry-derived temperature maps, non-filtered images, or flame radiation signals, how to produce a procedure to process the data and evaluate the stability of the flame is not clear. Second, challenges are also associated with practical issues, such as system installation in the combustion chamber and the protection of system from high temperature and fouling.

In the field of burner condition monitoring, as can be seen from the cited work (Section 2.4), soft computing techniques have been widely used to deal with the issues of fault detection,  $\text{NO}_x$  predication, and flame states identification. However, most of the work used global variables as the combustion process data (e.g., flow rates, pressure and flue gas composition, which provide very limited description of the process taking place inside the combustion chamber); very limited work has taken the flame characteristics into account due to the lack of suitable sensing and characterisation techniques. Moreover, the soft computing techniques used in these cases suffer from shortcomings as follows. For the fault detection, the widely used PCA-based technique has the assumption that the process data are linear. However, when a process is nonlinear, the monitoring of a process using a linear PCA model cannot perform properly. For the  $\text{NO}_x$  predication and flame state identification, ANNs are commonly used to correlate the combustion process data with the  $\text{NO}_x$  emissions or the flame states. However,

research work has suggested that the ANNs are prone to overtraining and can suffer from multiple local minima. With the progress of soft computing technologies, more advanced algorithms could be utilized to provide a better solution to these issues.

The literature review has clearly demonstrated that there is a certain gap between the existing technology for flame stability and burner condition monitoring and the requirements of industry. Based on the literature review, an instrumentation system incorporating broadband imaging and photodetector techniques is thought to be a promising and feasible solution. Unlike active laser-based techniques, it does not need any external illuminations/seeding; it is practical for industrial use; and the cost is much lower. Compared with the chemiluminescence and pyrometric imaging techniques, the hardware requirements of the system are relatively less demanding (no requirements for narrow band filters or expensive intensified cameras), and the applications are not restricted by flame properties (chemiluminescence imaging commonly applies to gaseous flames, and imaging-based pyrometry only applies to soot-laden flames).

## Chapter 3

### Theory of Flame Stability and Burner Condition Monitoring

#### 3.1 Introduction

This chapter presents the data-processing methods for flame stability and burner condition monitoring. The methods presented are based on the flame optical sensorial information captured by broadband imaging and photodetector, which have been identified (Chapter 2) as the most suitable flame sensing techniques for practical use in industrial furnaces.

Firstly, the chapter presents the image processing and spectral analysis techniques for flame stability monitoring, covering the following three different approaches:

- Evaluating the standard deviations of flame parameters that characterise a flame
- Analysing the power spectral density estimates and oscillation frequency of flame radiation signal
- Computing a universal flame stability index, which is proposed in this chapter and designed by combining the dynamic characteristics of seven parameters extracted from flame images in HSI (Hue, Saturation, Intensity) colour space

Then, the chapter gives the theory of soft computing techniques for burner condition monitoring, covering the following aspects:

- KPCA (Kernel Principal Components Analysis) technique for detecting abnormal conditions in a combustion process
- SVM (Support Vector Machines) technique for identifying flame state with respect to states previously characterised and predicting  $\text{NO}_x$  emissions

Lastly, the chapter depicts the measurement principle of soot temperature, emissivity and concentration in soot-laden flames.

## 3.2 Image Processing and Spectral Analysis Techniques for Flame Stability Monitoring

### 3.2.1 Standard Deviation of Flame Parameters

Since a noticeable phenomenon of an unstable flame is the large variation of its characteristic parameters, it is natural to consider using the variation of flame parameters as an indication of flame stability. A number of flame characteristic parameters can be extracted through digital imaging and image processing techniques, such as flame size, shape, brightness, oscillation frequency, and temperature distribution [3, 7, 11, 44]. These parameters characterise a flame in terms of its nature of geometry, luminance, and thermodynamics. The standard deviations of these parameters therefore can be used to reflect the variation and hence the stability of the flame.

The standard deviation of a parameter  $x$  is defined as follows,

$$\sigma_x = \left( \frac{1}{N-1} \sum_{i=1}^N (x_i - \mu_x)^2 \right)^{\frac{1}{2}}, \quad (3-1)$$

where  $\mu_x = \frac{1}{N} \sum_{i=1}^N x_i$ , and  $N$  is the number of readings of  $x$ .

Statistically, a low standard deviation of the parameter  $x$  indicates that the data points tend to be very close to the mean, indicating a stable state of the flame in terms of the parameter  $x$ , whereas a high standard deviation indicates that the data points are spread out over a large range of values, indicating the flame is unstable in terms of  $x$ .

### 3.2.2 Power Spectral Analysis and Oscillation Frequency

The second approach for the flame stability monitoring is through analysing the PSD (Power Spectral Density) estimates and oscillation frequency of the flame radiation signal captured by photodetector.

It has been observed that a turbulent flame in an industrial combustion system pulsates irregularly. The pulsation of the flame is referred to as “flickering”, whose characteristic can be reflected in the PSD estimates of the flame radiation signal. The PSD of a signal is defined as

$$p_i = \frac{1}{N} \left| \sum_{i=0}^{N-1} s_i e^{-j2\pi f_i} \right|^2, \quad (3-2)$$

where  $s_i$  is the  $i^{\text{th}}$  sample point of the signal,  $N$  is the signal length,  $f_i$  is the  $i^{\text{th}}$  frequency, and  $p_i$  is the power density of the  $i^{\text{th}}$  frequency component.

A quantitative frequency, known as oscillation frequency of the flame, can be computed from the PSD estimates. It is defined as the power-density-weighted average frequency of flame signal over the entire frequency range, and the weighting factors are the power densities of individual frequency components [7], i.e.,

$$F = \frac{\sum_{i=1}^n p_i f_i}{\sum_{i=1}^n p_i}, \quad (3-3)$$

where  $F$  is the oscillation frequency,  $f_i$  is the  $i^{\text{th}}$  frequency,  $p_i$  is the power density of the  $i^{\text{th}}$  frequency component, and  $n$  is the number of frequency components.

The PSD estimates of a flame radiation signal include various frequency components for a number of reasons [17]. The DC component is believed to depend on the volatility of the fuel, the size of the flame, and the brightness of the hot surrounding environment. The low frequency components in the flame signal are mainly attributed to its geometrical fluctuations due to aerodynamic or convective effects. The high frequency components reflect kinetic variations in the heat release rate of the reacting species or vibrational rotational energy transitions in intermediate radicals. These facts suggest that the PSD estimates and the oscillation frequency of the flame radiation signal can be used to assess the flame stability. Previous research has revealed that an unstable flame might result in high amplitude of low frequency components in its PSD estimates and a low oscillation frequency [7].

### 3.2.3 Universal Flame Stability Index

Visualization methods have been historically an invaluable diagnostic tool in combustion science. The 2-D images of a flame give visual and spatial information on the flame. An attempt has been made in the present work to assess the flame stability through the statistical analysis of flame colour images. A simple universal stability index is proposed here. By “universal”, we mean that the measurement approach can be applicable to various combustion cases without ad-hoc adaption.

The proposed simple universal stability index combines the dynamic characteristics of seven parameters derived from flame images in HSI (Hue, Saturation, and Intensity) space. It assesses the flame stability in the aspects of colour, geometry, and luminance. Figure 3.1 shows the measurement procedure of the proposed index, which can be divided into three steps: conversion of colour space, extraction of image features, and data fusion.

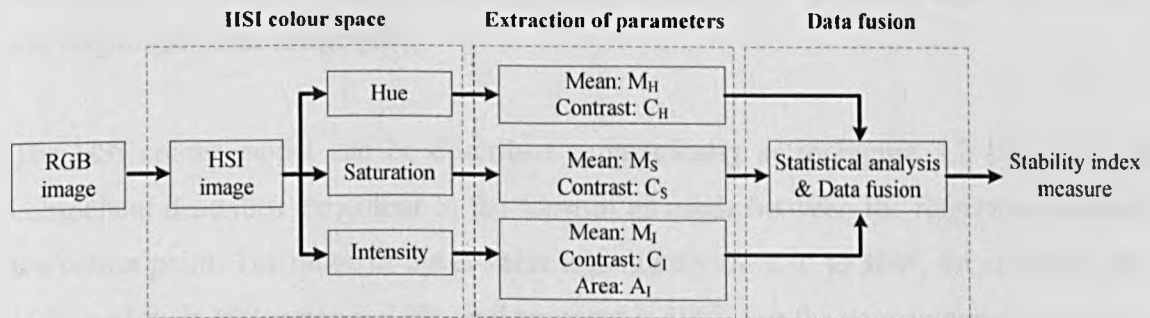


Figure 3.1 Measurement procedure of the universal flame stability index

#### 3.2.3.1 Conversion of Colour Space from RGB to HSI

The first step is to convert the format of the colour flame image from a RGB format to HSI.

The colour characteristics of a flame are closely linked with the flame emission spectra and depend on fuel properties and fuel-to-air ratio. The stability of the flame colour characteristics therefore should be taken into a consideration when assessing the overall flame stability. However, the original image captured by a colour camera is generally in RGB format, which is useful for colour display but not good for colour analysis due to the high correlation among R (Red), G (Green), and B (Blue) components [83]. In the RGB colour space, the colour and intensity are inseparably stored in the three primary colour components. When the intensity changes, all the three components will change accordingly.

The HSI model is another commonly used colour space in image processing, which separates the colour information of an image from its intensity information. Similar to the RGB model, the HSI model has three separate channels, corresponding to Hue (H), Saturation (S), and Intensity (I). The H component represents the dominant wavelength in the spectral distribution of light wavelengths, indicating basic colours. The S component is the measure of the purity of the colour, denoting the amount of white light mixed with the hue. The I component is determined by the amount of light, describing the brightness of an image [83].

The HSI colour model can be described geometrically as in Figure 3.2 [84]. The H component describes the colour in the form of an angle between the reference line and the colour point. The range of the H value is generally from  $0^\circ$  to  $360^\circ$ , for example, red is  $0^\circ$ , yellow is  $60^\circ$ , green is  $120^\circ$ , and magenta is  $300^\circ$ . For the convenience of analysis, the H value is normalized by  $360^\circ$  in the present study. The S component represents the perpendicular distance from the colour point to the axis. The range of S is [0, 1]. The nearer the point is to the centre axis, the lighter is the colour. The I component is the height of the colour point in the axis direction, ranging from 0 to 1. 0 represents black, while 1 means white. Each slice perpendicular to the axis is a plane with the same intensity.

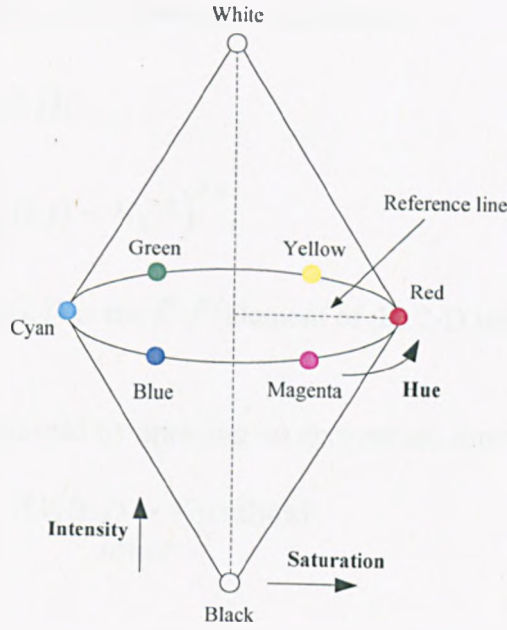


Figure 3.2 HSI colour space

The HSI coordinates can be transformed from the RGB space as follows [85]:

$$H = \begin{cases} \cos^{-1} \left\{ \frac{\frac{1}{2}[(R-G)+(R-B)]}{\sqrt{[(R-G)^2 + (R-B)(G-B)]^2}} \right\} / 360^\circ, & \text{if } B \leq G \\ 1 - \cos^{-1} \left\{ \frac{\frac{1}{2}[(R-G)+(R-B)]}{\sqrt{[(R-G)^2 + (R-B)(G-B)]^2}} \right\} / 360^\circ, & \text{if } B > G \end{cases} \quad (3-4)$$

$$S = 1 - \frac{3}{R+G+B} \times [\min(R, G, B)], \quad (3-5)$$

$$I = \frac{R+G+B}{3}. \quad (3-6)$$

### 3.2.3.2 Extraction of Image Features

From an HSI image, seven parameters, assigned as  $M_H$ ,  $M_S$ ,  $M_I$ ,  $C_H$ ,  $C_S$ ,  $C_I$ , and  $A_I$ , are extracted.  $M_H$ ,  $M_S$ , and  $M_I$  denote the mean values of H, S and I components, respectively, while  $C_H$ ,  $C_S$ , and  $C_I$  are the contrast values of the three components.  $A_I$  represents the flame area that is derived from the I image.

The mean  $M_k$  and contrast  $C_k$  of an image are defined as

$$M_k = \frac{1}{P \times Q} \sum_{i=0}^{P-1} \sum_{j=0}^{Q-1} V_k(i, j), \quad (3-7)$$

$$C_k = \left( \frac{1}{P \times Q} \sum_{i=0}^{P-1} \sum_{j=0}^{Q-1} (V_k(i, j) - M_k)^2 \right)^{0.5}, \quad (3-8)$$

where  $k = H, S, I$ , and  $V_k(i, j)$  is the  $i^{\text{th}}$ - $j^{\text{th}}$  element of the 2-D image of size  $P$  by  $Q$ .

The flame area  $A_I$  is determined by applying an appropriate threshold to the I image, i.e.,

$$A_I = \frac{1}{P \times Q} \sum_{i=0}^{P-1} \sum_{j=0}^{Q-1} \begin{cases} 1, & \text{if } V_I(i, j) > \text{Threshold} \\ 0, & \text{other} \end{cases}. \quad (3-9)$$

### 3.2.3.3 Data Fusion

Following the above, the universal stability index is defined as the combination of the standard deviations of the extracted parameters in the form as

$$\delta = \prod_{i=1}^n \left( \frac{|\sigma_{P_i}|_{\max} - \sigma_{P_i}}{|\sigma_{P_i}|_{\max}} \right)^{w_i} \in [0, 1], \quad (3-10)$$

where  $P_i \in \{M_H, M_S, M_I, C_H, C_S, C_I, A_I\}$ ,  $\sigma_{P_i}$  is the standard deviation of parameter  $P_i$ ,  $|\sigma_{P_i}|_{\max}$  is the theoretical maximum standard deviation of  $P_i$ ,  $n$  is the number of flame parameters considered, which is seven in the present study, and  $w_i$  is the weight for the corresponding parameter  $P_i$ . A larger weight can be given to a parameter that is more significant. In the present work,  $w_i$  equals to 2 for all parameters.

The theoretical maximum standard deviation of a parameter depends on the dynamic range and probability distribution of the parameter. Suppose  $x = \{x_i | i = 1, 2, \dots, N, x_i \in [0, L]\}$ , with an unknown probability distribution, the mean and standard deviation of  $x$  can be expressed as

$$\mu_x = \frac{1}{N} \sum_{i=1}^N x_i, \quad (3-11)$$

$$\sigma_x = \left( \frac{1}{N} \sum_{i=1}^N (x_i - \mu_x)^2 \right)^{\frac{1}{2}} \quad (3-12)$$

The range of  $\sigma_x$  can be determined by expanding (3-12), i.e.,

$$\begin{aligned} \sigma_x &= \left( \frac{1}{N} \sum_{i=1}^N \left( \left( x_i - \frac{L}{2} \right) - \left( \mu_x - \frac{L}{2} \right) \right)^2 \right)^{\frac{1}{2}} \\ &= \left( \frac{1}{N} \sum_{i=1}^N \left( x_i - \frac{L}{2} \right)^2 - \frac{2}{N} \sum_{i=1}^N \left( x_i - \frac{L}{2} \right) \cdot \left( \mu_x - \frac{L}{2} \right) + \frac{1}{N} \sum_{i=1}^N \left( \mu_x - \frac{L}{2} \right)^2 \right)^{\frac{1}{2}} \\ &= \left( \frac{1}{N} \sum_{i=1}^N \left( x_i - \frac{L}{2} \right)^2 - 2 \cdot \left( \mu_x - \frac{L}{2} \right) \cdot \frac{1}{N} \sum_{i=1}^N \left( x_i - \frac{L}{2} \right) + \left( \mu_x - \frac{L}{2} \right)^2 \right)^{\frac{1}{2}} \\ &= \left( \frac{1}{N} \sum_{i=1}^N \left( x_i - \frac{L}{2} \right)^2 - \left( \mu_x - \frac{L}{2} \right)^2 \right)^{\frac{1}{2}} \\ &\leq \left( \frac{1}{N} \sum_{i=1}^N \left( \left| x_i - \frac{L}{2} \right|_{max} \right)^2 \right)^{\frac{1}{2}} \\ &\leq \frac{L}{2} \end{aligned} \quad (3-13)$$

Thus, the theoretical maximum standard deviation  $\sigma_x$  of the parameter  $x$  is the half of the dynamic range of  $x$ , i.e.,  $\frac{L}{2}$ , and it can be achieved if and only if  $\mu_x = \frac{L}{2}$  and  $x_i = 0$  or  $L$ ,  $i = 1, 2, \dots, N$ . The dynamic ranges of H, S, and I, i.e.,  $[0, 1]$ , determine that  $M_H$ ,  $M_S$ ,  $M_I$ , and  $A_I \in [0, 1]$ , and  $C_H$ ,  $C_S$ ,  $C_I \in [0, 0.5]$ . Therefore,  $|\sigma_{M_H}|_{max}$ ,  $|\sigma_{M_S}|_{max}$ ,  $|\sigma_{M_I}|_{max}$  and  $|\sigma_{A_I}|_{max}$  are 0.5, while  $|\sigma_{C_H}|_{max}$ ,  $|\sigma_{C_S}|_{max}$  and  $|\sigma_{C_I}|_{max}$  are 0.25.

The features of the proposed index are as follows:

- The index evaluates the flame stability through analysing dynamic characteristics of colour, luminance and geometry of the flame. The colour is described by hue and saturation components, and the intensity component contains information on geometry and luminance.
- The measurement procedure does not require any adaption for new applications, regardless of fuel types, boiler structure and combustion conditions.
- The index has a fixed boundary, ranging from 0 to 1, which is desirable in metrology. The best value 1 is achieved if and only if all parameters are constant with time, indicating completely a stable state. The lowest value 0 occurs when the standard deviation of any parameter reaches its theoretical maximum value, indicating an extremely unstable state.
- The index is computationally simple, suitable for on-line measurement.

### 3.3 Soft Computing Techniques for Burner Condition Monitoring

This section firstly gives the definitions of the flame characteristics that are used as the process variables of a combustion process and the inputs of the KPCA and SVM for the burner condition monitoring. Then, it describes the theory of the KPCA and its work flow in the detection of abnormal conditions. Finally, it presents the theory of the SVM and its work flow in flame state identification and  $\text{NO}_x$  prediction.

#### 3.3.1 Flame Characteristics Used for KPCA and SVM Models

Generally, the number of flame characteristics that are measured can vary, depending upon the nature of the flame and the purpose of the measurement. In the present study, the selection of flame characteristic for the burner condition monitoring are based on the premise that the measurement approach of the characteristic does not depend on the fuel property, burner type, and combustion condition, and therefore can be applicable to various cases without ad-hoc adaption. The flame characteristics that may exist only under some particular conditions are of less interest and so are not considered. For example, flame ignition points are very important characteristics of a flame, indicating the stability position of the flame. However, it can be observed only from the flame that is detached from the nozzle; for an undetached flame, the flame ignition points are not applicable.

##### 3.3.1.1 Characteristics of Flame Radiation Signals

From flame radiation signals, characteristic parameters are extracted in time, frequency, and joint time-frequency domains.

Time domain parameters include DC, AC, skewness, and kurtosis. DC and AC indicate the intensity and turbulent fluctuations of the flame, respectively. Skewness and kurtosis are measures of the asymmetry and peakedness of the probability distribution of the signal in the time domain, respectively. They are denoted as

$$\bar{s} = \frac{1}{N} \sum_{i=1}^N s_i, \quad (3-14)$$

$$\tilde{s} = \sqrt{\frac{1}{N} \sum_{i=1}^N (s_i - \bar{s})^2}, \quad (3-15)$$

$$s_{ske} = \frac{1}{N} \sum_{i=1}^N \left( \frac{s_i - \bar{s}}{\tilde{s}} \right)^3, \quad (3-16)$$

$$s_{kur} = \frac{1}{N} \sum_{i=1}^N \left( \frac{s_i - \bar{s}}{\tilde{s}} \right)^4, \quad (3-17)$$

where  $s_i$  is the  $i^{\text{th}}$  sample point of a flame radiation signal, and  $N$  is the signal length.

Frequency domain adopts the flame oscillation frequency as its characteristic, which is given in (3-3) as the power-density-weighted average frequency over the entire frequency range.

In the joint time-frequency domain, flame parameters are extracted using wavelet analysis. Wavelet algorithms process a signal at different resolutions and thus have advantages in analysing situations where the signal contains discontinuities and sharp spikes [86]. In the present study, one-dimensional Daubechies wavelet db1 [87] is performed to decompose the flame signals to 6 levels, corresponding to seven different frequency bands as illustrated in Table 3.1. The energy contained in each band is taken as the characteristic parameter of that band, i.e.,

$$E_b = \sum_{b=1}^{N_b} CW_b(i)^2, \quad (3-18)$$

where  $b = A_6, D_6, D_5, \dots, D_1$ ,  $CW_b(i)$  is the  $i^{\text{th}}$  coefficient at band  $b$ , and  $N_b$  is the number of coefficients at band  $b$ . The seven bands correspond to detail coefficients at levels 1~6 and approximation coefficients at level 6.

Table 3.1 Frequency ranges of wavelet subspace

Wavelet subspace	$A_6$	$D_6$	$D_5$	$D_4$	$D_3$	$D_2$	$D_1$
Frequency range/Hz	0~7	8~15	16~31	32~63	64 ~127	128 ~255	256 ~511

### 3.3.1.2 Characteristics of Flame Images

From flame images, a number of geometric and luminous parameters are extracted [22]. The definitions of these parameters are given as follows.

Luminous region ( $R_f$ ): calculated by counting the number of pixels within a flame image (FI) with an appropriate threshold,  $\delta$ , i.e.,

$$R_f = \sum_{i \in FI} \sum_{j \in FI} \begin{cases} 1, & \text{if } G(i, j) \geq \delta \\ 0, & \text{other} \end{cases}, \quad (3-19)$$

where  $G(i, j)$  is the grey-level intensity of the  $i^{\text{th}}$ - $j^{\text{th}}$  element of the two-dimensional flame image, and  $\delta$  is the threshold that is used to define the luminous region.

Brightness ( $B_f$ ): defined as the mean grey-level of the luminous region of the flame normalized to the full-scale grey-level of the imaging system, i.e.,

$$B_f = \frac{1}{|R_f|} \sum_{i \in R_f} \sum_{j \in R_f} \frac{G(i, j)}{255} \times 100\%. \quad (3-20)$$

Non-uniformity ( $U_f$ ): represented by the average deviation of the grey-levels of individual pixels over the luminous region from the brightness, i.e.,

$$U_f = \frac{1}{R_f B_f} \sum_{i \in R_f} \sum_{j \in R_f} \left| \frac{G(i, j)}{255} - B_f \right| \times 100\%. \quad (3-21)$$

### 3.3.2 KPCA for Abnormal Condition Detection in a Combustion Process

Efficiency, reliability and safety are important issues in industrial process monitoring. Unlike traditional linear PCA based multivariate statistical process control, the KPCA model adopts the kernel method and thus is capable of handling nonlinear relationships between the variables that are used to characterise an industrial process. To detect

abnormal conditions in a combustion process, flame characteristics that are taken under known normal operating combustion condition should be used to train the KPCA model. The fitness of the new data to the constructed the KPCA model, measured by Hotelling's  $T^2$  statistic and Q statistic, can then be used for the indication of unusual variability within the normal space, and hence the detection of anomalous or off-design condition in a combustion system.

In this section, the principle of the KPCA and Hotelling's  $T^2$  and Q statistics is presented, following by the detailed work flow of the KPCA for the detection of abnormal conditions in a combustion process.

### 3.3.2.1 Kernel Principal Component Analysis

A detailed description of KPCA can be found in [88, 89]. Given a set of nonlinear data with zero mean,  $\mathbf{x}_k \in R^m$ ,  $m$  is the dimension of the data space,  $k = 1, \dots, N$ ,  $\sum_{k=1}^N \mathbf{x}_k = \mathbf{0}$ , the key idea of the KPCA is to project  $\mathbf{x}_k$  in the input space into a high-dimensional space, known as the feature space, through nonlinear mapping  $\Phi(\cdot)$ , so that the mapped data  $\Phi(\mathbf{x}_k)$  in the feature space can be linearly distributed. Kernel-based methods allow that the dot product of two vectors  $\Phi(\mathbf{x}_i)$  and  $\Phi(\mathbf{x}_j)$  in the feature space can be calculated as the function of corresponding vectors  $\mathbf{x}_i$  and  $\mathbf{x}_j$ , i.e.,

$$\langle \Phi(\mathbf{x}_i), \Phi(\mathbf{x}_j) \rangle = k(\mathbf{x}_i, \mathbf{x}_j), \quad (3-22)$$

thus, there is no need to explicitly define or carry out the nonlinear mapping  $\Phi(\cdot)$ . The function  $k(\cdot, \cdot)$  is called the kernel function. There exist a number of representative kernel functions as follows [90]:

- Polynomial kernel:

$$k(\mathbf{x}_i, \mathbf{x}_j) = \langle \mathbf{x}_i, \mathbf{x}_j \rangle^d, \quad (3-23)$$

- Sigmoid kernel:

$$k(\mathbf{x}_i, \mathbf{x}_j) = \tanh(\beta_0 \langle \mathbf{x}_i, \mathbf{x}_j \rangle + \beta_1), \quad (3-24)$$

- Radial basis kernel:

$$k(\mathbf{x}_i, \mathbf{x}_j) = \exp\left(-\|\mathbf{x}_i - \mathbf{x}_j\|^2 / c\right), \quad (3-25)$$

where  $d$ ,  $\beta_0$ ,  $\beta_1$  and  $c$  are specified by the user.

The computation of the eigenvectors in the feature space is similar to that of the PCA. The covariance matrix  $\bar{\mathbf{C}}$  in the feature space can be expressed as

$$\bar{\mathbf{C}} = \frac{1}{N} \sum_{i=1}^N \Phi(\mathbf{x}_i) \Phi(\mathbf{x}_i)^T, \quad (3-26)$$

where it is assumed that the mapped data in the feature space are centred, i.e.,  $\sum_{k=1}^N \Phi(\mathbf{x}_k) = \mathbf{0}$ . The diagonalization of the covariance matrix  $\bar{\mathbf{C}}$  requires solving eigenvalue equation

$$\lambda \mathbf{v} = \bar{\mathbf{C}} \mathbf{v}, \quad (3-27)$$

where  $\lambda \geq 0$  and  $\mathbf{v}$  represent eigenvalue and eigenvector, respectively. Equation (3-27) is equivalent to

$$\lambda \langle \Phi(\mathbf{x}_k), \mathbf{v} \rangle = \langle \Phi(\mathbf{x}_k), \bar{\mathbf{C}} \mathbf{v} \rangle, \quad (3-28)$$

for all  $k = 1, \dots, N$ . Because all solutions  $\mathbf{v}$  with  $\lambda \neq 0$  lie in the span of  $\Phi(\mathbf{x}_1), \dots, \Phi(\mathbf{x}_N)$ , there exist coefficients  $\beta_i$ , ( $i = 1, 2, \dots, N$ ) such that

$$\mathbf{v} = \sum_{i=1}^N \beta_i \Phi(\mathbf{x}_i). \quad (3-29)$$

Substituting (3-26) and (3-29) into (3-28) yields

$$\lambda \sum_{i=1}^N \beta_i \langle \Phi(\mathbf{x}_k), \Phi(\mathbf{x}_i) \rangle = \frac{1}{N} \sum_{i=1}^N \beta_i \langle \Phi(\mathbf{x}_k), \sum_{j=1}^N \Phi(\mathbf{x}_j) \rangle \langle \Phi(\mathbf{x}_j), \Phi(\mathbf{x}_i) \rangle, \quad (3-30)$$

for all  $k = 1, \dots, N$ . It is clear that, in (3-30), only the computations of the dot products of mapped vectors in feature space are required, and they can be done easily through the kernel function, as illustrated in (3-22).

To obtain coefficients  $\beta_i$  ( $i = 1, 2, \dots, N$ ), define an  $N \times N$  kernel matrix  $\mathbf{K}$  by its  $i^{\text{th}}$ - $j^{\text{th}}$  element  $K_{ij}$ ,

$$K_{ij} = \langle \Phi(\mathbf{x}_i), \Phi(\mathbf{x}_j) \rangle. \quad (3-31)$$

Then, (3-30) can be rewritten as

$$\lambda \sum_{i=1}^N \beta_i K_{ki} = \frac{1}{N} \sum_{i=1}^N \beta_i \sum_{j=1}^N K_{kj} K_{ji}, \quad (3-32)$$

for all  $k = 1, \dots, N$ . This leads

$$\lambda \mathbf{K} \boldsymbol{\beta} = \frac{1}{N} \mathbf{K}^2 \boldsymbol{\beta}, \quad (3-33)$$

where  $\boldsymbol{\beta} = [\beta_1, \dots, \beta_N]^T$ . The solution of (3-33) can be found through solving the eigenvalue problem [88], i.e.,

$$\lambda \boldsymbol{\beta} = \frac{1}{N} \mathbf{K} \boldsymbol{\beta}. \quad (3-34)$$

Let  $\lambda_1 \geq \lambda_2 \geq \dots \geq \lambda_N$  and  $\boldsymbol{\beta}^1, \boldsymbol{\beta}^2, \dots, \boldsymbol{\beta}^N$  represent the eigenvalues and corresponding complete set of eigenvectors of problem (3-34), respectively, then the normalization of  $\mathbf{v}_k$  in the feature space, i.e., realization of

$$\langle \mathbf{v}_k, \mathbf{v}_k \rangle = 1, \quad (3-35)$$

for all  $k = 1, \dots, p$ , can be done through scaling corresponding  $\boldsymbol{\alpha}^k$  by factor  $1/\sqrt{\lambda_k}$ . This can be justified by substituting  $\mathbf{v}_k = \sum_{i=1}^N \alpha_i^k \Phi(\mathbf{x}_i)$  into (3-35),

$$\begin{aligned} 1 &= \sum_{i=1}^N \sum_{j=1}^N \beta_i^k \beta_j^k \langle \Phi(\mathbf{x}_i), \Phi(\mathbf{x}_j) \rangle \\ &= \sum_{i=1}^N \sum_{j=1}^N \beta_i^k \beta_j^k K_{ij} \\ &= \langle \boldsymbol{\beta}^k, \mathbf{K} \boldsymbol{\beta}^k \rangle \\ &= \lambda_k \langle \boldsymbol{\beta}^k, \boldsymbol{\beta}^k \rangle. \end{aligned} \quad (3-36)$$

After solving the problem (3-34), the kernel principal components vector  $\mathbf{t}$  of a test vector  $\mathbf{x}_t$  can be calculated by projecting  $\Phi(\mathbf{x}_t)$  onto the eigenvectors  $\mathbf{v}_k$  in feature space, i.e.,

$$t_k = \langle \mathbf{v}_k, \Phi(\mathbf{x}_t) \rangle = \sum_{i=1}^N \beta_i^k \langle \Phi(\mathbf{x}_i), \Phi(\mathbf{x}_t) \rangle, \quad (3-37)$$

where  $\beta_i^k$  is the  $i^{\text{th}}$  element of the eigenvector  $\boldsymbol{\beta}^k$  in (3-34),  $k = 1, \dots, p$ , and  $p$  is the number of kernel principal components retained.

It should be noted that the assumption  $\sum_{k=1}^N \Phi(\mathbf{x}_k) = \mathbf{0}$  in (3-26) can be realized by substituting the kernel matrix  $\mathbf{K}$  with

$$\tilde{\mathbf{K}} = \mathbf{K} - \mathbf{1}_N \mathbf{K} - \mathbf{K} \mathbf{1}_N + \mathbf{1}_N \mathbf{K} \mathbf{1}_N, \quad (3-38)$$

where  $\mathbf{1}_N \in R^{N \times N}$ , and all elements of  $\mathbf{1}_N$  have same value of  $\frac{1}{N}$ .

### 3.3.2.2 Hotelling's $T^2$ Statistic and Q Statistic

Once the KPCA model of a combustion process is trained, the occurrence of abnormal conditions can be judged by computing the variation of new data within the model as well as the fitness of the new data to the model.

Suppose the kernel principal components vector of new data  $\mathbf{x}_{\text{new}}$  is denoted as  $\mathbf{t}' = [t'_1, \dots, t'_p]$ , where  $\mathbf{t}'$  is derived from (3-37). The variation of  $\mathbf{x}_{\text{new}}$  within the KPCA model can be assessed by Hotelling's  $T^2$  statistic, known as Mahalanobis distance, i.e.,

$$T^2 = [t_1, \dots, t_p] \Lambda^{-1} [t_1, \dots, t_p]^T, \quad (3-39)$$

where  $\Lambda^{-1}$  is the diagonal matrix of the inverse of eigenvalues  $(\lambda_1, \dots, \lambda_p)$ . The goodness-of-fit of  $\mathbf{x}_{\text{new}}$  to the KPCA model can be assessed by Q statistic, known as SPE (Squared Prediction Error) [89], i.e.,

$$Q = \sum_{j=1}^n t_j^2 - \sum_{j=1}^p t_j^2. \quad (3-40)$$

An abnormal condition is identified if both  $T^2$  and  $Q$  statistics exceed their confidence limits. The confidence limit of  $T^2$  statistic can be obtained by the means of  $F$ -distribution, i.e.,

$$T_{p,N,\alpha}^2 \sim \frac{p(N-1)}{N-p} F_{p,N-p,\alpha}, \quad (3-41)$$

where  $F_{p,N-p,\alpha}$  is the  $F$ -distribution with  $p$  and  $N$  degrees of freedom with the significance level of  $100(1 - \alpha)\%$ . In this study,  $p$  is the number of PCs and  $N$  is the number of samples in the KPCA model. The confidence limit of  $Q$  statistic can be computed from its approximate distribution,  $Q_\alpha \sim g x_h^2$ , i.e.,

$$Q_\alpha = \theta_1 \left[ 1 + \frac{\theta_2 h_0 (h_0 - 1)}{\theta_1^2} + \frac{z_\alpha \sqrt{2\theta_2 h_0^2}}{\theta_1} \right]^{1/h_0}, \quad (3-42)$$

where  $\theta_i = \sum_{j=p+1}^N \lambda_j^i$  ( $i = 1, 2$ ),  $h_0 = 1 - (2\theta_1\theta_2/3\theta_2^2)$ , and  $z_\alpha$  is the standard normal deviate corresponding to the upper  $100(1 - \alpha)\%$ .

### 3.3.2.3 Work Flow of KPCA

Like MSPC techniques, the KPCA based process monitoring is also based on the promise that virtually all dynamic process has a unique noise or variation signature. Changes in these signatures may indicate that a significant change in the process, process equipment, or sensor has occurred or will occur. The utilization of the KPCA for combustion process monitoring involves two procedures, i.e., KPCA training, and on-line monitoring.

#### A. KPCA Training Procedure

The training of the KPCA model of a combustion process is achieved by using the above-described KPCA algorithm to process the flame characteristics obtained under the normal combustion condition to derive the kernel matrix  $\mathbf{K}$  in (3-31), and its eigenvalues  $\lambda_1, \dots, \lambda_N$  and eigenvectors  $\beta^1, \beta^2, \dots, \beta^N$  in (3-34). The derived information

defines the KPCA model of the combustion process under the normal condition. The detailed procedure of KPCA training can be summarized as follows:

- (1) Acquire flame sensorial information (flame images and radiation signals) under the normal combustion condition.
- (2) Extract flame characteristics from raw data, as described in Section 3.3.1.
- (3) Scale the data using the mean and standard deviation of each characteristic.
- (4) Suppose  $N$  samples of  $m$  flame characteristics are used as the inputs of KPCA training procedure, compute the kernel matrix  $\mathbf{K}$  of the input data, as in (3-31).
- (5) Centre the kernel matrix  $\mathbf{K}$ ,  $\tilde{\mathbf{K}} = \mathbf{K} - \mathbf{1}_N \mathbf{K} - \mathbf{K} \mathbf{1}_N + \mathbf{1}_N \mathbf{K} \mathbf{1}_N$ , as in (3-38).
- (6) Calculate eigenvectors  $\beta^1, \beta^2, \dots, \beta^N$  by solving the eigenvalue problem,  $\lambda \beta = \frac{1}{N} \mathbf{K} \beta$ , as in (3-34), and normalize  $\beta^k$  by  $1/\sqrt{\lambda_k}$ , as in (3-36).
- (7) Determine the control limits of  $T^2$  and  $Q$  statistics, as in (3-41) and (3-42).

### B. Online Monitoring Procedure

Figure 3.3 shows the flow chart of the KPCA based online monitoring procedure, which can be summarized as follows:

- (1) Acquire new flame raw sensorial information under test condition.
- (2) Extract flame characteristics from new data.
- (3) Scale the data using the mean and standard deviation of each characteristic obtained from training procedure.
- (4) Compute kernel vector  $K_t$ ,  $[K_t]_i = k(\mathbf{x}_t, \mathbf{x}_i)$ , where  $\mathbf{x}_t \in \mathbb{R}^m$  is the scaled test data, and  $\mathbf{x}_i$  is the normal operating data used in training procedure,  $i = 1, \dots, N$ .
- (5) Centre the test kernel vector  $K_t$ ,  $\tilde{K}_t = K_t - \mathbf{1}_t \mathbf{K} - K_t \mathbf{1}_N + \mathbf{1}_t \mathbf{K} \mathbf{1}_N$ , where  $\mathbf{K}$  is the kernel matrix derived in training procedure.
- (6) Extract principal components via  $t_k = \langle \mathbf{v}_k, \Phi(\mathbf{x}_t) \rangle = \sum_{i=1}^N \alpha_i^k \langle \Phi(\mathbf{x}_t), \Phi(\mathbf{x}_i) \rangle$ .
- (7) Calculate the  $T^2$  and  $Q$  statistics of the test data  $\mathbf{x}_t$ .
- (8) To identify an abnormal condition if both  $T^2$  and  $Q$  statistics exceed the confidence limits.

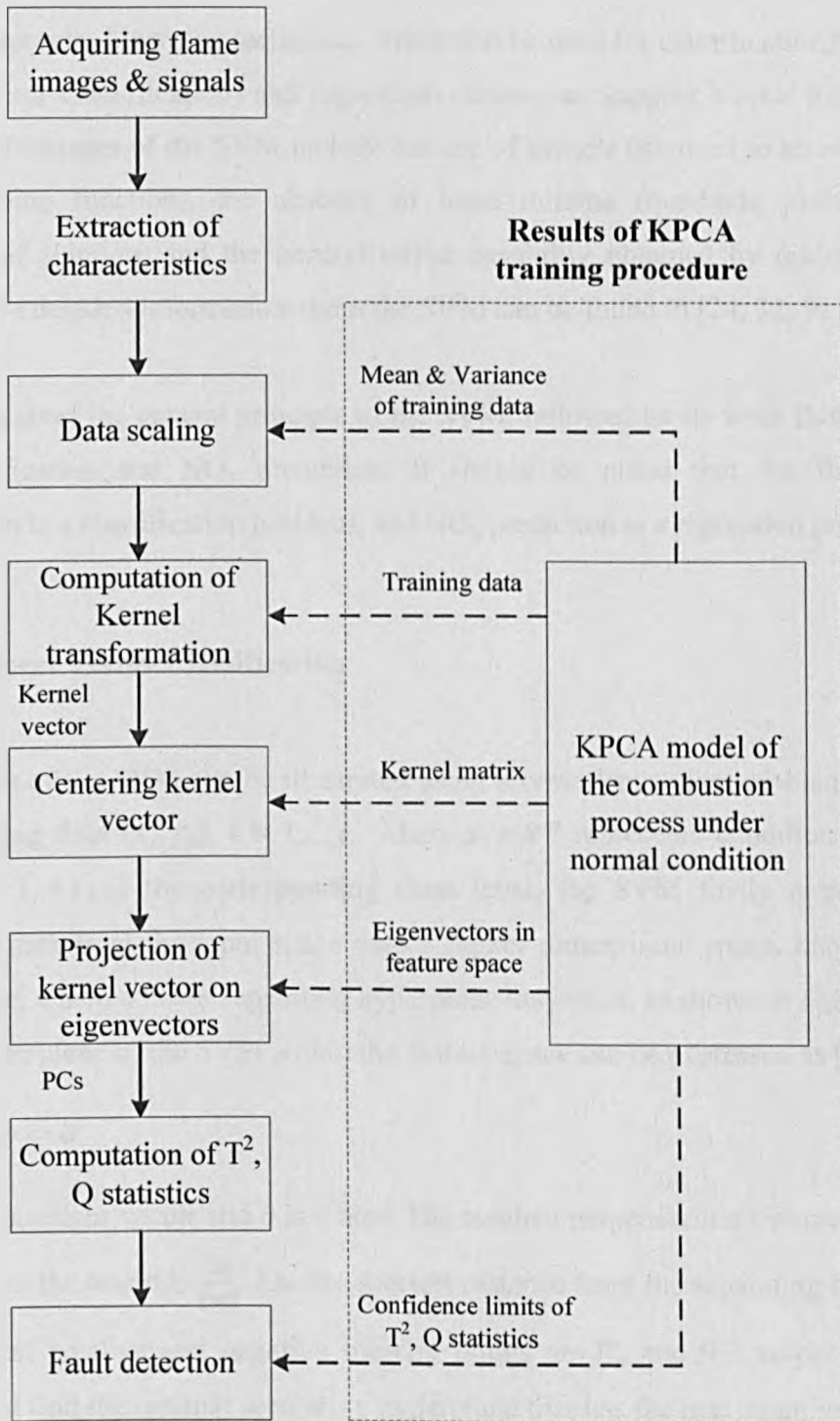


Figure 3.3 Flow chart of KPCA-based combustion process monitoring

### 3.3.3 SVM for Flame State Identification and NO<sub>x</sub> Prediction

SVM is a supervised learning technique, which can be used for classification (known as Support Vector Classification) and regression (known as Support Vector Regression). The main advantages of the SVM include the use of kernels (no need to know the non-linear mapping function), the absence of local minima (quadratic problem), the sparseness of solution, and the generalization capability obtained by optimizing the margin. More detailed information about the SVM can be found in [24, 32, 91].

This section gives the general principle of the SVM, followed by its work flow in flame state identification and NO<sub>x</sub> prediction. It should be noted that the flame state identification is a classification problem, and NO<sub>x</sub> prediction is a regression problem.

#### 3.3.3.1 Support Vector Classification

The key idea of the SVM can be illustrated using a typical two-class problem. Given a set of training data  $\{\mathbf{x}_i, y_i\}$ ,  $i = 1, \dots, l$ , where  $\mathbf{x}_i \in R^m$  represents condition attributes and  $y_i = \{-1, +1\}$  is the corresponding class label, the SVM firstly maps linearly inseparable data from the input space onto a higher dimensional space, known as the feature space, where a linear separating hyperplane may exist, as shown in Figure 3.4. A decision hyperplane of the SVM within the feature space can be expressed as [91]

$$\mathbf{w}^T \Phi(\mathbf{x}) + b = 0, \quad (3-43)$$

where  $\mathbf{w}$  is a weight vector and  $b$  is a bias. The resulted perpendicular distance from the hyperplane to the origin is  $\frac{|b|}{\|\mathbf{w}\|}$ . Let the shortest distance from the separating hyperplane to the closest positive and negative training points are  $D_+$  and  $D_-$ , respectively, the SVM tries to find the optimal separating hyperplane that has the maximum margin (i.e., the maximum sum of  $D_+$  and  $D_-$ ).

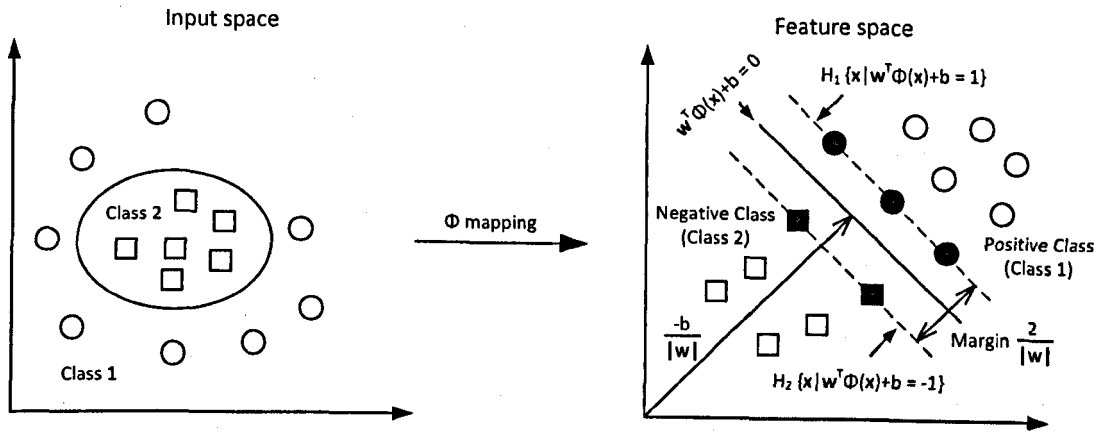


Figure 3.4 Key idea of SVM in a two-class problem (Gil et al. [24])

The separating hyperplane with maximum margin satisfies the following conditions,

$$\mathbf{w}^T \phi(\mathbf{x}_i) + b \geq +1, \text{ for } y_i = +1, \quad (3-44)$$

$$\mathbf{w}^T \phi(\mathbf{x}_i) + b \leq -1, \text{ for } y_i = -1, \quad (3-45)$$

which can be expressed equivalently as

$$y_i [\mathbf{w}^T \phi(\mathbf{x}_i) + b] \geq 1. \quad (3-46)$$

Suppose there exist training points which give equality in (3-44) lying on the hyperplanes  $H_1: \mathbf{w}^T \phi(\mathbf{x}_i) + b = +1$  and training points which give the equality in (3-45) lying on the hyperplanes  $H_2: \mathbf{w}^T \phi(\mathbf{x}_i) + b = -1$ , and these two hyperplanes  $H_1$  and  $H_2$  are in parallel and no training data fall between them, then the perpendicular distances from the origin to the hyperplanes  $H_1$  and  $H_2$  are  $\frac{|1-b|}{\|\mathbf{w}\|}$  and  $\frac{|-1-b|}{\|\mathbf{w}\|}$ , respectively. Therefore,  $D_+ = D_- = \frac{1}{\|\mathbf{w}\|}$  and the margin is  $\frac{2}{\|\mathbf{w}\|}$ . Hence, to calculate the optimal separating hyperplane with the maximum margin is equivalent to minimizing  $\|\mathbf{w}\|$  under the conditions of (3-46). The training points that give the equality in (3-46) and lie on one of the hyperplanes  $H_1$  and  $H_2$  are called support vectors.

In practical, the optimal separating hyperplane can be obtained by solving the following quadratic optimization problem [32], i.e.,

$$\min_{\mathbf{w}, b, \xi} \frac{1}{2} \mathbf{w}^T \mathbf{w} + C \sum_{i=1}^n \xi_i,$$

$$\text{subject to } \begin{cases} y_i(\mathbf{w}^T \Phi(\mathbf{x}_i) + b) \geq 1 - \xi_i, & i = 1, \dots, n, \\ \xi_i > 0, \end{cases} \quad (3-47)$$

where  $\xi_i$  is the slack variable, and  $C > 0$  is the user-specified penalty parameter of the error term. The slack variable  $\xi_i$  and the error penalty  $C$  are introduced for handling the possibility of training points violating the edges of the margin.

The problem of (3-47) is usually solved through its dual problem in the input space, i.e.,

$$\min_{\alpha} \frac{1}{2} \alpha^T \mathbf{Q} \alpha + \mathbf{e}^T \alpha,$$

$$\text{subject to } \begin{cases} \mathbf{y}^T \alpha = 0, \\ 0 \leq \alpha_i \leq C, \end{cases} \quad i = 1, \dots, l, \quad (3-48)$$

where  $\mathbf{e}$  is the vector of all ones,  $\mathbf{Q}$  is an  $l$  by  $l$  positive semi-definite matrix,  $Q_{ij} = y_i y_j k(\mathbf{x}_i, \mathbf{x}_j) \equiv y_i y_j \langle \Phi(\mathbf{x}_i), \Phi(\mathbf{x}_j) \rangle$ .

The decision function, which can be used to classify new data  $\mathbf{x}$ , is

$$\text{sgn}(\sum_{i=1}^n y_i \alpha_i k(\mathbf{x}_i, \mathbf{x}) + b). \quad (3-49)$$

### 3.3.3.2 Support Vector Regression

Given a set of data points,  $\{(\mathbf{x}_1, z_1), \dots, (\mathbf{x}_l, z_l)\}$ ,  $\mathbf{x}_i \in R^m$ ,  $z_i \in R^1$ , the optimisation problem of support vector regression can be expressed as

$$\min_{\mathbf{w}, b, \xi, \xi^*} \frac{1}{2} \mathbf{w}^T \mathbf{w} + C \sum_{i=1}^n \xi_i + C \sum_{i=1}^n \xi_i^*,$$

$$\text{subject to } \begin{cases} \mathbf{w}^T \Phi(\mathbf{x}_i) + b - z_i \leq \epsilon + \xi_i \\ z_i - \mathbf{w}^T \Phi(\mathbf{x}_i) - b \leq \epsilon + \xi_i^* \\ \xi_i, \xi_i^* \geq 0, \end{cases} \quad i = 1, \dots, l \quad (3-50)$$

The dual problem of (3-50) is

$$\min_{\alpha, \alpha^*} \frac{1}{2} (\alpha - \alpha^*)^T Q (\alpha - \alpha^*) + \epsilon \sum_{i=1}^n (\alpha_i + \alpha_i^*) + \sum_{i=1}^n z_i (\alpha_i - \alpha_i^*), \text{subject to}$$

$$\sum_{i=1}^l (\alpha_i - \alpha_i^*) = 0, \quad 0 \leq \alpha_i, \alpha_i^* \leq C, \quad i = 1, \dots, l, \quad (3-51)$$

where  $Q_{ij} = k(x_i, x_j) \equiv \langle \phi(x_i), \phi(x_j) \rangle$ .

The approximate function is

$$\sum_{i=1}^l (\alpha_i^* - \alpha_i) k(x_i, x) + b. \quad (3-52)$$

### 3.3.3.3 Work Flow of SVM

The work flows of the SVM for flame state identification and NO<sub>x</sub> prediction are similar, including scaling data, selecting kernel function, searching proper kernel parameters, training the SVM model, and testing the trained SVM model.

The first step of building the SVM model is to scale the attributes of training data to fall in the range [-1, 1]. Previous experiences have suggested that the SVM can be made more efficient if proper scaling is performed. The main purposes of scaling include firstly avoiding attributes in greater numeric ranges dominating those in smaller numeric range, and secondly avoiding numerical difficulties during the calculation [32]. It should also be noted that the same scaling factors should be used for the testing data.

The radial basis function (RBF) is selected as the kernel function of the SVM in the present study. There are four commonly used basic kernels, i.e., linear, polynomial, sigmoid, and RBF. Compared with other three kernels, the RBF is a reasonable choice due to its intrinsic advantages. Unlike the linear kernel, the RBF is capable of handling the case when the relation between model inputs and outputs is nonlinear. Compared with the polynomial kernel, the RBF kernel has less hyper-parameters, which can reduce the complexity of the model. Moreover, a sigmoid kernel may be not valid under some parameters, while the RBF kernel has no such problem.

The RBF kernel has two unknown parameters,  $C$  and  $\gamma$ . To determine the most suitable values of  $C$  and  $\gamma$  for flame state identification and  $\text{NO}_x$  prediction, a cross-validation approach can be used. Specifically, the training set is divided into a number of subsets (in the present study, five subsets) with an equal size. Sequentially one subset is tested using the model trained on the remaining subsets. Thus, each instance of the whole training set is predicted once. The cross-validation accuracy is defined as the percentage of data which are correctly classified (for flame state identification), or MSE (mean squared error) (for  $\text{NO}_x$  prediction). The  $C$  and  $\gamma$  with which the best validation accuracy is obtained are taken as the kernel parameters to train the whole training set. The cross-validation procedure can ameliorate or prevent the over-fitting problem.

After the determination of  $C$  and  $\gamma$ , the SVM model is trained by solving the optimization problems, as shown in (3-48) and (3-51). Then the trained model can be used to classify the flame state (3-49) or predict the  $\text{NO}_x$  emissions (3-52).

For the classification problem (identification of flame state), the performance of the trained model is evaluated by the percentage of data which are correctly classified, i.e.,

$$\text{Success rate} = \frac{\text{Number of correctly classified data}}{\text{Number of total testing data}} \times 100\%. \quad (3-53)$$

For the regression problem (prediction of  $\text{NO}_x$ ), the MSE and correlation coefficient are used, i.e.,

$$\text{MSE} = \frac{1}{N} \sum_{i=1}^N (f(\mathbf{x}_i) - y_i)^2, \quad (3-54)$$

$$r = \frac{(N \cdot \sum_{i=1}^N f(\mathbf{x}_i) \cdot y_i - \sum_{i=1}^N f(\mathbf{x}_i) \cdot \sum_{i=1}^N y_i)}{\sqrt{[N \cdot \sum_{i=1}^N f(\mathbf{x}_i)^2 - (\sum_{i=1}^N f(\mathbf{x}_i))^2] \cdot [N \cdot \sum_{i=1}^N y_i^2 - (\sum_{i=1}^N y_i)^2]}}, \quad (3-55)$$

where  $\{\mathbf{x}_i, y_i\}$ ,  $i = 1, \dots, N$ , are the training data, and  $f(\mathbf{x}_i)$  is the predicted value of  $y_i$ .

### 3.4 Measurement of Soot Temperature, Emissivity and Concentration in Soot-Laden Flames

In soot-laden flames, such as heavy-oil-fired flame studied in the present work (Chapter 5 and Chapter 6), combustion is dominated by the intense radiation from the soot particles. For such a flame, the temperature of the combustion gases can be estimated by measuring the temperature of soot particles, because the difference between the two temperatures is negligible (<1K) when thermal equilibrium is attained. The two-colour method has been widely used to measure temperature of soot-laden flames where the emissivity of the medium is unknown. The fundamental aspects of the two-colour method can be found elsewhere [1, 41].

In the present study, instead of using the complex beam splitting and narrow-bandpass filtering approach, the system (described in Chapter 4) derives flame temperature from the relationship between the primary colours of the images captured by a RGB colour camera. The camera has three separate channels corresponding to primary colours Red (R), Green (G) and Blue (B). Each image frame produced can be disintegrated into three principal images R, G, and B. A combination of the colour-banded images can thus be used for the determination of the flame temperature distribution based on the two-colour principle. In this study, the R and G images were chosen, i.e.,

$$T = \frac{C_2 \left( \frac{1}{\lambda_G} - \frac{1}{\lambda_R} \right)}{\ln \frac{G(\lambda_R, T)}{G(\lambda_G, T)} + \ln \frac{S_{\lambda_R}}{S_{\lambda_G}} + \ln \left( \frac{\lambda_R}{\lambda_G} \right)^5}, \quad (3-56)$$

where  $T$  is the temperature of soot particles,  $C_2$  is the second Planck's constant  $1.4387770 \times 10^{-2} \text{mK}$ , and  $G(\lambda_R, T)$  and  $G(\lambda_G, T)$  are the grey-level intensities of images from the R and G channels, respectively.  $\lambda_R$  and  $\lambda_G$  are the peak wavelengths of the spectral ranges corresponding to the R and G channels, and are 540 nm and 615 nm, respectively.  $S_{\lambda_R}$  and  $S_{\lambda_G}$  are the spectral sensitivities of the system for  $\lambda_R$  and  $\lambda_G$ , respectively. Ratio  $S_{\lambda_R}/S_{\lambda_G}$  is the instrument factor, which can be determined through a calibration procedure using a standard temperature source (Section 4.4.2).

The choice of R and G images for the temperature calculation instead of other combinations is because the sensor of the camera gives higher spectral sensitivities for the R and G channels than that for the B channel and thus a better signal-to-noise ratio can be achieved. It must also be stressed that the use of primary colour images for the temperature measurement offers advantages in simplicities in the system design, calibration and operation. It would, however, result in some errors in the temperature calculation due to the fact that each primary colour covers not only one single wavelength but a certain range of wavelengths. But it would not affect the general trend of the calculated temperature distribution. In fact, experimental results show that the system has very good measurement accuracy with reference to a standard temperature source (Section 4.4.2).

Once the flame temperature is determined from (3-56), the emissivity of soot particles in the flame at wavelength  $\lambda_R$  for temperature  $T$ ,  $\varepsilon_{\lambda_R}(T)$ , can be estimated by its definition, i.e.,

$$\varepsilon_{\lambda_R}(T) = \frac{M(\lambda_R, T)}{M_b(\lambda_R, T)}, \quad (3-57)$$

where  $M(\lambda_R, T)$  and  $M_b(\lambda_R, T)$  are the monochromatic emissive power of a non-blackbody (e.g., soot particles) and that of a blackbody, respectively. For the given imaging system, the relationship between the grey-level intensity of images and the monochromatic emissive power of the non-blackbody can be expressed by

$$G(\lambda_R, T) = AS_{\lambda_R}M(\lambda_R, T), \quad (3-58)$$

and for blackbody, the relationship can be expressed by

$$G_b(\lambda_R, T) = AS_{\lambda_R}M_b(\lambda_R, T), \quad (3-59)$$

where  $G(\lambda_R, T)$  and  $G_b(\lambda_R, T)$  are the grey-level intensities of the R images of the non-blackbody and the blackbody captured by the imaging system for temperature  $T$ , respectively. The relationship between  $G_b$  and  $T$  can be determined through the calibration by using a blackbody source (Section 4.4.2).  $A$  is an instrument constant which is independent of wavelength and reflects the effect of various factors including

the radiation attenuation due to the optical system and atmosphere, observation distance, lens properties, and signal conversion. Substitute (3-58) and (3-59) into (3-57), we get

$$\varepsilon_{\lambda_R}(T) = \frac{G(\lambda_R, T)}{G_b(\lambda_R, T)}. \quad (3-60)$$

In practice, the emissivity of soot particles can also be estimated from the widely used empirical equation proposed by Hottel and Broughton [92], i.e.,

$$\varepsilon_{\lambda}(T) = 1 - e^{(-KL/\lambda^{\gamma})}, \quad (3-61)$$

where  $K$  is the absorption coefficient,  $L$  is the geometrical thickness of the flame along the optical axis of the imaging system, and  $\gamma$  is an empirical parameter depending upon  $\lambda$ . For the visible spectral range,  $\gamma$  is considered to be a fixed value of 1.39 for a steady luminous flame [92]. Rearranging (3-61) yields

$$KL = -\lambda^{\gamma} \ln(1 - \varepsilon_{\lambda}). \quad (3-62)$$

Thus,

$$KL = -\lambda_R^{\gamma} \ln\left(1 - \frac{G(\lambda_R, T)}{G_b(\lambda_R, T)}\right). \quad (3-63)$$

Previous studies have revealed that  $KL$  is proportional to the concentration of soot particles in the flame [41]. Although an estimate of the volumetric and gravimetric density of soot can be obtained if some assumptions are made, the  $KL$  factor is used in the present study to investigate the soot concentration of a flame.

### 3.5 Summary

This chapter has firstly described the principles of the image processing and spectral analysis techniques for flame stability monitoring. Three different approaches have been presented, including evaluating the standard deviation of flame parameters, analysing power spectral density and oscillation frequency, and computing a simple universal flame stability index. The simple universal flame stability index is proposed by combining the dynamic characteristics of seven parameters extracted from flame images in the HSI colour space. The index assesses the flame stability in terms of its colour, geometry, and luminance. The advantages of the index are that it has a fixed boundary, and it is simple in computation and applicable to various flames without ad-hoc adaptation. The presented approaches have been used to assess the stability of flames on a 9MW<sub>th</sub> industrial-scale combustion test facility (Chapter 5) and a 660MW<sub>th</sub> full-scale boiler (Chapter 6).

In addition, the chapter has also presented the principles of soft computing techniques for burner condition monitoring. Specifically, the KPCA model is for the early detection of abnormal conditions in a combustion process, and the SVM model for the identification of flame state and the prediction of NO<sub>x</sub> emissions. A number of flame characteristics are selected as the inputs of the KPCA and SVM models. Compared with the traditional linear PCA based process monitoring technique, the KPCA based technique adopts kernel method, capable of handling nonlinear process data. Kernel method is also adopted in SVM. The advantages of the SVM over the widely used ANNs (Artificial Neural Networks) are that it has a simple geometric interpretation and a sparse solution. The performance of the KPCA and SVM are demonstrated and compared with that of the PCA and ANNs by using the real flame data obtained from a 9MW<sub>th</sub> industrial-scale combustion test facility (Chapter 5).

## Chapter 4

### System Description

#### 4.1 Introduction

This chapter describes the design, implementation and evaluation of the instrumentation system for flame stability and burner condition monitoring under the research programme.

An embedded photodetector and signal-processing board, which incorporates three different photodiodes covering ultraviolet, visible and infrared spectral bands respectively, is developed for analysing the power spectral density and oscillation frequency of a flame. A standard frequency-varying light source is used as an idealised flame to evaluate the performance of the embedded board.

A digital RGB camera is used to capture the flame images, from where a number of parameters can be derived, including geometric and luminous characteristics, two-dimensional temperature distribution, etc. The effects of various factors on the imaging system, including sensor dark current, exposure time, master gain, gain boost, and R/G/B gains, are analysed. The temperature measurement of the system is calibrated by using a blackbody furnace as a standard temperature source. The accuracy of temperature measurement is verified by applying the system to measuring the true temperature of a standard tungsten lamp.

## 4.2 System Design and Implementation

Figure 4.1 shows the block diagram of the flame monitoring system developed. The system consists of a rigid optical probe, an optical-beam-splitting unit, an embedded photodetector and signal-processing board (EPSB), a digital camera, and a mini-motherboard with associated application software. The optical probe, which is protected by a water-cooled jacket, is used to penetrate the furnace wall and transmit the light of flame to the EPSB and the camera. The objective lens of the optical probe has a 90° viewing angle and its surface is kept dust-free by purging airflow. The beam splitter divides the light of flame into two beams. The first beam is received by the photodiodes on the embedded board for the analysis of power spectral density and the measurement of flame oscillation frequency. The second beam is captured by the digital camera for the measurement of flame geometric and luminous parameters, temperature distribution, etc. This arrangement ensures that the system takes the concurrent measurements of flame images and radiation signals.

Figure 4.2 shows the physical implementation of the system. The optical probe and all optical and electronic parts are integrated as a single unit, offering the system excellent portability and robustness. Dedicated application software is also developed as an integral part of the system.

The system can be divided into three subsystems:

- Photodetector subsystem: the embedded photodetector and signal-processing board (EPSB)
- Imaging subsystem: the optical probe, optical lens, and digital camera
- Computing subsystem: the mini-motherboard

The detailed technical and operational considerations about each subsystem are presented successively in the following sections.

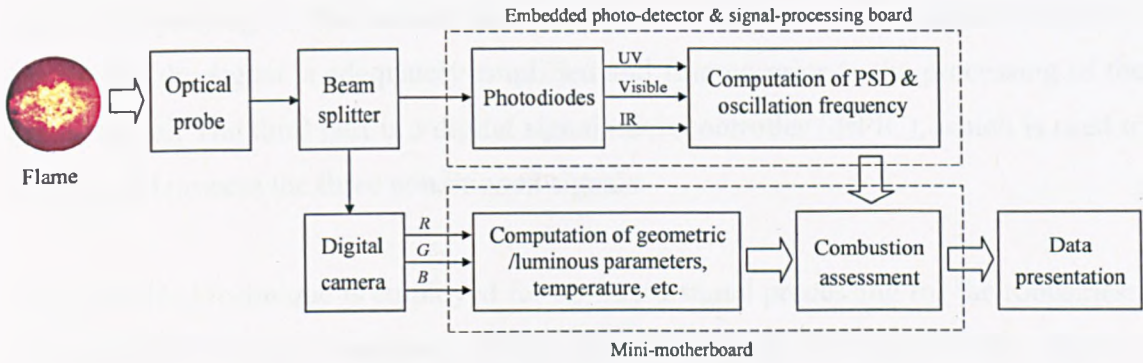


Figure 4.1 Block diagram of the flame monitoring system

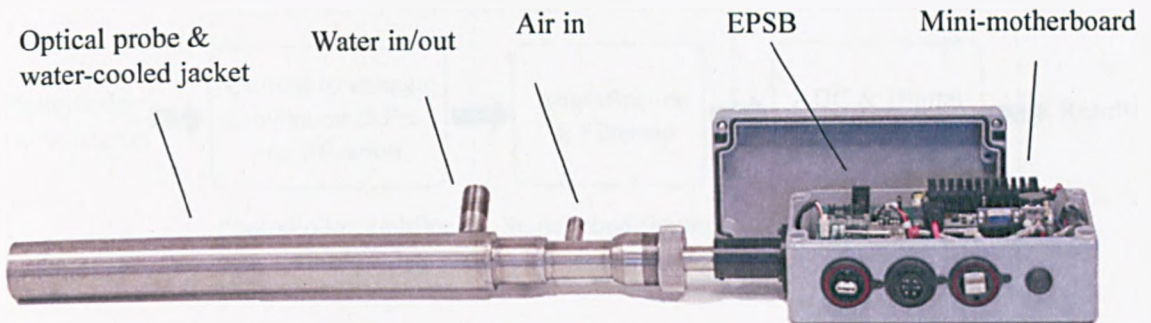


Figure 4.2 Physical implementation of the flame monitoring system

### 4.2.1 Photodetector Subsystem

Figure 4.3 shows the block diagram of the photodetector subsystem, i.e., the embedded photodetector and signal-processing board, which is developed for the analysis of the power spectral density and measurement of flame oscillation frequency.

The embedded board has three separate photodiodes, covering ultraviolet (UV), visible (VIS), and infrared (IR) spectral bands, respectively. These three photodiodes are placed as close as possible and in the optical path of flame light. The photodiodes convert the incoming flame light intensity into current signals corresponding to three spectral bands. Each photodiode has its own signal processing channel, which is divided into three parts based on its functions. The first part is a photodiode amplifier unit, which is used to convert a weak current induced on the photodiode into a voltage signal

and pre-amplifying it. The second part is a signal conditioning unit, which is used to ensure that the signal is adequately amplified and filtered prior to the processing of the digital signal. The third part is a digital signal microcontroller (dsPIC), which is used to digitize and process the three conditioned signals.

The embedded technique is employed for on-board signal processing for the robustness, compactness and fast response of the system. Figure 4.4 shows the physical implementation of the embedded board. Detailed schematic and PCB layout of the circuit are given in Appendix 1.

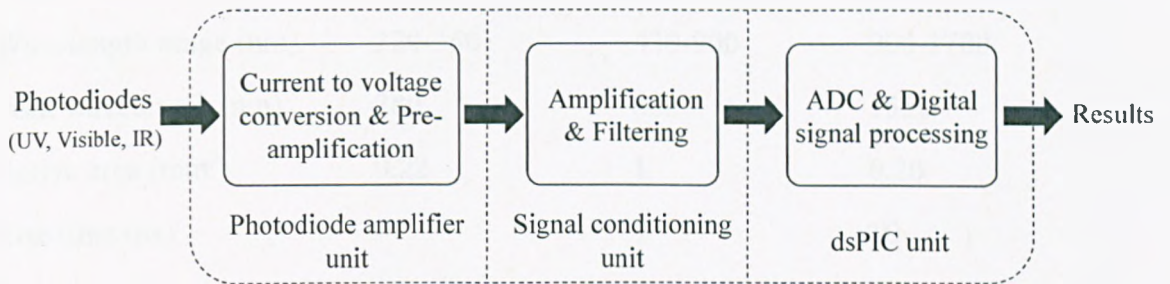


Figure 4.3 Block diagram of the embedded photodetector and signal-processing board

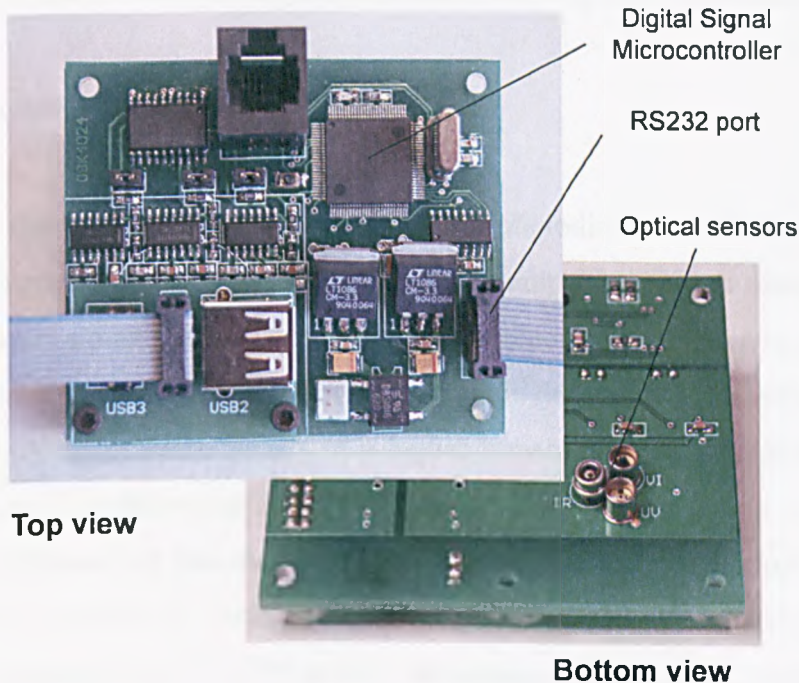


Figure 4.4 Physical implementation of the embedded photodetector and signal-processing board

#### 4.2.1.1 Photodiodes

Three photodiodes covering UV, VIS and IR spectral bands are used to capture the optical radiation of the flame at different spectral bands. The type and specifications of the photodiodes selected are summarized in Table 4.1.

Table 4.1 Specifications of the photodiodes [93-95]

Photodiode Name	Ultraviolet	Visible	Infrared
Type	SG01M	OSD1-5T	NT62-271
Wavelength range (nm)	220-360	430-900	900-1700
Peak wavelength (nm)	280	800	1550
Active area (mm <sup>2</sup> )	0.22	1	0.20
Rise time (ns)	--	7	10
Capacitance (pf)	80	7-35	18.5
Dark current (nA)	0.002	0.2-1	0.2
Responsivity (A/W)	0.13	0.18-0.21	0.95

#### 4.2.1.2 Amplifier Unit

Figure 4.5 shows the schematic diagram of the photodiode amplifier unit. In order to achieve a high sensitivity, a low bias current op-amp TLV2774 is selected to act as a transimpedance op-amp, converting a weak photodiode current into a voltage signal and pre-amplifying it. The gain of the amplifier unit depends on the value of feedback resistor  $R_F$ . A larger value results in a higher transimpedance gain but also a greater thermal noise. The determination of the feedback resistor depends on the sensitivity of the photodiode and the radiation spectrum of the flame to be monitored. From on-site experiments (Chapter 5), three different feedback resistors, i.e.,  $10\text{M}\Omega$ ,  $330\text{k}\Omega$  and  $680\text{k}\Omega$ , are selected for UV, VIS and IR photodiodes, respectively. Furthermore, since the transimpedance amplifier operating at very high gains has a high tendency to give rise to an oscillation at some high frequency above the gain bandwidth cut-off, the

feedback capacitor  $C_F$  of 2pf parallel to  $R_F$  is used to suppress the oscillation to ensure the loop stability of the unit [96].

### 4.2.1.3 Signal Conditioning Unit

The signal conditioning unit is used to further amplify and filter the flame signal from the photodiode amplifier unit before Analogue-to-Digital Converters (ADC). Instead of a conventional mechanical potentiometer, a digitally-controlled 64-position potentiometer  $R_P$  (DS1844-100) is used for gain adjustment, so that the system can be automatically adapted to a wide range of combustion conditions through software adjustment. Previous research has suggested that the energy of a flame signal mainly distributes between 0~200Hz [97]. Therefore, the sampling rate of ADC should be greater than 400Hz in order to obtain the complete power spectrum of the signal. In the present study, a sampling rate of 1024 Hz is selected and a second-order Sallen-Key low-pass filter with a cut-off frequency of 500Hz is used to avoid spectrum aliasing problem caused by digitalization. The signal conditioning unit is shown schematically in Figure 4.6. As three signal channels share an identical circuit structure, only one channel is depicted in the figure. Figure 4.7 shows the simulated frequency response of the second-order Sallen-Key low pass filter using TINA [98].

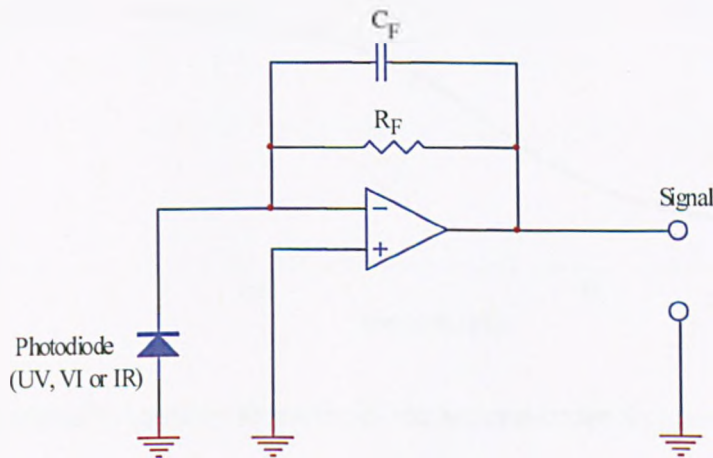


Figure 4.5 Schematic diagram of the photodiode amplifier unit

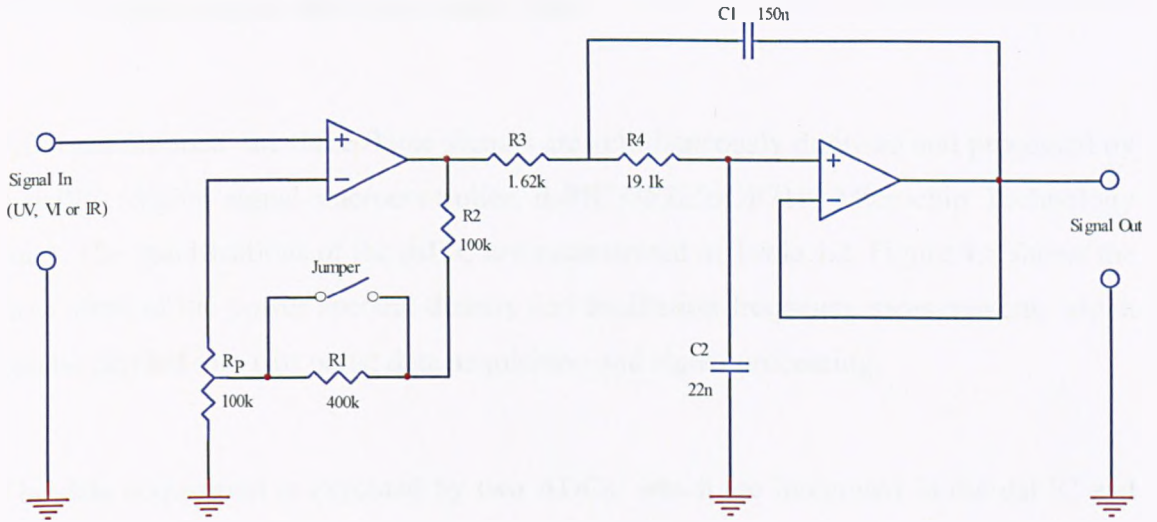


Figure 4.6 Schematic diagram of the signal conditioning unit

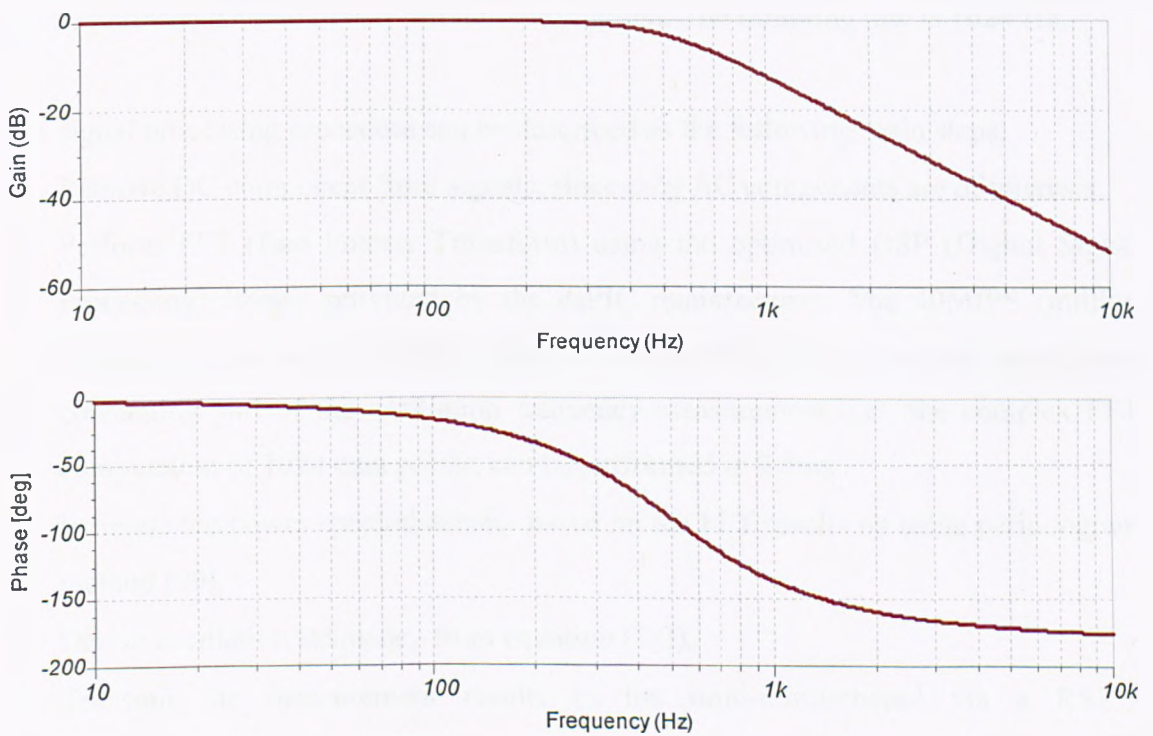


Figure 4.7 Simulated frequency response of the second-order Sallen-Key low pass filter using TINA

#### 4.2.1.4 Digital Signal Microcontroller Unit

After conditioned, the three flame signals are simultaneously digitised and processed by a dsPIC (digital signal microcontroller, dsPIC33FJ256GP710, Microchip Technology Inc.). The specifications of the dsPIC are summarized in Table 4.2. Figure 4.8 shows the flow chart of the power spectral density and oscillation frequency measurement, which can be divided into two parts: data acquisition and signal processing.

The data acquisition is executed by two ADCs, which are integrated in the dsPIC and capable of simultaneously sampling up to 10-bit four input channels. In the present work, only three of the four channels are used. The Direct Memory Access (DMA) technique is adopted to allow the ADCs to digitize the analogue signals and access the system memory, independently of the central processing unit, so the data acquisition can be performed continuously without interruption. The sampling rate is 1024 Hz.

The signal processing procedure can be described as the following main steps:

- Remove DC component from signals, since only AC components are of interests.
- Perform FFT (Fast Fourier Transform) using the optimised DSP (Digital Signal Processing) library provided by the dsPIC manufacturer. The 40MIPS (million instructions per second) CPU speed of the dsPIC ensures that the most time-consuming part of the oscillation frequency measurement, i.e., the complex FFT computation of 1024 data points, can be performed in 2.5ms.
- Estimate the power spectral density based on the FFT results by using periodogram method [99].
- Derive oscillation frequency from equation (3-3).
- Transmit the measurement results to the mini-motherboard via a RS232 communication port.

The embedded technique enables all three flame signals to be digitized and processed on an online continuous basis. It should also be noted that a self-gain-adjustment mechanism is also integrated into the software system to ensure that the amplitude of the signals are within a proper range, not too weak or saturated.

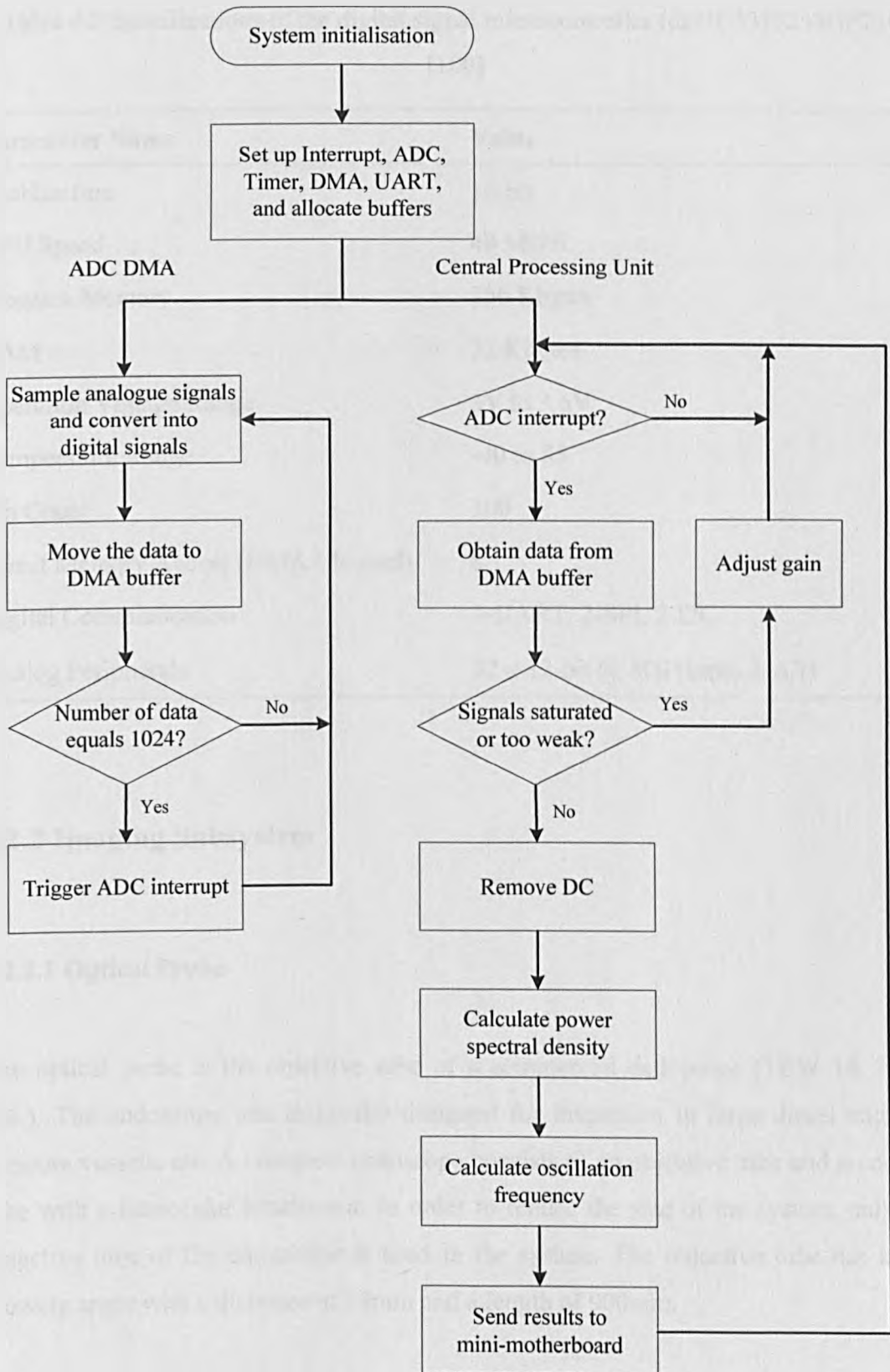


Figure 4.8 Flow chart of oscillation frequency measurement

Table 4.2 Specifications of the digital signal microcontroller (dsPIC33FJ256GP710)  
[100]

Parameter Name	Value
Architecture	16-bit
CPU Speed	40 MIPS
Program Memory	256 Kbytes
RAM	32 Kbytes
Operation Voltage Range	3V to 3.6V
Temperature Range	-40 to 85
Pin Count	100
Direct Memory Access (DMA Channel)	8
Digital Communication	2-UART, 2-SPI, 2-I2C
Analog Peripherals	32 × 12-bit @ 500 (ksps) 2-A/D

## 4.2.2 Imaging Subsystem

### 4.2.2.1 Optical Probe

The optical probe is the objective tube of a commercial endoscope (TEW 18, HSW Ltd.). The endoscope was originally designed for inspection in large diesel engines, pressure vessels, etc. A complete endoscope consists of an objective tube and an ocular tube with a monocular attachment. In order to reduce the size of the system, only the objective tube of the endoscope is used in the system. The objective tube has a 90° viewing angle with a diameter of 18mm and a length of 900mm.

### 4.2.2.2 Digital Camera

The digital camera used in the system is an industrial RGB colour type (UI-1640SE-C, IDS Ltd.) with a 1/3 inch CMOS sensor and a resolution of 1280H×1024V at 25 frames per second. The camera features a compact size of 34×32×27 mm. It also features a partial scan mode, which allows the camera to capture images up to 265 frames per second with a resolution of 320H×256V, making it ideal for imaging a fast-changing object such as a flame. The detailed specifications of the camera are given in Table 4.3.

Table 4.3 Specifications of the camera (UI-1640SE-C) [101]

Parameter Name	Value
Interface & Power Supply	USB
Lens Mount	C-Mount
Sensor Technology	CMOS (Aptina)
Resolution	1280H×1024V
Resolution Depth	8bit (10bit ADC)
Sensor Size	1/3 inch
Optical Size	4.6×3.6 mm
Pixelpitch	3.60 $\mu$ m
Shutter	Rolling
Max. fps in Freerun Mode	25 fps
Exposure Time in Freerun/Trigger Mode	37 $\mu$ s – 10s
AOI/ Modes	horizontal + vertical
Subsampling Modes	horizontal + vertical
Dimensions H/W/L	34 mm, 32 mm, 27 mm
Weight	62 g

### 4.2.2.3 Optical Lens

A compact non-zooming imaging lens (MVL50L, Thorlabs Ltd.), with a focal length of 50mm and viewing-angles of  $5.5^\circ(\text{H}) \times 4.1^\circ(\text{V})$ , is used to focus the light from the optical probe onto the CMOS sensor of the digital camera. The lens features a manually adjustable focus and iris. The adjustable focus enables the system to image objects at different distances. The adjustable iris (f/2.8 to f/22) can be used to control the depth of field as well as the amount of light that reaches the imaging sensor. The diameter of the aperture is measured in f-stops. A lower f-stop number opens the aperture, admitting more light onto the imaging sensor but narrowing the depth of field, whilst a higher f-stop number reduces the aperture and admits less light onto the sensor but deepens the depth of field. In the present work, a deep depth of field is desirable so that the system can obtain a clear image of the flame along the optical path.

## 4.2.3 Computing Subsystem

### 4.2.3.1 Mini-Motherboard

A high-performance mini-motherboard (PICO820, Axiomtek Ltd.) is integrated in the system to acquire and process images captured by the digital camera. The low power consumption mini-motherboard features with a 1.6 GHz processor and an ultra-compact size of 100mm×72mm. A 16 GB high speed industrial CompactFlash card is used as the storage device, wherein the Window XP operation system is installed. The mini-motherboard also performs as the master board for controlling and receiving data from the photodetector subsystem so as to achieve parallel and real time signal processing. All the measurement results are transmitted to a remote computer system via Ethernet. A brief description about the PICO820 mini-motherboard is given in Table 4.4.

Table 4.4 Specifications of the mini-motherboard (PICO820) [102]

Parameter Name	Value
CPU	Intel Atom processor Z530 1.6 GHz
Size	100×72mm
Board thickness	1.6mm
I/O	2 COM, 4 USB 2.0, 1 10/100Mbps Ethernet
System memory	DDR2-400/533 max. up to 2GB
SSD	1×CompactFlash™ type-II
Power requirements	+5V DC @ 1.625A

#### 4.2.3.2 Software

Dedicated computing software was developed using standard C++ in the Microsoft Visual Studio environment.

The GUI (Graphical User Interface) of the software is designed based on MFC (Microsoft Foundation Class) library. A typical screenshot of the GUI is shown in Figure 4.9. The GUI provides an on-line display of flame image and radiation signals as well as the measured flame characteristic parameters, including 2-D temperature distribution, power spectral densities, geometrical and luminous parameters, etc. The GUI also gives the full management of the software system, including the start, stop, pause and continuation of the operating process, the control of the digital camera (exposure time and gains), the EPSB, and the data log.

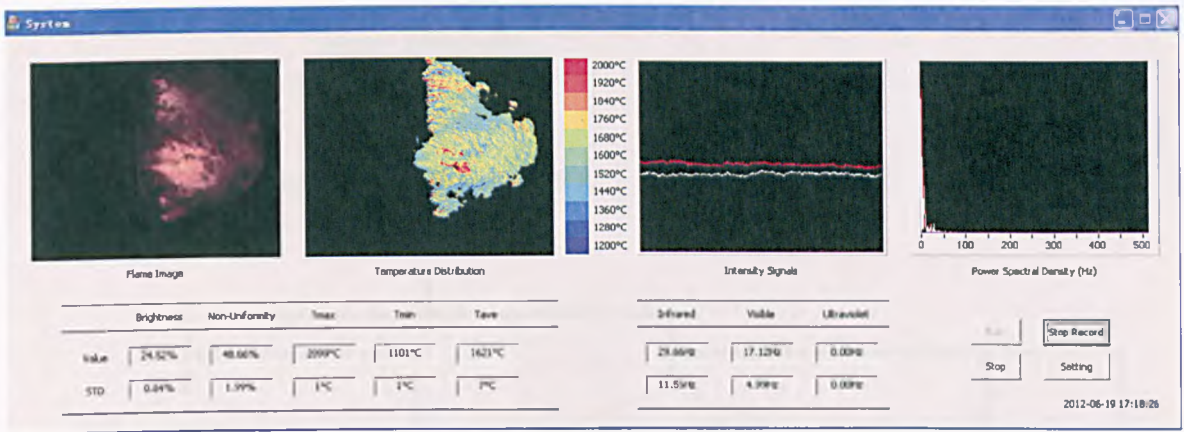


Figure 4.9 Screenshot of the graphical user interface

The work flow of the software is illustrated in Figure 4.10. On the one hand, the mini-mother board serves as the master board, receiving raw flame radiation signals and their processed results from EPSB and displaying them on an online basis. On the other hand, it acquires and processes the flame images, which can be described as the following main steps:

- Setup camera (exposure time, gain, etc.) and allocate memory buffers for image acquisition.
- Acquire image from allocated memory, and check the brightness of the image. If the image is over-exposed or too dark, adjust the exposure time and/or gain settings accordingly.
- Extract flame characteristics, including geometrical and luminous parameters, flame stability index, 2-D temperature distribution, etc.
- Display and record the results, and transmit the results to remote computer if required.

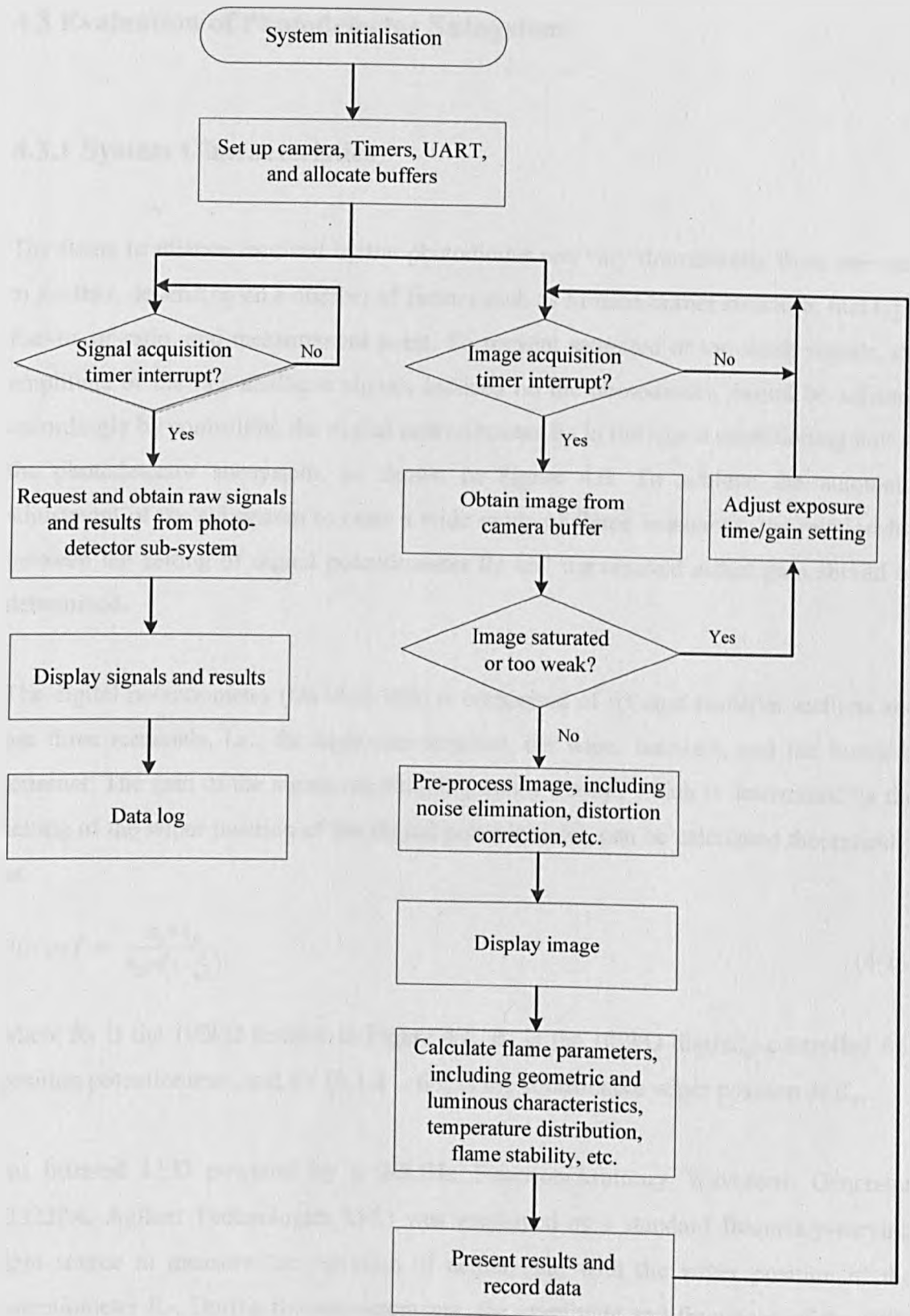


Figure 4.10 Flow chart of measurement procedure of computing subsystem

## 4.3 Evaluation of Photodetector Subsystem

### 4.3.1 System Characteristics

The flame irradiance received by the photodiodes can vary dramatically from one case to another, depending on a number of factors such as furnace/burner structure, fuel type, fuel-to-air ratio, and measurement point. To prevent saturated or too weak signals, the amplitude of the raw analogue signals induced on the photodiodes should be adjusted accordingly by controlling the digital potentiometer  $R_p$  in the signal conditioning unit of the photodetector subsystem, as shown in Figure 4.6. To achieve the automatic adjustment of the subsystem to cater a wide range of flame irradiance, the relationship between the setting of digital potentiometer  $R_p$  and the resulted actual gain should be determined.

The digital potentiometer (DS1844-100) is comprised of 63 equi-resistive sections and has three terminals, i.e., the high-side terminal, the wiper terminal, and the low-side terminal. The gain of the signal conditioning unit,  $PGcoef$ , which is determined by the setting of the wiper position of the digital potentiometer, can be calculated theoretically as

$$PGcoef = \frac{R_1 + R_p}{R_p \times \left(1 - \frac{s}{63}\right)}, \quad (4-1)$$

where  $R_1$  is the 100k $\Omega$  resistor in Figure 4.6,  $R_p$  is the 100k $\Omega$  digitally-controlled 64-position potentiometer, and  $s \in [0, 1, 2 \dots 63]$  is the controllable wiper position of  $R_p$ .

An infrared LED powered by a 20MHz Function/Arbitrary Waveform Generator (33220A, Agilent Technologies Ltd.) was employed as a standard frequency-varying light source to measure the variation of actual gain with the wiper position of the potentiometer  $R_p$ . During the measurements, the amplitude and frequency of the LED light were kept constant (waveform of the function generator: sine). The gain was measured based on the peak-to-peak value of the captured sine signal. Figure 4.11 shows the variation of the theoretical and actual gains with the wiper position of the

digital potentiometer  $R_p$  (as three signal channels share an identical circuit structure, only the result of infrared channel is presented here). It has been found that the theoretical values are well-matched with measured results, and the maximum relative error is about 0.33%.

### 4.3.2 Evaluation of Oscillation Frequency Measurement

The standard frequency-varying light source was also used to evaluate the accuracy of the oscillation frequency measurement. Figure 4.12 (a) shows a typical example of the signal captured by the system when the standard frequency-varying light source was set to 20Hz, whilst Figure 4.12 (b) shows the corresponding result of power spectral density estimate. Figure 4.13 shows the comparison between the measured and reference frequencies. Each data point is the average of ten instantaneous values. It was found that the relative error of the frequency measurement is no greater than 2% over the frequency range from 0 to 500 Hz. (The relative error is defined as the absolute error divided by the true value).

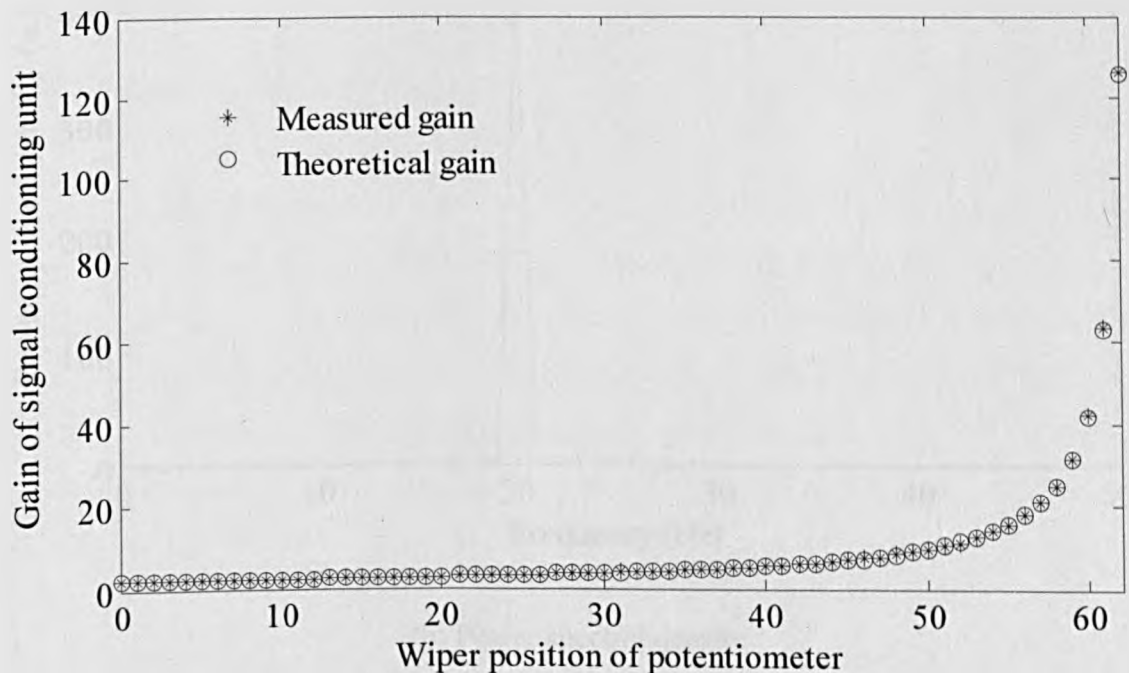
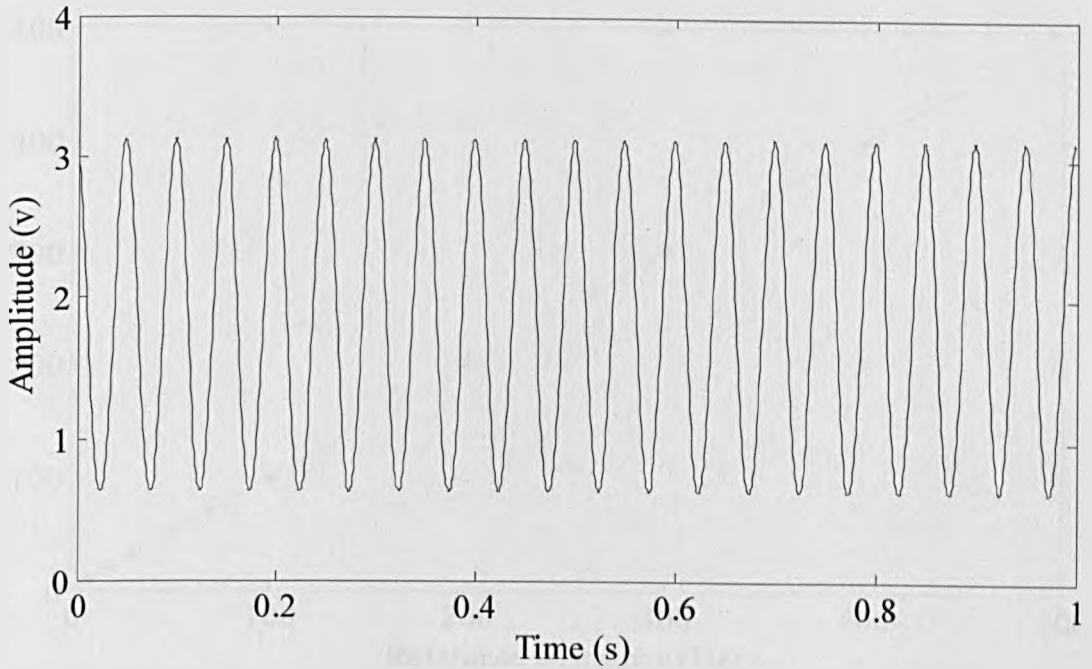
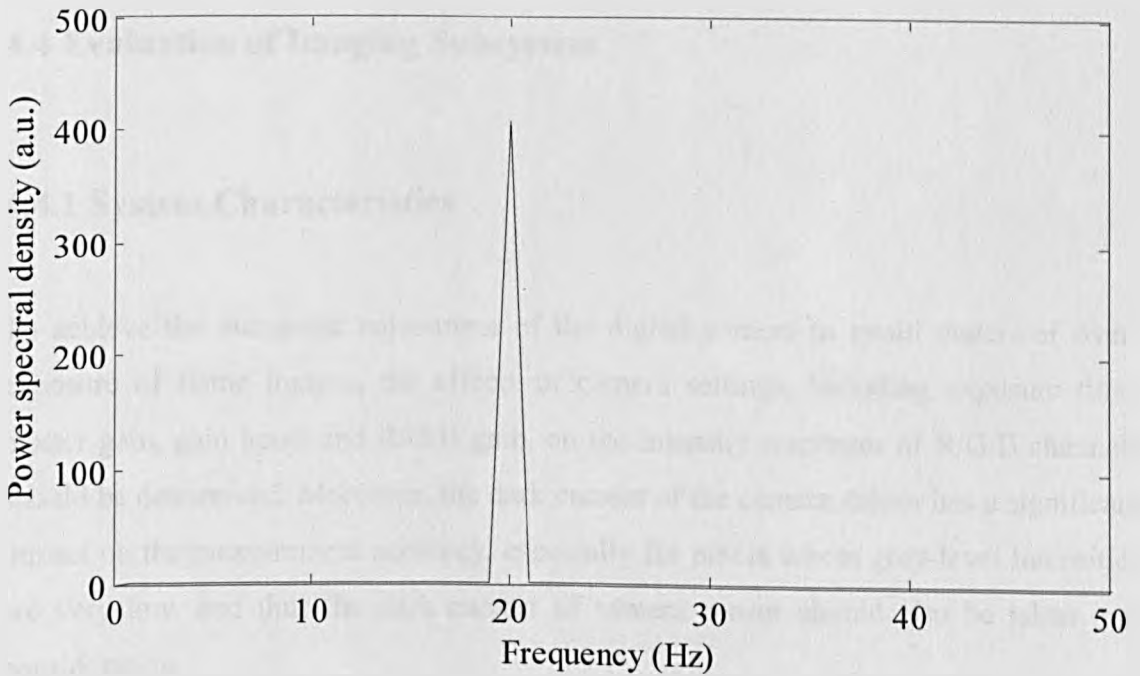


Figure 4.11 Variation of gain with the wiper position of the digital potentiometer



(a) Time domain



(b) Power spectral density

Figure 4.12 A typical example of the signal captured and its corresponding power spectral density

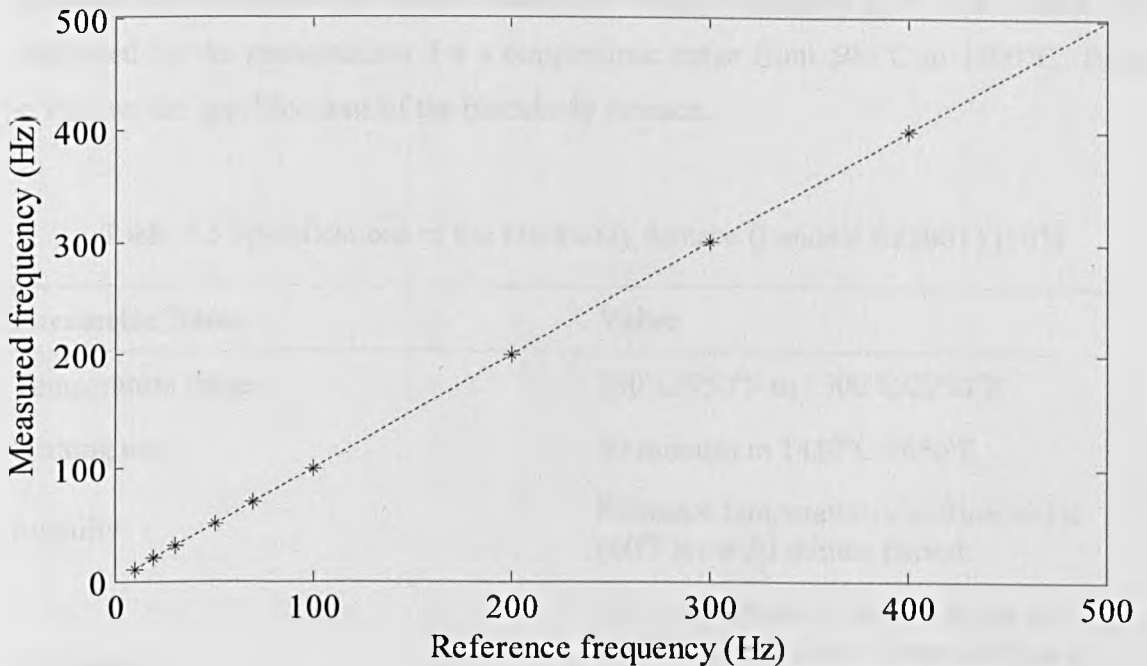


Figure 4.13 Comparison between the measured and reference frequencies

## 4.4 Evaluation of Imaging Subsystem

### 4.4.1 System Characteristics

To achieve the automatic adjustment of the digital camera to avoid under- or over-exposure of flame images, the effects of camera settings, including exposure time, master gain, gain boost and R/G/B gain, on the intensity responses of R/G/B channels should be determined. Moreover, the dark current of the camera sensor has a significant impact on the measurement accuracy, especially for pixels whose grey-level intensities are very low, and thus the dark current of camera sensor should also be taken into consideration.

All above-mentioned factors were evaluated using a standard blackbody furnace (Landcal R1500T, as show in Figure 4.21), which has a very stable irradiance under a given temperature. The blackbody furnace has a blackbody cavity of 45mm inner

diameter and 100mm length with an emissivity of approximately 0.99. The furnace was calibrated by the manufacturer for a temperature range from 500°C to 1500°C. Table 4.5 shows the specifications of the blackbody furnace.

Table 4.5 Specifications of the blackbody furnace (Landcal R1500T) [103]

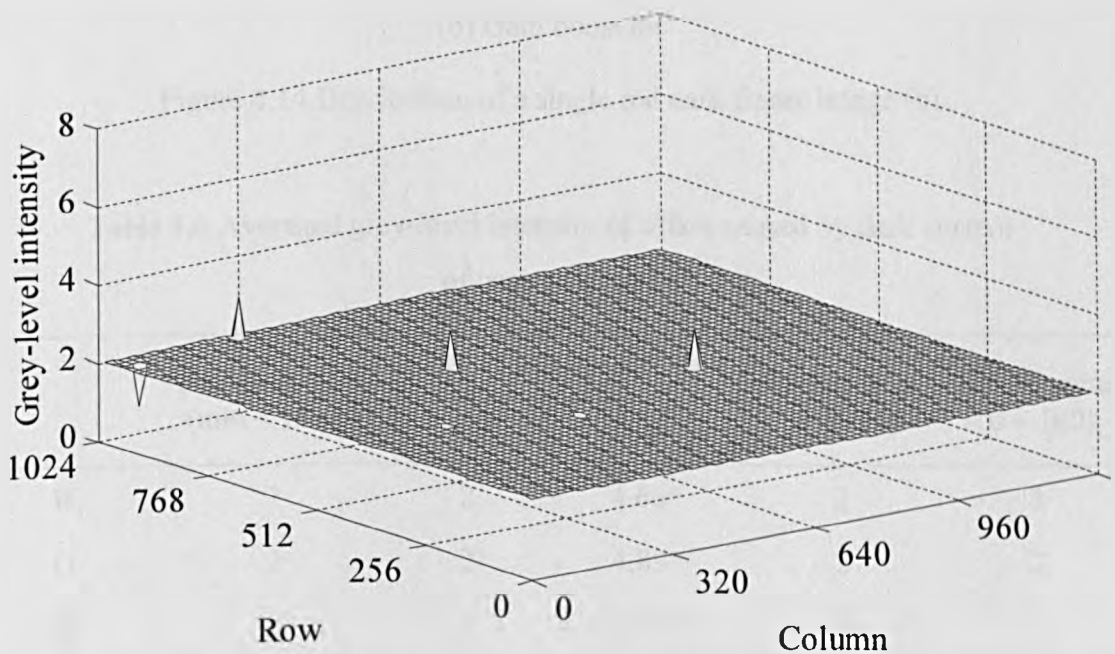
Parameter Name	Value
Temperature range	500°C/950°F to 1500°C/2750°F
Heating rate	30 minutes to 1450°C/2650°F
Stability	Radiance temperature variation $< \pm 1\text{K}$ ( $\pm 0^\circ\text{F}$ ) over 20 minute period
Uniformity	The temperature gradients across the middle 40mm of the 45mm cavity are within $\pm 2^\circ\text{C}$ at 500°C, and within $\pm 1^\circ\text{C}$ at 1500°C
Radiation cavity	
Material	Silicon carbide
Design	Cylinder with 120° conical end
Inner diameter	45mm/1.8in
Inner length	100mm/4.0in. When the radiation cavity is installed in the source, the distance from front face to cone point is 145mm/5.7in
External aperture	Approx. 38mm/1.5in.
Emissivity	Approximately 0.99 at short wavelengths

#### 4.4.1.1 Sensor Dark Current

The dark current of camera sensor was assessed by covering the cap of the camera to produce a complete dark environment. Table 4.6 shows the measured average grey-level intensity of dark frames under different camera settings. As can be seen, among the tested settings, the offset caused by sensor dark current is affected only by the setting of the gain boost, irrespective of exposure time, master gain, and R/G/B gains.

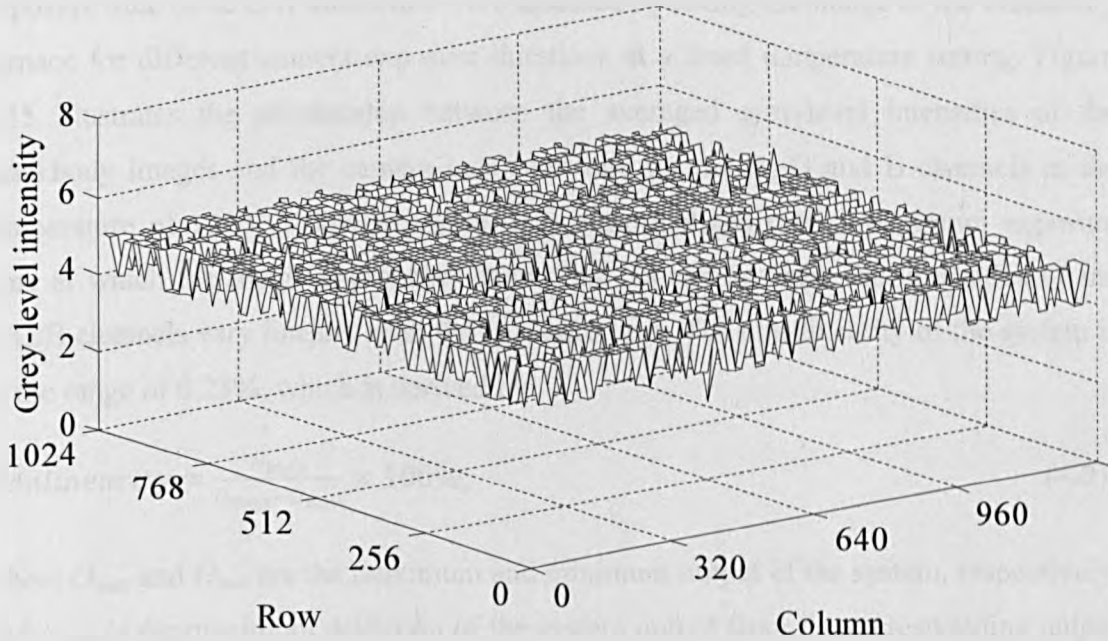
The offset caused by sensor dark current increases when gain boost is enabled. Figure 4.14 (a) and (b) show the offset distribution of the red channel of the camera, which was generated from a single dark frame at the settings of gain boost off (disabled) and on (enabled), respectively. The corresponding distributions of the green and blue channels are very similar, therefore only the result of the red channel is given. When the gain boost is off, 99.94% pixels of the image have same grey-level intensity of 2. When the gain boost is on, the offset are mainly distributed at grey-level intensities of 4 and 5.

The result is important for the temperature measurement that is based on the two-colour method. The corresponding dark frame should be subtracted from the image before the calculation of temperature.



(a) Gain boost off

Figure 4.14 Distribution of a single red dark frame image (a)



(b) Gain boost on

Figure 4.14 Distribution of a single red dark frame image (b)

Table 4.6 Averaged grey-level intensity of offset caused by dark current of camera sensor

	Exposure time (min ~ 10ms)	Gain boost		Master gain (0 ~ 100)	R/G/B gains (0 ~ 100)
		Off	On		
R	2	2	4.66*	2	2
G	2	2	4.89*	2	2
B	2	2	4.77*	2	2

\*The grey-level intensities of individual pixels are distributed at 4 and 5.

#### 4.4.1.2 Exposure Time

The exposure time of an image is determined by the electrical shutter of the digital camera, which can be controlled through software. The adjustment of the exposure time can be used to avoid the under- and over-exposure of the image. The effects of the

exposure time on R/G/B intensities were assessed by taking the image of the blackbody furnace for different camera exposure durations at a fixed temperature setting. Figure 4.15 illustrates the relationship between the averaged grey-level intensities of the blackbody images and the camera exposure time for the R, G and B channels at the temperature of 1250°C. The exposure time is normalized to the maximum exposure time at which the image approaches saturation. As can be seen, the intensities of the R/G/B channels vary linearly with the exposure time. The non-linearity of the system is in the range of 0.23%, which is derived by

$$\text{Nonlinearity} = \frac{N_{max}}{O_{max} - O_{min}} \times 100\%, \quad (4-2)$$

where  $O_{max}$  and  $O_{min}$  are the maximum and minimum output of the system, respectively, and  $N_{max}$  is the maximum deviation of the system output from the corresponding output of an idealized linear system.

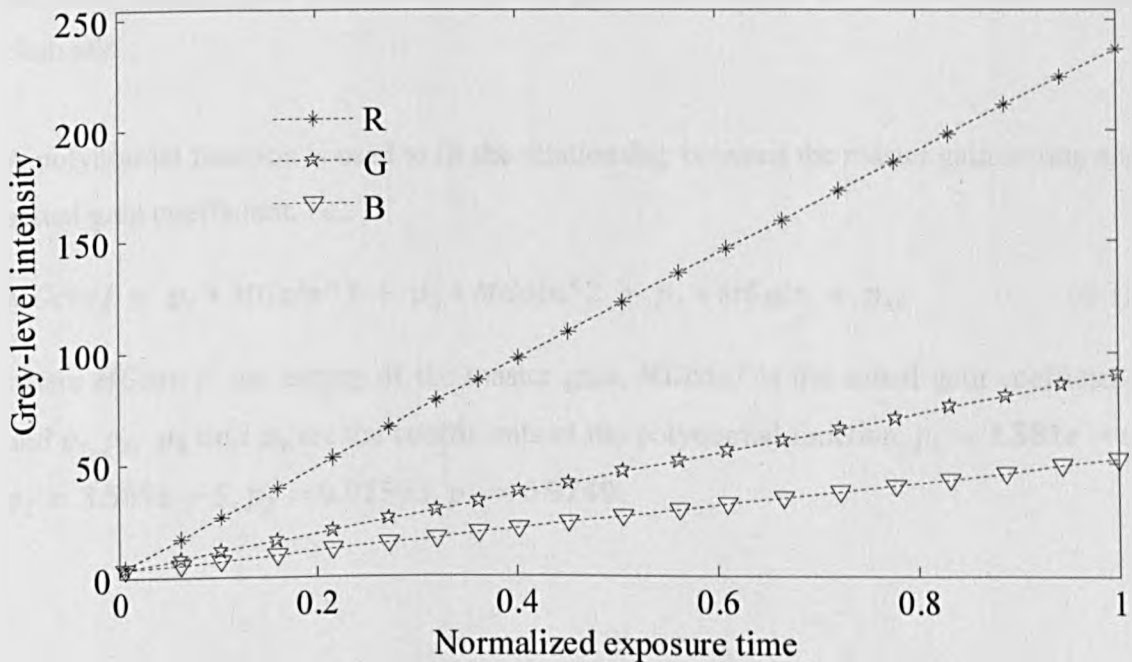


Figure 4.15 Relationship between the averaged grey-levels of blackbody images and camera exposure time for camera R, G and B channels

### 4.4.1.3 Master Gain

Three types of gain settings, i.e., master gain, gain boost, and R/G/B gains, can be used to control the intensity sensitivities of the R/G/B channels. The master gain and R/G/B gains can be varied from 0 to 100, while the gain boost can be set “on” or “off”. All three types of gain settings control the analogue image signal gain. The analogue adjustments can be made directly in the sensor, which achieves better results than adjustments via software. However, the relationships between these camera gain settings and the actual gain coefficients are unknown, and therefore should be analysed.

Frame images of the blackbody source were captured at various master gain settings. The relationships between the grey-level intensities of the R/G/B channels and the setting of master gain are shown in Figure 4.16. Figure 4.17 illustrates the variation of the corresponding actual gain coefficient with the setting of the master gain, which is obtained through normalizing the grey-levels by that at master gain setting of 0. As can be seen, master gain produces the same gain coefficients for all the three R/G/B channels.

A polynomial function is used to fit the relationship between the master gain setting and actual gain coefficient, i.e.,

$$MGcoef = p_1 * MGain^3 + p_2 * MGain^2 + p_3 * MGain + p_4, \quad (4-3)$$

where  $MGain$  is the setting of the master gain,  $MGcoef$  is the actual gain coefficient, and  $p_1, p_2, p_3$  and  $p_4$  are the coefficients of the polynomial function,  $p_1 = 1.581e - 6$ ,  $p_2 = 3.589e - 5$ ,  $p_3 = 0.01595$ ,  $p_4 = 0.9749$ .

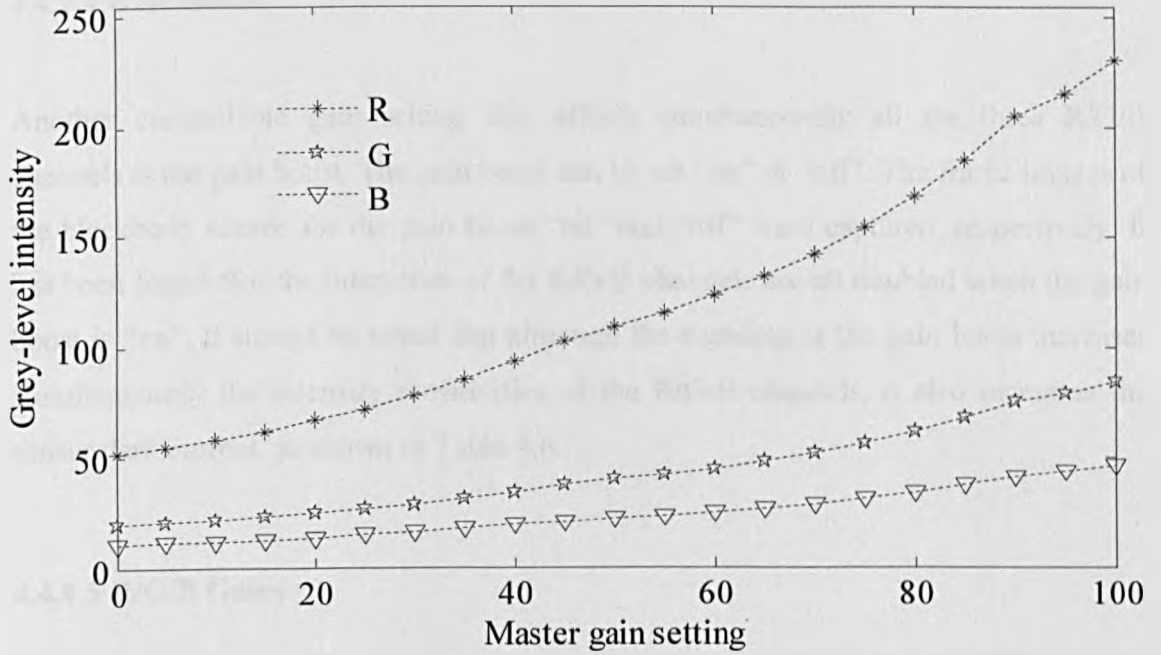


Figure 4.16 Variations of pixel value with master gain setting

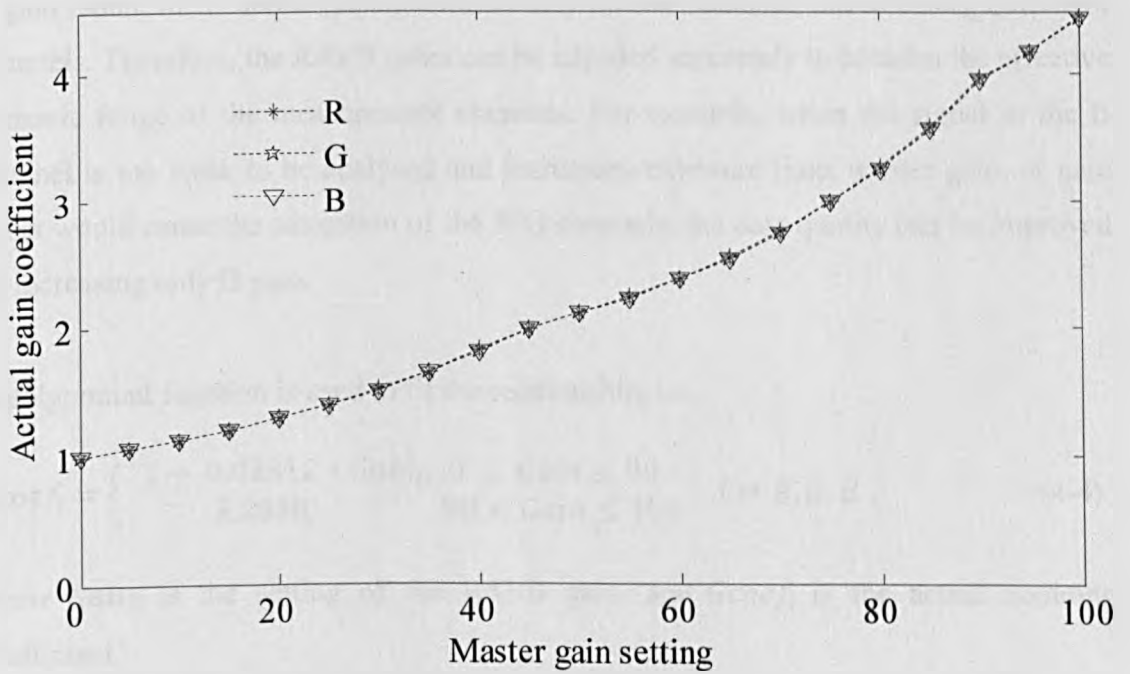


Figure 4.17 Variations of actual gain coefficient with master gain setting

#### 4.4.1.4 Gain Boost

Another controllable gain setting that affects simultaneously all the three R/G/B channels is the gain boost. The gain boost can be set “on” or “off”. The frame images of the blackbody source for the gain boost “on” and “off” were captured, respectively. It has been found that the intensities of the R/G/B channels are all doubled when the gain boost is “on”. It should be noted that although the enabling of the gain boost increases simultaneously the intensity sensitivities of the R/G/B channels, it also increases the sensor dark current, as shown in Table 4.6.

#### 4.4.1.5 R/G/B Gains

The R/G/B gains can vary from 0 to 100. The frame images of the blackbody source for various R/G/B gains were captured. The corresponding relationships between the grey-level intensities and the R/G/B gains are shown in Figure 4.18, 4.19 and 4.20, respectively. As can be seen, unlike the exposure time, master gain and gain boost, the R gain (same for G and B gains) controls only its own channel, not affecting other two channels. Therefore, the R/G/B gains can be adjusted separately to broaden the effective dynamic range of the measurement channels. For example, when the signal in the B channel is too weak to be analysed and increasing exposure time, master gain, or gain boost would cause the saturation of the R/G channels, the data quality can be improved by increasing only B gain.

A polynomial function is used to fit the relationship, i.e.,

$$Gcoef_i = \begin{cases} 1 + 0.02312 * Gain_i, & 0 \leq Gain \leq 90 \\ 2.0808, & 90 < Gain \leq 100 \end{cases} \quad i = R, G, B, \quad (4-4)$$

where  $Gain_i$  is the setting of the R/G/B gain, and  $Gcoef_i$  is the actual zooming coefficient.

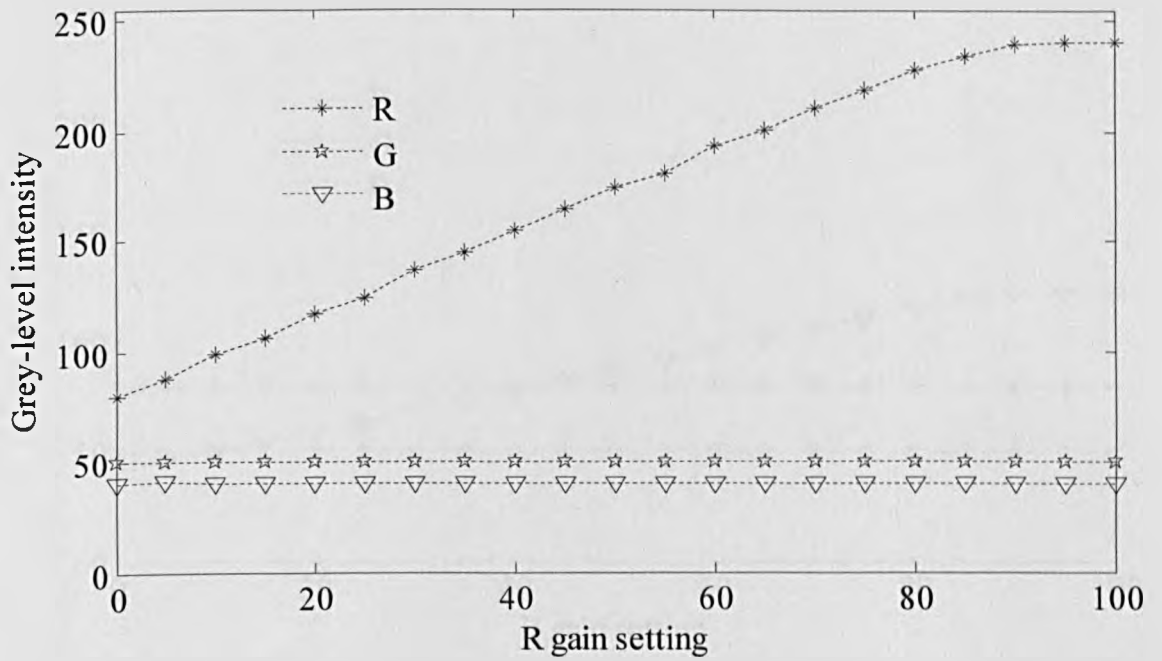


Figure 4.18 Pixel values for various R gain settings

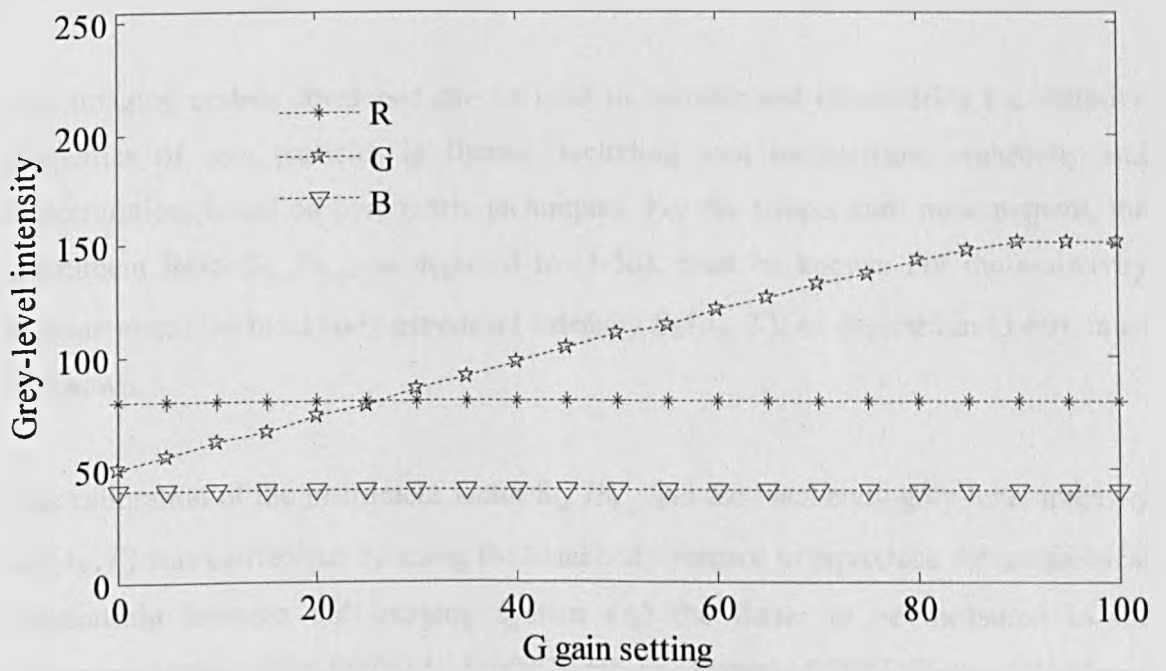


Figure 4.19 Pixel values for various G gain settings

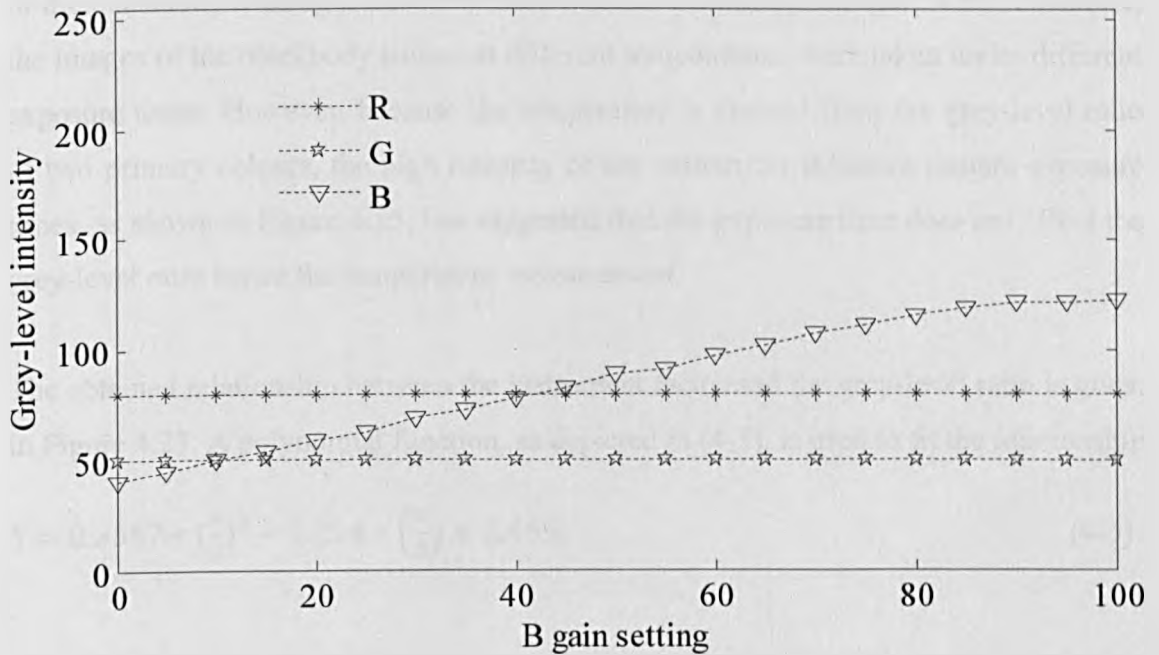


Figure 4.20 Pixel values for various B gain settings

#### 4.4.2 Calibration of Temperature Measurement

The imaging system developed can be used to monitor and characterize the emissive properties of soot particles in flames, including soot temperature, emissivity and concentration, based on pyrometric techniques. For the temperature measurement, the instrument factor  $S_{\lambda_R}/S_{\lambda_G}$ , as depicted in (3-56), must be known. For the emissivity measurement, the blackbody grey-level intensity  $G_b(\lambda_R, T)$ , as depicted in (3-60), must be known.

The calibration of the instrument factor  $S_{\lambda_R}/S_{\lambda_G}$  and the blackbody grey-level intensity  $G_b(\lambda_R, T)$  was carried out by using the blackbody furnace to reproduce the geometrical relationship between the imaging system and the flame to be measured in the temperature range from 900°C to 1500°C with an interval of 50°C. Figure 4.21 shows the experimental setup of the system for temperature calibration. It should be noted that because the radiation intensity of the blackbody furnace varies in a very wide range from temperature 900° to 1500°, it is inevitable to obtain under or over-exposed images

of the blackbody if using a fixed exposure time, as illustrated in Figure 4.22. Therefore, the images of the blackbody source at different temperatures were taken under different exposure times. However, because the temperature is derived from the grey-level ratio of two primary colours, the high linearity of the system for different camera exposure times, as shown in Figure 4.15, has suggested that the exposure time does not affect the grey-level ratio hence the temperature measurement.

The obtained relationship between the instrument factor and the grey-level ratio is given in Figure 4.23. A polynomial function, as depicted in (4-5), is used to fit the relationship.

$$S = 0.3557 * \left(\frac{R}{G}\right)^2 - 1.294 * \left(\frac{R}{G}\right) + 2.469. \quad (4-5)$$

Figure 4.24 shows the variation of the grey-level intensity of the R channel of the blackbody image with the temperature at the normalized exposure time of 1.7 ms. It has been found that the variation is satisfied by a Gaussian function, i.e.,

$$G_b(\lambda_R, T) = 3340 * e^{-\left(\frac{T-2214}{443}\right)^2}. \quad (4-6)$$

It should be noted that the sensor offset (dark response) was subtracted before the calibration. In addition, the calibration of the system was conducted under the room temperature (20°C~25°C). There was unfortunately no opportunity and condition for calibrating the system under industrial environments during the period of this study. However, industrial on-site experiments (Chapter 5) showed that the water-cooling jacket can effectively prevent the imaging unit of the system from the excessive heat from combustion chamber, and thus the temperature within the imaging unit mainly depends on the surrounding environment (30°C~40°C) of combustion chamber and the heat released by the electronic components within the imaging unit. It was also found that after eight hours on-line operation under the industrial environment, the system still worked normally without over-heating problem and the temperature of camera case remained cool, which suggests that the industrial environment might not significantly affect temperature measurement of the system.

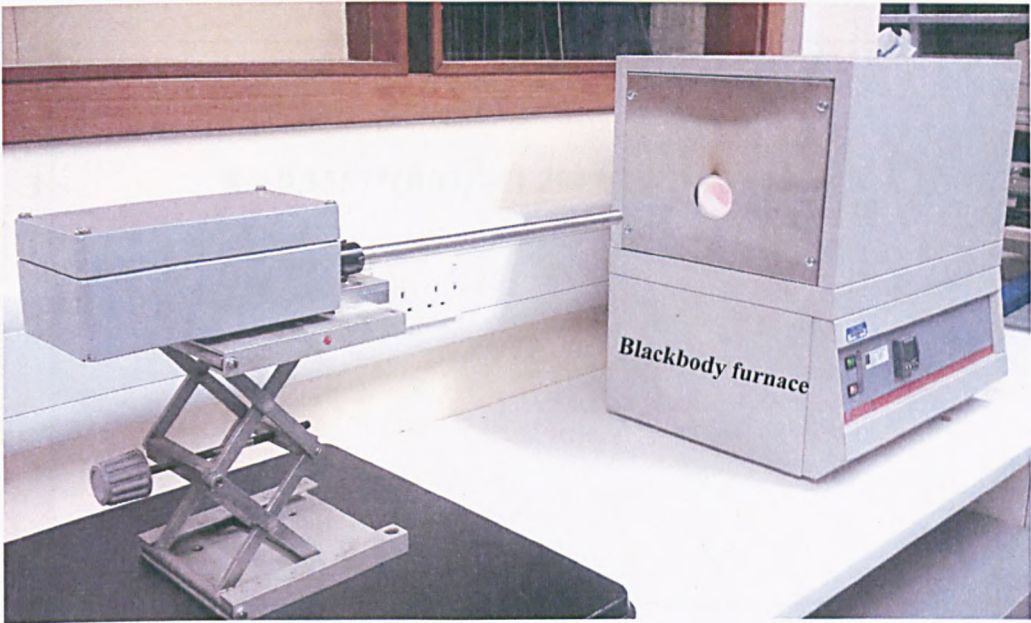


Figure 4.21 Experimental setup of the temperature calibration using blackbody furnace

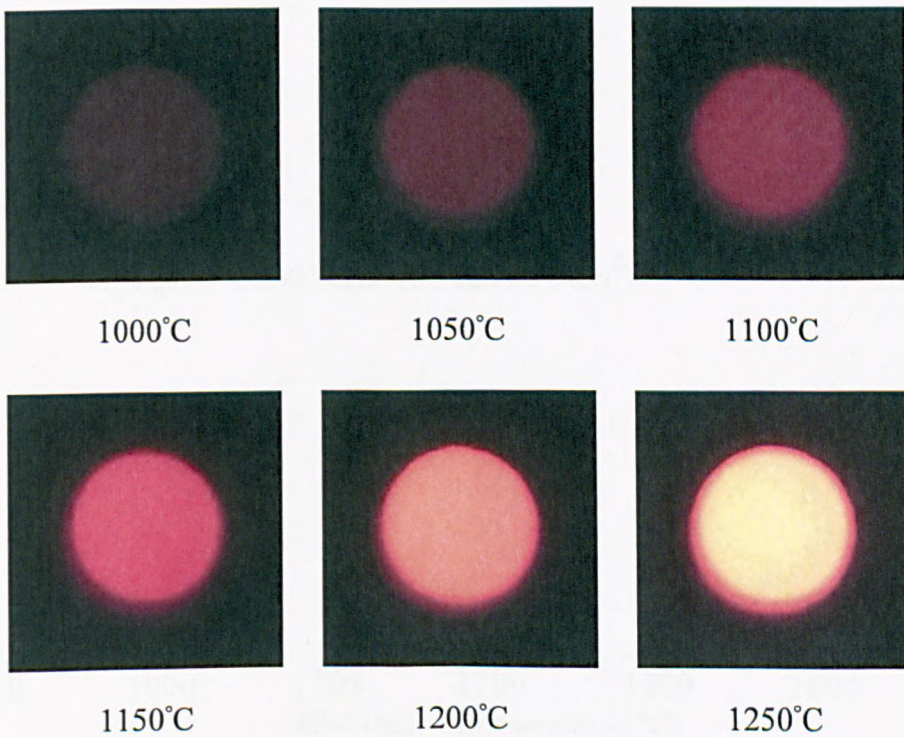


Figure 4.22 Blackbody images captured for different temperatures settings under the same camera exposure time

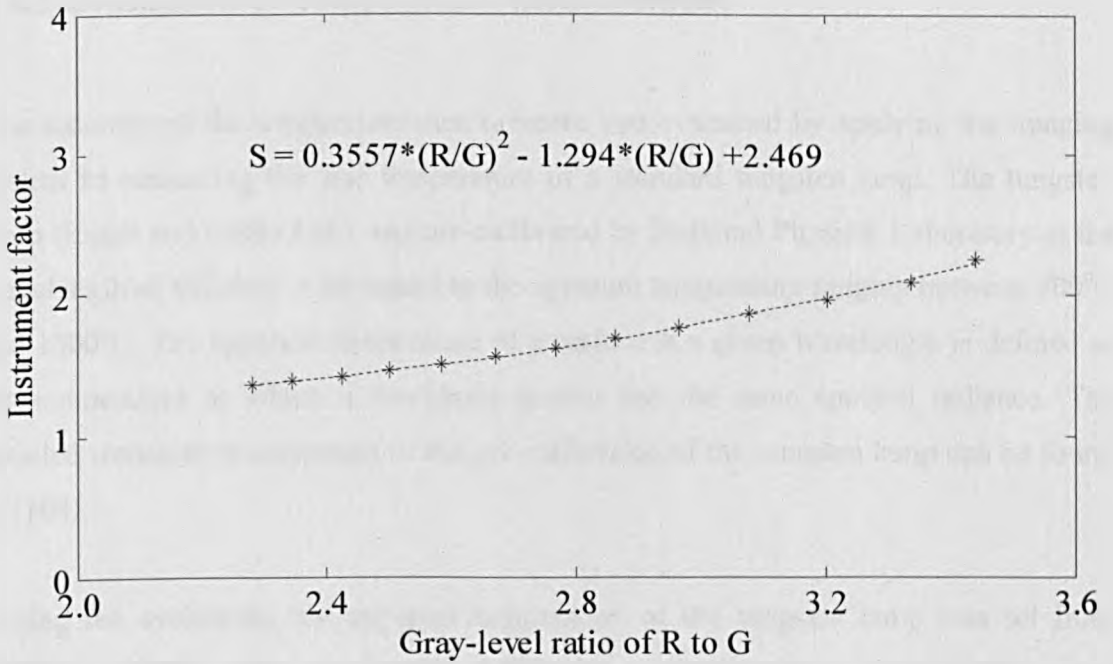


Figure 4.23 Variation of instrument factor with grey-level ratio

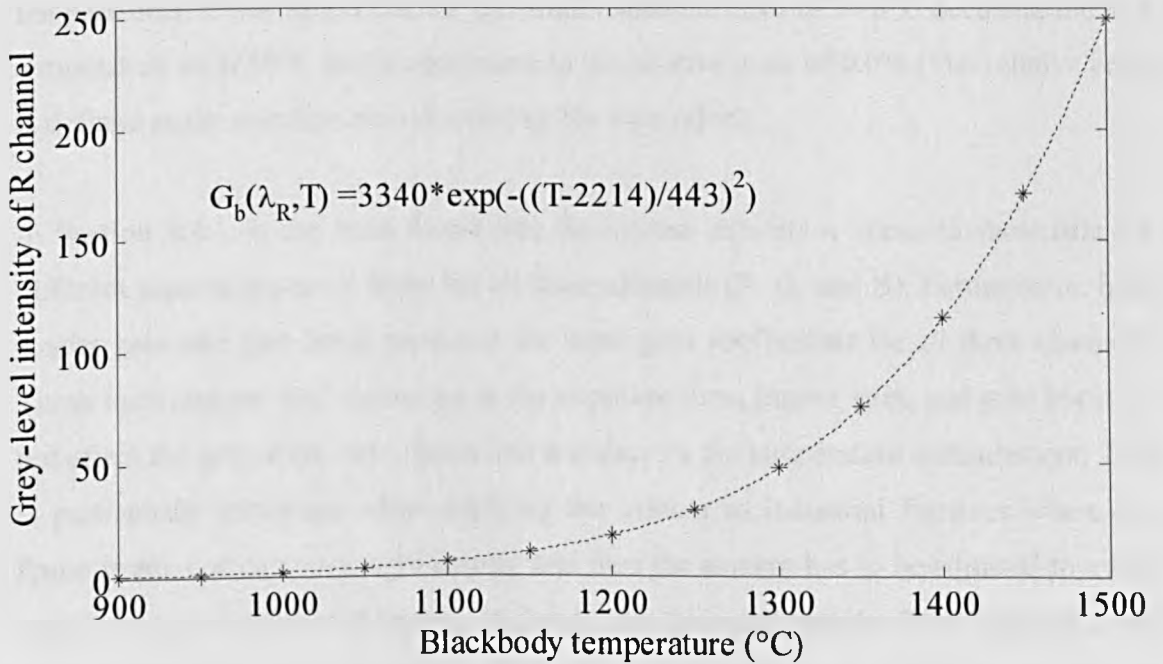


Figure 4.24 Relationship between the grey-level intensities of R component and blackbody temperature

### 4.4.3 Evaluation of Temperature Measurement

The accuracy of the temperature measurement was evaluated by applying the imaging system to measuring the true temperature of a standard tungsten lamp. The tungsten lamp (Engel and Gibbs Ltd.) was pre-calibrated by National Physical Laboratory at the wavelength of 662.4nm with regard to the apparent temperature ranging between 700°C and 1500°C. The apparent temperature of a surface at a given wavelength is defined as the temperature at which a blackbody source has the same spectral radiance. The detailed technical specification of the pre-calibration of the tungsten lamp can be found in [104].

During the evaluation, the apparent temperature of the tungsten lamp was set from 900°C to 1500°C with an interval of 50°C by controlling the current of the power supply. The corresponding true temperatures of the tungsten lamp, which can be derived from its apparent temperature by using the method given in [11], varied from 958°C to 1650°C. Figure 4.25 shows the comparison between measured and reference temperatures. It was found that the maximum absolute error of 14.8°C occurs at the true temperature of 1650°C and is equivalent to the relative error of 0.9% (The relative error is defined as the absolute error divided by the true value).

In Section 4.4.1, it has been found that the system exhibits a linear characteristic for different camera exposure times for all three channels (R, G, and B). Furthermore, both master gain and gain boost produces the same gain coefficients for all three channels. These facts suggest that variations in the exposure time, master gain, and gain boost do not affect the grey-level ratio, hence the accuracy of the temperature measurement. This is particularly important when applying the system to industrial furnaces where the flame irradiance can vary significantly and thus the camera has to be adjusted to avoid under- or over-exposure of images. It should also be noted that the R/G/B gains control only their corresponding individual channels, and the adjustment of R/G/B gains would affect the grey-level ratio and hence the temperature measurement. Therefore, the effect of R/G/B gains on the grey-level ratio, as shown in Figure 4.18, 4.19 and 4.20, must be considered in the temperature calculation if the adjustment of R/G/B gains is required.

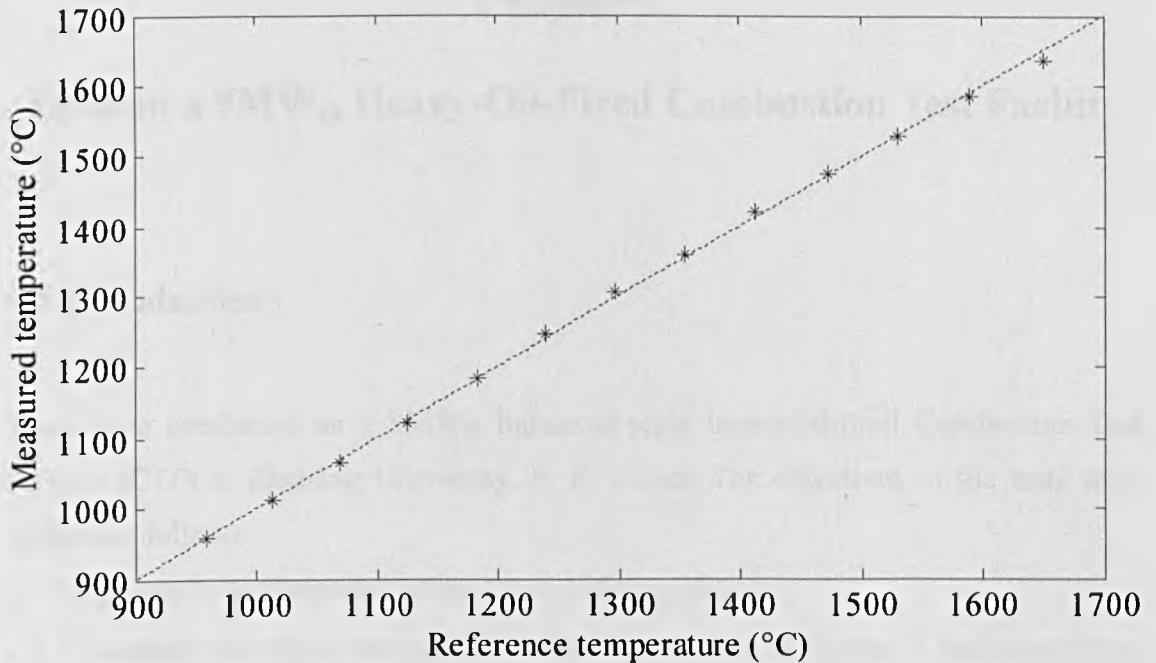


Figure 4.25 Comparison between the measured and reference temperatures

## 4.5 Summary

An instrumentation system for monitoring flame stability and burner condition in industrial boilers has been designed and implemented. The system operates on optical sensing and digital imaging techniques.

The performance of the oscillation frequency measurement of the system has been evaluated by using a standard frequency-varying light source. The relative error is no greater than 2% (frequency range: 0 to 500Hz). In order to achieve automatic adjustment of the camera to avoid under- and over-exposure of flame images, the effects of various factors, including sensor dark current, exposure time, master gain, gain boost and R/G/B gains, on the intensity responses of the R/G/B channels of the camera, have been analysed. The temperature measurement of the system has been calibrated by using a blackbody furnace as a standard temperature source. The accuracy of the temperature measurement has been verified by applying the system to measuring the true temperature of a standard tungsten lamp. The maximum error of 14.8°C occurs at the true temperature of 1650°C (equivalent to the relative error of 0.9%).

## Chapter 5

### Tests on a 9MW<sub>th</sub> Heavy-Oil-Fired Combustion Test Facility

#### 5.1 Introduction

Tests were conducted on a 9MW<sub>th</sub> industrial-scale heavy-oil-fired Combustion Test Facility (CTF) at Zhejiang University, P. R. China. The objectives of the tests were defined as follows:

- To assess the performance of the flame imaging system
- To evaluate the effectiveness of the methods presented in Chapter 3, including flame stability assessment, KPCA based abnormal condition detection, and SVM based NO<sub>x</sub> prediction and flame state identification
- To investigate the characteristics of heavy oil flames under different combustion conditions

A wide range of combustion conditions were created during the tests, including variations in the swirl vane angle of Tertiary Air (TA), the swirl vane position of Secondary Air (SA), the ratio of Primary Air (PA) to total air, the ratio of Overfire Air (OFA) to total air and the nozzle position of OFA. Previous studies suggested that these burner parameters affect significantly the aerodynamics of the entering air flow and its mixture level with fuel thus the structure and stability of the flame. The impacts of these burner parameters on the stability and characteristics of heavy oil flame are reported in this chapter.

To evaluate the effectiveness of the KPCA for combustion process monitoring, abnormal conditions were created deliberately by setting the CTF deviated from its baseline configuration. The performance of the KPCA model will be evaluated and compared with that of the PCA model. Furthermore, the results of the SVM in the prediction of NO<sub>x</sub> emission and identification of flame state will be presented and compared with that of the ANNs.

## 5.2 Experimental Conditions

### 5.2.1 Combustion Test Facility and System Installation

The 9MW<sub>th</sub> heavy-oil-fired CTF at Zhejiang University was constructed to assess the performance of the scaled model of a burner designed for a heavy-oil-fired boiler.

Figure 5.1 shows the overview of the CTF. The CTF has an 11 meters long horizontal cylindrical combustion chamber with an internal cross-section of 1.3 metres in diameter. Heavy oil fuel was atomised by steam, and injected into the combustion chamber through an oil gun, and then mixed with surrounding PA, SA, and TA successively. OFA technique is adopted in the CTF to reduce NO<sub>x</sub> emissions. Four OFA nozzle ports are fitted along the combustion chamber of the CTF.

Figure 5.2 shows the schematic diagram of the CTF and the installation location of the flame imaging system. The CTF is fitted with a number of viewing ports around the chamber. The imaging system was installed through one of the viewing ports that is at the side of furnace close to the front wall. The resulting field of view of the imaging system was about 1.3 metres in diameter along the burner axis. The root region of the flame, which is regarded as the primary reaction zone of the combustion process in terms of energy conversion and emission formation, was fully observed.

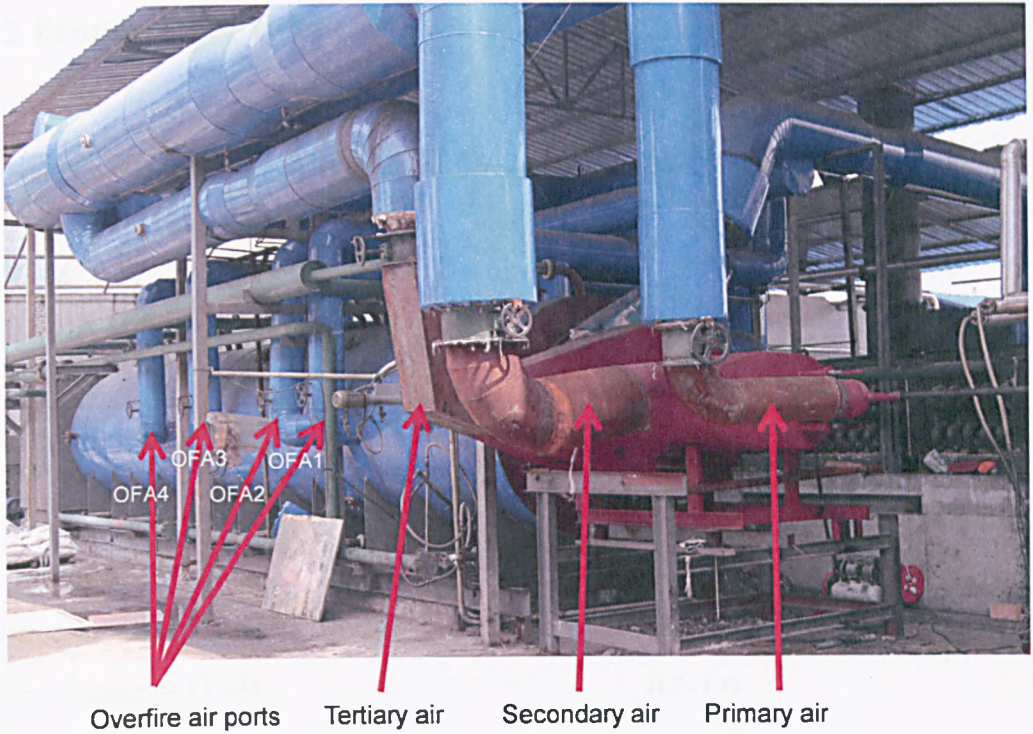


Figure 5.1 The 9MW<sub>th</sub> heavy-oil-fired combustion test facility

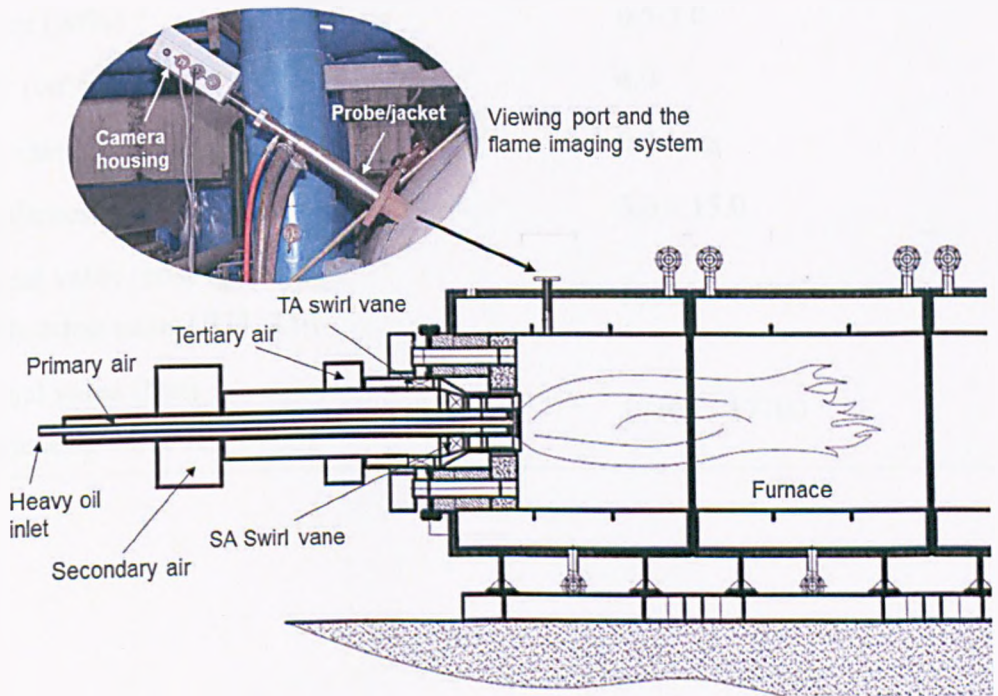


Figure 5.2 Schematic diagram of the combustion test facility and the installation location of the flame imaging system

## 5.2.2 Properties of Heavy Oil

The heavy oil used in the tests stemmed from Saudi Arabia. The properties of the heavy oil are listed in Table 5.1.

Table 5.1 Specifications of the heavy oil tested

Parameter Name	Value
Flash point (°C)	65
Pour point (°C)	24
Kinematic Viscosity @50°C (cSt)	380-400
Water content % (Vol)	0.2-1.0
Carbon (wt%)	85-87
Hydrogen (wt%)	10-12
Nitrogen (wt%)	0.1-0.4
Oxygen (wt%)	0.5-3.0
Sulfur (wt%)	4.0
Ash content (wt%)	0.2 Max
Asphaltenes (wt%)	5.0 – 15.0
Thermal value gross (gross)	18300 – 18700
High heating value (BTU/Lb)	
Thermal value (Net)	17300 - 17700
Low heating value (BTU/Lb)	

### 5.2.3 Test Programme and Measured Flame Parameters

The distribution of the air supplies (PA, SA, TA and OFA) and the configuration of the swirl vanes (angle and position) affects significantly the aerodynamics of the entering air flow and its mixture level with oil fuel thus the structure and stability of the flame. To investigate the impacts of these factors on the characteristics of oil flames, a wide range of combustion conditions were created on the CTF, including

- Variations in the swirl vane angle of tertiary air
- Variations in the swirl vane position of secondary air
- Variations in the ratio of primary air to total air
- Variations in the ration of overfire air to total air and its nozzle position

The entire test programme lasted two days. During the tests, an oil-free air compressor was used to supply the purging air (flow rate: 20 litres per minutes; pressure: 2 bars) to clean the tip lens of the optical probe. Water supply was provided to cool system jacket. The on-site experiments showed that the air purging and water cooling approach is capable of keeping the optical system dust-free and preventing its over-heating problem effectively, provided that the period of continual operation is within eight hours (the maximum period of the continual test during the test programme).

Detailed test programme is summarized in Table 5.2. When a specific factor was tested, other factors were kept constant. For each test, the measured parameters include the flame stability index, power spectral density, oscillation frequency, and temperature. To present the obtained results statistically, each data point is an average of 50 instantaneous values. The standard deviation of each data point was also computed and is shown as an error bar in corresponding figures. The  $\text{NO}_x$  emissions of flue gas, which were measured concurrently by a gas analyser during the tests, are also given.

To evaluate the performance of the computing algorithms presented in Section 3.3 for the burner condition monitoring, a total of 27 flame characteristics were extracted from flame sensorial data and used as the inputs of the KPCA and SVM models. The detailed description about these flame characteristics have been given in Section 3.3.1.

Table 5.2 Summary of the test programme on the 9MW<sub>th</sub> combustion test facility

No	Test	Distribution of air supply				Configuration of swirl vanes		
		Primary air (%)	Secondary air (%)	Tertiary air (%)	Overfire air (%)	Swirl vane position of secondary air (mm)	Swirl vane angle of tertiary air	
1	Swirl vane angle of tertiary air	17%	43%	40%	0	--	25°	
							35°	
							45°	
2	Swirl vane position of secondary air	17%	43%	40%	0	--	-17	
							30	
							65	
3	Ratio of primary air to total air	43	43	46	0	--	--	
				43				
				40				
				37				
				34				
4	Ratio and nozzle position of overfire air	17.0	43.0	40.0	0	--	--	
					14.5			15.0*
					14.0			17.5*
					13.6			20.0*

\*Two different OFA nozzles were tested (OFA2 and OFA3).

## 5.3 Results of Flame Stability Monitoring

### 5.3.1 Different Swirl Vane Angles of Tertiary Air

The swirling intensity of air flow affects significantly the intermixing of atomised oil fuel and air flow hence subsequent combustion performance. The adjustable settings of the CTF that are capable of controlling the swirling intensity of air flow include the swirl vane angle of the TA and the swirl vane position of the SA. This section presents the test results for the different swirl vane angles of the TA.

The TA swirl vane angle determines the direction of the tertiary air flow. It is defined as the angle between the swirl vane and the plane perpendicular to the burner axis. The TA swirl vane angle of the burner can be varied from  $0^\circ$  to  $90^\circ$ . When the angle is  $0^\circ$  the TA inlet is fully closed, whilst when  $90^\circ$  the TA inlet is fully open without any swirling. Under the same flow rate, a smaller swirl angles gives a stronger swirling intensity.

During the test, three different swirl vane angles of the TA, i.e.,  $25^\circ$ ,  $35^\circ$ , and  $45^\circ$ , were created. Figure 5.3 shows the typical examples of instantaneous heavy oil flame images obtained under these three conditions. It should be noted that the images were over-exposed deliberately for an observation and presentation purpose. A direct comparison among the images has suggested that a greater TA swirl vane angle resulted in a stretched flame. This can be understood by the fact that the stronger the swirling intensity of the tertiary air, the stronger centrifugal force the air flow has, resulting in a wide spread angle of the flame.

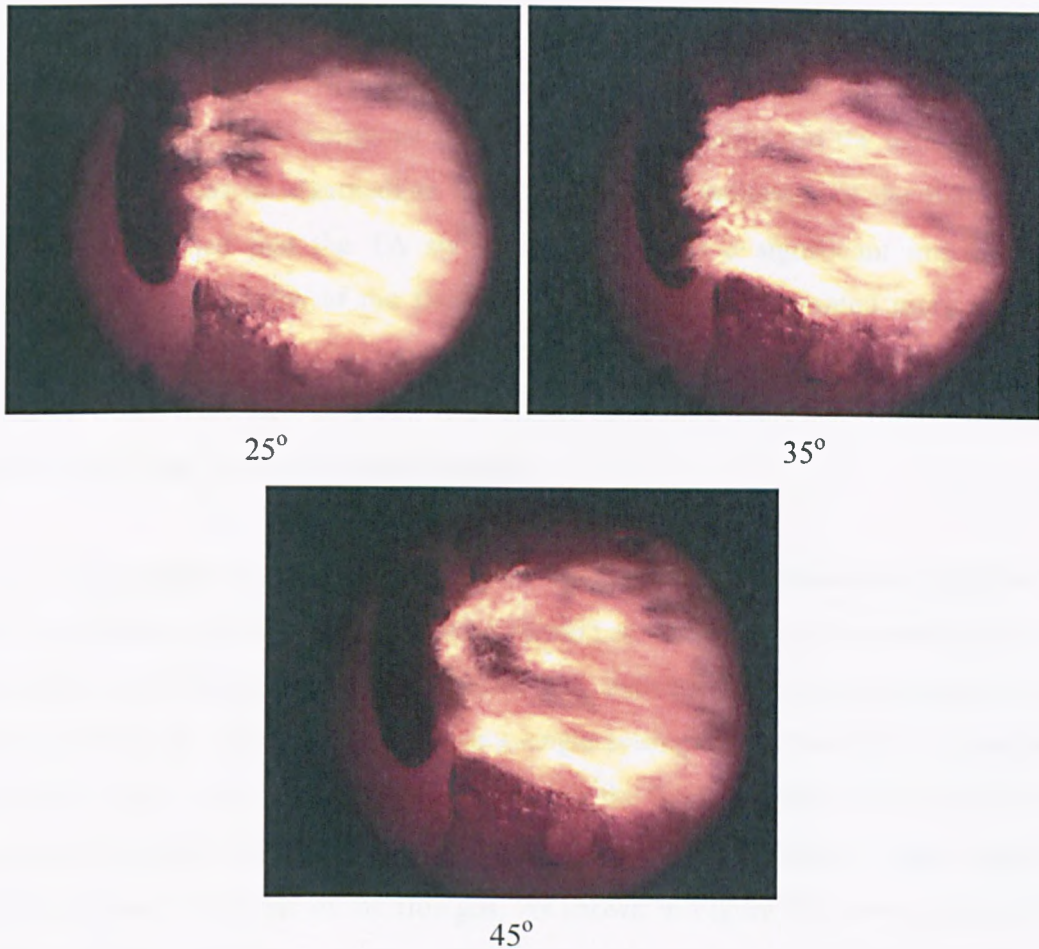


Figure 5.3 Flame images taken for different swirl vane angles of tertiary air

Figure 5.4 shows the variation of the stability index (Section 3.2.3) with the TA swirl vane angle. As mentioned, each data point is an average of 50 instantaneous values, and the standard deviation is shown as error bars in the figure. The stability index increased with the vane angle, which suggests that an increased TA swirl vane angle would result in improved flame stability. The lowest stability index is observed at  $25^\circ$ , suggesting the flame is relatively unstable under such a swirl vane angle setting.

This result is in line with the results of the PSD and oscillation frequency of the flame. Figure 5.5 and 5.6 illustrate typical examples of the PSD estimates (Section 3.2.2) of the flame radiation signals taken in the visible and infrared bands for the test conditions, respectively. As can be seen, for both the visible and infrared bands, the amplitude of the low-frequency components for  $25^\circ$  (0~10Hz) is much higher than that for  $35^\circ$  and  $45^\circ$ , whilst the high-frequency components are very similar in all three cases. Previous

studies have revealed that the low-frequency components in the flame signal are mainly attributed to its geometrical fluctuations due to aerodynamic or convective effects, whilst the high-frequency components reflect kinetic variations in the heat release rate or energy transitions in intermediate radicals. The PSD estimates of the flame signals have thus suggested that the TA swirl vane angle has a significant impact on the geometrical characteristics of the flame. This has been demonstrated more clearly in Figure 5.7 where the weighted oscillation frequency (Section 3.2.2) has shown an increased trend with the TA swirl vane angle, indicating increased flame stability in terms of the flame geometric characteristics.

Figure 5.8 suggests a slight increase in the averaged flame temperature with the TA swirl vane angle. An increased standard deviation of the average temperature (shown as error bars in the figure) is also observed at 25°, indicating a greater fluctuation of the flame temperature under such a swirl vane angle setting. It can therefore be concluded that, under the TA swirl vane angles 35° and 45°, the flame is more stable in terms of its geometric, luminous and fluid-dynamic characteristics. This finding is also consistent with the emission analysis of the flue gas. As shown in Figure 5.9, the volume of NO<sub>x</sub> in the flue gas decreases with the swirl vane angle, suggesting that it is crucial to maintain a stable flame for reduced NO<sub>x</sub> emissions.

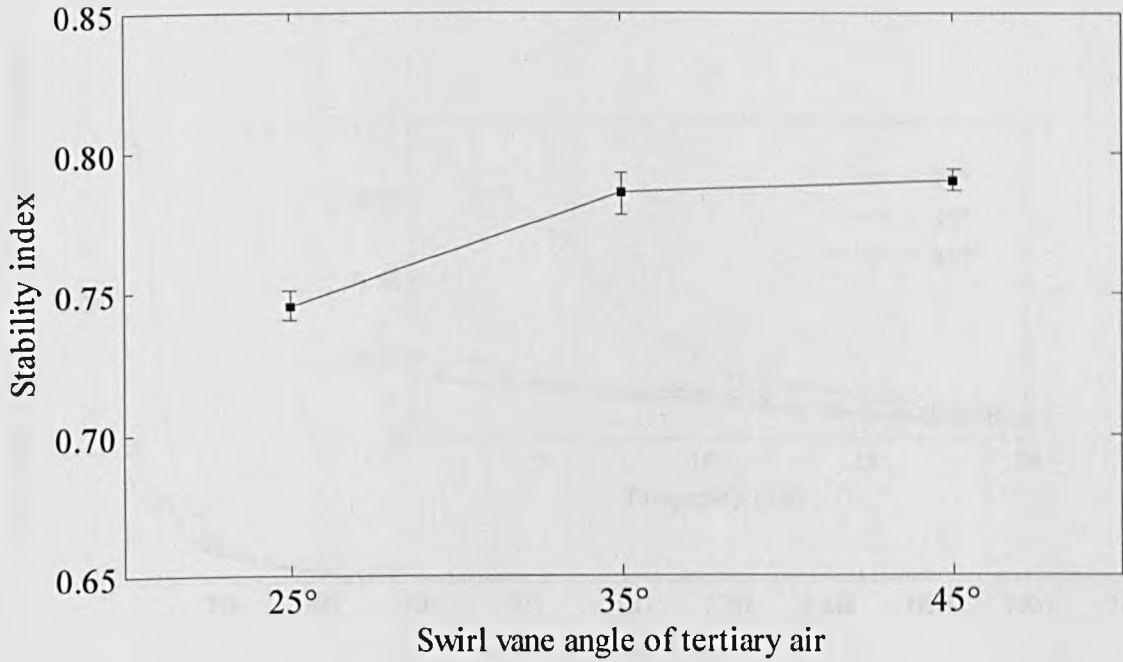


Figure 5.4 Variations of stability index with the swirl vane angle of tertiary air

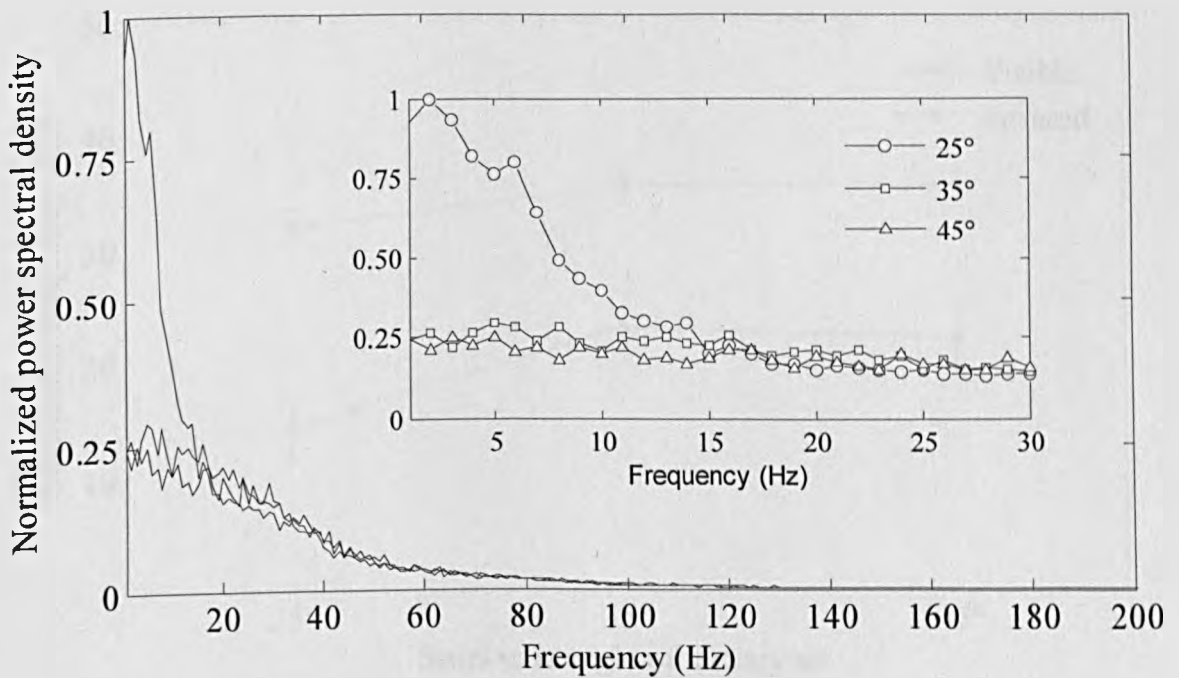


Figure 5.5 Variations of power spectral density estimates of flame radiation signal in visible band with the swirl vane angle of tertiary air

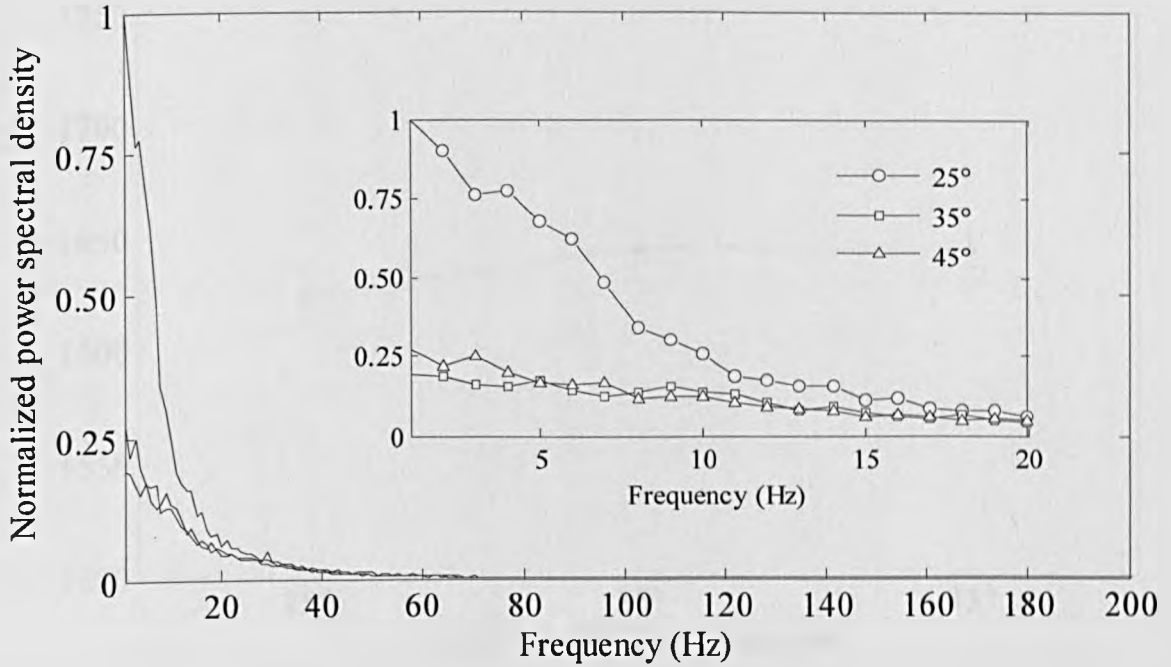


Figure 5.6 Variations of power spectral density estimates of flame radiation signal in infrared band with the swirl vane angle of tertiary air

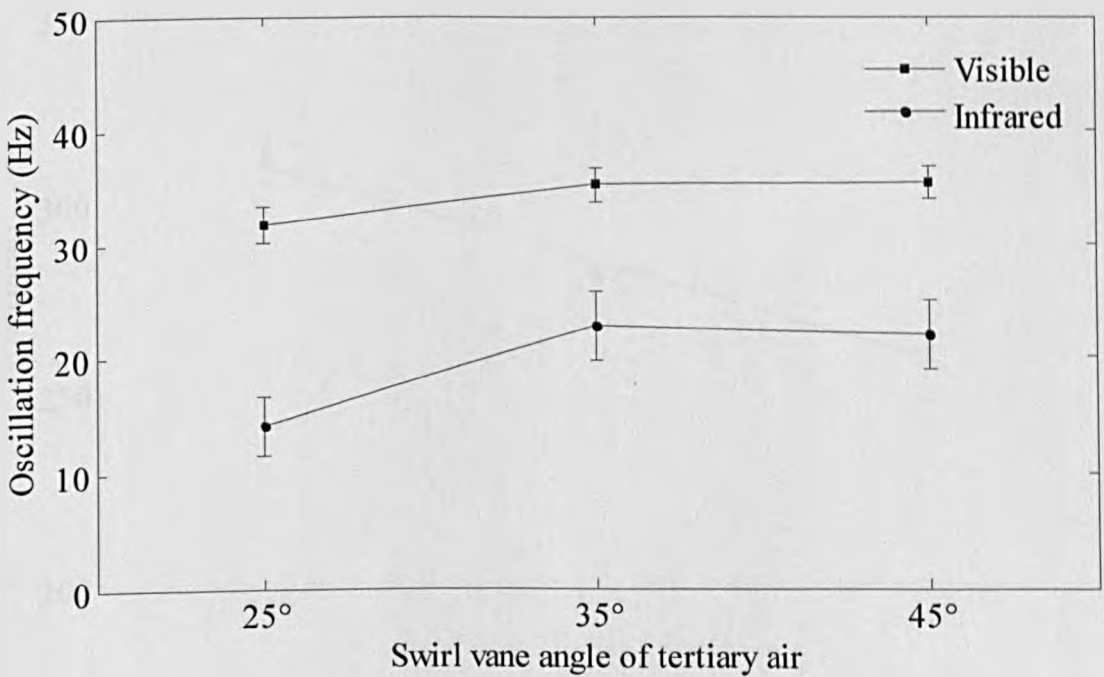


Figure 5.7 Variations of oscillation frequency with the swirl vane angle of tertiary air

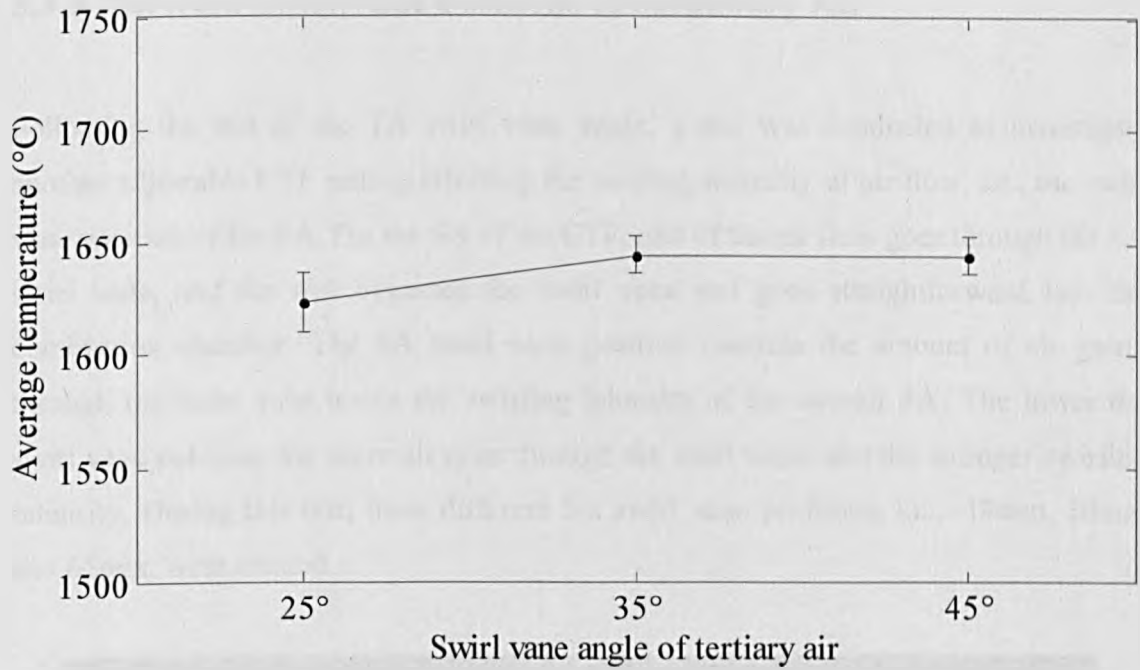


Figure 5.8 Variations of average temperature with the swirl vane angle of tertiary air

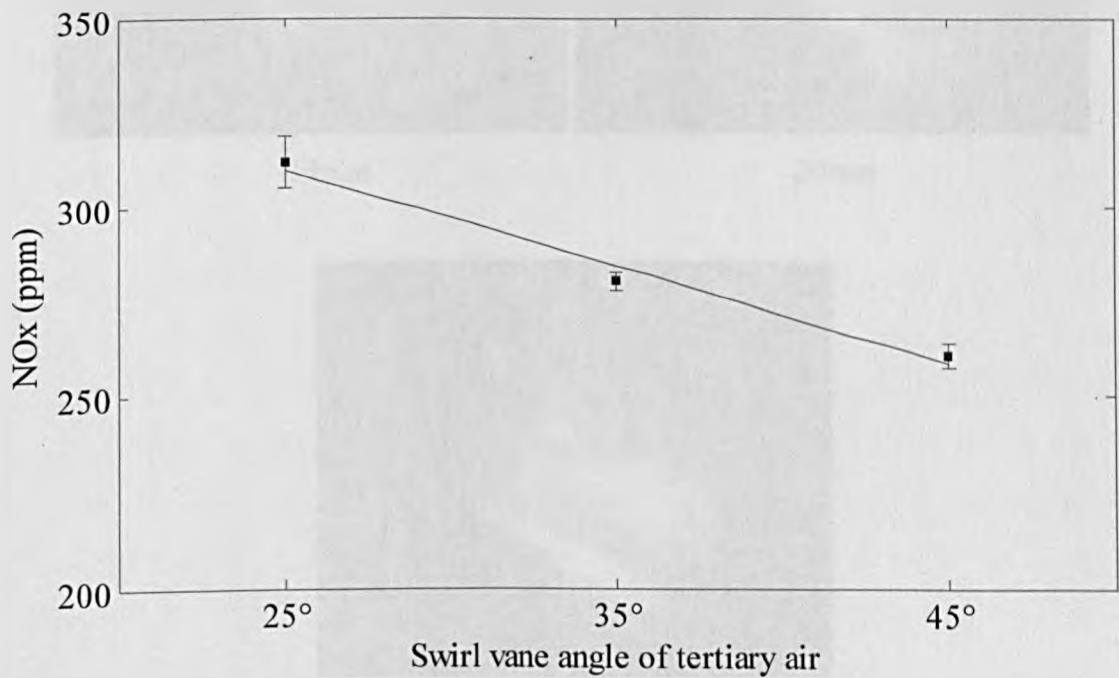


Figure 5.9 Variations of NO<sub>x</sub> emission with the swirl vane angle of tertiary air

### 5.3.2 Different Swirl Vane Positions of Secondary Air

Following the test of the TA swirl vane angle, a test was conducted to investigate another adjustable CTF setting affecting the swirling intensity of air flow, i.e., the swirl vane position of the SA. For the SA of the CTF, part of the air flow goes through the SA swirl vane, and the rest bypasses the swirl vane and goes straightforward into the combustion chamber. The SA swirl vane position controls the amount of air going through the swirl vane hence the swirling intensity of the overall SA. The lower the swirl vane position, the more air goes through the swirl vane, and the stronger swirling intensity. During this test, three different SA swirl vane positions, i.e., -17mm, 30mm and 65mm, were created.

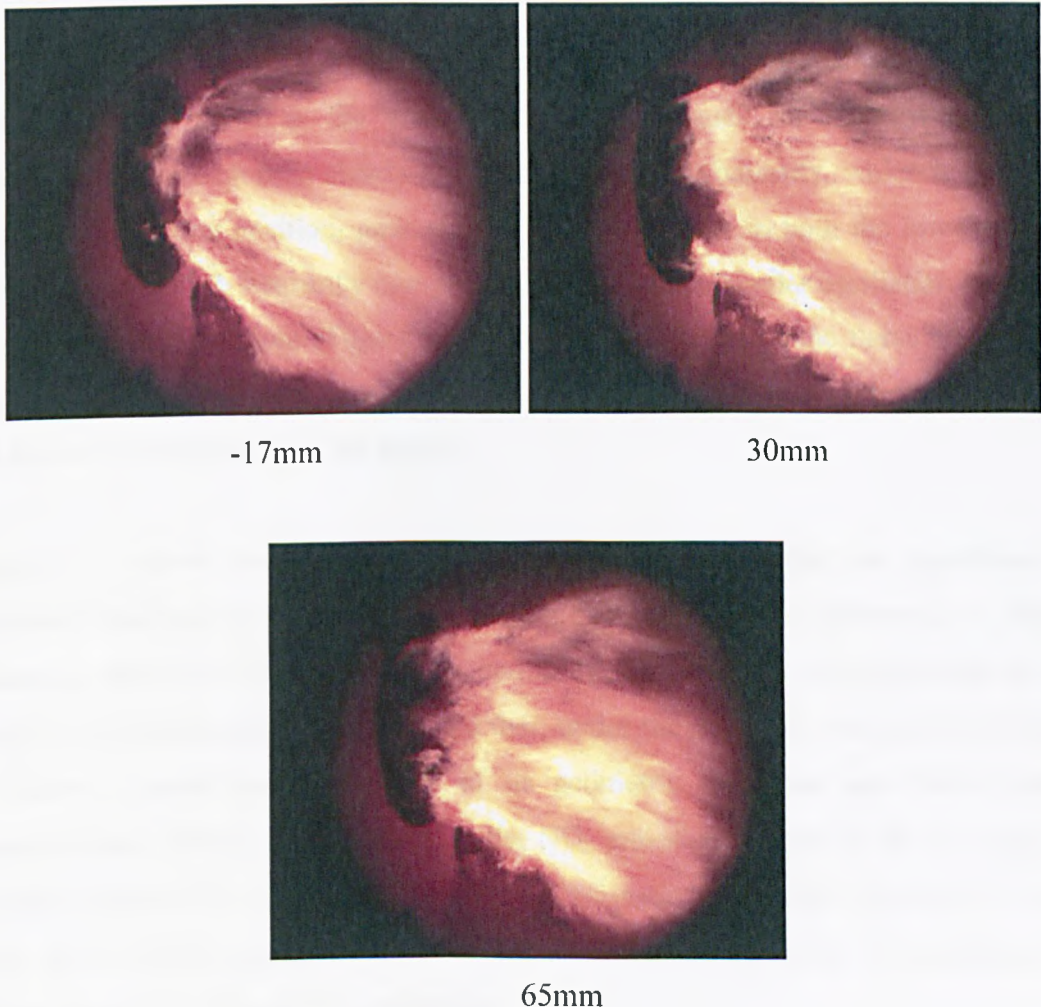


Figure 5.10 Flame images taken for different swirl vane positions of secondary air

Figure 5.10 shows the typical examples of instantaneous heavy oil flame images for different SA swirl vane positions. Similar to the influence of the TA swirl vane angle, a direct comparison among the images has suggested that a greater SA swirl vane position resulted in a slightly stretched flame. This can be understood by the fact that the stronger the swirling intensity of the secondary air, the more air goes swirly towards away from the burner axis due to the effect of centrifugal force, resulting in a wide spread angle of the flame.

Figure 5.11 shows the variations of measured stability index with the SA swirl vane position. The stability indices at -17mm and 30mm are similarly low, about 0.67, while an increased stability index is observed at 65mm, indicating a more stable flame under such a vane position setting.

Figure 5.12 and 5.13 illustrate the typical examples of the PSD estimates of the flame radiation signals taken in the visible and infrared bands for the test conditions, respectively. It can be seen clearly that a strong swirling intensity, which is generated by a low swirl vane position, gave rise to high amplitudes in both the low-frequency components and high frequency components, resulting in a similar oscillation frequency for all three vane positions (Figure 5.14). The PSD estimates of the flame signals have suggested that the SA swirl vane position has a significant impact on both geometrical and kinetic characteristics of the flame.

Figure 5.15 shows the averaged flame temperature under the test conditions. A decreased standard deviation of the average temperature is observed at 65mm, indicating improved flame stability in terms of fluid-dynamic characteristics at this condition. It can therefore be concluded that, under the SA swirl vane position 65mm, the flame is more stable in terms of its geometric, luminous and fluid-dynamic characteristics. This is also in line with the  $\text{NO}_x$  emission analysis of the flue gas. As shown in Figure 5.16, the volume of  $\text{NO}_x$  emissions in the flue gas reached its lowest value at SA 65mm among the three tested conditions, suggesting the importance of flame stability for reduced  $\text{NO}_x$  emissions.

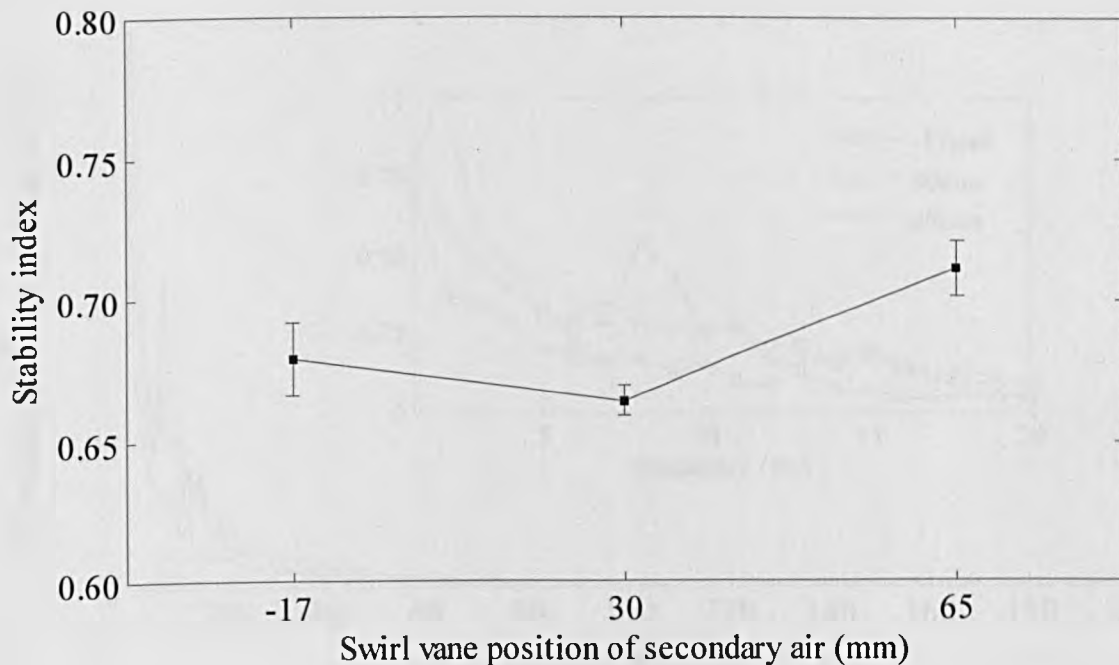


Figure 5.11 Variations of flame stability index with the ratio of primary air to total air

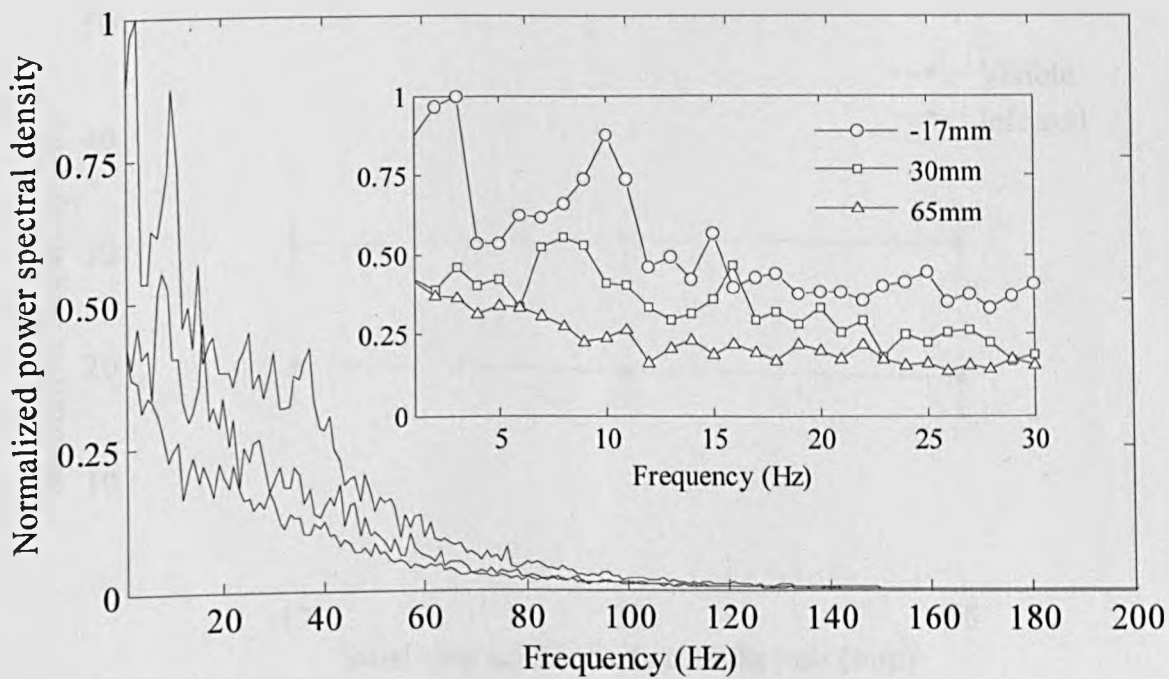


Figure 5.12 Variations of power spectral density estimates of flame radiation signals in visible band with the ratio of primary air to total air

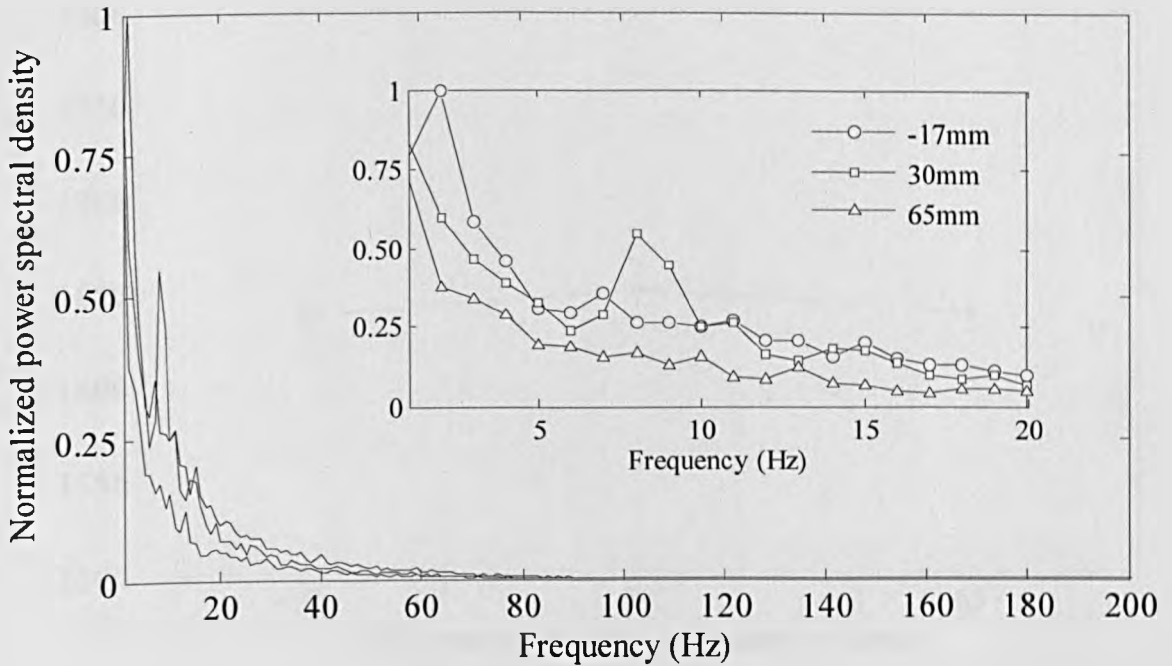


Figure 5.13 Variations of power spectral density estimates of flame radiation signals in infrared band with the ratio of primary air to total air

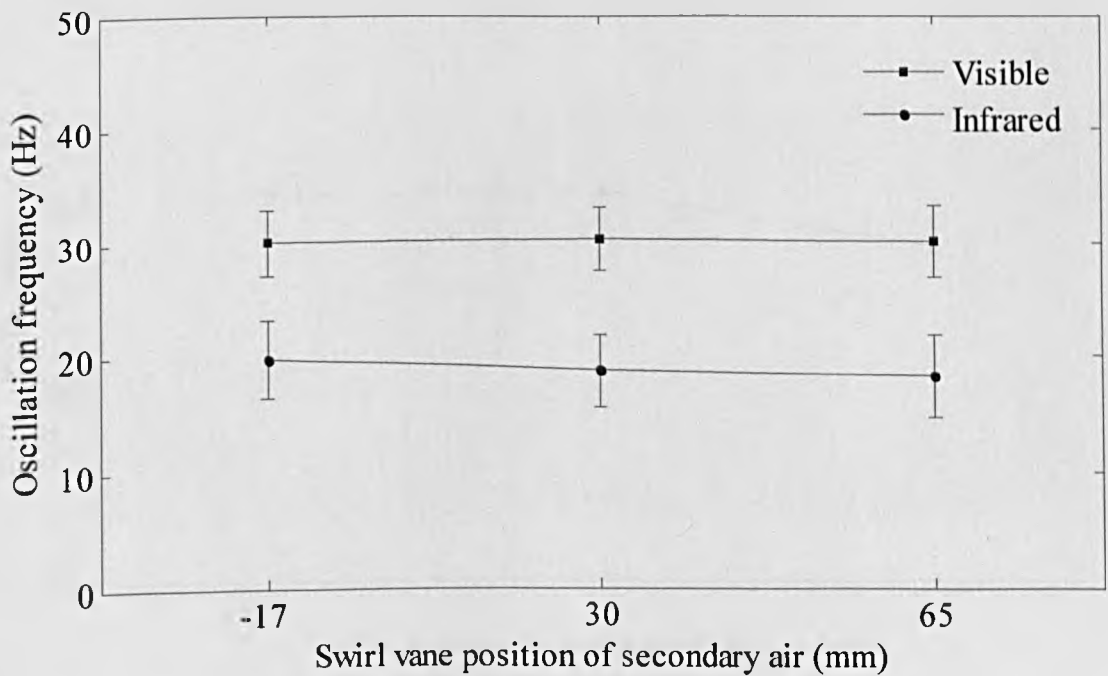


Figure 5.14 Variations of oscillation frequency with the ratio of primary air to total air

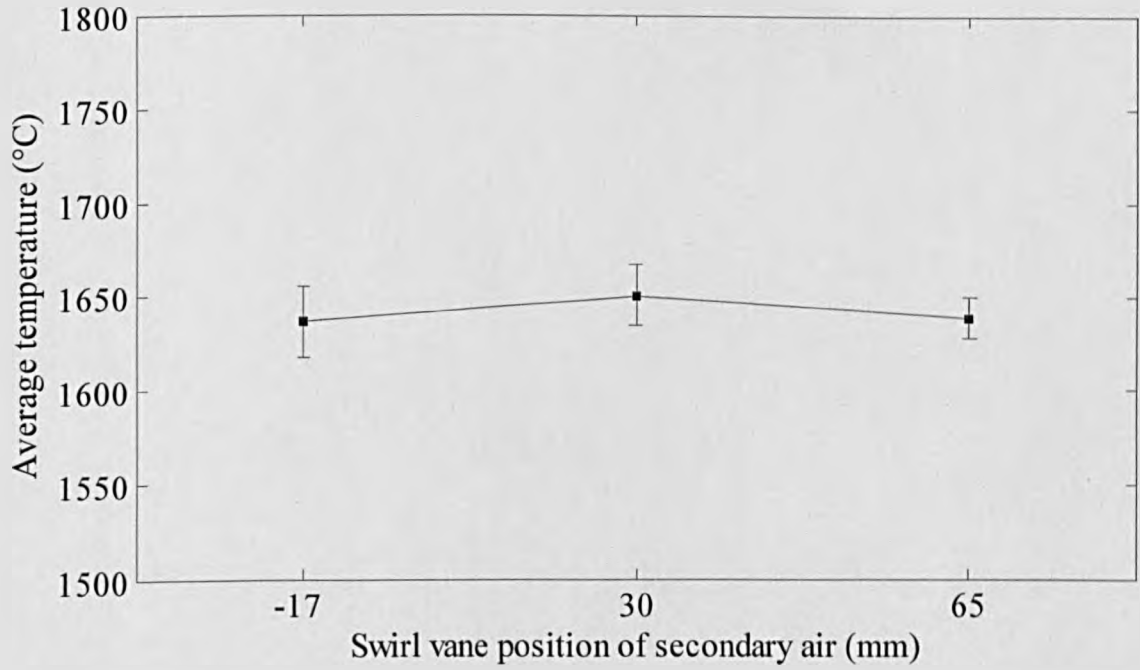


Figure 5.15 Variations of average temperature with the swirl vane position of secondary air

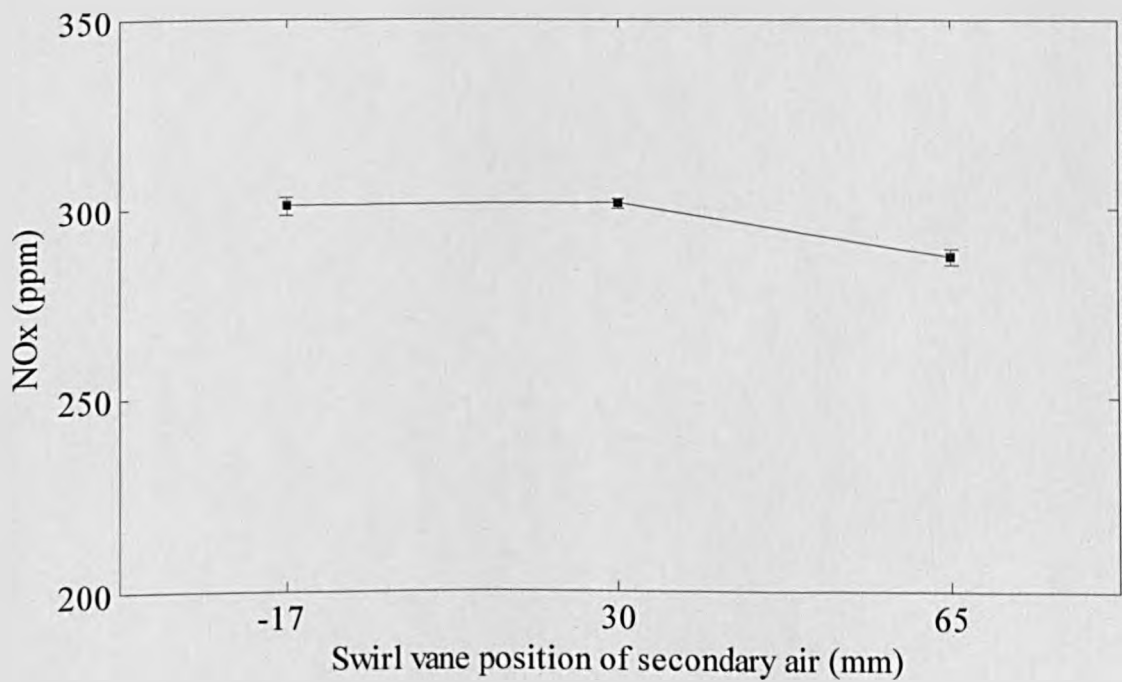
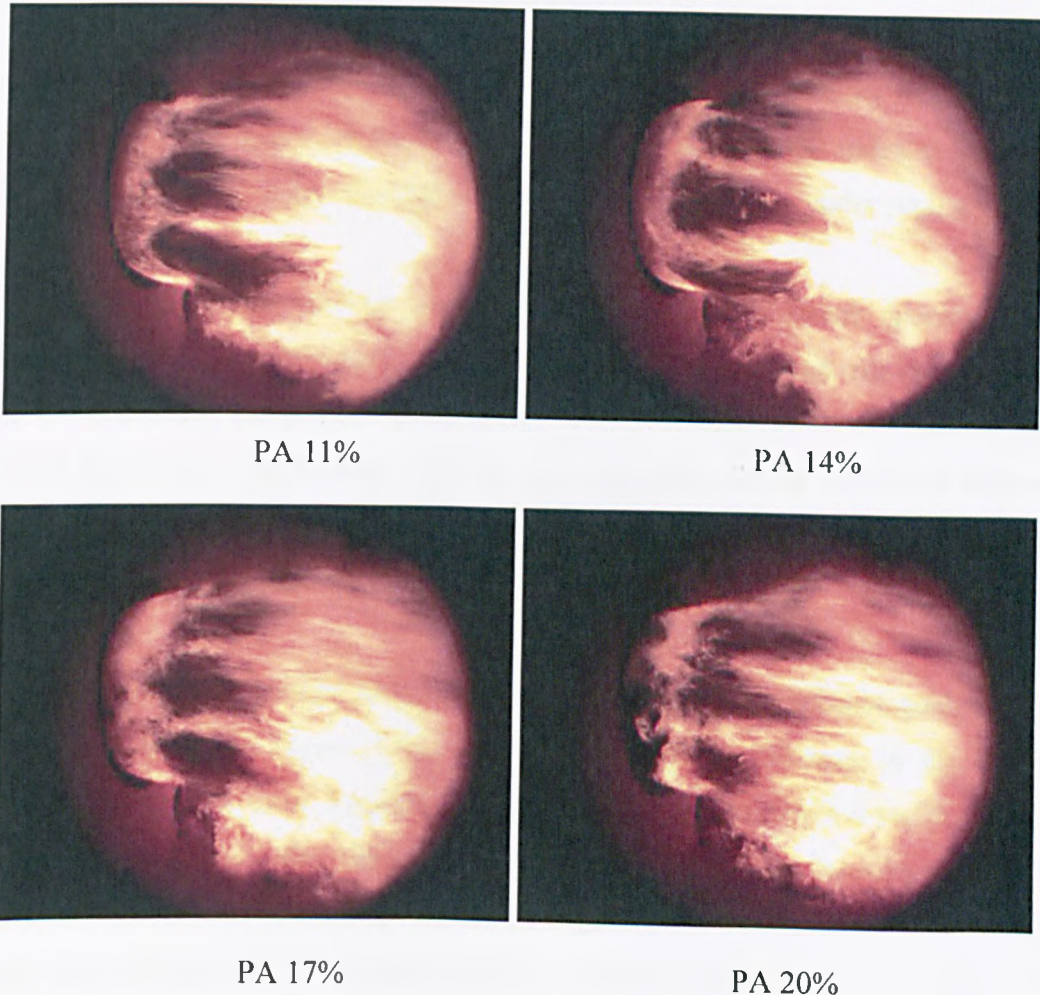


Figure 5.16 Variations of NO<sub>x</sub> emission with the swirl vane position of secondary air

### 5.3.3 Different Ratios of Primary Air to Total Air

The purpose of this test was to investigate the impacts of the spatial distribution of air flow on the stability and characteristics of the heavy oil flame. During this test, the total air flow rate ( $9100\text{Nm}^3/\text{h}$ ) and the ratio of SA to total air (43%) provided for the burner were kept constant. When the ratio of PA to total air increased, the ratio of TA to total air decreased by the same degree correspondingly. Five different PA ratios, i.e., 11%, 14%, 17%, 20% and 23% were tested. Figure 5.17 shows the typical images of the instantaneous heavy oil flame under different PA ratios.





PA 23%

Figure 5.17 Flame images taken for different ratios of primary air to total air

Figure 5.18 suggests that with the increase of the PA ratio, the stability index increases gradually, indicating improved flame stability. The lowest stability index value of 0.71 is obtained at PA 11%, suggesting the flame is relatively unstable under such a PA ratio.

The result of the flame stability index is supported by the power spectral density analysis, as illustrated in Figure 5.19 and 5.20. It has been observed that the amplitudes of the low-frequency components ( $<10\text{Hz}$ ) at PA 11% in both visible and infrared bands are much higher than that at other conditions, resulting the lowest oscillation frequency among the five test conditions (Figure 5.21), which indicates an increased geometrical fluctuation at such a condition.

The result of the flame stability index is also consistent with the emission analysis of the flue gas. As shown in Figure 5.23, the volume of  $\text{NO}_x$  emissions in the flue gas decreases with the PA ratio, suggesting that it is crucial to maintain a stable flame for reduced  $\text{NO}_x$  emissions. The decreased  $\text{NO}_x$  emissions may also be relevant with the slightly decreased temperature, as shown in Figure 5.22. It has been found that the average flame temperature decreased slightly with the increase of the PA ratio. The slightly decreased temperature may be due to the distribution of the fuel spray of the burner. The fuel is lean inside and rich outside within the cross-section of the burner axis. With the increase of the PA ratio, the TA decreased accordingly, resulting in a decreased oxygen concentration in the fuel rich zone hence a decreased temperature.

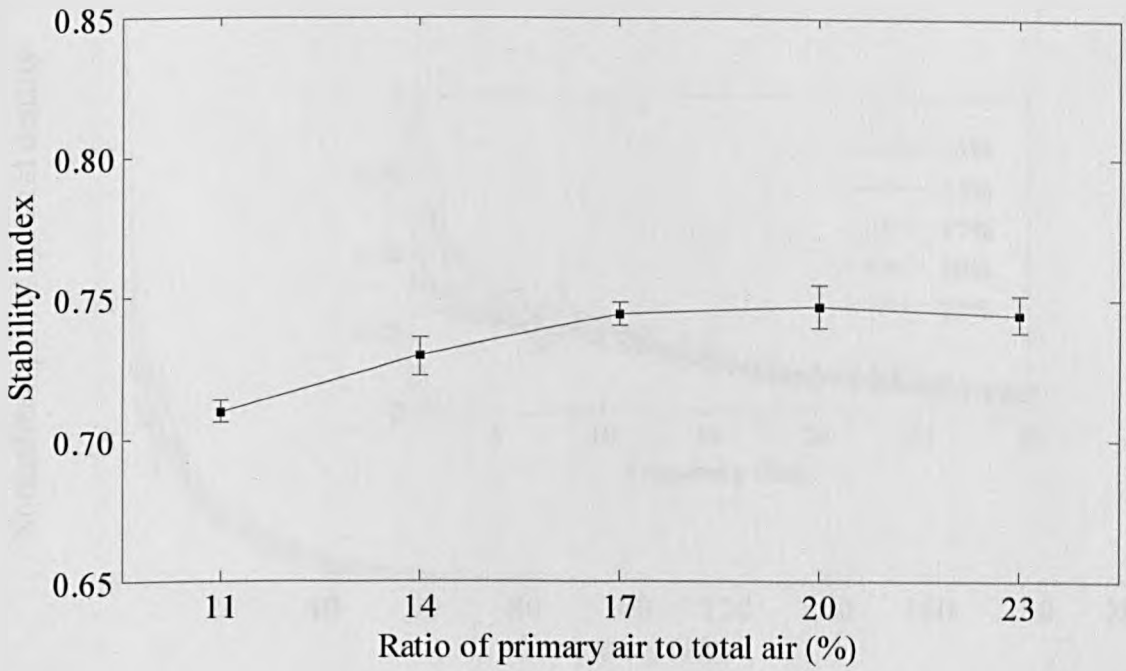


Figure 5.18 Variations of flame stability index with the ratio of primary air to total air

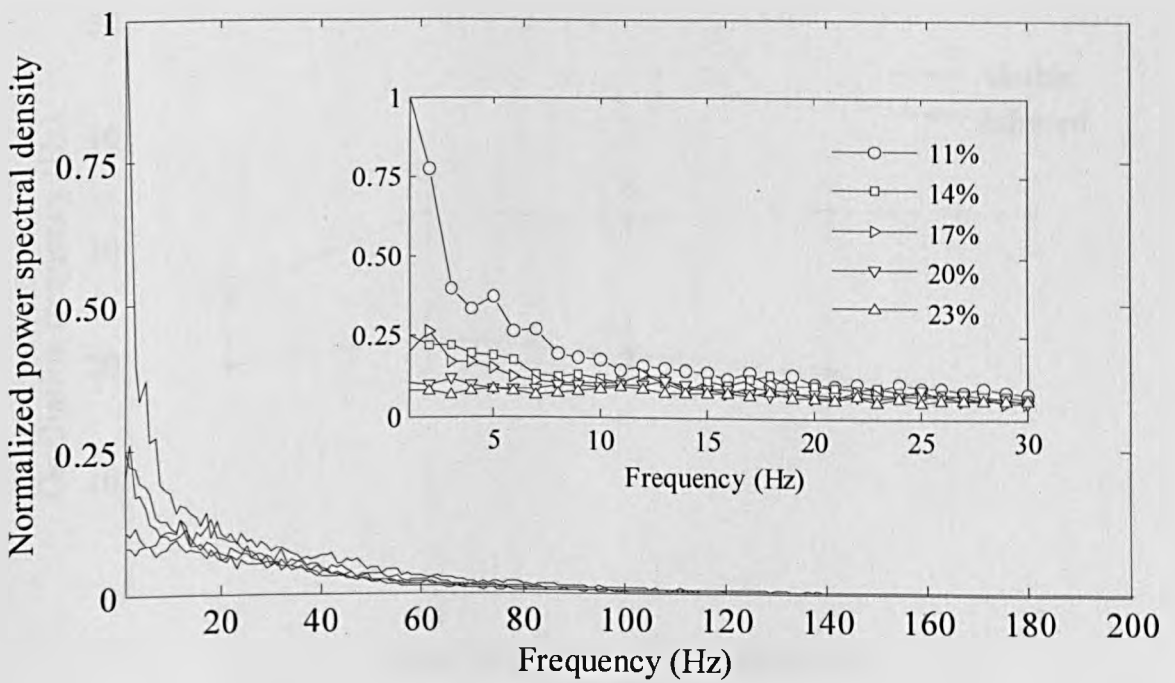


Figure 5.19 Variations of power spectral density estimates of flame radiation signals in visible band with the ratio of primary air to total air

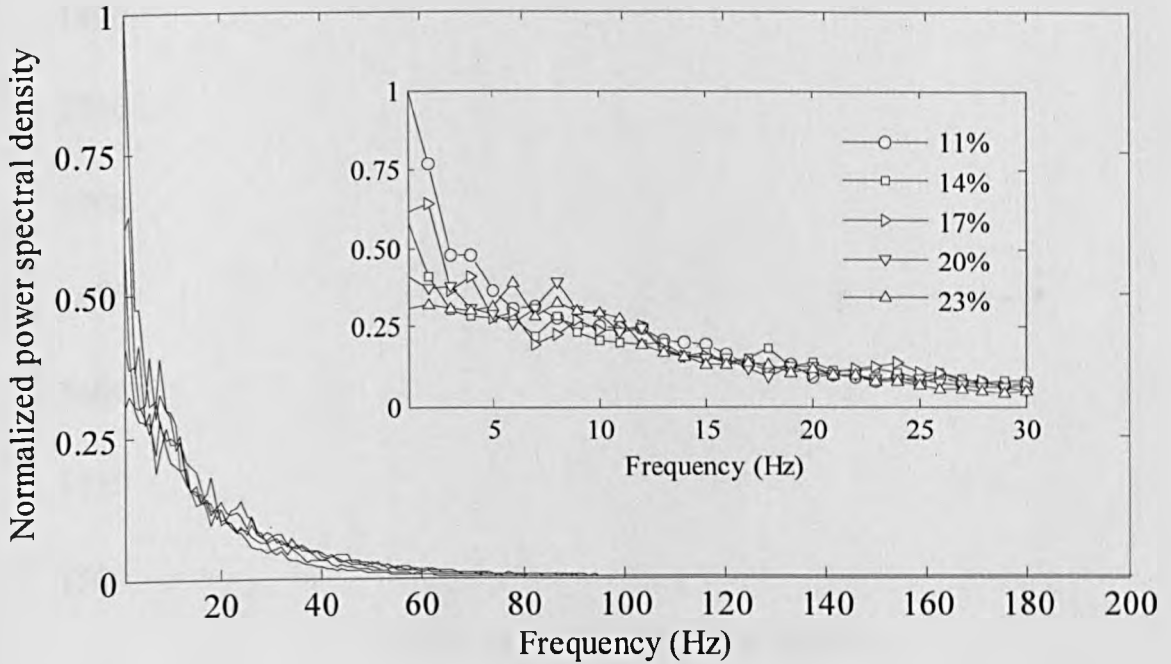


Figure 5.20 Variations of power spectral density estimates of flame radiation signals in infrared band with the ratio of primary air to total air

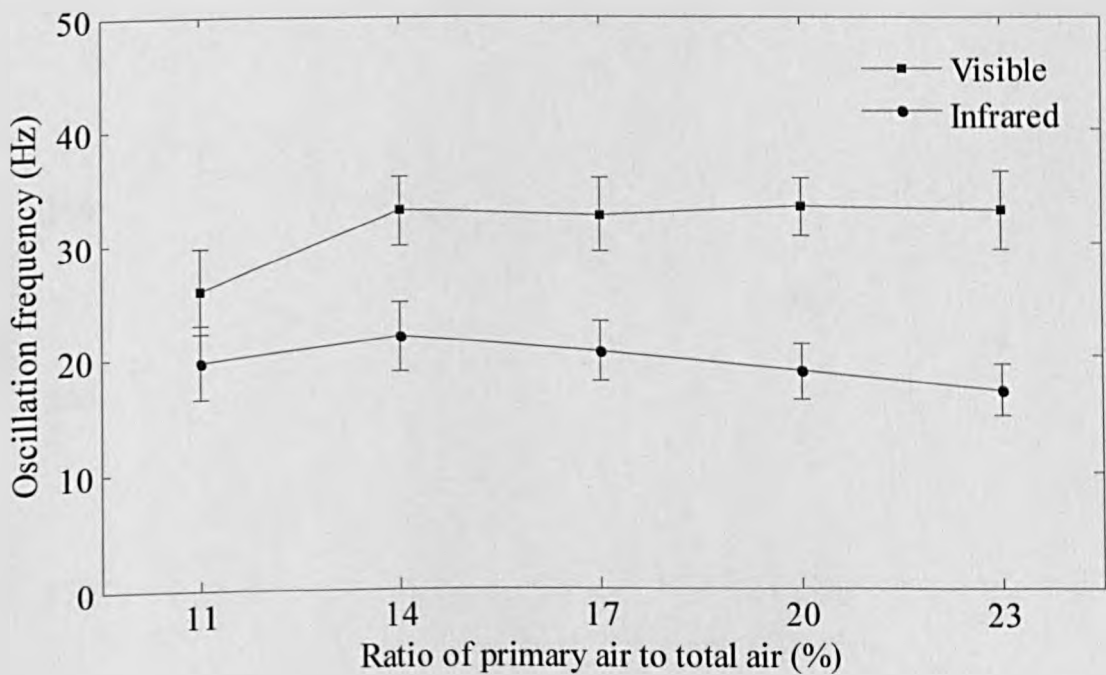


Figure 5.21 Variations of oscillation frequency with the ratio of primary air to total air

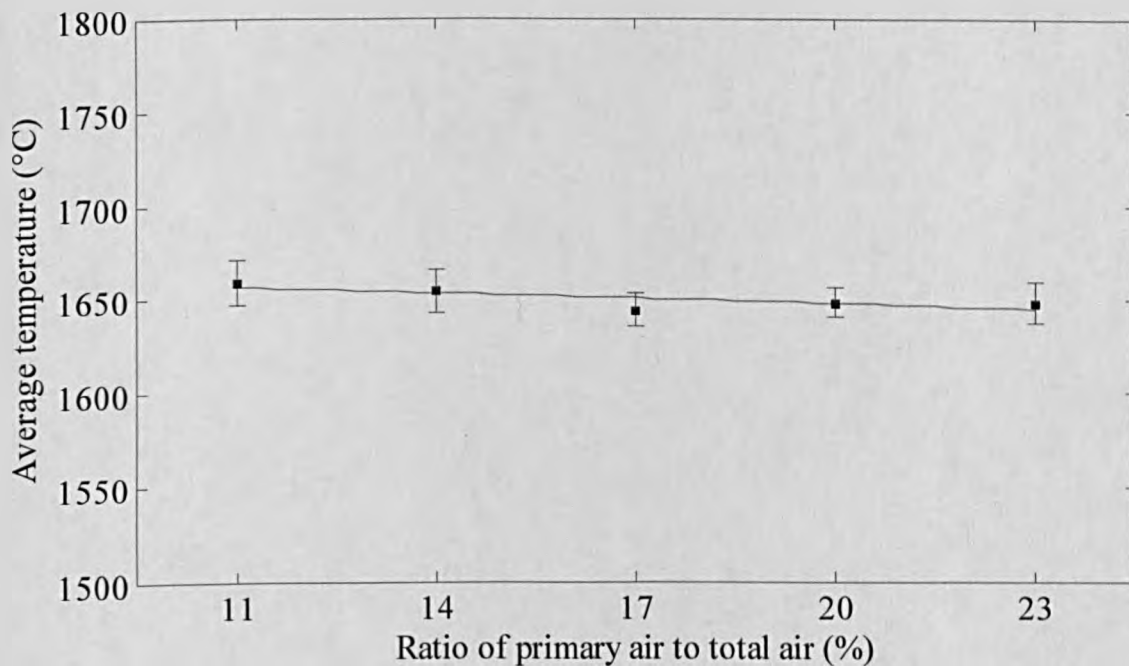


Figure 5.22 Variation of average temperature with the ratio of primary air to total air

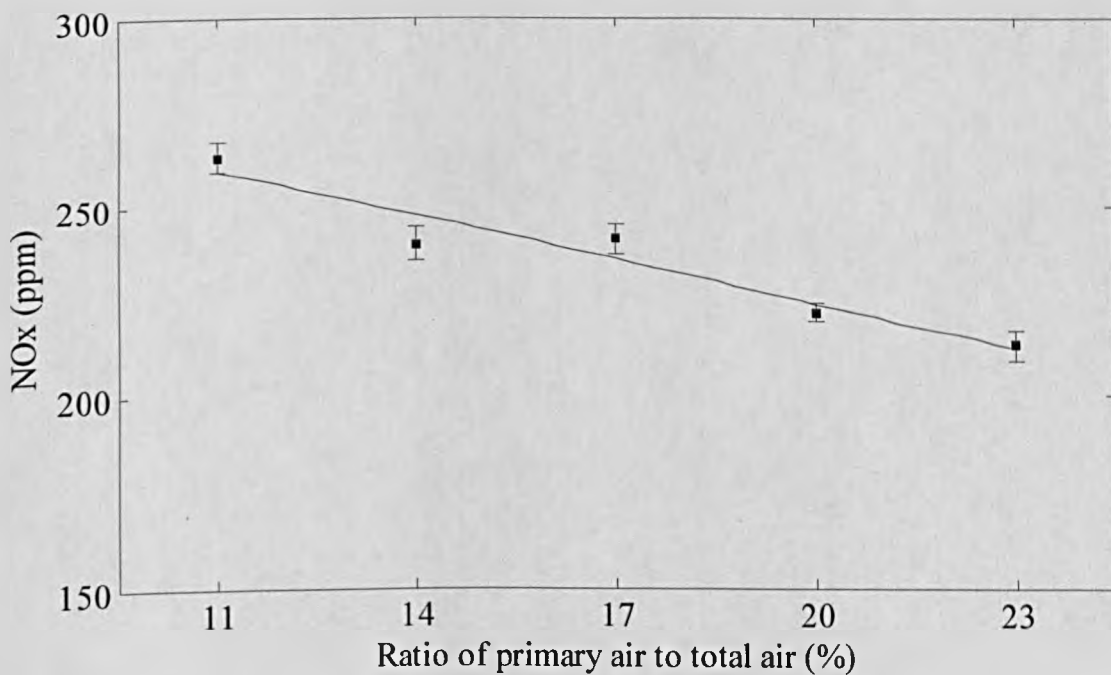


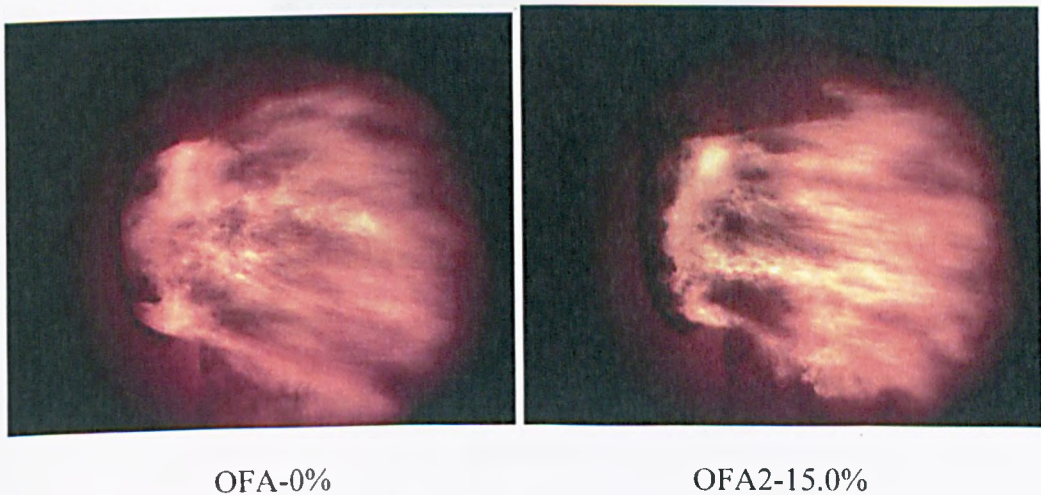
Figure 5.23 Variations of NO<sub>x</sub> emission with the ratio of primary air to total air

### 5.3.4 Different Ratios and Nozzle Positions of Overfire Air

The OFA is an effective technology for reducing  $\text{NO}_x$  emissions from a combustion process. Combustion air is reduced from the burner to create a fuel rich condition in the primary combustion zone. Fuel-bound nitrogen conversion to  $\text{NO}$  is inhibited in the furnace. More importantly, the peak flame temperature is reduced to limit thermal  $\text{NO}_x$  formation. A large amount of air is then fed and intersected the combustion gases in the downstream of the furnace to complete the combustion [105].

A test was conducted on the CTF to reveal the impacts of the ratio of OFA to total air, and the location of OFA nozzle port on the stability and characteristics of the heavy oil flame. The second and third OFA nozzles, assigned OFA2 and OFA3 (Figure 5.1), were tested. The distances from the burner outlet to the two OFA nozzle ports are 4.5m and 6.6m, respectively. For each OFA port, four different OFA ratios were created, i.e., 0%, 15.0%, 17.5% and 20.0%, whilst the total air was kept constant during the test.

Figure 5.24 shows typical examples of instantaneous flame images under tested conditions. A direct comparison between the OFA flame and non-OFA flame (OFA 0%) has suggested that the OFA flame has a stretched shape (the spread angle of the flame is narrowed) due to the reduced amount of SA and TA.



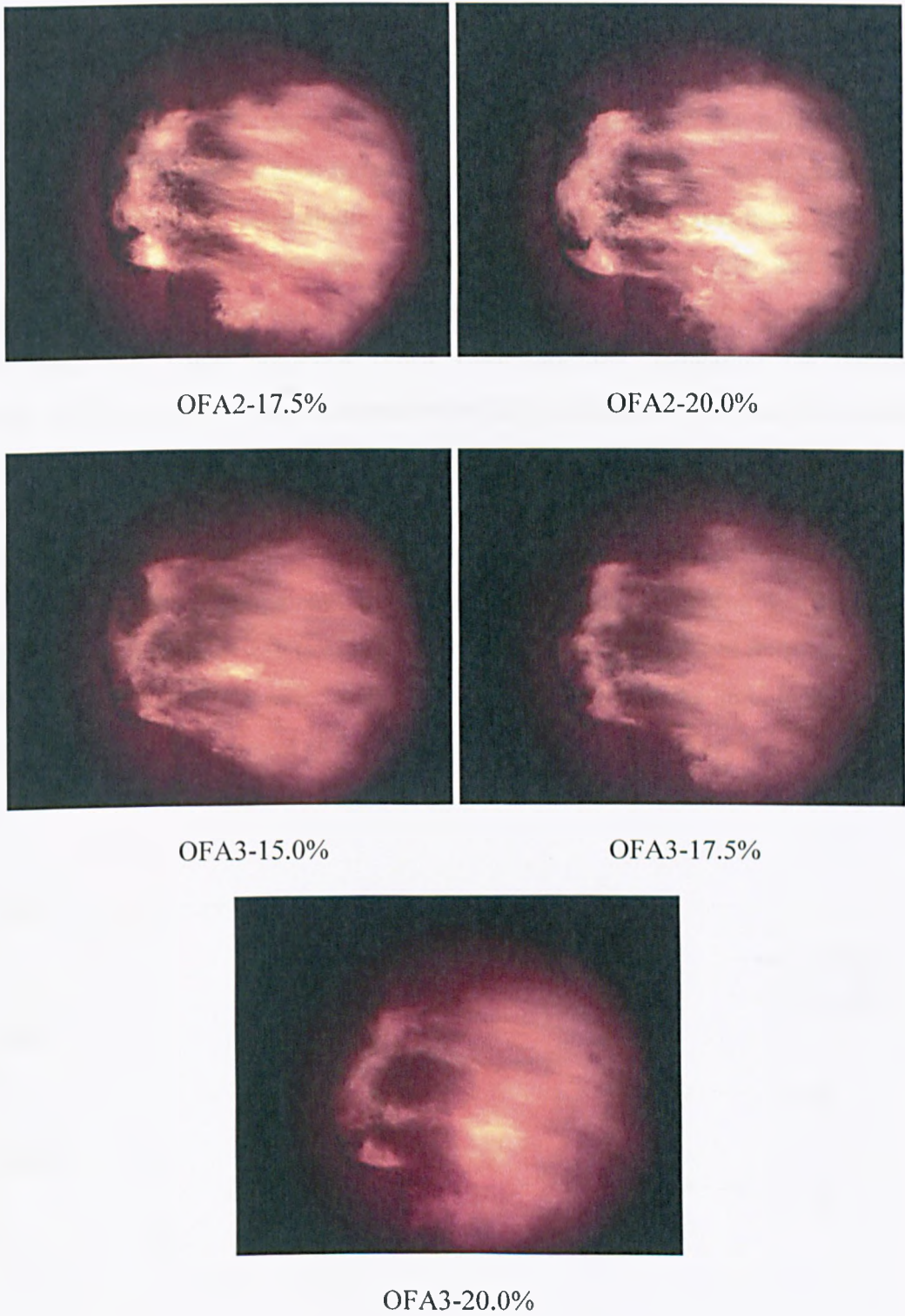


Figure 5.24 Flame images taken for different ratios of overfire air for different nozzle positions

### 5.3.4.1 Flame Stability

Figure 5.25 illustrates the variations of the stability index with the ratio and nozzle position of the OFA. It has been found that the flame stability does not deteriorate with the OFA used in all the cases studied, provided that the OFA is less than 20%. On the contrary, as shown in power spectral density results (Figure 5.26 and 5.27), the amplitude of the low-frequency components ( $<10\text{Hz}$ ) under the OFA condition is much lower than that under non-OFA (OFA 0%) condition, indicating the decreased geometric fluctuations of the flame under the OFA conditions. This may be explained by the fact that, within a certain range, less oxygen in the primary combustion zone would decrease the combustion intensity and hence improved flame stability. The result of the oscillation frequency also shows a very similar trend as that of the stability index. The lowest oscillation frequency is observed at OFA 0%, indicating decreased flame stability. In addition, the results of both stability index and oscillation frequency suggest that under the same OFA ratio, nozzle OFA3 gives better flame stability than nozzle OFA2, which may be relevant to the nozzle position of OFA3, which is further from the burner than that of OFA2.

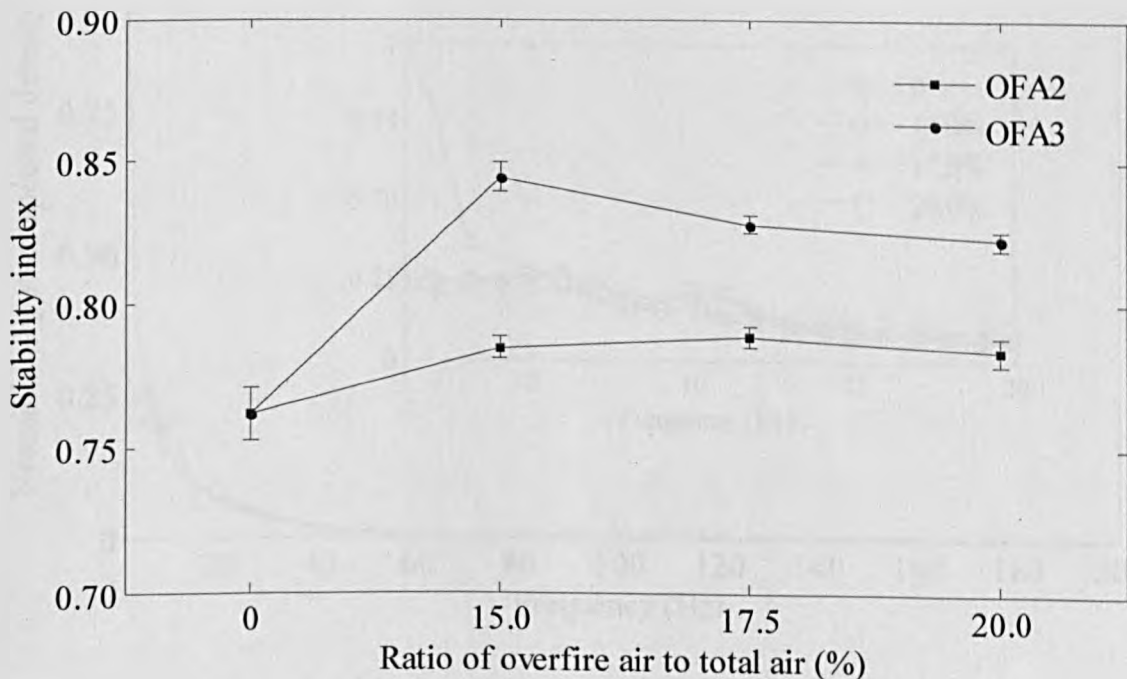


Figure 5.25 Variations of stability index with ratio and position of overfire air

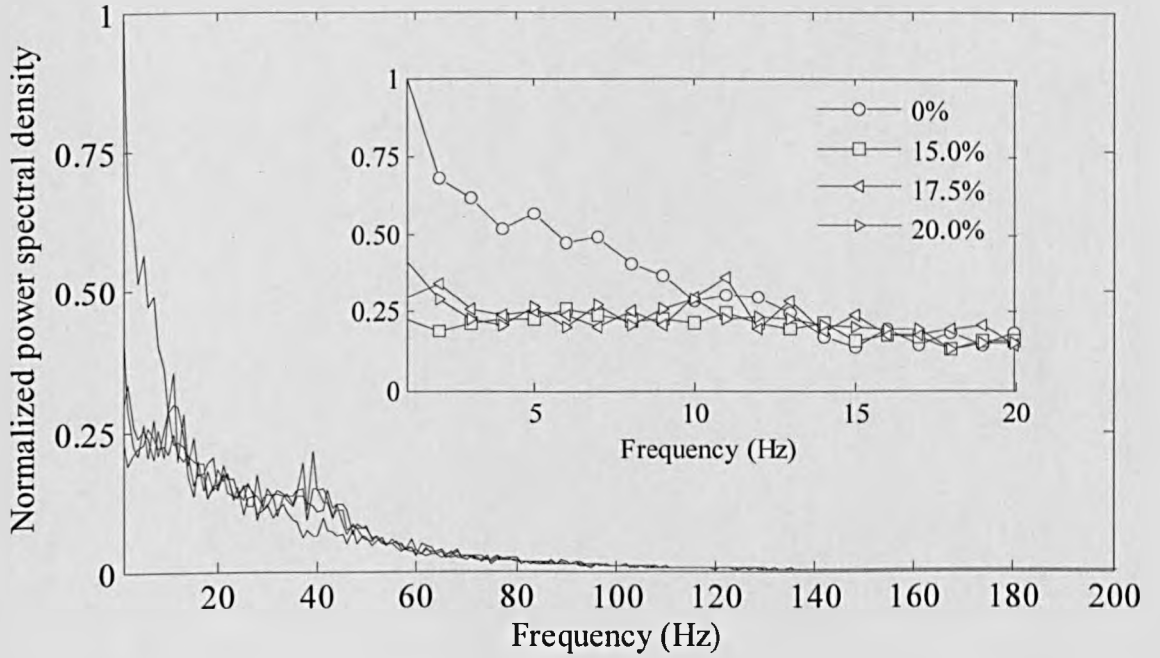


Figure 5.26 Variations of power spectral density estimates of flame radiation signal in visible band with the ratio of overfire air (OFA2)

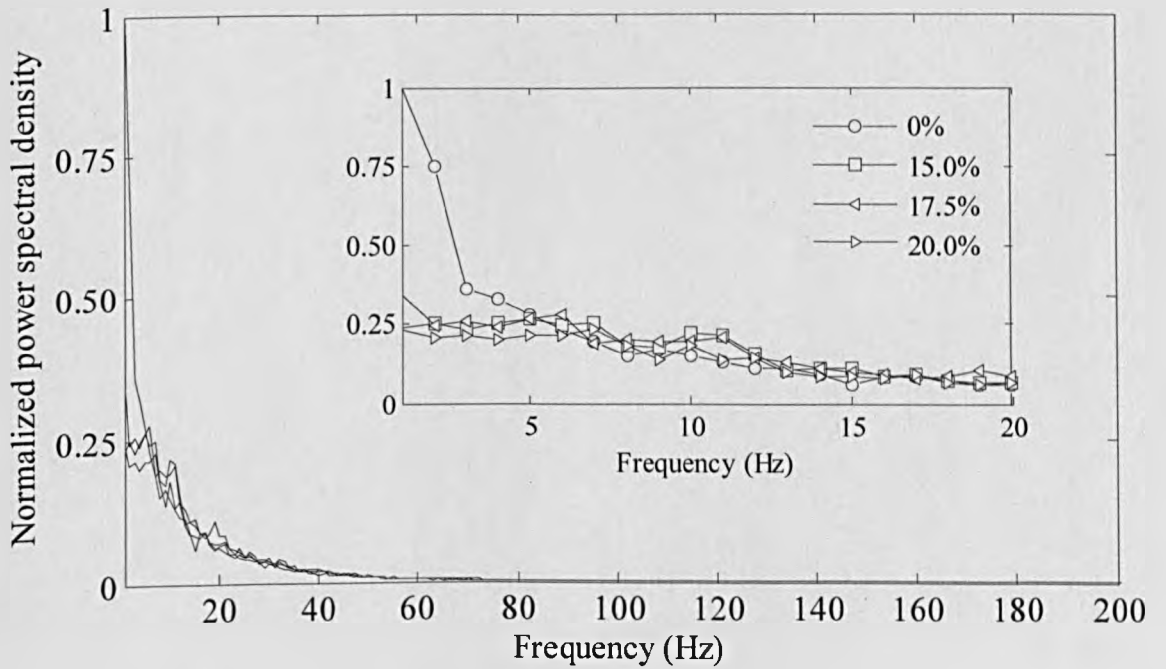


Figure 5.27 Variations of power spectral density estimates of flame radiation signal in infrared band with the ratio of overfire air (OFA2)



Figure 5.28 Variations of oscillation frequency with ratio and position of overfire air

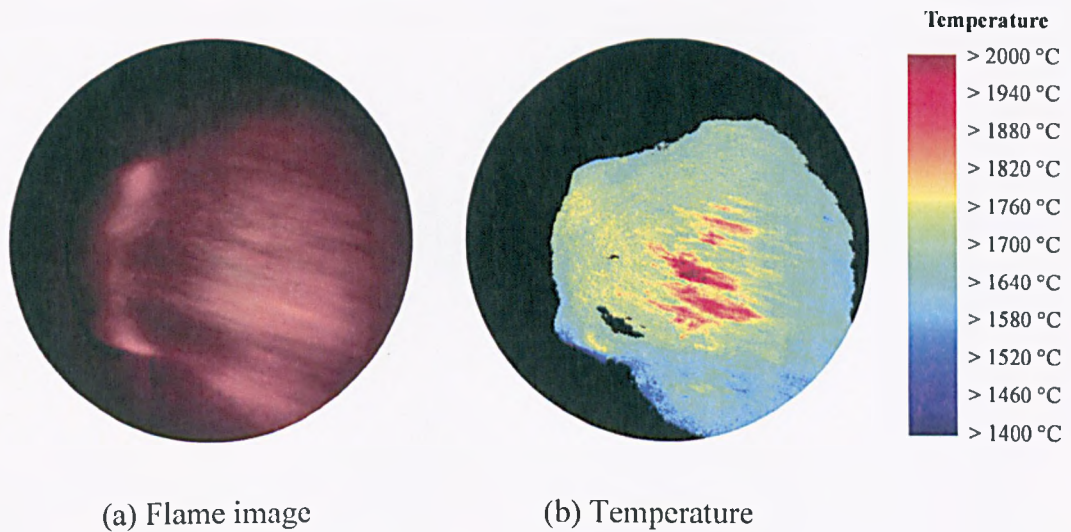
#### 5.3.4.2 Soot Temperature, Emissivity and Concentration

Figure 5.29 (a) illustrates a typical averaged image of the heavy oil flame, which is derived from 20 instantaneous images taken at the non-OFA condition (OFA 0%). The corresponding distributions of temperature, emissivity and KL factor are shown in pseudo-colour in Figure 5.29 (b), (c) and (d), respectively.

Figure 5.30 shows the variation of the measured average temperature of the flame with the ratio of the OFA to total air and its nozzle position. The decreased temperature can be explained by the fact that the higher the OFA, the less the air (PA, SA and TA) in the primary combustion zone, resulting in a reduced combustion intensity and hence the temperature. The decline in the temperature suppresses the thermal- $\text{NO}_x$  formation. On the other hand, the reduction of the oxygen concentration in the primary zone of the flame leads to less fuel-N conversion to  $\text{NO}_x$  [105]. This is evidenced by the emission analysis data where  $\text{NO}_x$  in flue gas has shown an almost linearly decreasing trend with the flame temperature, as shown in Figure 5.31. Furthermore, under the same OFA ratio,

the OFA3 results in a lower flame temperature and  $\text{NO}_x$  emission than the OFA2. This is due to a longer delay, associated to the location of the OFA3 port, in the mixing between the combustion gases from the primary zone and the OFA. The longer delay increases the residence time of the combustion gases in the zones with low oxygen concentrations, resulting in the reduced concentration of nitrogen radicals reaching the secondary zone (OFA zone) and, thus, the reduced conversion of these radicals to  $\text{NO}_x$  [105].

Figure 5.32 and 5.33 depict the average emissivity and concentration of soot particles within the flame, respectively, under the test conditions. Increased soot emissivity and concentration ( $KL$  factor) are observed for an increased OFA. This may be due to the fact that the reduction of oxygen concentration in the primary combustion zone could promote the formation process of soot [106]. It is also noted that the bottom part of the flame exhibits a higher emissivity and soot concentration, as shown in Figure 5.29 (c) and (d). This phenomenon may be caused by a non-even distribution of fuel.



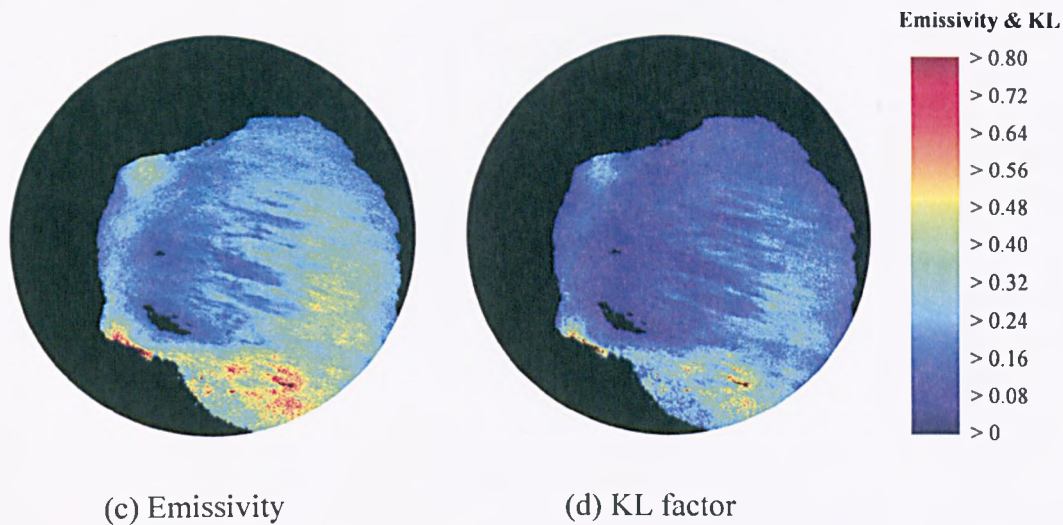


Figure 5.29 Averaged image of the heavy oil flame and the corresponding distributions of soot temperature, emissivity and concentration

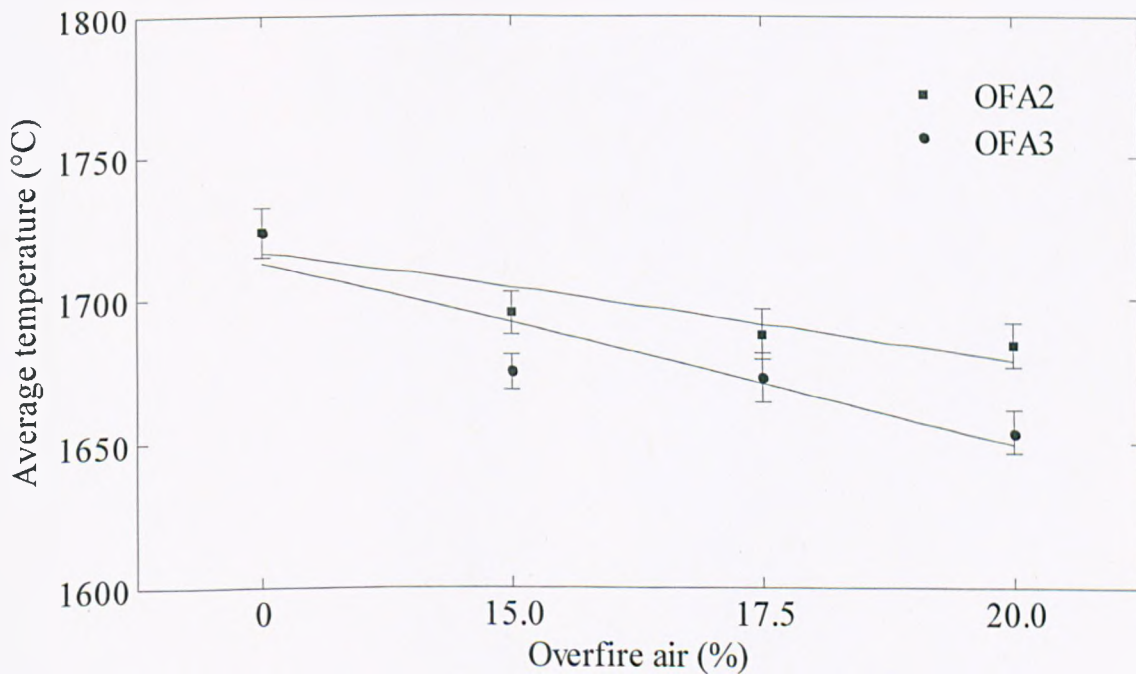


Figure 5.30 Variations of average temperature with the ratios and nozzle positions of overfire air

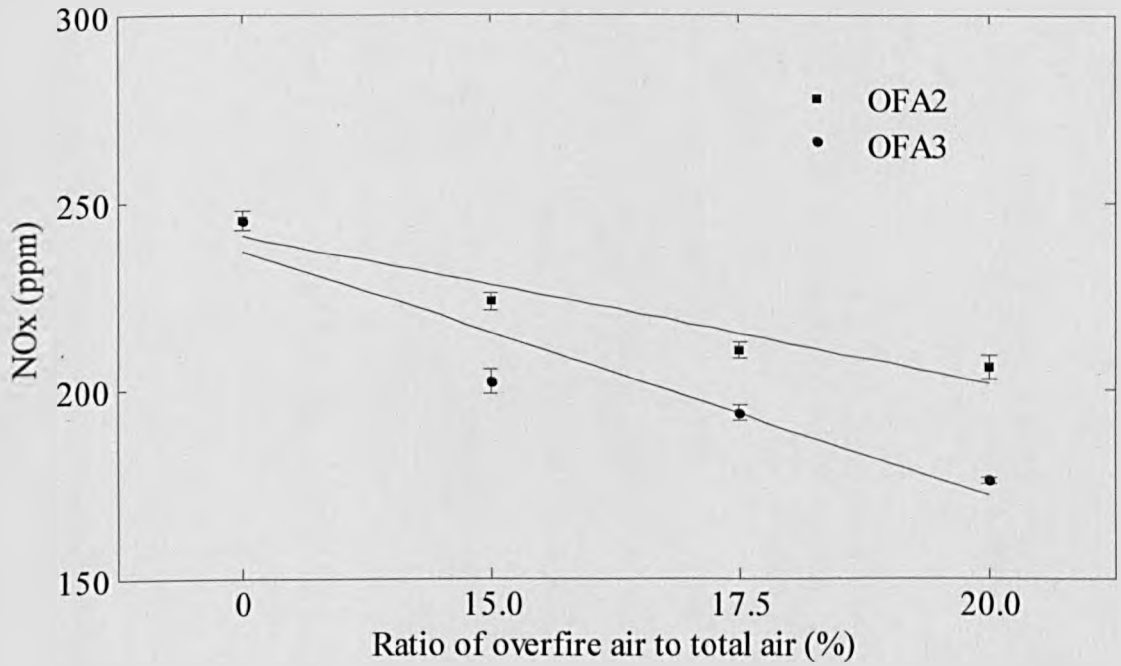


Figure 5.31 Variations of NO<sub>x</sub> emission with the ratios and nozzle positions of overfire air

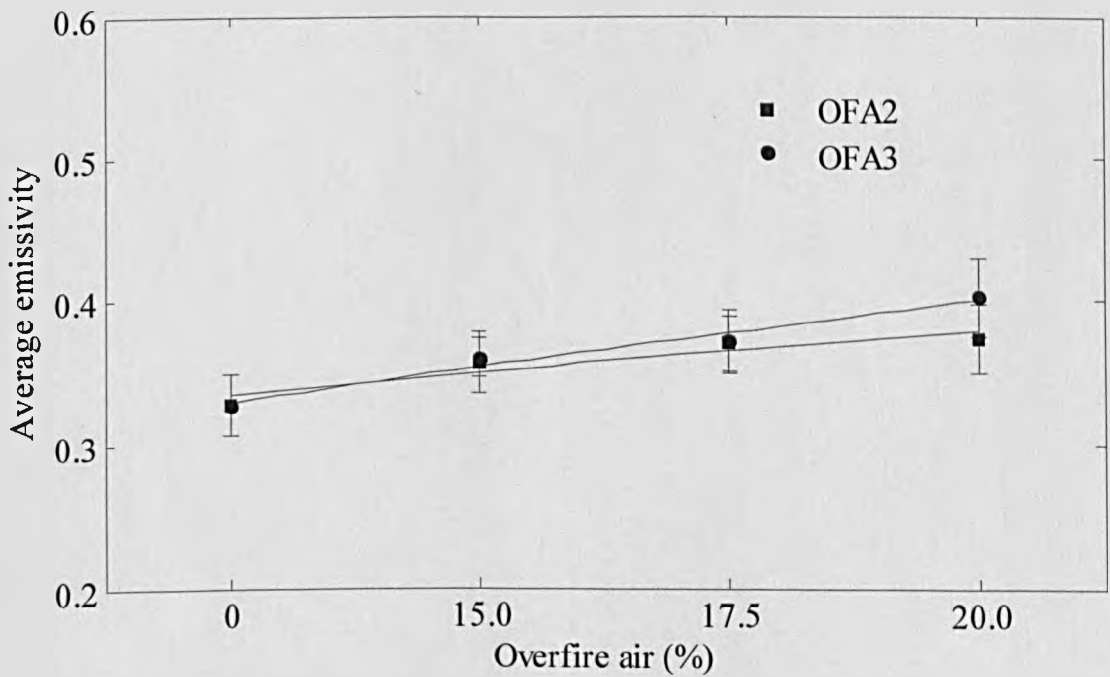


Figure 5.32 Variations of average emissivity with the ratios and nozzle positions of overfire air

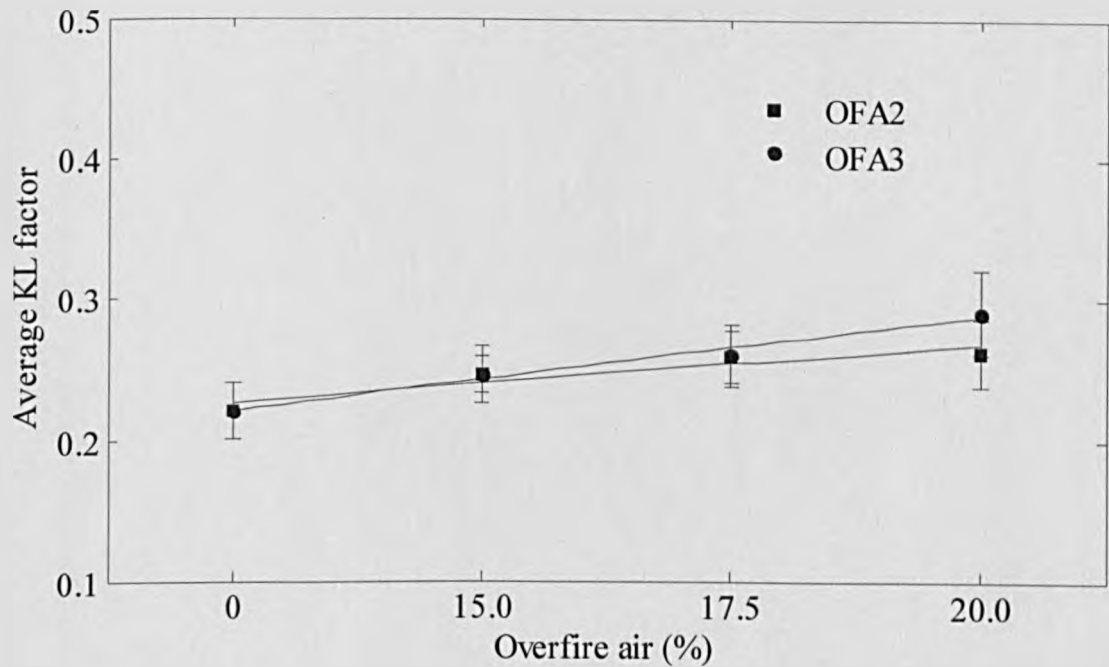


Figure 5.33 Variations of  $KL$  factor with the ratios and nozzle positions of overfire air

### 5.3.5 Correlation between Flame Stability and $NO_x$ Emission

From the above presented experimental results obtained under a wide range of combustion conditions, it can be seen that for a specific test, low  $NO_x$  emissions is generally obtained under the stable condition. In order to illustrate more clearly the correlations between the flame stability and  $NO_x$  emission, the measured flame stability index and corresponding  $NO_x$  emission during all tests are shown in Figure 5.34. It is evident that the volume of  $NO_x$  emission in the flue gas decreases with improved flame stability, suggesting that it is crucial to maintain a stable flame for reduced  $NO_x$  emissions. This finding is supported by the analysis of correlations between the oscillation frequency, especially visible band, and the  $NO_x$  emission (as show in Figure 5.35 and 5.36), which shows low  $NO_x$  emission were achieved generally with a high oscillation frequency (indicating better flame stability).

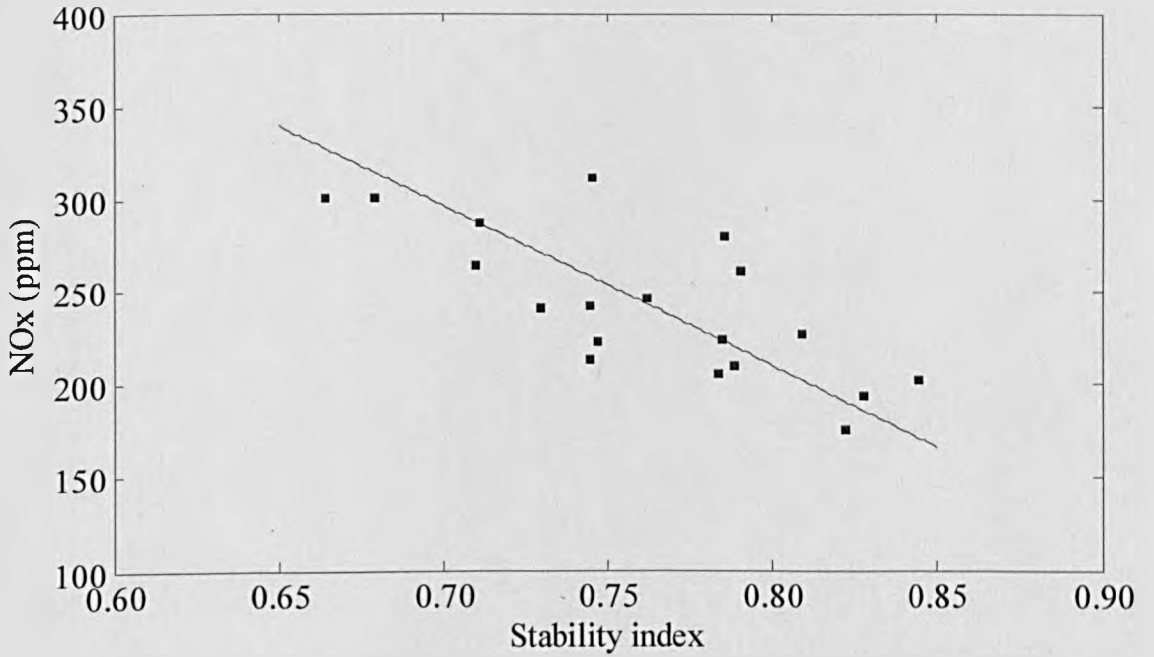


Figure 5.34 Variations of NO<sub>x</sub> emission with measured flame stability index

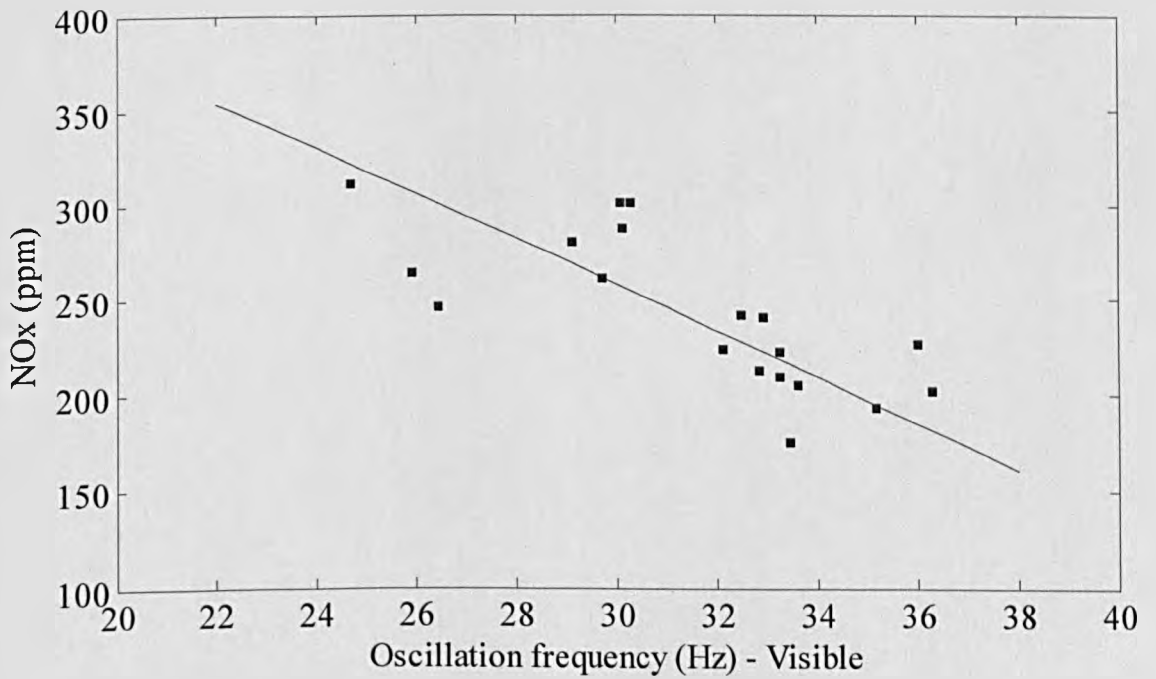


Figure 5.35 Variations of NO<sub>x</sub> emission with the measured oscillation frequency in visible band

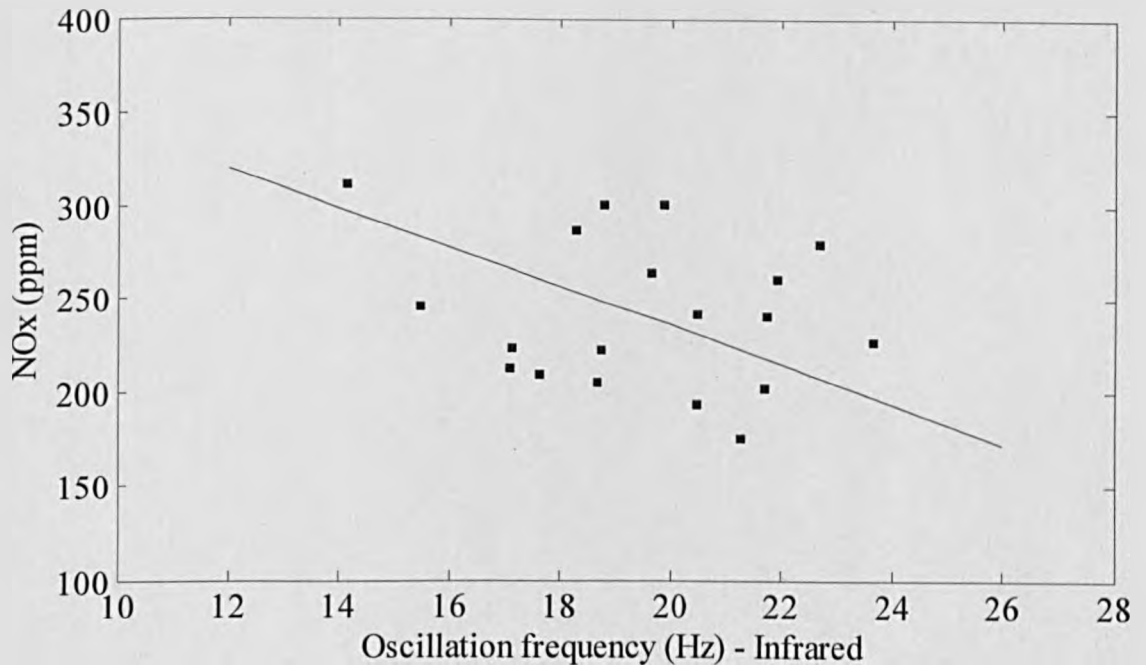


Figure 5.36 Variations of  $\text{NO}_x$  emission with the measured oscillation frequency in infrared band

## 5.4 Results of Burner Condition Monitoring

### 5.4.1 Detection of Abnormal Conditions in a Combustion Process Using KPCA

To evaluate the effectiveness of the KPCA based method for detecting abnormal conditions in a combustion process (Section 3.3.2), two different normal conditions were considered, i.e., one without overfire air (non-OFA) and one with overfire air (OFA).

For the non-OFA normal condition, the total air flow rate was set for  $9100\text{Nm}^3\text{h}^{-1}$  (PA: 17%, SA: 43%, and TA: 40%). An abnormal condition was deliberately created by setting the swirl vane position of the SA deviated from its baseline configuration of 65mm.

For the OFA normal condition, the total air flow rate was kept the same as that of the non-OFA normal condition ( $9100\text{Nm}^3\text{h}^{-1}$ ), but with a different air distribution (PA: 14.5%, SA: 36.5%, TA: 34%, and OFA: 15%). An abnormal condition was also deliberately created by setting the OFA deviated from its baseline configuration of 15%.

It should be noted that it is not possible to make a real combustion fault because of the safety and cost considerations, and therefore the above-mentioned artificial abnormal conditions were created. However, it does not necessarily mean that these artificial abnormal conditions might happen in combustion systems. The key point of the experiments here is to test the performance of the KPCA based method for detecting the changes in flame pattern caused by unanticipated changes in burner conditions.

For a comparison purpose, both the KPCA and the PCA models were built based on the same set of training data under each normal condition. Each sample, also known as an observation, contains 27 variables as listed in Section 3.3.1. Both visible and infrared signals were considered (the ultraviolet signal was too weak to be detected in the case studied). The KPCA was carried out based on the approach as described in Section 3.3.2. The PCA was performed through the single value decomposition of input matrix  $X$  as follows:

$$X = USV^T, \quad (5-1)$$

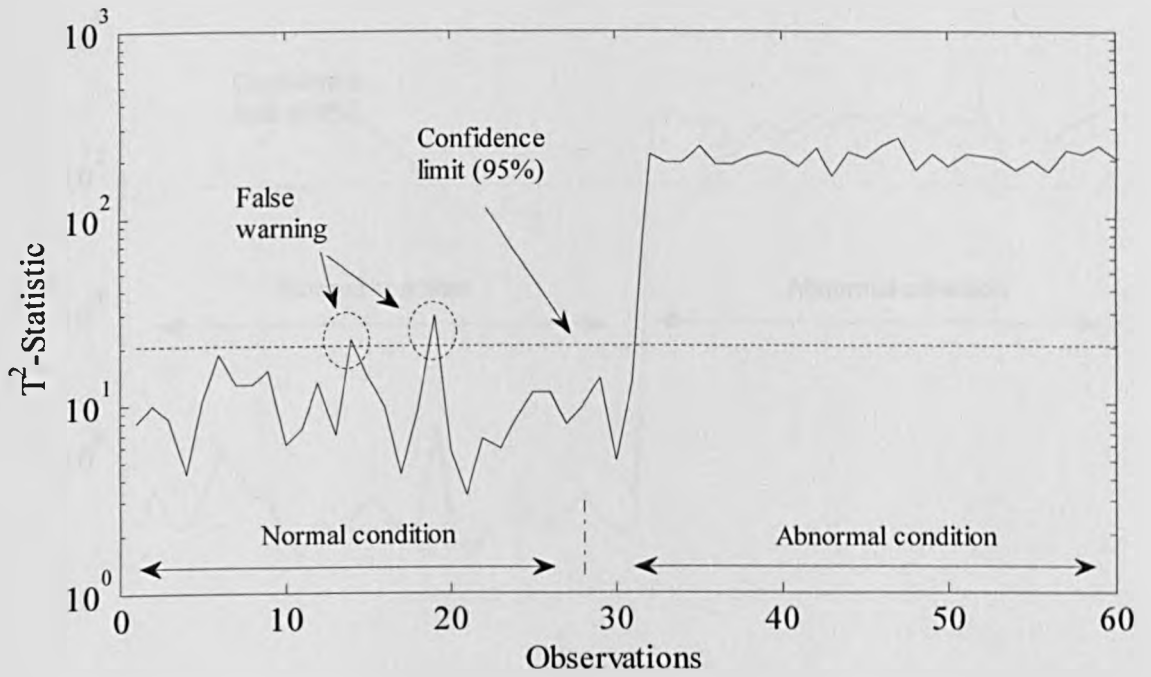
where  $S$  is a diagonal matrix containing the square roots of the variances of columns of  $X$  in descending order, and  $U$  and  $V$  are orthonormal matrices [107]. Small values of variance in  $S$  are regarded as noises and neglected in the PCA in order to reduce the number of variables in  $X$ . In the present case, the first 10 principal components, which represent more than 85% of the variation in the original 27 variables, were used to derive the  $T^2$  and  $Q$  statistics.

Figure 5.37 and 5.38 show the results of the  $T^2$  and  $Q$  statistics of both models when they were applied to monitor the non-OFA and OFA combustion processes. The corresponding 95% confidence limit is plotted as the dash line in each figure. For both conditions, the first 30 test samples were obtained from normal conditions, while the remainder from corresponding abnormal conditions. It can be seen that both the KPCA

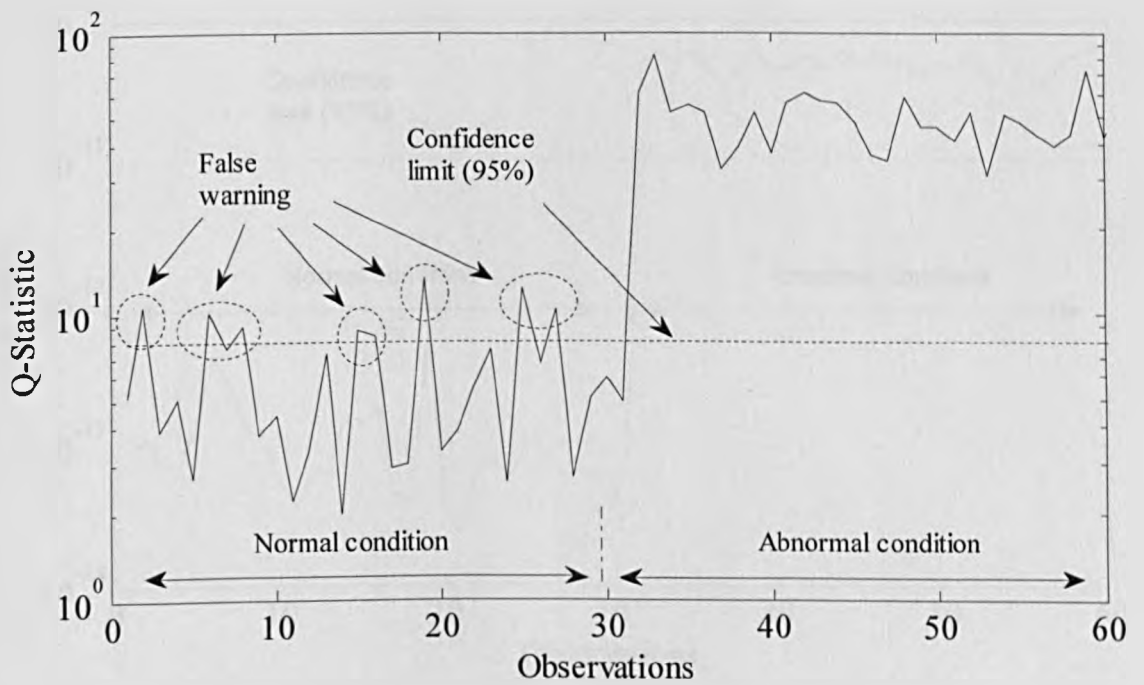
and the PCA can correctly detect the artificial faults. However, compared with the PCA, the KPCA exhibits clearly a better performance in several aspects. The relative difference of the statistics of the KPCA between the normal and abnormal conditions is much higher than that of the PCA in both  $T^2$  and Q statistics, which may imply that the nonlinear KPCA model is more capable of illustrating the discrepancy between the normal and abnormal conditions. Furthermore, the PCA produced noticeable false warnings, especially the Q statistic, whilst the KPCA shows no false warning at all. This problem may be also caused by the assumption of the PCA that the data in the input space are linear which may not reflect the truth. Another important factor which may be relevant to this problem is the size of the training samples. The number of samples used to establish the PCA model may not be sufficient to represent the characteristics of the normal condition.

In order to investigate the impact of the size of the training samples on the accuracy of the fault detection of both models, the data set of the non-OFA normal condition (a total of 150 samples) was divided randomly into two parts, i.e., one training set  $t\%$ , one test set  $1-t\%$ . Different percentages of the training set were created, varying from 30% to 90%. For each percentage, the same procedure was repeated 100 times in order to eliminate the possible error caused by individual samples.

Figure 5.39 shows the variation of the average false warning rate with the size of training data. The false warning rate is defined as the ratio of the number of false warnings to the number of test samples. It can be seen that the false warning rates of the  $T^2$  statistic for both models are less affected by the training data size, about 4% in the PCA model and 0% in the KPCA model. The false warning rate of the Q statistic of the PCA model decreases gradually with the percentage of the training data, from maximum of 38% at the training data of 30% to the minimum of 15% at the training data of 90%, while the KPCA model gives a very consistent performance, 0% false warning, irrespective of the data set size. The results suggest that the KPCA model can provide not only a better representation of data in the normal condition but also a good performance even when the number of the training samples is limited.

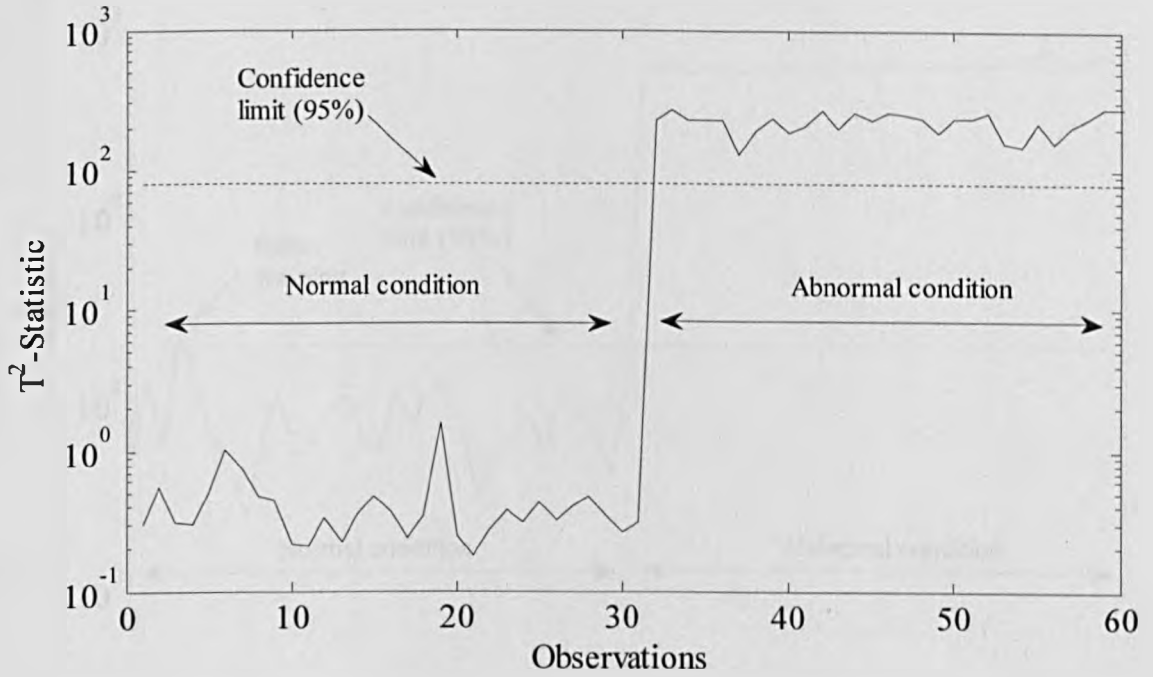


(a) PCA –  $T^2$  statistic

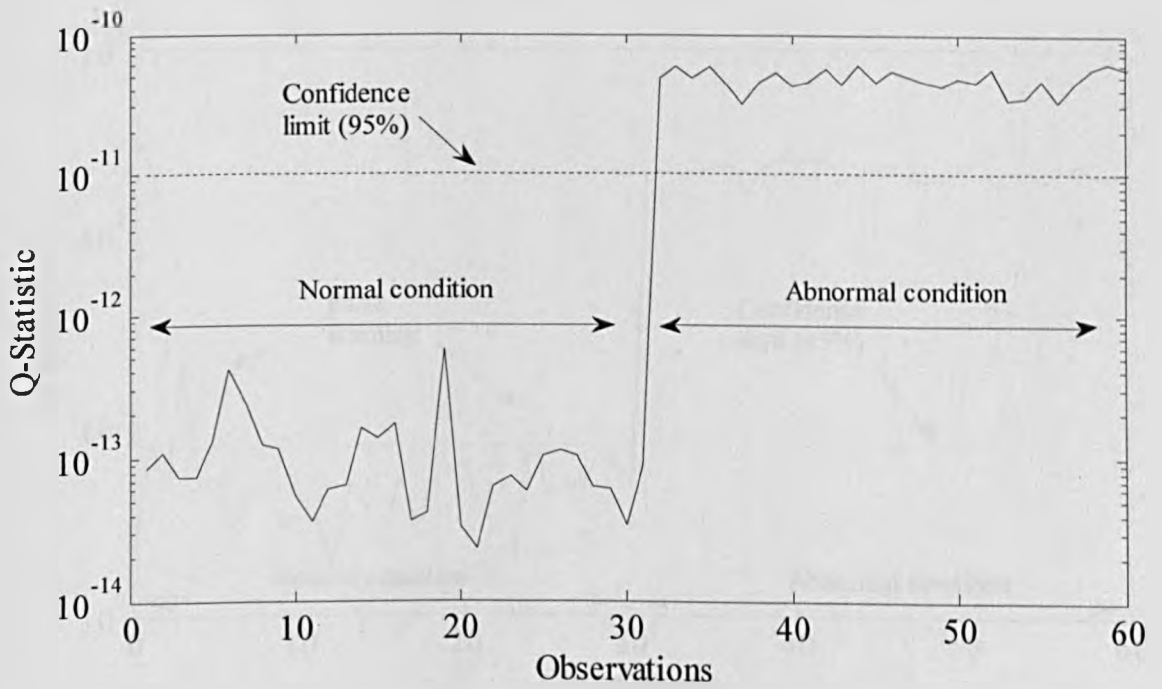


(b) PCA – Q statistic

Figure 5.37 Monitoring charts of non-OFA combustion process ((a)~(b))

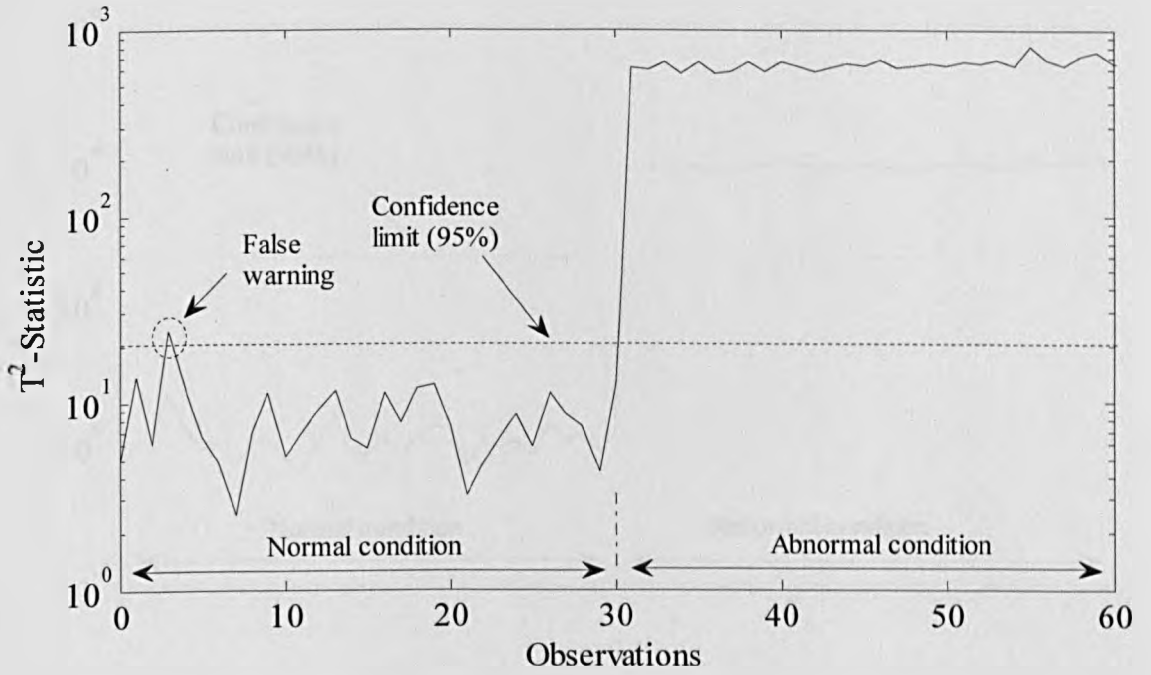


(c) KPCA –  $T^2$  statistic

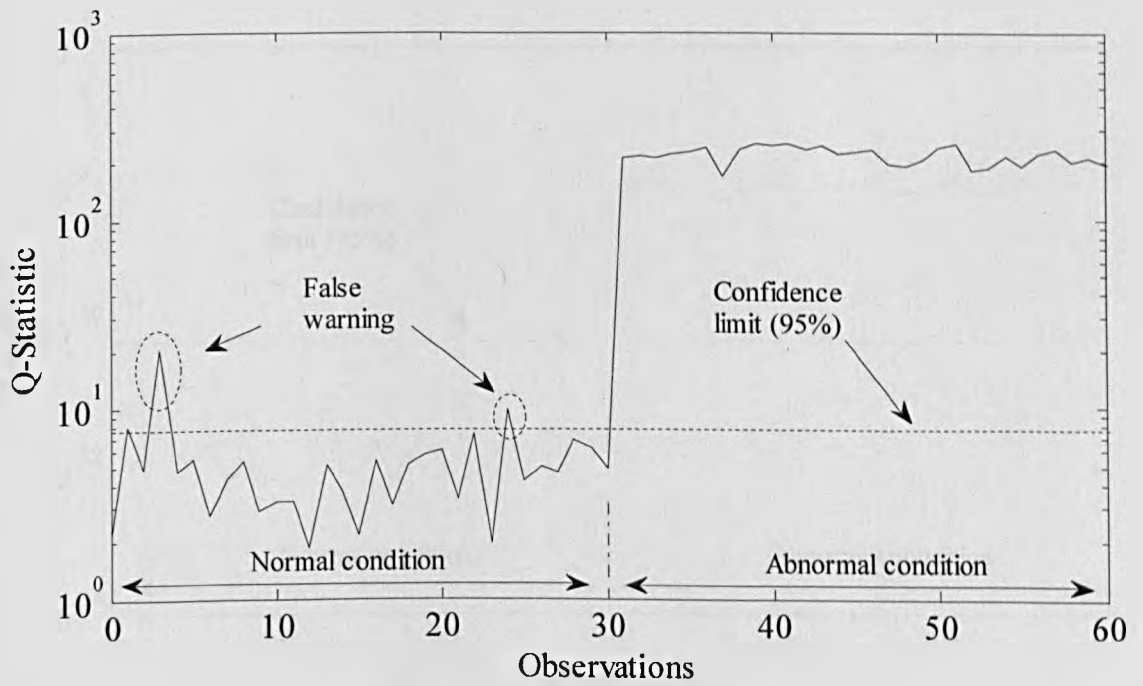


(d) KPCA – Q statistic

Figure 5.37 Monitoring charts of non-OFA combustion process ((c)~(d))

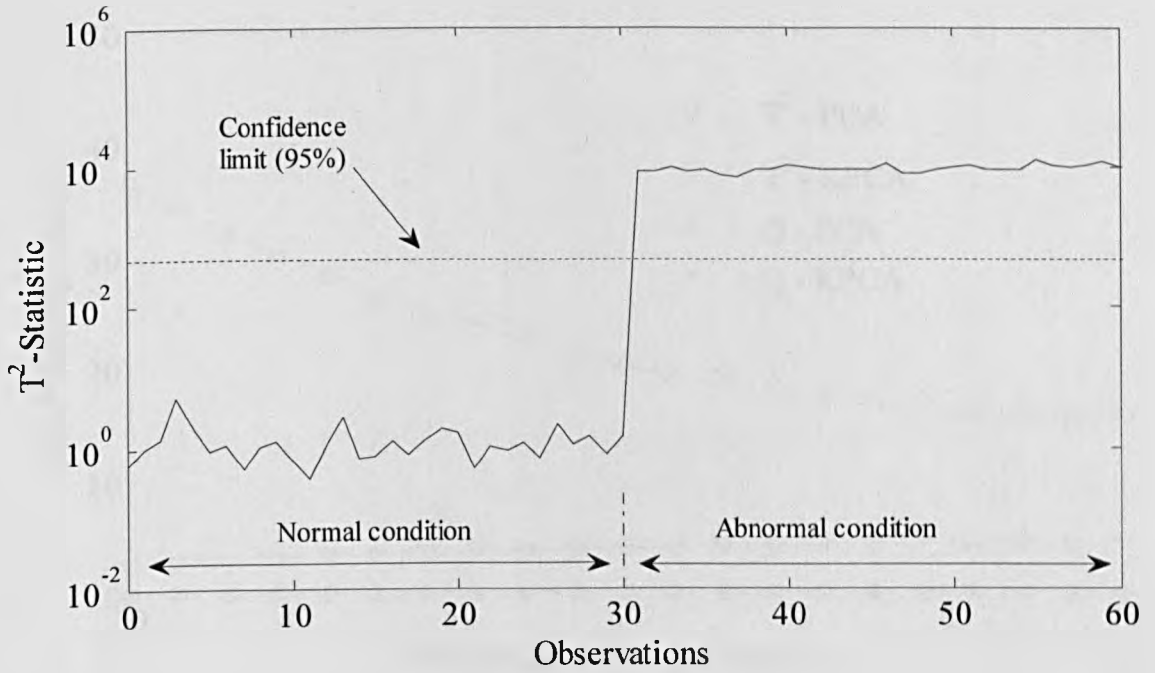


(a) PCA –  $T^2$  statistic

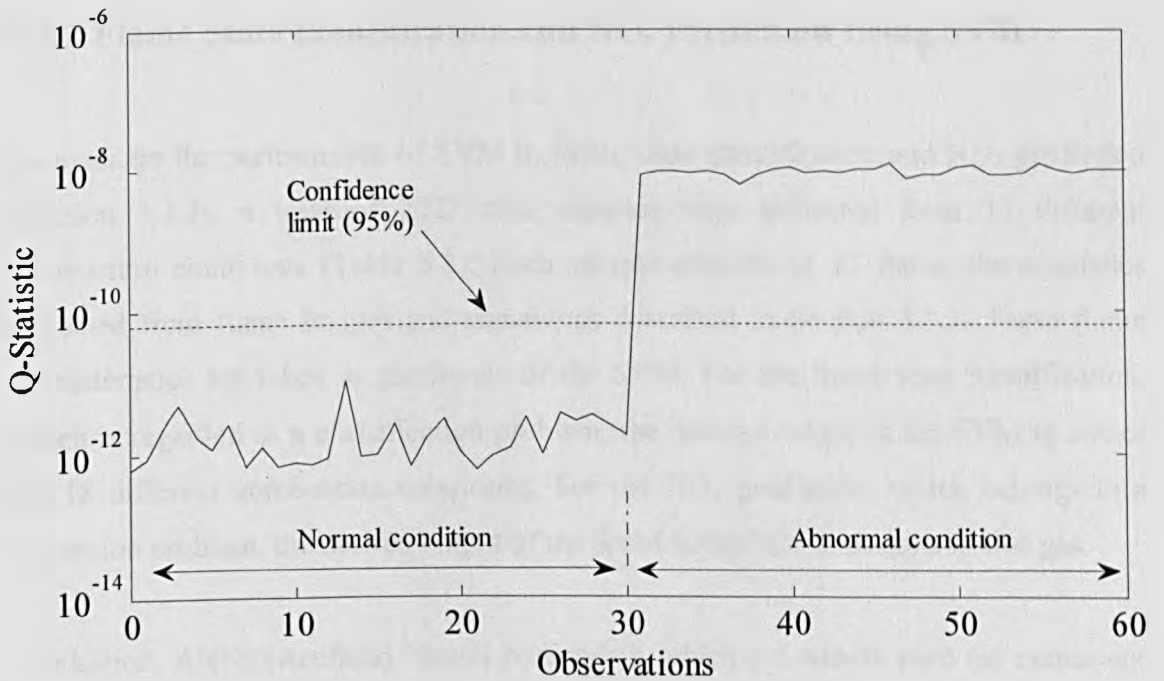


(b) PCA – Q statistic

Figure 5.38 Monitoring charts of OFA combustion process ((a)~(b))



(c) KPCA –  $T^2$  statistic



(d) KPCA – Q statistic

Figure 5.38 Monitoring charts of OFA combustion process ((c)~(d))

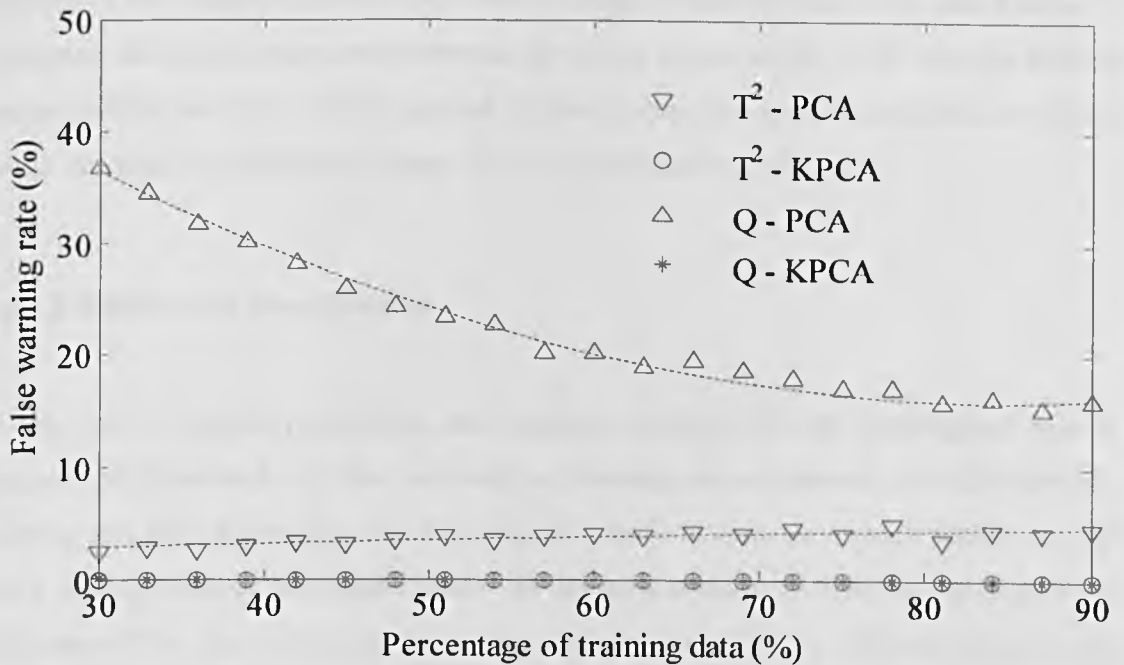


Figure 5.39 Variation of false warning rate with training data size

#### 5.4.2 Flame State Identification and NO<sub>x</sub> Prediction Using SVM

To evaluate the performance of SVM in flame state identification and NO<sub>x</sub> prediction (Section 3.3.3), a total of 2223 data samples were collected from 18 different combustion conditions (Table 5.2). Each sample consists of 27 flame characteristics extracted from flame images and signals, as described in Section 3.3.1. These flame characteristics are taken as the inputs of the SVM. For the flame state identification, which is regarded as a classification problem, the desired output of the SVM is one of the 18 different combustion conditions. For the NO<sub>x</sub> prediction, which belongs to a regression problem, the desired output of the SVM is the NO<sub>x</sub> emissions in flue gas.

In addition, ANNs (Artificial Neural Networks), which are widely used (as mentioned in Chapter 2) in flame state identification and NO<sub>x</sub> prediction, are also built to compare with SVM. ANNs are inspired by the way biological nervous systems process information. A neural network is comprised of a large number of non-linear processing elements (neurones), which are highly interconnected via weighted connections. The

weights of the connections are determined through a learning procedure, which aims to minimize the mean square error between the actual output of the ANN and the desired output. ANNs have been widely applied for both pattern recognition and function fitting problems. Detailed description about ANN can be found in [108, 109].

#### 5.4.2.1 Flame State Identification

In the field of pattern recognition, the database collected for the investigated case is generally divided randomly into two sets, i.e., training set and test set, typically 80% for training and 20% for testing. The training set is used to train the model, whilst the test set is used to evaluate the trained model. In the present study, in order to investigate the influence of the size of training set on the performance of SVM, different training sets were created. The size of training sets with respect to the database varied from 10% to 90% with an interval 5% and the corresponding test sets varied from 90% to 10%.

For each training set size, the same training set was used to train both of the SVM and ANN models. The SVM model was trained based on the procedure described in Section 3.3.3.3 with the parameters of  $C$  32 and  $\gamma$  0.3. The ANN adopted a three-layer neural network, which has 27, 30 and 18 neurons in the input, hidden and output layers, respectively. The architecture of the neural network is shown in Figure 5.40. Tangent sigmoid transfer function was used for both the hidden and output layers. Resilient Backpropagation learning algorithm was used to train the network. It should be noted that other ANN Backpropagation learning algorithms [110] were also tested such as Levenberg-Marquardt, Bayesian Regularization, Conjugate Gradient, One Step Secant, and BFGS Quasi-Newton. In the present case (flame state identification), Resilient Backpropagation obtained the best performance among these learning algorithms.

After the training procedure, the trained SVM and NN models were tested by using the training and test sets. The performance is expressed by the percentage of data which are correctly classified, namely the success rate. To eliminate the possible error caused by individual instances, the procedure of database division, model training and testing was repeated for 20 times.

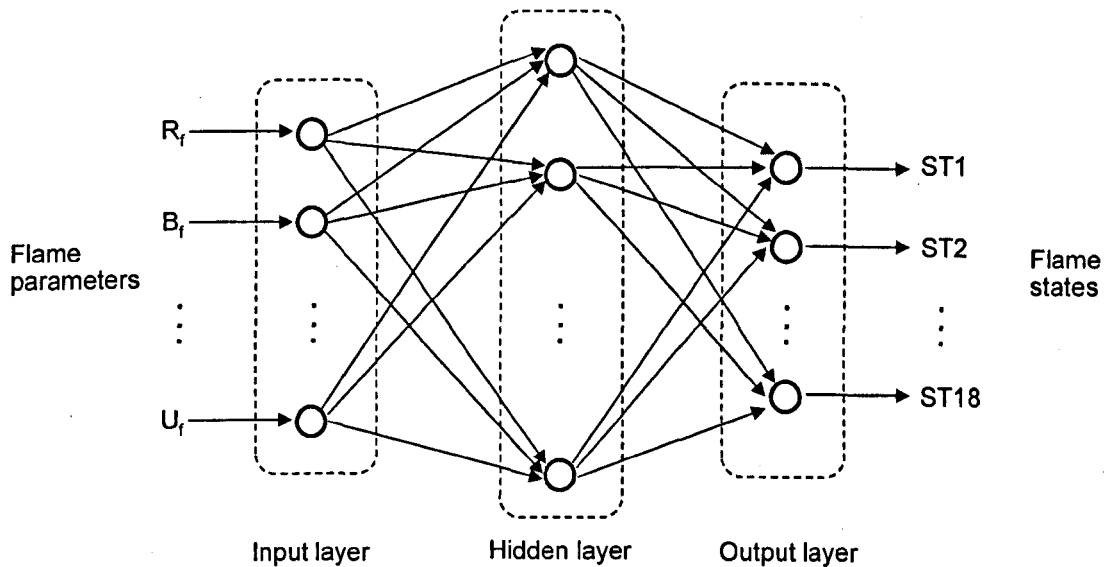


Figure 5.40 Architecture of the neural network for flame state identification

Figure 5.41 shows the success rates of the trained SVM and ANN models when they are applied to classify the training data. It has been found that the ANN gives a higher success rate (98.2%~99.4%) than the SVM (96.2%~96.9%) in classifying training data over the whole tested conditions.

However, when applied to the test data, as show in Figure 5.42, the SVM achieved a better performance than the ANN, especially when the training data size is small. Figure 5.43 and 5.44 show the detailed success rates of both models for classifying test data in twenty trials under the training set size 80% and 15%, respectively. As can be seen, when 80% data were used for training, the performance of the SVM and the ANN are similar, 95.08% and 94.22%, respectively. However, when 10% data were used for training, the difference between the success rates of the SVM (85.2%) and the ANN (73.9%) increased to 11.3%. The better performance is ascribed to the good generalization ability of the SVM. On the other hand, the success rates of the SVM and the ANN increase gradually with the size of training set. This can be understood that more training data, more patterns the models can learn, resulting in a better performance, which also suggests that adequate data should be collected to represent all the possible patterns of a dynamic process so as to achieve a reliable flame state identification.

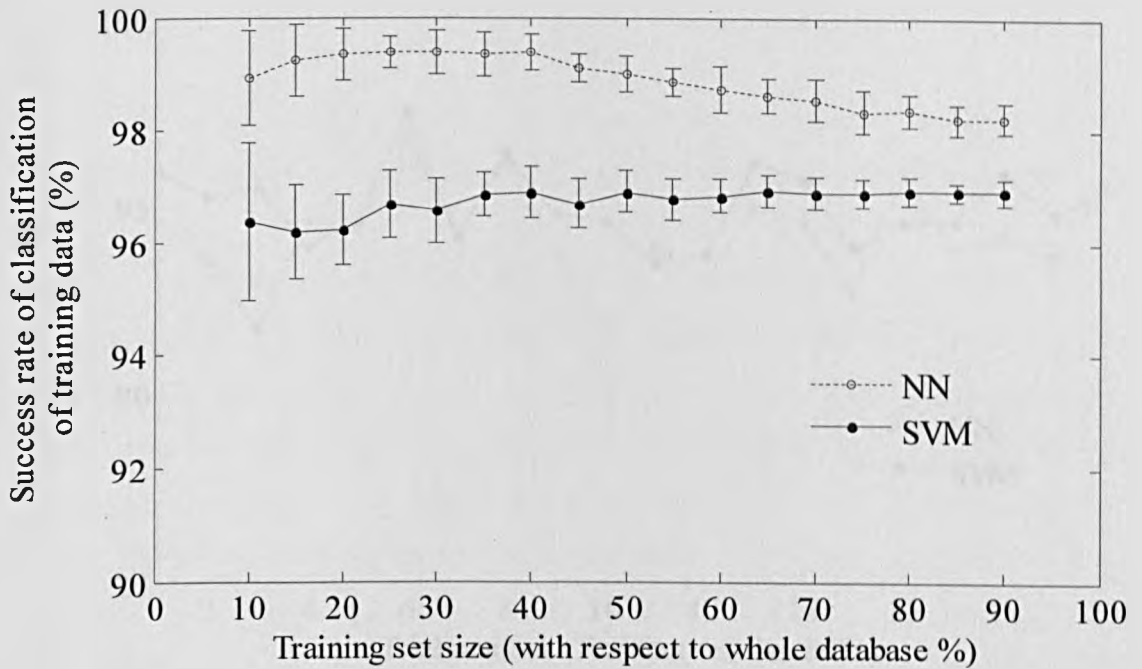


Figure 5.41 Variations of the success rate of classification of training data with training set size

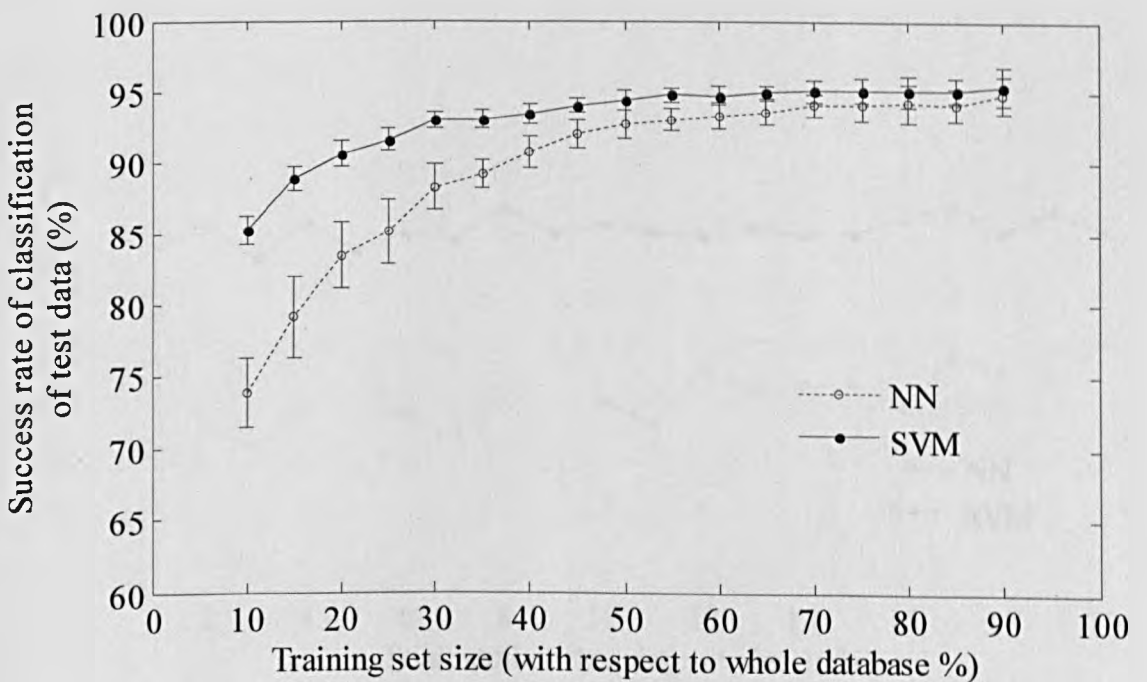


Figure 5.42 Variations of the success rate of classification of testing data with training set size

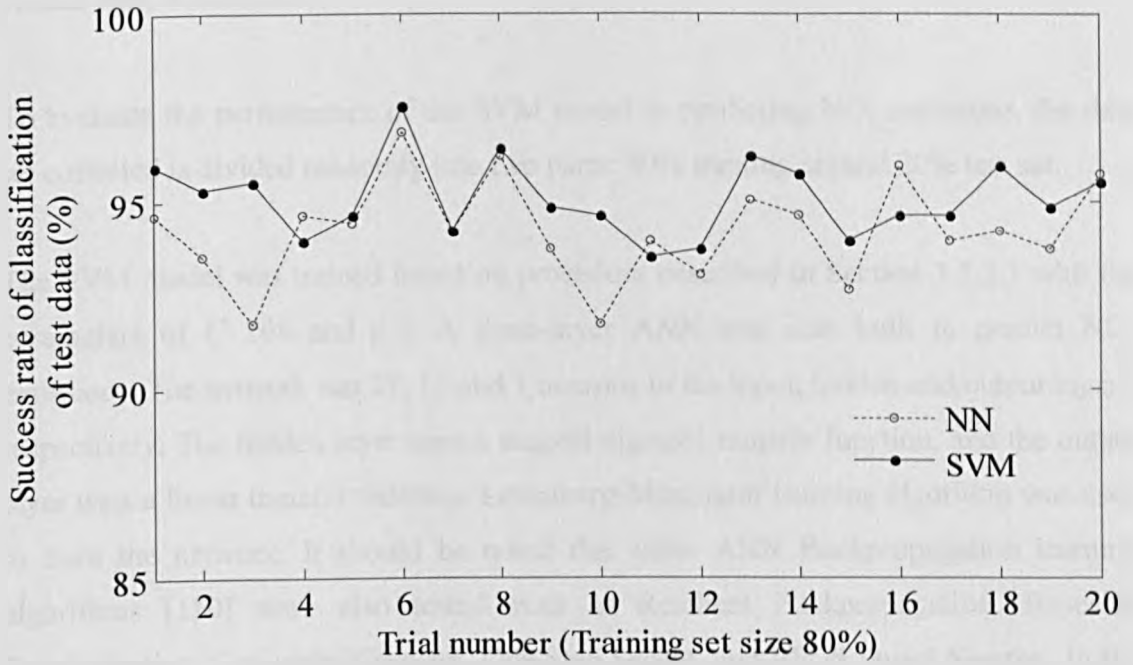


Figure 5.43 Success rate of classification of testing data in one hundred trials (training set size 80%)

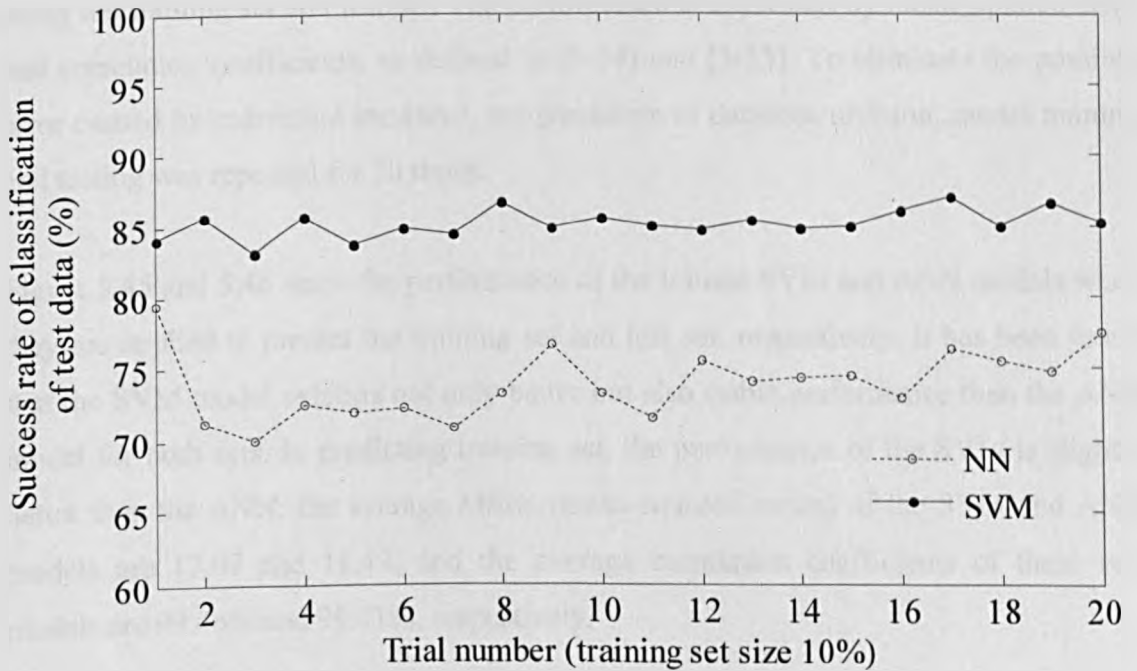


Figure 5.44 Success rate of classification of testing data in one hundred trials (training set size 10%)

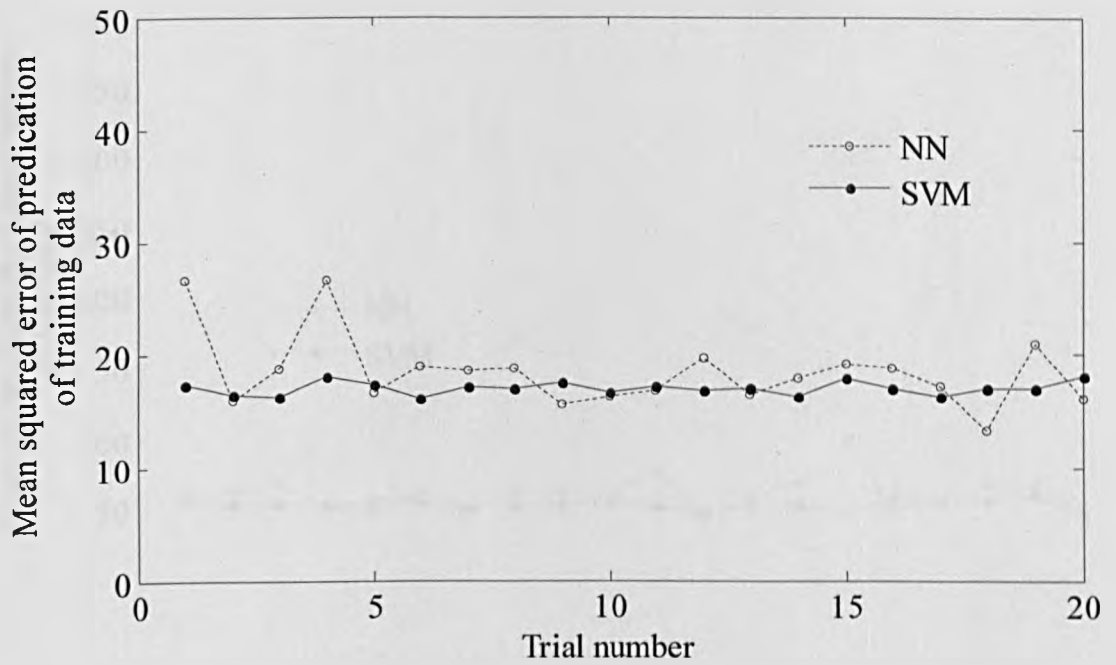
### 5.4.2.2 NO<sub>x</sub> Prediction

To evaluate the performance of the SVM model in predicting NO<sub>x</sub> emissions, the data set collected is divided randomly into two parts: 80% training set and 20% test set.

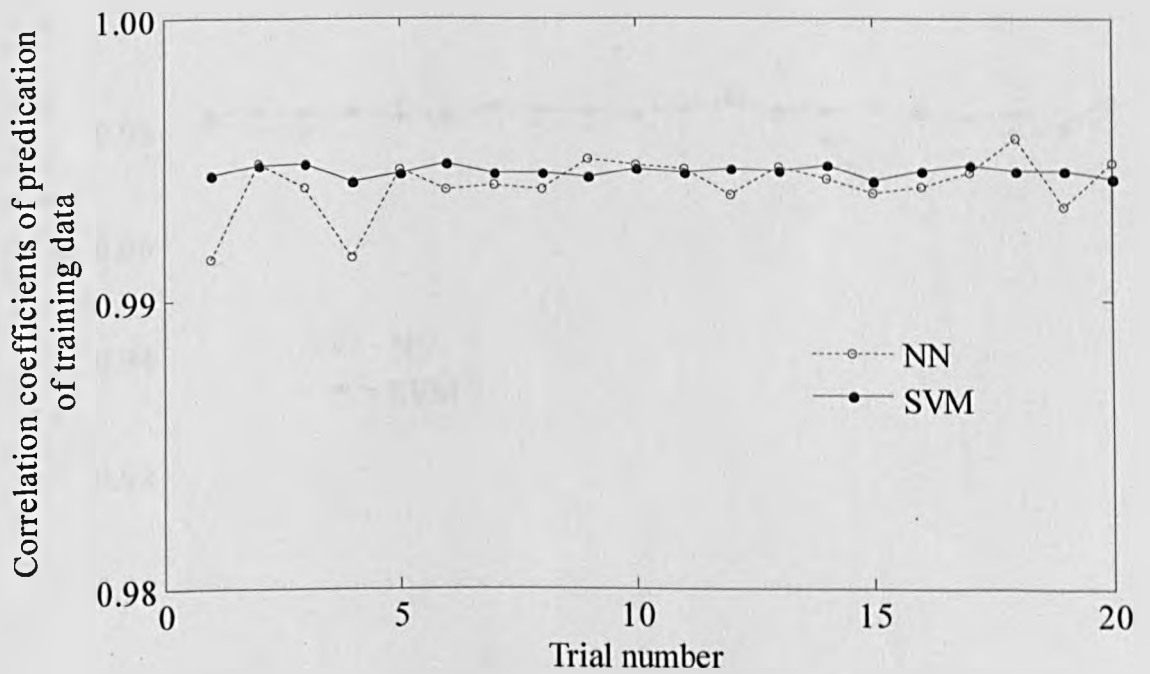
The SVM model was trained based on procedure described in Section 3.3.3.3 with the parameters of  $C$  108 and  $\gamma$  3. A three-layer ANN was also built to predict NO<sub>x</sub> emissions. The network has 27, 10 and 1 neurons in the input, hidden and output layers, respectively. The hidden layer uses a tangent sigmoid transfer function, and the output layer uses a linear transfer function. Levenberg-Marquardt learning algorithm was used to train the network. It should be noted that other ANN Backpropagation learning algorithms [110] were also tested such as Resilient Backpropagation, Bayesian Regularization, Conjugate Gradient, One Step Secant, and BFGS Quasi-Newton. In the present case (NO<sub>x</sub> prediction), Levenberg-Marquardt obtained the best performance among these learning algorithms and hence it is used for comparison with SVM.

After the training procedure, the trained SVM and the ANN models were tested by using the training set and test set. The performance is expressed by mean squared error and correlation coefficients, as defined in (3-54) and (3-55). To eliminate the possible error caused by individual instances, the procedure of database division, model training and testing was repeated for 20 times.

Figure 5.45 and 5.46 show the performance of the trained SVM and ANN models when they are applied to predict the training set and test set, respectively. It has been found that the SVM model exhibits not only better but also stable performance than the ANN model for both sets. In predicting training set, the performance of the SVM is slightly better than the ANN; the average MSEs (mean squared errors) of the SVM and ANN models are 17.07 and 18.49, and the average correlation coefficients of these two models are 99.46% and 99.41%, respectively.

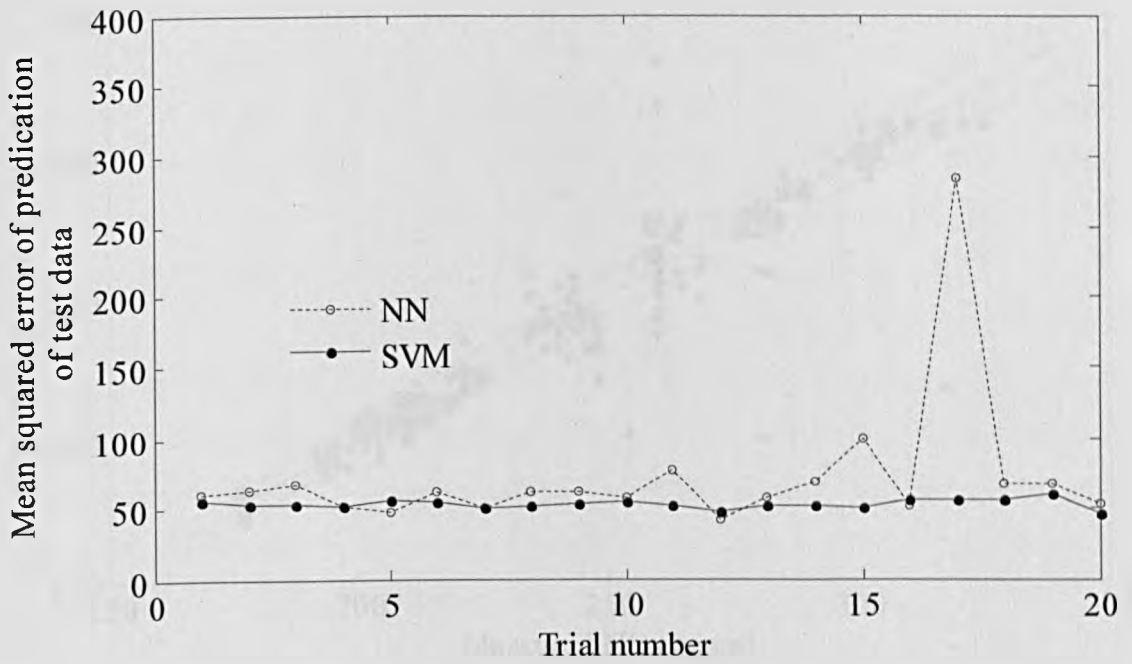


(a) Mean squared error

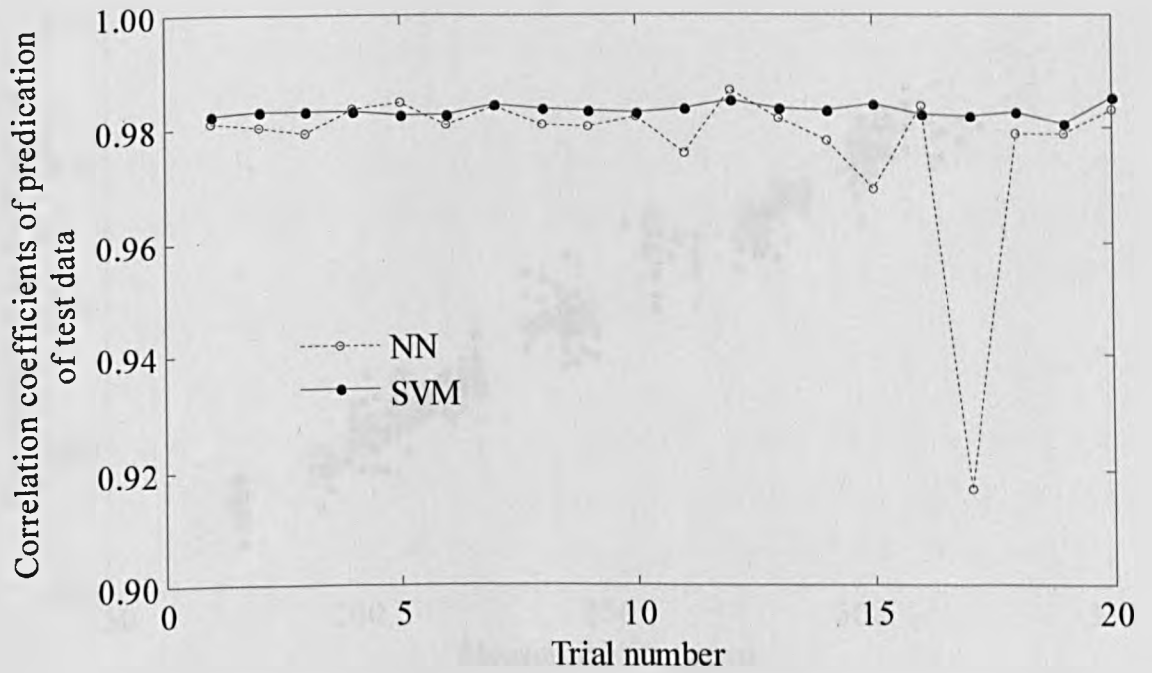


(b) Correlation coefficients

Figure 5.45 Performance of SVM and NN for NO<sub>x</sub> prediction (training data)

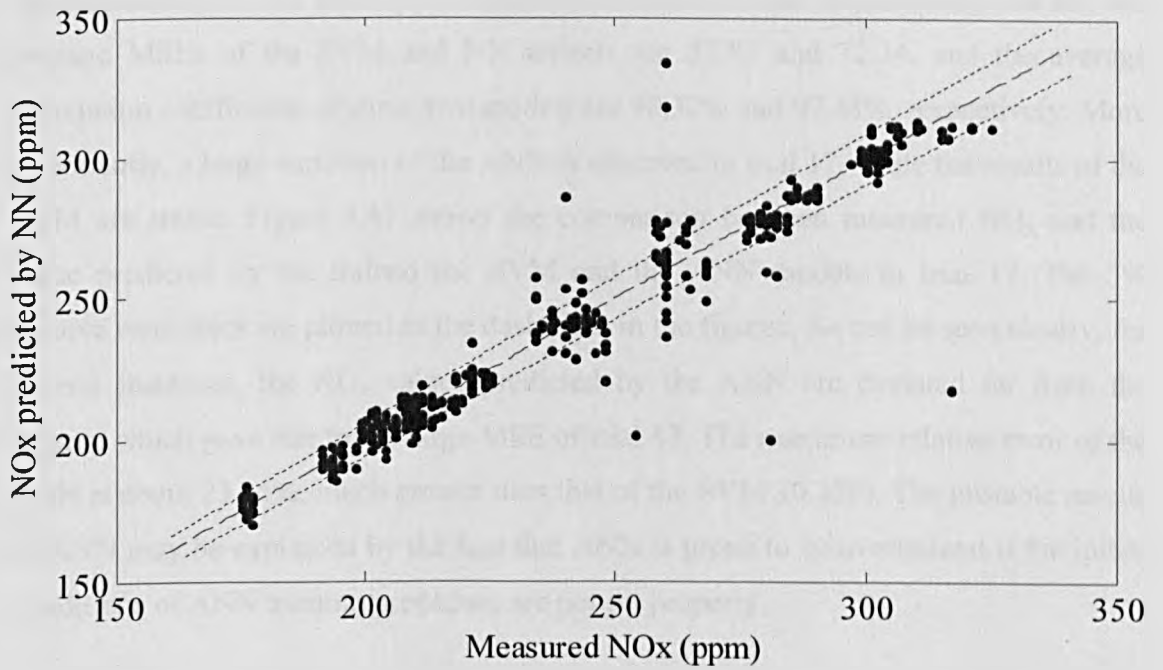


(a) Mean squared error

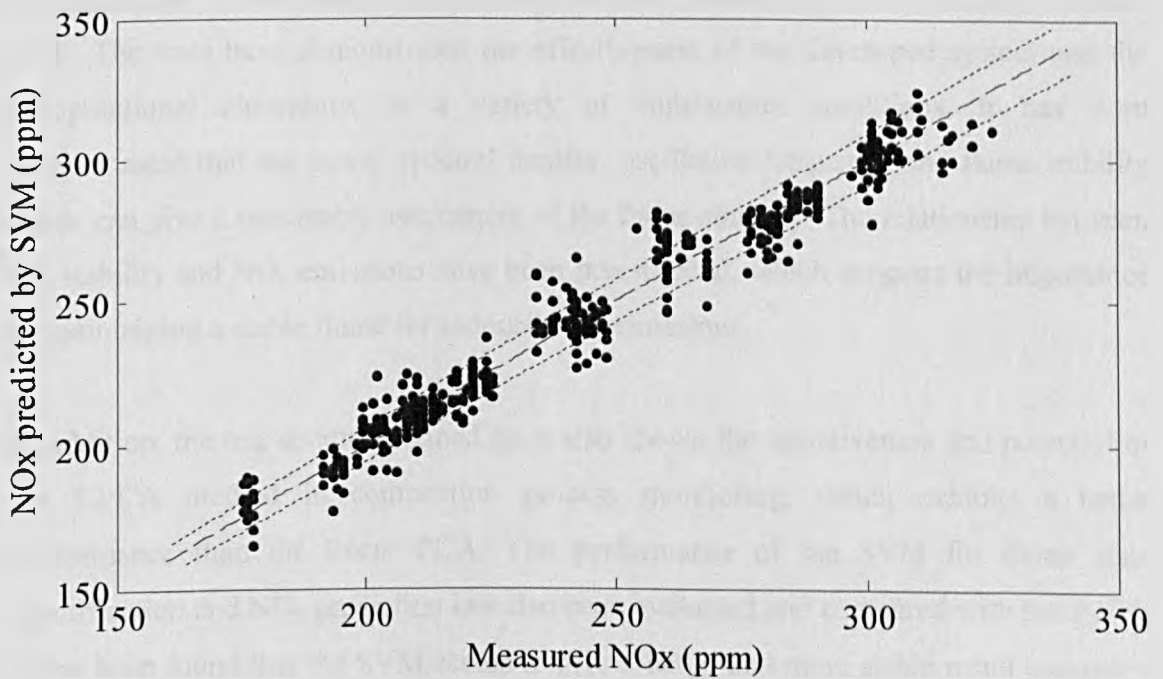


(b) Correlation coefficients

Figure 5.46 Performance of SVM and NN for NO<sub>x</sub> prediction (test data)



(a) NN



(b) SVM

Figure 5.47 Comparison between predicted and measured NO<sub>x</sub> emissions

The superiority of the SVM over the ANN is more evident in predicting test set; the average MSEs of the SVM and NN models are 52.87 and 72.34, and the average correlation coefficients of these two models are 98.32% and 97.48%, respectively. More importantly, a large variation of the ANN is observed in trial 17, while the results of the SVM are stable. Figure 5.47 shows the comparison between measured  $\text{NO}_x$  and the value predicted by the trained the SVM and the ANN models in trial 17. The 3% relative error lines are plotted as the dash lines in the figures. As can be seen clearly, for several instances, the  $\text{NO}_x$  values predicted by the ANN are deviated far from the targets, which gave rise to the large MSE of trial 17. The maximum relative error of the ANN is about 23.15%, much greater than that of the SVM 10.22%. The unstable results of ANN may be explained by the fact that ANN is prone to be overtrained if the initial conditions of ANN training procedure are not set properly.

## 5.5 Summary

A wide range of combustion conditions have been created on a 9MW<sub>th</sub> heavy-oil-fired CTF. The tests have demonstrated the effectiveness of the developed system and the computational algorithms in a variety of combustion conditions. It has been demonstrated that the power spectral density, oscillation frequency and flame stability index can give a reasonable assessment of the flame stability. The relationship between the stability and  $\text{NO}_x$  emissions have been investigated, which suggests the importance of maintaining a stable flame for reduced  $\text{NO}_x$  emissions.

In addition, the test results obtained have also shown the effectiveness and potential of the KPCA method in combustion process monitoring, which exhibits a better performance than the linear PCA. The performance of the SVM for flame state identification and  $\text{NO}_x$  prediction has also been evaluated and compared with the ANNs. It has been found that the SVM seems to give a better and more stable result compared to the ANN algorithms tested in the present study (Backpropagation neural networks), which may be explained by the good generalization ability of SVM.

## Chapter 6

### Tests on a 660MW<sub>th</sub> Heavy-Oil-Fired Boiler

#### 6.1 Introduction

Industrial tests were carried out on a 660MW<sub>th</sub> heavy-oil-fired boiler in a power station in Saudi Arabia. The boiler was newly constructed but encountered a severe vibration problem when the boiler load increased to a certain level. The occurrence of the vibration endangers seriously the safe and normal operation of the boiler. The problem was recognized as thermo-acoustic combustion instability after initial test, which was carried out to analyse the spectrum of the combustion acoustic signal captured from the boiler. However, the trigger/cause of the onset of thermo-acoustic vibration was unknown, which motivated this investigation. The objectives of the flame imaging tests on the boiler were as follows:

- To assess the performance of the flame imaging system in a full-scale industrial combustion environment
- To investigate the characteristics, particularly stability, of oil flames by using the flame imaging system, so as to reveal the cause of the boiler vibration

This chapter firstly gives a brief description about the theory of thermo-acoustic combustion instability, followed by the spectral analysis results of the combustion acoustic signals taken under the normal operation condition as well as the vibration condition. Then, it introduces the experimental conditions of the flame imaging tests, including the structure of the boiler, the installation of the flame imaging system, and the test programme, following by the results of the tests and discussed.

## 6.2 Thermo-Acoustic Combustion Instability

### 6.2.1 Theory of Thermo-Acoustic Instability

Thermo-acoustic combustion instabilities refer to self-sustained combustion oscillation at or near the acoustic frequency of the combustion chamber, which is the result of closed-loop coupling between unsteady heat release and pressure fluctuations [34]. Figure 6.1 illustrates the feedback loop responsible for the self-excited oscillations in the combustion chamber [111]. It is believed that disturbance in fuel flow (e.g., fluctuations in equivalent ratio, flow velocity and pressure) excites oscillations in heat release rate. The heat release oscillations generate acoustic oscillations. The acoustic oscillations would introduce the disturbance into the fuel flow, closing the feedback loop. If two conditions are satisfied, the amplitude of acoustic oscillation will grow in time until it saturates. First, the heat release oscillation is properly phased with the fluctuating acoustic pressure, as stated in Rayleigh's criterion [112], i.e.,

$$\frac{1}{L} \int_0^L p' q' dt > 0, \quad (6-1)$$

where  $p'$  and  $q'$  are the pressure and heat release oscillation, respectively,  $t$  is time and  $L$  is the time period. Second, the rate of energy added to the acoustic field by the combustion process exceeds the rate of energy dissipation [112]. When the energy of acoustic oscillation is high enough, the self-sustained acoustic oscillation will give rise to the vibration of the combustion chamber.

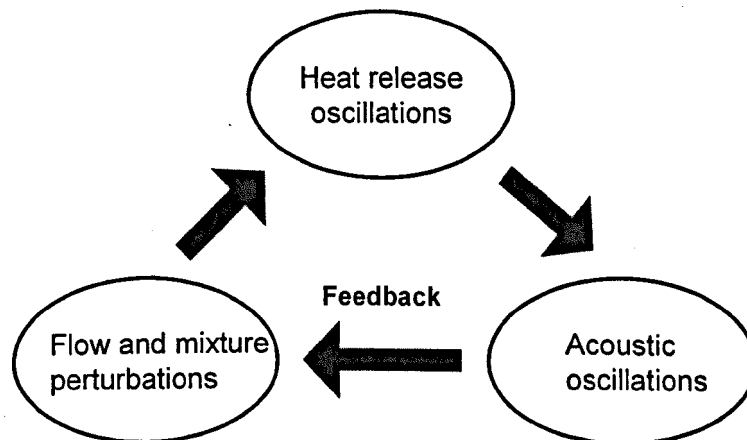


Figure 6.1 Feedback loop responsible for thermo-acoustic instability [111]

Thermo-acoustic combustion instability generally occurs at frequencies associated with the natural acoustic modes of the combustion chamber, e.g., bulk, axial and transverse modes. The nature acoustic frequency  $F_a$  of a combustion chamber can be estimated by

$$F_a = \frac{c_T}{2 \cdot D}, \quad (6-2)$$

$$c_T = c_0 \sqrt{\frac{T}{273}}, \quad (6-3)$$

where  $c_T$  is the speed of sound at absolute temperature  $T$  in degrees Kelvin,  $c_0$  is the speed of sound at temperature 273°K, and  $D$  is the geometric dimension of the combustion chamber (e.g., width, height, and depth).

### 6.2.2 Acoustic Characteristics of the Tested Boiler

Initial test was carried out to investigate the combustion acoustic characteristics of the tested boiler by using a microphone sensor. Figure 6.2 shows the spectrum of the acoustic signal obtained at the boiler load 300MW<sub>th</sub> at which the boiler operated normally without vibration, whilst Figure 6.3 shows that obtained at 340MW<sub>th</sub> at which the boiler vibration occurred. It has been found that the peak frequency located at about 29.5Hz for both test conditions, and when the vibration occurred at 340MW<sub>th</sub>, the amplitude of the peak frequency increased dramatically, up to 8 times of that at 300MW<sub>th</sub>.

The peak frequency 29.5Hz is consistent with the theoretical thermo-acoustic oscillation frequency of the boiler, which can be derived from (6-2) and (6-3), given the width of the boiler (from front wall to rear wall)  $D=14\text{m}$  and the average temperature within the boiler  $T=1500^\circ\text{C}$ . Furthermore, the acoustic oscillation frequency 29.5Hz is also in line with the vibration frequency of the boiler, which was measured by vibration sensors. These results have thus suggested that the vibration of the boiler is actually a phenomenon of thermo-acoustic combustion instability. However, what is the trigger/cause of the thermo-acoustic vibration is not clear, which motivated the following flame imaging study.

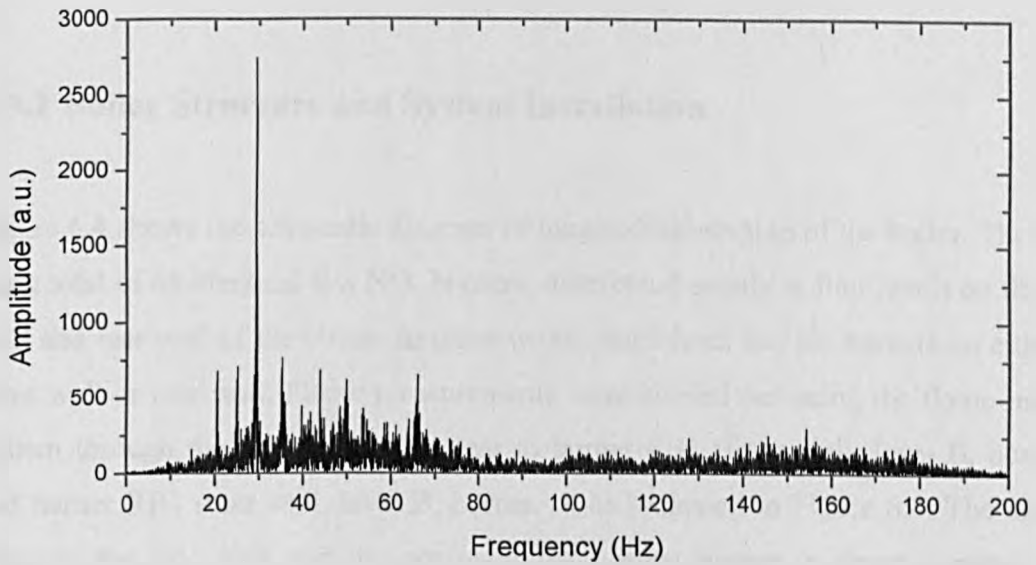


Figure 6.2 Spectrum of the combustion acoustic signal obtained at boiler load  $300\text{MW}_{\text{th}}$  (non-vibration)

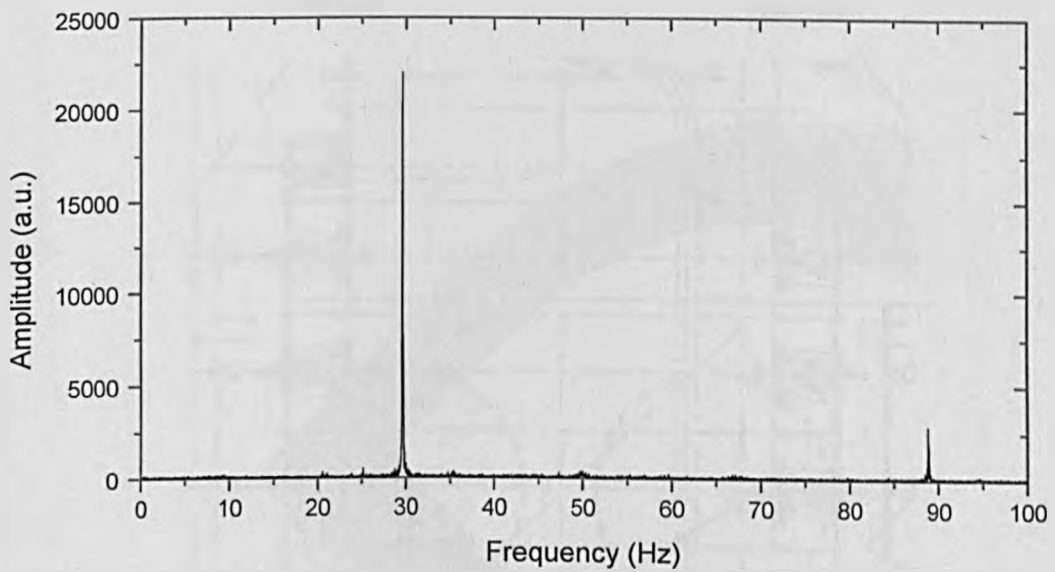


Figure 6.3 Spectrum of the combustion acoustic signal obtained at boiler load  $340\text{MW}_{\text{th}}$  (vibration)

## 6.3 Experimental Conditions

### 6.3.1 Boiler Structure and System Installation

Figure 6.4 shows the schematic diagram of longitudinal-section of the boiler. The boiler has a total of 48 identical low  $\text{NO}_x$  burners, distributed evenly at four levels on the front wall and rear wall of the boiler. In other words, each level has six burners on either the front wall or rear wall. Flame measurements were carried out using the flame imaging system through the side view ports near to burner FB1 (front wall, level B, burner 1) and burner RB1 (rear wall, level B, burner 1), as indicated in Figure 6.4. The distance between the side wall and the centre of the nearest burner is about 3 meters. The resulting effective field of view is about 3.5 to 4 meters (part of view is blocked by the wall). Figure 6.5 shows the on-site installation of the flame imaging system during the test.

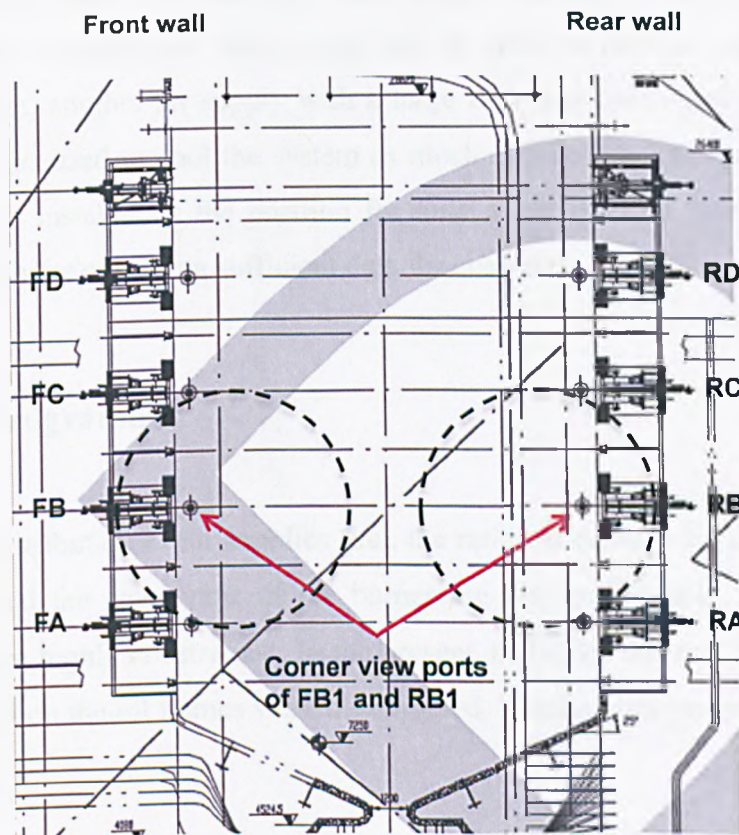


Figure 6.4 Schematic diagram of longitudinal-section of the 660MW<sub>th</sub> boiler



Figure 6.5 Flame imaging system and its installation

A purging air with a flow rate of about 20 litres per minutes was used to keep the lens of the optical probe clean. Unfortunately, water supply was not available on the platform where the flame imaging test was carried out. In order to prevent system from overheating problem, another air supply with a large flow rate (estimated above 150 litres per minutes) was used to cool the system as much as possible, and for each condition, the system was installed at the position for only a short period (about five minutes, which is enough for collecting sufficient data for analysis).

### 6.3.2 Test Programme

Because the distribution of air supplies (i.e., the ratios of primary air and secondary air to total air) and the swirl vane of the burner are not configurable, the possible test conditions were highly constrained. In the present study, the impacts of nozzle rotation and boiler load on the oil flames were investigated. Detailed test programme is listed in Table 6.1.

Table 6.1 Summary of the test programme on the 660MW<sub>th</sub> boiler

No	Test	Burner	Condition
1	Nozzle rotation	FB1 & RB1	285MW <sub>th</sub> , before nozzle rotated
			285MW <sub>th</sub> , after nozzle rotated
2	Boiler load	RB1	285MW <sub>th</sub> , after nozzle rotated
			430MW <sub>th</sub> , after nozzle rotated
			450MW <sub>th</sub> , after nozzle rotated

## 6.4 Results and Discussions

### 6.4.1 Impact of Nozzle Rotation

The nozzle shape and position of the burner oil gun affect significantly the intermixing of oil spray and air flow and hence the combustion performance. This test was carried out to investigate the impact of the nozzle rotation on the stability of the flames. Figure 6.6 shows the front view of the burner used in the boiler and its nozzle. Heavy oil was atomised into very small droplets by steam and injected into the furnace through the holes of the nozzle, and then mixed with surrounding primary air and secondary air, successively. The nozzle has six pairs of holes distributed evenly, as shown in Figure 6.6. The six pairs of holes are designed to be aligned with six baffles. The baffles, as the name suggests, are used to obstruct the intermixing of the air flow and the atomised oil gas that injected behind the baffles, and thus delay the combustion, so as to achieve a low NO<sub>x</sub> emission.

Flame data were captured at both FB1 and RB1 under the condition when the nozzle and the baffles were aligned as originally designed, and under the condition when they were misaligned after deliberately rotating the nozzle by a certain degree to achieve better intermixing of air flow and oil spray. Figure 6.7 and 6.8 show the typical examples of instantaneous heavy oil flame images obtained at FB1 and RB1, respectively.

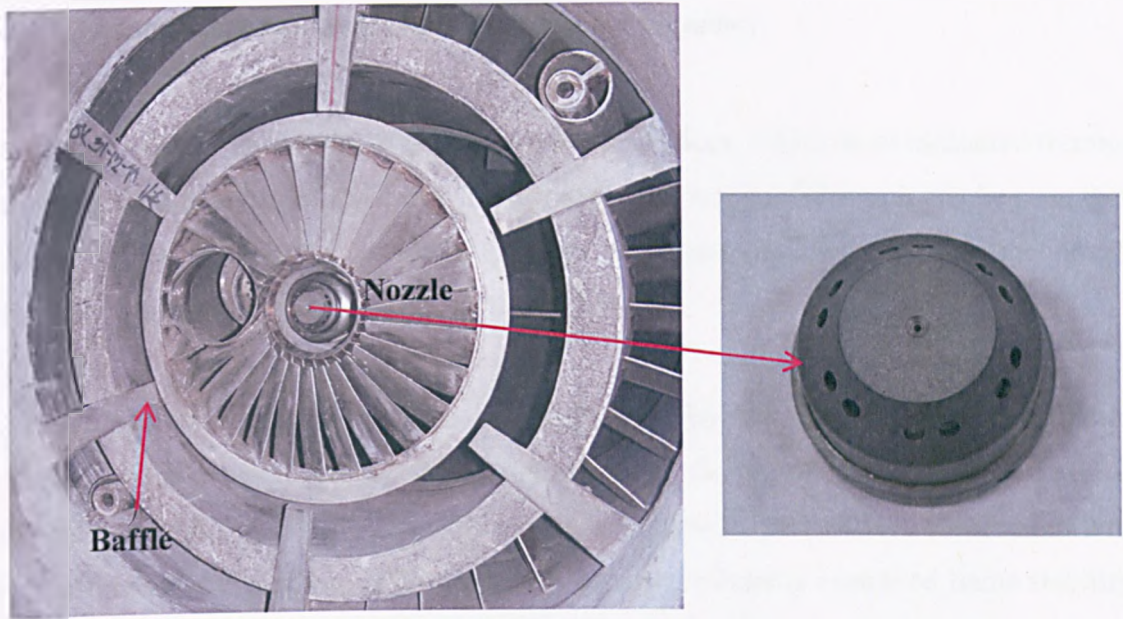


Figure 6.6 Front view of the burner and the nozzle

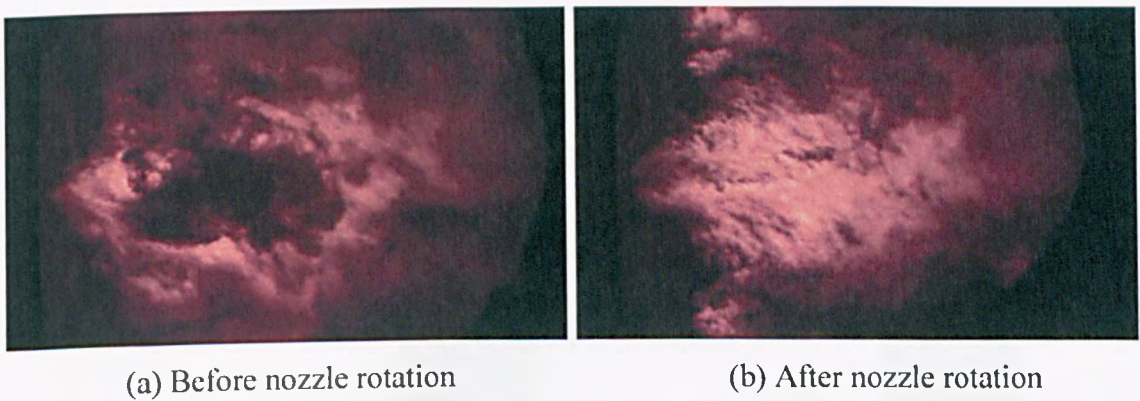


Figure 6.7 Flame images taken at burner FB1

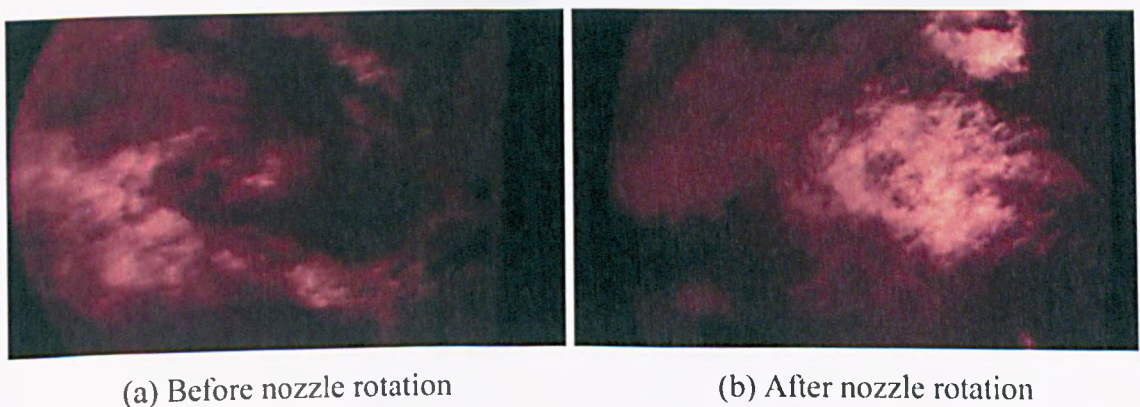


Figure 6.8 Flame images taken at burner RB1

### 6.4.1.1 Flame Stability Index and Oscillation Frequency

Figure 6.9 shows the results of the flame stability indices, which were measured through the statistical analysis of the flame images under the test conditions. It can be seen that, for both FB1 and RB1, the stability index increased significantly after the nozzle rotation, suggesting the improved flame stability.

The results of the stability index are supported by the data of flame oscillation frequency that were captured simultaneously with the flame images. As depicted in Figure 6.10, after nozzle rotation, increased oscillation frequencies are observed in both the infrared and visible bands for the tested burners, indicating improved flame stability. The improved flame stability can be attributed to the better intermixing of the oil spray and air flow.

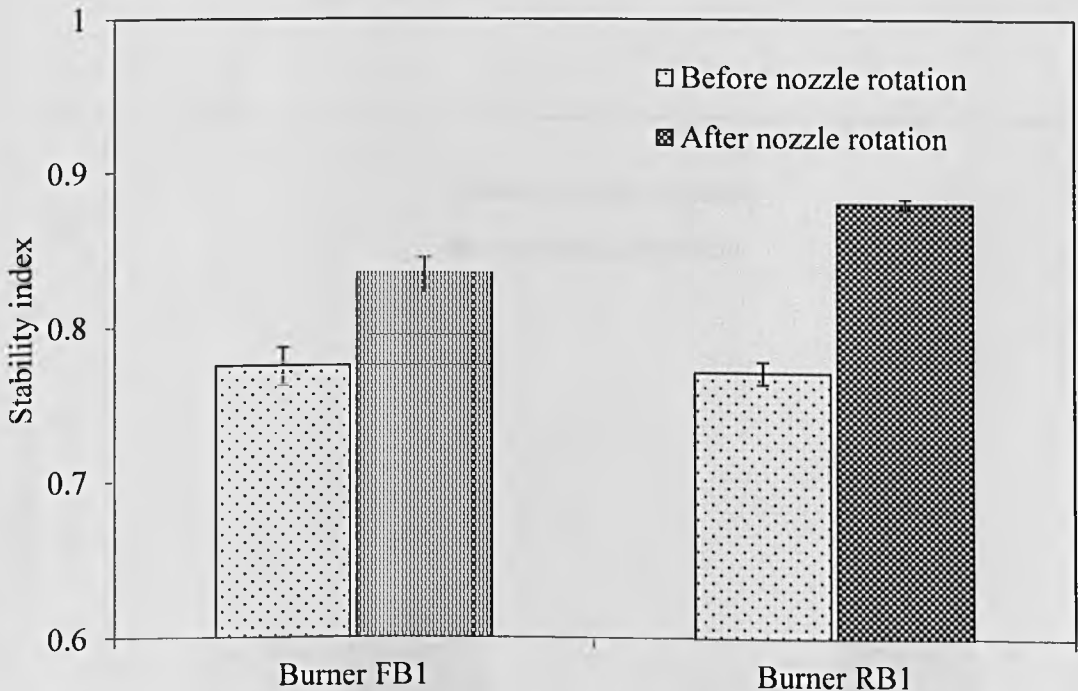
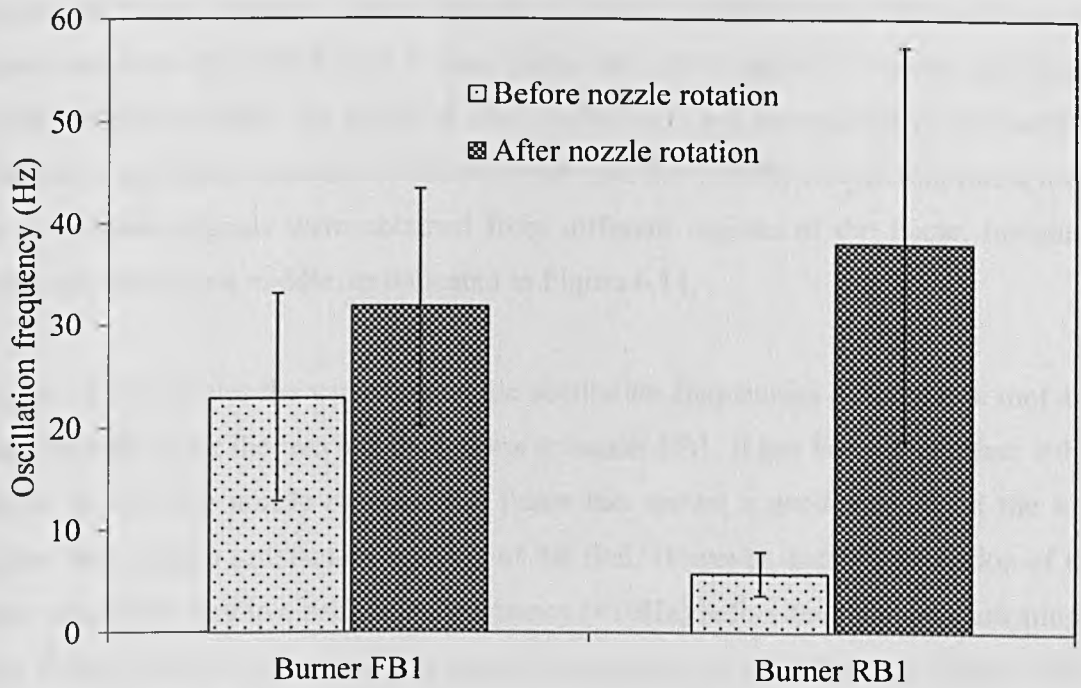
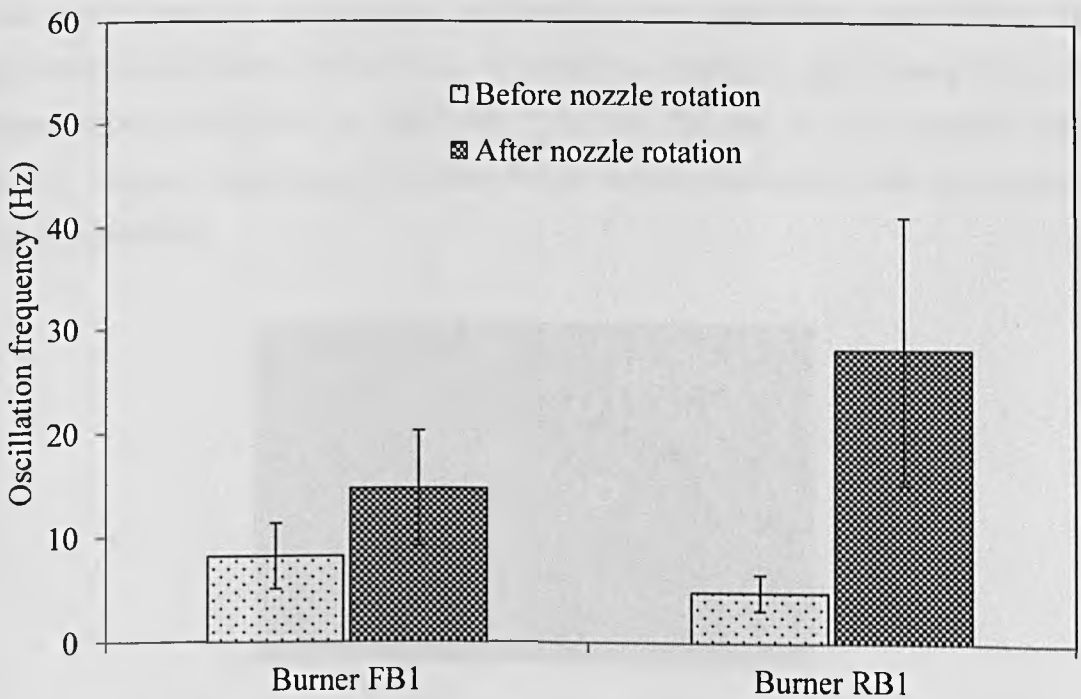


Figure 6.9 Comparison of flame stability indices before and after nozzle rotation



(a) Infrared band



(b) Visible band

Figure 6.10 Comparison of oscillation frequencies of whole flame before and after nozzle rotation

Before the nozzle rotation, a large amount of unburnt contents was observed from the flame images as shown in Figure 6.7 (a), particularly in the middle section of the flame, which indicates clearly the delay of the combustion, and consequently, the stability problem of the flame. In order to further investigate the stability in different flame areas, flame radiation signals were obtained from different regions of the flame, including flame root and flame middle, as indicated in Figure 6.11.

Figure 6.12 illustrates the variations of the oscillation frequencies of the flame root and flame middle under the two test conditions at burner FB1. It has been found that, either before or after the nozzle rotation, the flame has shown a good stability at the root region, indicating a satisfactory ignition of the fuel. However, the middle region of the flame exhibits a very low oscillation frequency ( $<10\text{Hz}$ ) before the rotation, indicating a poor flame stability at the middle regions. The situation is improved significantly after the nozzle rotation. This finding is further confirmed by the results obtained from burner RB1, as shown in Figure 6.13.

After nozzle rotation, the vibration problem has been ameliorated significantly. The maximum non-vibration boiler load, at which the boiler is approaching vibration, increased from 340MWth to 480MWth. This may be due to that improved flame stability reduced significantly the disturbance in the combustion and thus thermo-acoustic instability.

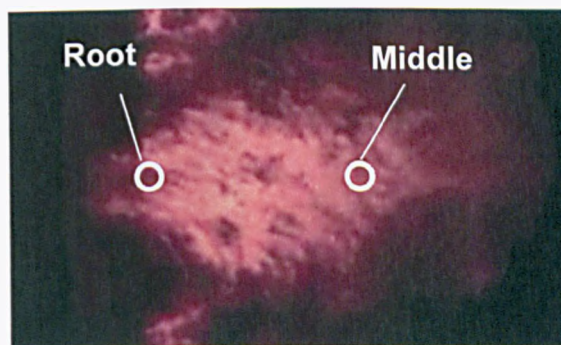
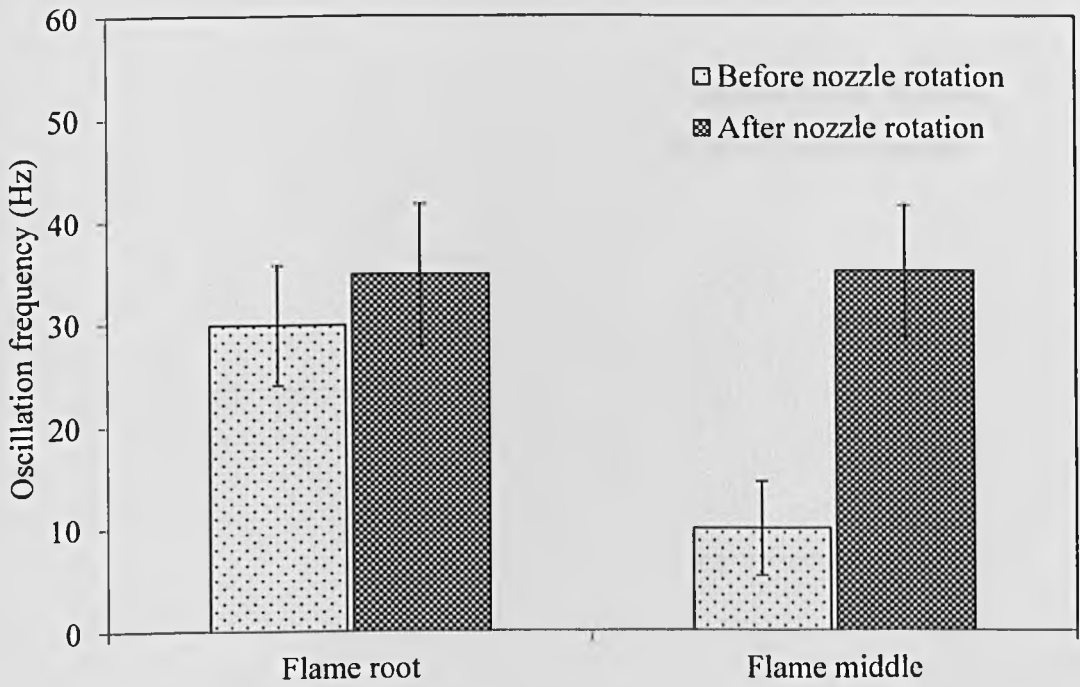
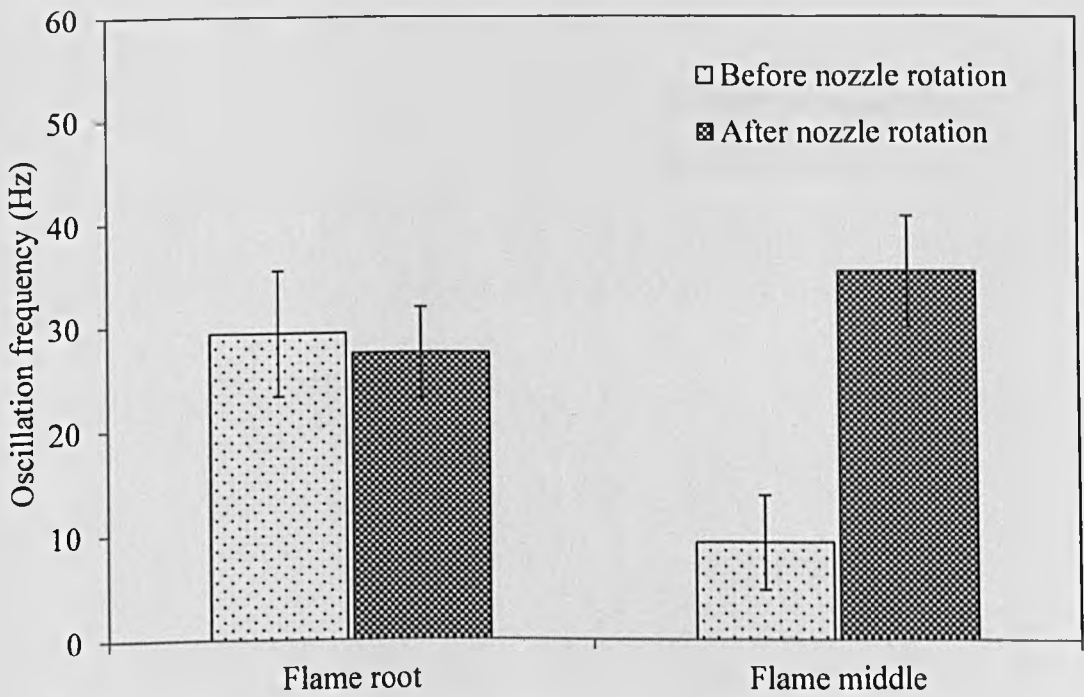


Figure 6.11 Location of measurement points of flame oscillation frequency

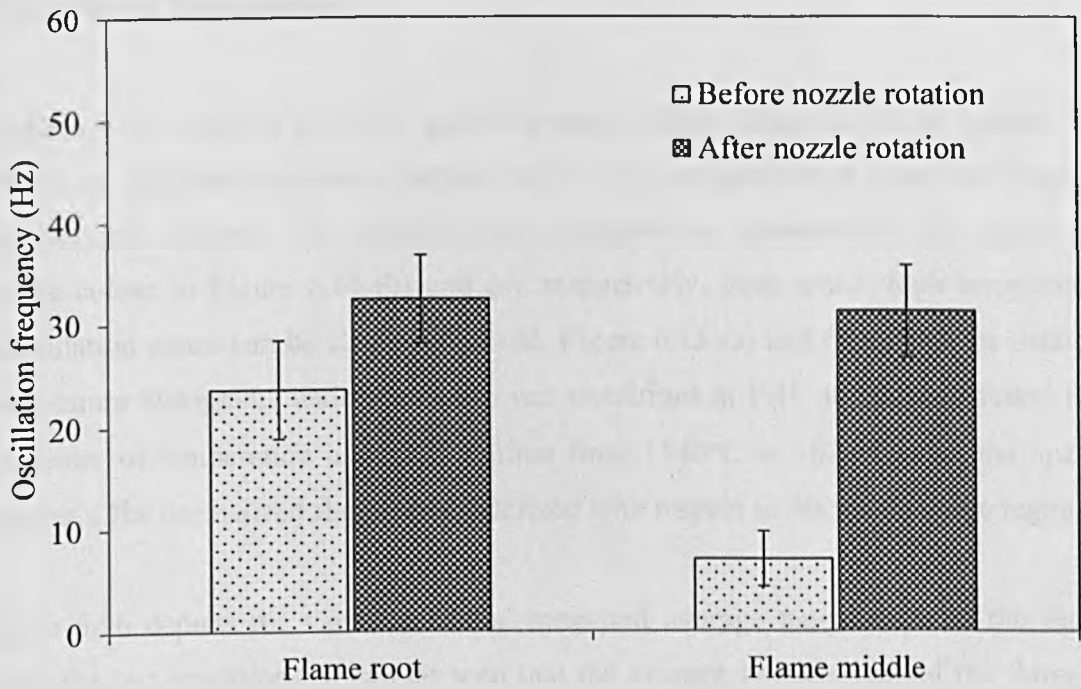


(a) Infrared band

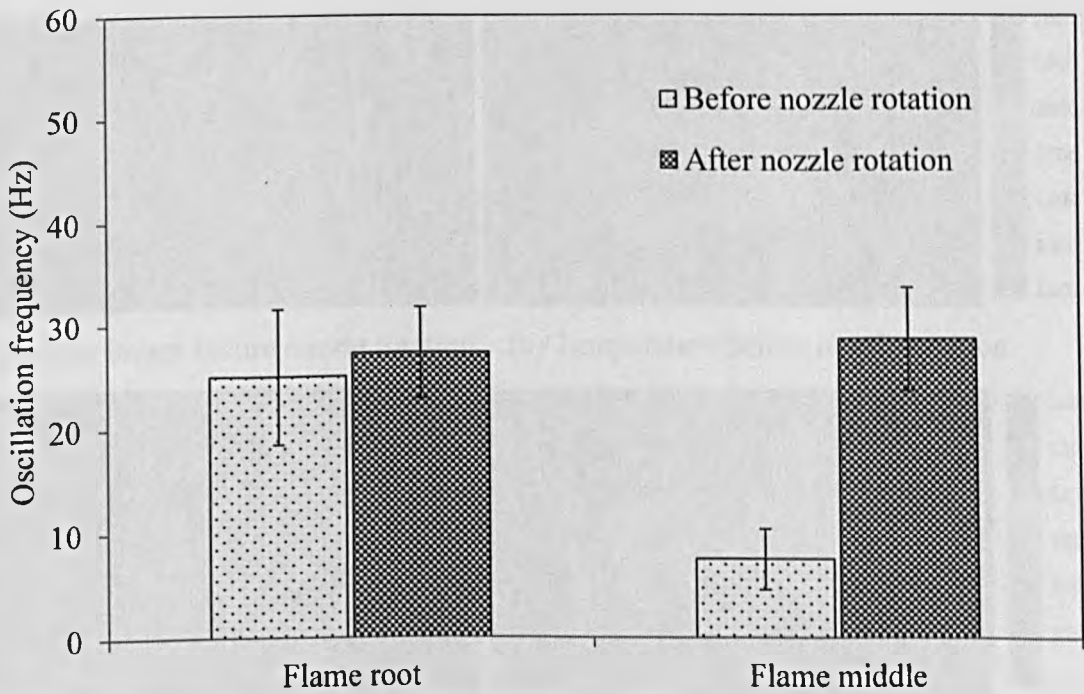


(b) Visible band

Figure 6.12 Comparison of oscillation frequencies in different flame areas before and after nozzle rotation at burner FB1



(a) Infrared band



(b) Visible band

Figure 6.13 Comparison of oscillation frequencies in different flame areas before and after nozzle rotation at burner RB1

### 6.4.1.2 Flame Temperature

Figure 6.14 (a) and (c) show the typical averaged flame images taken at burner FB1 before and after nozzle rotation, respectively. Each averaged image is derived from 20 instantaneous images. The corresponding temperature distributions are shown in pseudo-colour in Figure 6.14 (b) and (d), respectively, from which high temperature recirculation zones can be clearly observed. Figure 6.15 (a) and (b) depict the detailed temperature histograms under these two test conditions at FB1. It has been found that the centre of temperature histogram shifted from 1540°C to 1620°C after the nozzle rotation. (The normalized flame area is defined with respect to the whole flame region.)

Figure 6.16 depicts the variation of the measured average temperature of the flame under the test conditions. It can be seen that the average temperatures of the flame at both FB1 and RB1 increased by 70 - 90°C. The increased temperature can be explained by the better mixture of the oil spray and air flow and hence intensified combustion.

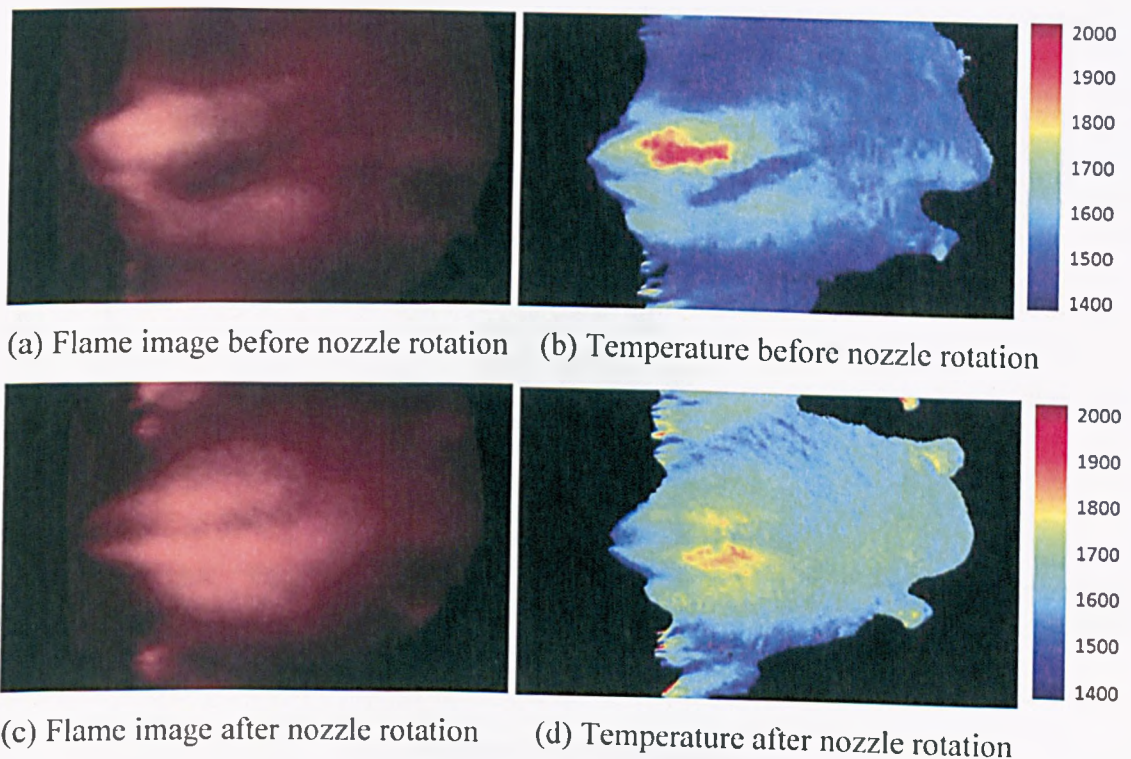
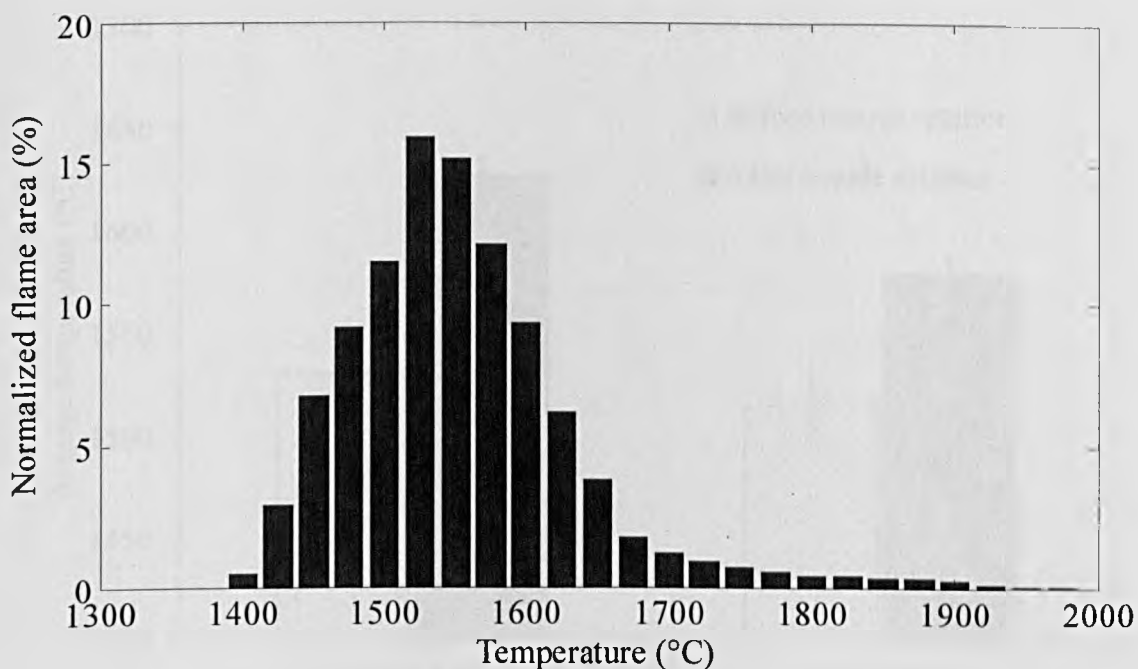
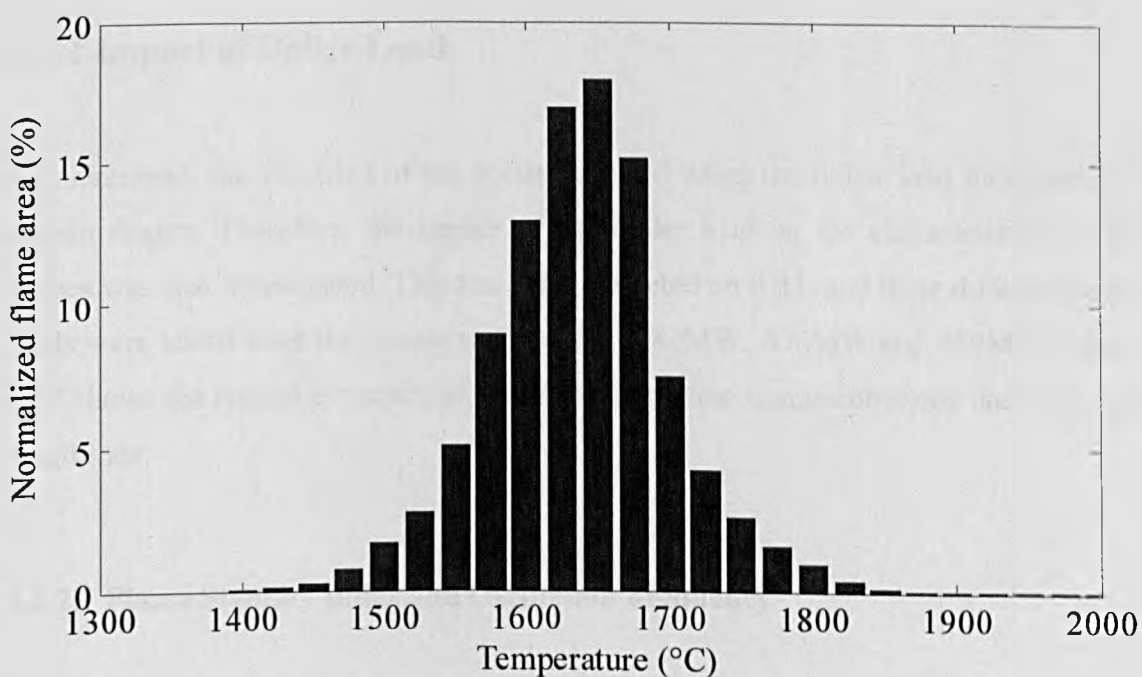


Figure 6.14 Averaged flame images and the corresponding temperature distributions at burner FB1



(a) Before nozzle rotation



(b) After nozzle rotation

Figure 6.15 Temperature histogram of the flame at burner FB1

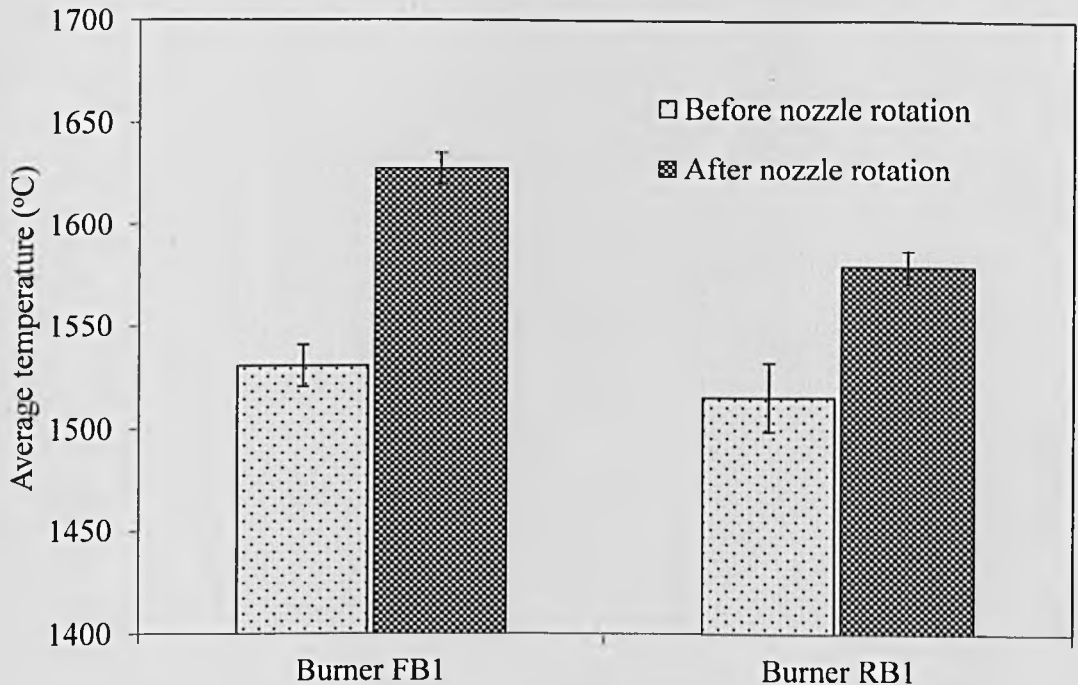


Figure 6.16 Comparison of average flame temperature before and after nozzle rotation

## 6.4.2 Impact of Boiler Load

As mentioned, the vibration of the boiler occurred when the boiler load increased to a certain degree. Therefore, the impact of the boiler load on the characteristics of the flames was also investigated. This test was conducted on RB1, and three different boiler loads were tested after the nozzle rotation, i.e., 280MW, 430MW and 450MW. Figure 6.17 shows the typical examples of instantaneous flame images obtained under the test conditions.

### 6.4.2.1 Flame Stability Index and Oscillation Frequency

Figure 6.18 shows the variation of the flame stability index with the boiler load. It has been found that the flame stability index decreased gradually with the load, suggesting that the flame became more unstable when the boiler load increased. The result is consistent with the analysis of the oscillation frequency of whole flame, as shown in

Figure 6.19. Decreased oscillation frequencies are observed in both infrared and visible bands at a high load, indicating decreased flame stability.

The stability of different flame areas was also tested. Figure 6.20 illustrates the variations of the oscillation frequencies of the flame root and middle areas with the boiler load. The plots suggest that the root region of the flame has a good stability under different loads, indicating a satisfactory stable ignition of the fuel. However, the stability at the middle region of the flame decreased with the furnace load.

The results further support the conclusion drawn from the tests of the nozzle rotation that the vibration is prone to occur when the flame is unstable. Therefore, actions should be taken to improve the flame stability, especially the middle region of the flame, so as to ameliorate vibration problem.

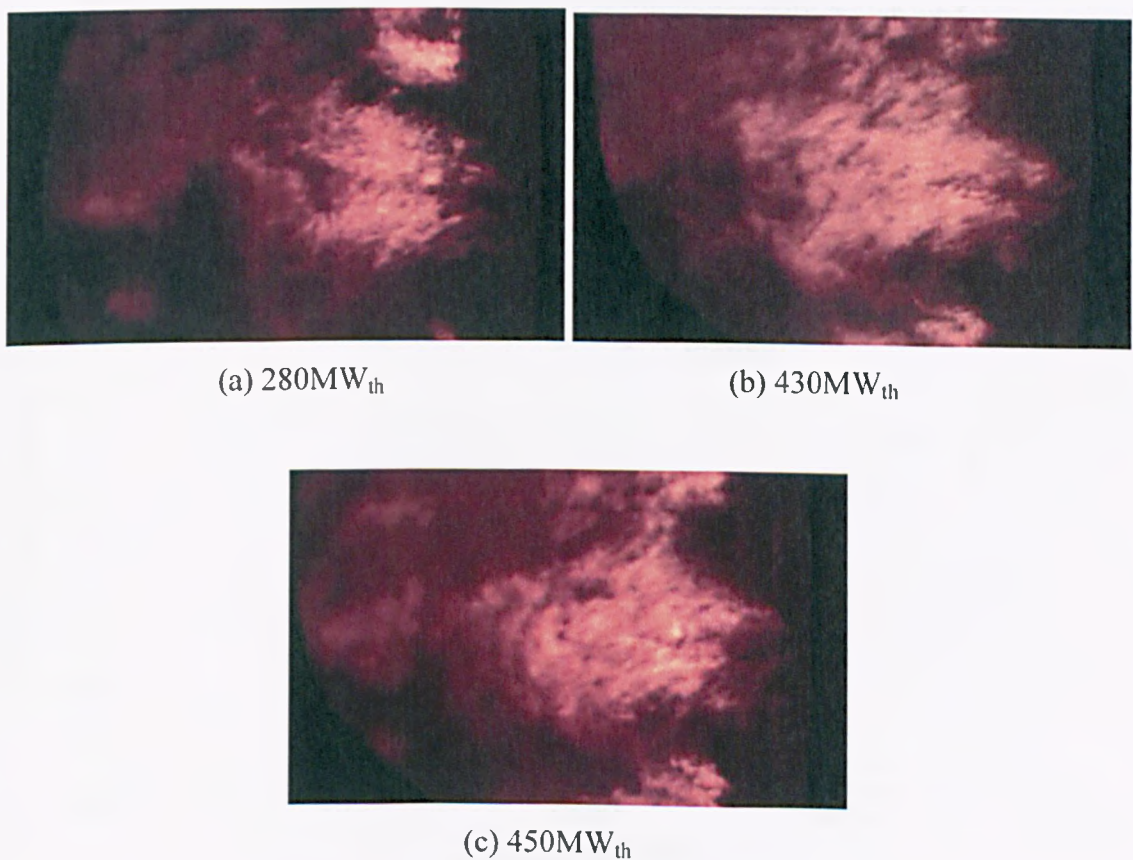


Figure 6.17 Flame images taken under different boiler loads at burner RB1

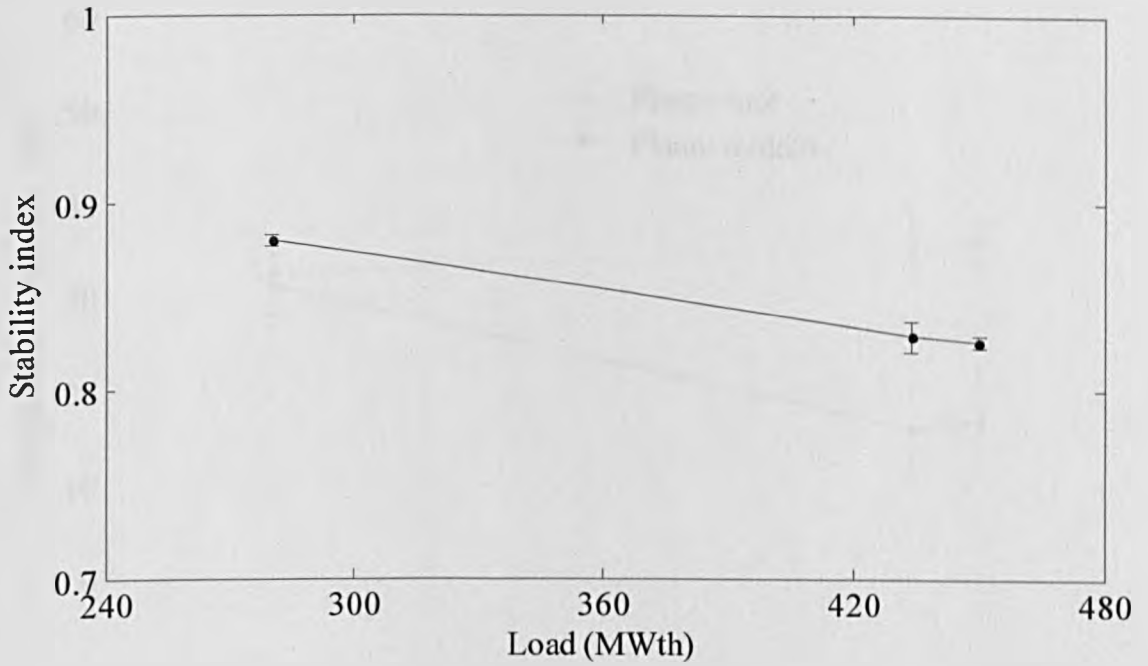


Figure 6.18 Variation of flame stability index with boiler load

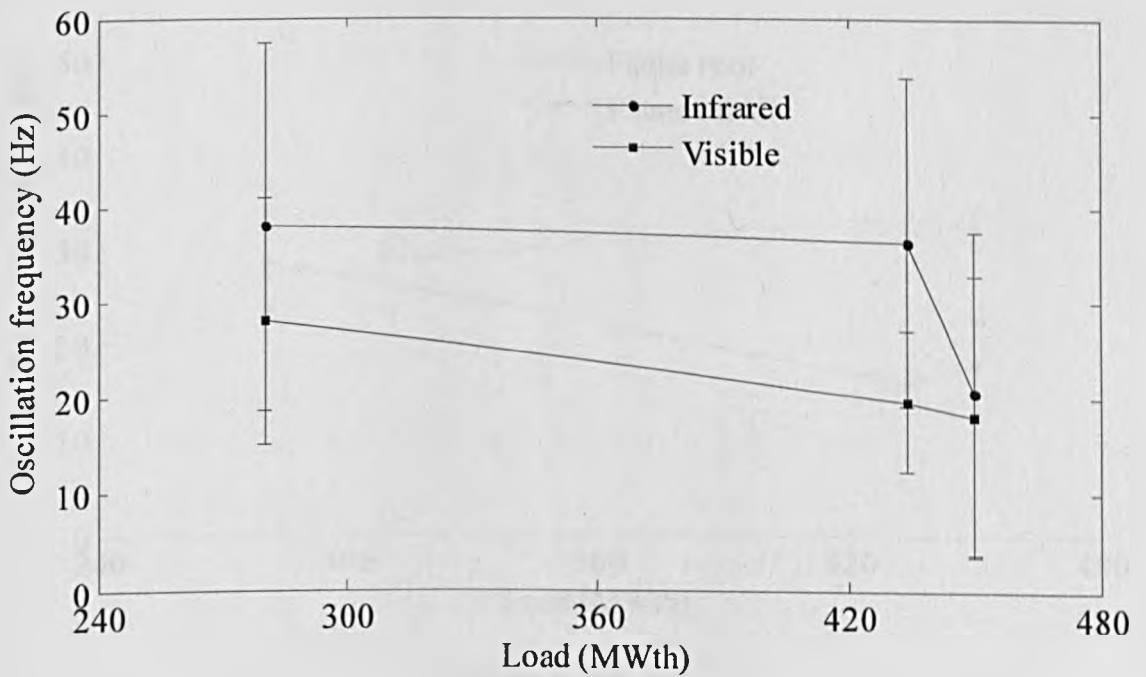
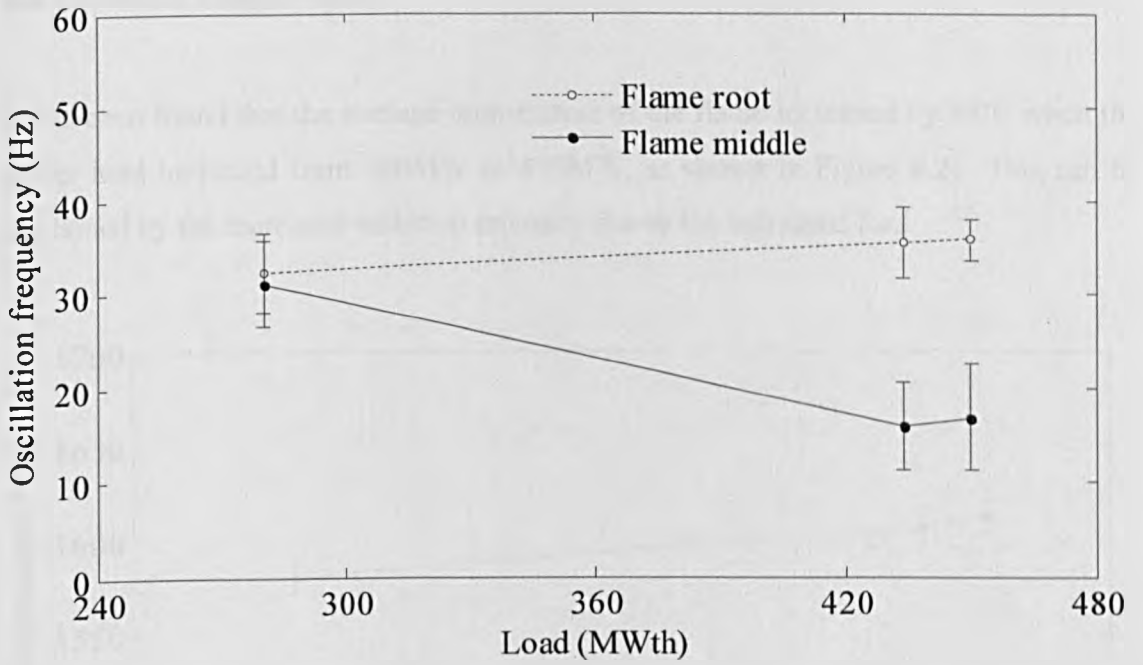
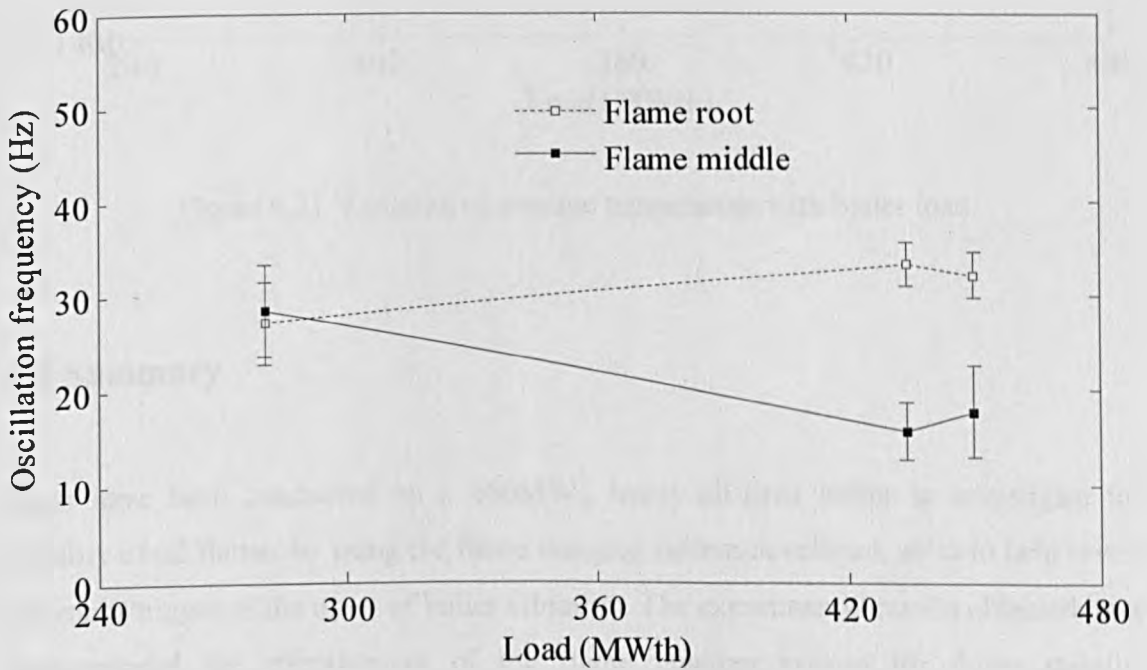


Figure 6.19 Variation of oscillation frequency of whole flame with boiler load



(a) Infrared band



(b) Visible band

Figure 6.20 Variations of oscillation frequencies of different flame regions with boiler load

### 6.4.2.2 Flame Temperature

It has been found that the average temperature of the flame increased by 40°C when the boiler load increased from 280MW to 470MW, as shown in Figure 6.21. This can be explained by the increased radiation intensity due to the increased load.

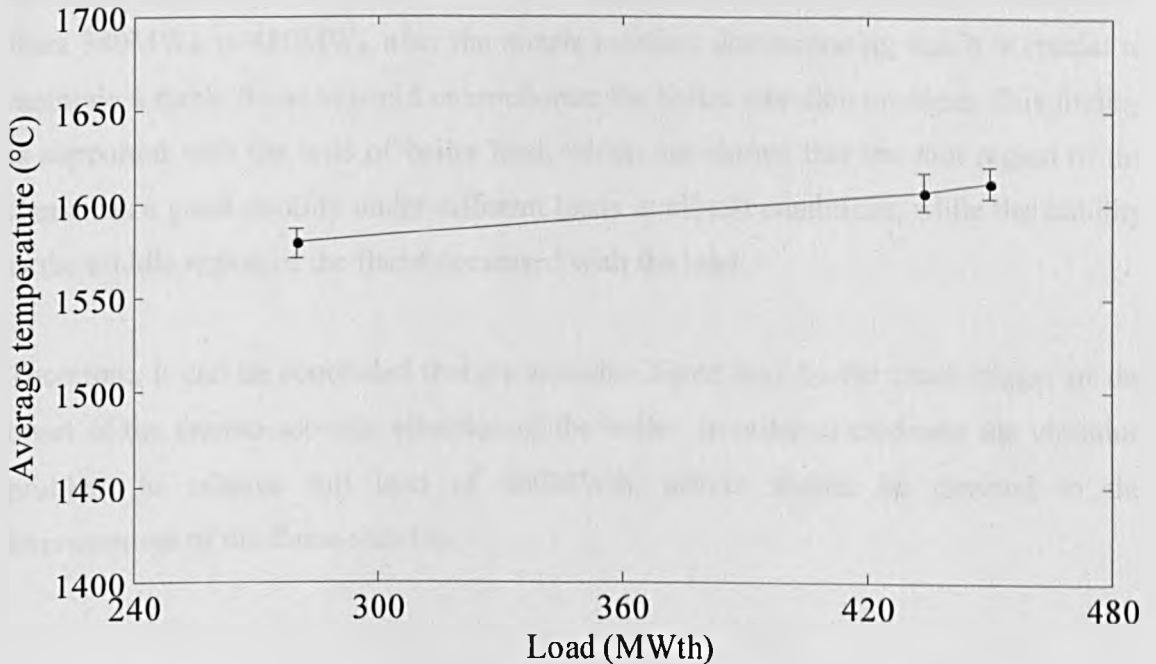


Figure 6.21 Variation of average temperature with boiler load

## 6.5 Summary

Tests have been conducted on a 660MW<sub>th</sub> heavy-oil-fired boiler to investigate the stability of oil flames by using the flame imaging system developed, so as to help reveal the cause/trigger of the onset of boiler vibration. The experimental results obtained have demonstrated the effectiveness of the flame imaging system for flame stability monitoring.

During the tests, the impacts of the nozzle rotation and the boiler load on the flame stability were investigated. In the test of nozzle rotation, it has been found that, either before or after nozzle rotation, the flame has shown a good stability at the root region, indicating a satisfactory ignition of the fuel. However, the middle region of the flame has shown a poor stability in this region at both test burners before the nozzle rotation. After the nozzle rotation, the stability of the flame, particularly in its middle region, increased significantly. The maximum non-vibration boiler load increased significantly from 340MW<sub>th</sub> to 480MW<sub>th</sub> after the nozzle rotation, demonstrating that it is crucial to maintain a stable flame to avoid or ameliorate the boiler vibration problem. This finding is supported with the tests of boiler load, which has shown that the root region of the flame has a good stability under different loads in all test conditions, while the stability at the middle region of the flame decreased with the load.

Therefore, it can be concluded that the unstable flame may be the cause/trigger of the onset of the thermo-acoustic vibration of the boiler. In order to eliminate the vibration problem to achieve full load of 660MW<sub>th</sub>, efforts should be directed to the improvement of the flame stability.

## Chapter 7

### Conclusions and Recommendations for Future Work

#### 7.1 Introduction

The research work presented in this thesis is concerned with the development of a methodology for flame stability and burner condition monitoring in fossil-fuel-fired furnaces. A prototype instrumentation system, operating on optical sensing, digital imaging, signal/imaging processing, and soft computing techniques, has been designed and implemented. The system has been evaluated on a 9MW<sub>th</sub> heavy-oil-fired combustion test facility and on a 660MW<sub>th</sub> heavy-oil-fired boiler. Test results have demonstrated that the system is capable of providing a quantitative assessment of flame stability under a wide range of combustion conditions, and give an effective detection of abnormal conditions, indication of flame state, and prediction of NO<sub>x</sub> emissions in the furnace.

This chapter presents the conclusions that have been drawn from the research programme conducted and makes recommendations for future work in the field.

#### 7.2 Conclusions

##### 7.2.1 Instrumentation System

The instrumentation system developed is comprised of a rigid optical probe, a beam-splitting unit, an EPSB (embedded photodetector and signal-processing board), a digital camera, and a mini-motherboard with associated application software. The system is capable of measuring simultaneously a number of flame parameters, including oscillation frequency, power spectral density, geometric and luminous characteristics,

two-dimensional temperature distribution, flame stability index, etc. The integration of the optical probe and all optical and electronic components as a single unit has offered the system excellent portability and robustness. The digital camera and the photodetectors have been proven to be capable of accommodating themselves to a wide range of flame radiation intensities with the aid of dedicated software. The EPSB has been proven robust and offered fast response for the measurement of the power spectral density and oscillation frequency of a flame. The mini-motherboard, as the computing core of the system, has shown a high performance in processing data and executing algorithms.

The performance of the oscillation frequency measurement of the system has been evaluated by using a standard frequency-varying light source. The results have demonstrated that the system is capable of measuring the oscillation frequency of an unknown light source with a relative error no greater than 2% (frequency range: 0 to 500Hz).

The temperature measurement of the system has been calibrated by using a blackbody furnace as a standard temperature source. The accuracy of temperature measurement has been verified by applying the system to measuring the true temperature of a pre-calibrated standard tungsten lamp. The maximum error of 14.8°C has been found at a true temperature of 1650°C and is equivalent to a relative error of 0.9%. (The relative error is defined as the absolute error divided by the true value).

In addition, the camera sensor dark current, and the impacts of various camera settings (including exposure time, master gain, gain boost and R/G/B gains) on the intensity responses of camera R/G/B channels, have been analysed using the standard blackbody furnace as a stable radiation source. The non-linearity of the system has been found in the range of 0.23%. The obtained results have been taken into account in software to achieve automatic adjustment of the camera to avoid under- and over-exposure of flame images, which has been proven effective in on-site tests.

Results obtained on both an industrial-scale combustion test facility and a full-scale boiler have demonstrated that the developed system, including all optical, mechanical,

electronic and computing elements, as well as the application software, is operational and reliable in hostile industrial environments.

### **7.2.2 Tests on the 9MW<sub>th</sub> Combustion Test Facility**

Extensive tests were conducted on a 9MW<sub>th</sub> heavy-oil-fired combustion test facility. A wide range of combustion conditions were created, including variations in the swirl vane angle of tertiary air (TA), the swirl vane position of secondary air (SA), the ratio of primary air (PA) to total air, the ratio of overfire air (OFA) to total air and the nozzle position of OFA. For each test, flame parameters were quantified, including power spectral density, oscillation frequency, flame stability index, and temperature. As a result of the tests, a better understanding of the characteristics of the oil flame and its stability has been achieved. A number of conclusions can be drawn from the presented results.

#### **7.2.2.1 Flame Stability**

The TA swirl vane angle affects significantly the aerodynamics of the entering air flow and its mixture level with fuel and hence the stability of the flame. It has been found that a high TA swirl vane angle gives rise to a stretched flame, improved stability and reduced NO<sub>x</sub> emissions. Under TA swirl vane angle 25°, the flame is unstable in terms of its geometric, luminous and fluid-dynamic characteristics.

Similar to the results of TA swirl vane angle, improved flame stability and reduced NO<sub>x</sub> emissions have also been observed at a decreased swirling intensity that resulted from a high SA swirl vane position. The flame is more stable at SA swirl vane position 65mm than at -17mm and 30mm.

The results of different ratios of PA to total air have suggested that the increased PA would result in improved flame stability, slightly decreased temperature, and decreased NO<sub>x</sub> emissions, provided that the primary air is less than 23%.

Overfire air is a well-known technology for reducing  $\text{NO}_x$  emissions from a combustion process as it can achieve a decreased flame temperature. The test results have shown that the temperature of the oil flame decreased with the overfire air, resulting in reduced  $\text{NO}_x$  emissions. The comparisons between results from different nozzle positions of overfire air suggest that a longer delay in the injection of overfire air would increase the residence time of the combustion gases in low-oxygen concentration zones, resulting in decreased temperature and  $\text{NO}_x$  emissions. It has also been observed that an increased overfire air would result in increased soot emissivity and concentration ( $KL$  factor). Furthermore, it has been found that the flame stability doesn't deteriorate with the overfire air in all cases studied, provided that the overfire air is less than 20%.

Moreover, the correlation between the flame stability (expressed by flame stability index and oscillation frequency) and  $\text{NO}_x$  emissions obtained during all the tests has been investigated (Section 5.3.5). The results have suggested that it is crucial to maintain a stable flame for reduced  $\text{NO}_x$  emissions.

In summary, the experimental results have demonstrated the satisfactory sensitivity of the system to the variations in combustion conditions tested. It has also been proven that the power spectral density, oscillation frequency and flame stability index can be used as effective parameters for assessing the flame stability.

### **7.2.2.2 Burner Condition Monitoring**

A range of flame characteristics have been extracted from flame images and signals. These flame characteristics have been used as the inputs of the KPCA model for the detection of abnormal conditions, and as the inputs of the SVM model for flame state identification and  $\text{NO}_x$  prediction.

The results discussed in Section 5.4.1 have demonstrated the effectiveness of the KPCA model for detecting abnormal conditions in a combustion process. The KPCA model has exhibited clearly a better performance than a traditional linear PCA model in several aspects. Firstly, although both of the KPCA and PCA can correctly detect the artificially

created faults, the KPCA gives no false warnings whilst the PCA produced noticeable false-positive results. Secondly, the KPCA produces a very stable and accurate indication, little affected by the training set size, whilst the performance of the PCA decreases gradually with the decreased training set size. The better performance of the KPCA has revealed that KPCA is more capable of tackling the nonlinear relationship between flame characteristics than the PCA.

The results presented in Section 5.4.2 have demonstrated the superior performance of SVM in flame state identification and  $\text{NO}_x$  prediction. Compared to the ANN algorithms tested in the present study (Backpropagation neural networks), the SVM seems to have a higher success rate and less demand for the training set size in the flame state identification, and give a better and more stable performance in the  $\text{NO}_x$  prediction. The better performance of SVM is believed to be attributed to its good generalization ability (less prone to over-fitting). In addition, it should be noted that although the present work focused on the prediction of  $\text{NO}_x$  emissions from power plants, the presented soft computing technique is applicable to the prediction of other pollution emissions such as  $\text{SO}_2$ .

In summary, the test results have demonstrated the effectiveness of the selected flame characteristics and the soft computing techniques for burner condition monitoring.

### **7.2.3 Tests on the 660MW<sub>th</sub> Boiler**

Tests have been conducted on a 660MW<sub>th</sub> heavy-oil-fired boiler to investigate the characteristics, particularly the stability, of oil flames using the flame imaging system developed. The experimental results have further demonstrated the effectiveness of the system for flame stability monitoring on a full-scale industrial boiler.

The results presented in Section 6.4 have revealed that the boiler load and the radial position of burner's nozzle have a significant impact on the flame stability. Either before or after the nozzle rotated, the flame has shown a good stability at the root region, indicating a satisfactory ignition of the fuel. However, the middle region of the flame

has shown a better stability after the nozzle rotated than before the nozzle rotated. The improved flame stability caused by the rotation of the nozzle has resulted in an increased boiler load without a vibration. This finding has been supported by the tests for different boiler loads, which also shows that the root region of the flame has a good stability under different loads in all test conditions, whilst the stability in the middle region of the flame decreased with the load. It can therefore be concluded that the poor flame stability may be the cause/trigger of the thermo-acoustic vibration of the boiler. In order to solve the vibration problem so as to achieve the full load of  $660\text{MW}_{\text{th}}$ , efforts should be directed to the improvement of flame stability.

### **7.3 Recommendations for Future Work**

The work presented in this thesis has demonstrated the usefulness and potential of the outcomes of the research programme. However, the digital imaging and soft computing based techniques for the flame stability and burner condition monitoring are still in their development stage. There are a number of areas that require further research and development. This section outlines the areas that should be pursued over the next few years.

One of possible hardware improvements is the camera. A camera with a higher colour depth (e.g., 12bit Gigabit camera) will extend significantly the dynamic range of the temperature measurement. In addition, the use of a 3CCD camera will provide a true spatial colour distribution and hence more accurate temperature distribution measurement. Another possible hardware improvement lies in the mini-motherboard and its operation system. Window XP is used as the operation system in the current mini-motherboard due to the limitation of the camera driver. With the progress of embedded computer and industrial camera technologies, a customised embedded operation system can be used to provide a more reliable and robust solution, more importantly, a lower power consumption.

One of potential research areas is to incorporate a spectrometer element into the developed flame imaging system for monitoring the spectroscopic characteristics of

flame radicals. The spectroscopic characteristics of the flame radicals are closely linked with the composition of the fuel burnt and thus might be very useful for on-line fuel tracking. In addition, the intensities of radicals Sodium (Na) and Potassium (K) are closely related to the concentration of alkali chlorides, which are the main cause of furnace fouling and corrosion. Therefore, the radical information of the flame provided by the spectrometer might be used for monitoring alkali chlorides concentration and hence predicting furnace slagging and corrosion.

Another potential research area is to integrate acoustic technique with optical/imaging techniques for advanced flame monitoring. The acoustic information inside the furnace reflects the heat release characteristics of the combustion process and can be used to assess the performance of the furnace such as thermo-acoustic vibration, as illustrated in Section 6.2.2. In addition, the peak frequency of acoustic signal depends on the average temperature of the combustion chamber. It is possible to incorporate a microphone sensor in the two-colour pyrometry to achieve more the accurate measurement of the flame temperature and thus a better understanding of the combustion process.

In addition, better engineering to the system is required to enhance the operability, durability and robustness of the system. Furthermore, the calibration of the system for temperature measurement was conducted under the room temperature in the present study. It is worth calibrating the system under the industrial environments and investigating the effects of industrial environments on the temperature measurement of the system in a long duration. Further trials on industrial furnaces are also required to evaluate the system under wider combustion conditions including coal and biomass firing. Moreover, since an industrial boiler is generally a multi-burner system, it is also desirable to test the system through the sight-tube of an individual burner, where the existing flame detector is installed.

Finally, the work reported in this thesis offers very useful quantitative information either for a control system to automatically adjust the combustion process, or for a boiler operator to diagnose the flame state and manually regulate the process. For example, the measured flame stability and temperature and the predicted  $\text{NO}_x$  emissions can be used directly for a control system to drive a control, as they are meaningful

combustion parameters of practical relevance. The identified flame state can be used indirectly to drive a control if it is linked with a combustion parameter such as air/fuel flow rate and equivalence ratio. The indication of the occurrence of abnormal combustion events can be used to inform operators the change of combustion condition and hence immediate actions can be taken. The work reported in this thesis has demonstrated the potential of the advanced flame monitoring technique. It is envisaged that the completion of such technique will lead to a robust instrumentation system for control and diagnosis of industrial combustion processes.

## References

- [1] Y. Huang, Y. Yan, and G. Riley, "Vision-based measurement of temperature distribution in a 500-kW model furnace using the two-colour method," *Measurement*, vol. 28, pp. 175-183, 2000.
- [2] H. C. Bheemul, G. Lu, and Y. Yan, "Three-dimensional visualization and quantitative characterization of gaseous flames," *Measurement Science and Technology*, vol. 13, pp. 1643-1650, Oct 2002.
- [3] G. Lu, Y. Yan, and M. Colechin, "A digital imaging based multifunctional flame monitoring system," *IEEE Transactions on Instrumentation and Measurement*, vol. 53, pp. 1152-1158, 2004.
- [4] P. M. Brisley, G. Lu, Y. Yan, and S. Cornwell, "Three-dimensional temperature measurement of combustion flames using a single monochromatic CCD camera," *IEEE Transactions on Instrumentation and Measurement*, vol. 54, pp. 1417-1421, 2005.
- [5] G. Guillermo, G. Lu, and Y. Yan, "Three-dimensional tomographic reconstruction of the luminosity distribution of a combustion flame," *IEEE Transactions on Instrumentation and Measurement*, vol. 56, pp. 1300-1306, 2007.
- [6] J. Krabicka, G. Lu, and Y. Yan, "Profiling and characterization of flame radicals by combining spectroscopic imaging and neural network techniques," *IEEE Transactions on Instrumentation and Measurement*, vol. 60, pp. 1854-1860, 2011.
- [7] Y. Huang, Y. Yan, G. Lu, and A. Reed, "On-line flicker measurement of gaseous flames by images processing and spectral analysis," *Measurement Science and Technology*, vol. 10, pp. 726-733, 1999.
- [8] G. Lu, Y. Yan, and D. D. Ward, "Advanced monitoring, characterisation and evaluation of gas-fired flames in a utility boiler," *Journal of the Institute of Energy*, vol. 73, pp. 43-49, 2000.
- [9] H. C. Bheemul, G. Lu, and Y. Yan, "Digital imaging-based three-dimensional characterization of flame front structures in a turbulent flame," *IEEE Transactions on Instrumentation and Measurement*, vol. 54, pp. 1073-1078, 2005.

- [10] Y. Yan, G. Lu, and M. Colechin, "Monitoring and characterisation of pulverised coal flames using digital imaging techniques," *Fuel*, vol. 81, pp. 647-655, 2002.
- [11] G. Lu and Y. Yan, "Temperature profiling of pulverized coal flames using multicolor pyrometric and digital imaging techniques," *IEEE Transactions on Instrumentation and Measurement*, vol. 55, pp. 1303-1308, 2006.
- [12] G. Lu, Y. Yan, M. Colechin, and R. Hill, "Monitoring of oscillatory characteristics of pulverized coal flames through image processing and spectral analysis," *IEEE Transactions on Instrumentation and Measurement*, vol. 55, pp. 226-231, 2006.
- [13] G. Lu, Y. Yan, S. Cornwell, M. Whitehouse, and G. Riley, "Impact of co-firing coal and biomass on flame characteristics and stability," *Fuel*, vol. 87, pp. 1133-1140, 2008.
- [14] J. Smart, G. Lu, Y. Yan, and G. Riley, "Characterisation of an oxy-coal flame through digital imaging," *Combustion and Flame*, vol. 157, pp. 1132-1139, 2010.
- [15] W. Wojcik, A. Kotyra, P. Komada, and T. Golec, "Detection of combustion instabilities using the wavelet transform in industrial conditions," in *Proceedings of SPIE*, 2002, pp. 72-76.
- [16] A. Fichera, C. Losenno, and A. Pagano, "Experimental analysis of thermo-acoustic combustion instability," *Applied Energy*, vol. 70, pp. 179-191, 2001.
- [17] A. R. Jones, "Flame failure detection and modern boilers," *Journal of Physics E: Scientific Instruments*, vol. 21, pp. 921-928, 1988.
- [18] R. Khatami and Y. A. Levendis, "On the deduction of single coal particle combustion temperature from three-color optical pyrometry," *Combustion and Flame*, vol. 158, pp. 1822-1836, 2011.
- [19] J. Ballester and T. Garcí'a-Armingol, "Diagnostic techniques for the monitoring and control of practical flames," *Progress in Energy and Combustion Science*, vol. 36, pp. 375-411, 2010.
- [20] J. S. Gaffney and N. A. Marley, "The impacts of combustion emissions on air quality and climate – From coal to biofuels and beyond," *Atmospheric Environment*, vol. 43, pp. 23-36, 2009.

- [21] E. Ikonen, K. Najim, and U. Kortela, "Neuro-fuzzy modelling of power plant flue-gas emissions," *Engineering Applications of Artificial Intelligence*, vol. 13, pp. 705-717, 2000.
- [22] G. Lu, "Advanced monitoring, characterisation and evaluation of fossil fuel fired flames," Ph.D. Thesis, The University of Greenwich, UK, 2000.
- [23] L. Zimmer, S. Tachibana, T. Yamamoto, Y. Kurosawa, and K. Suzuki, "Evaluation of chemiluminescence as sensor for lean premixed combustion," presented at the 4th Symposium on Smart Control of Turbulence, 2003.
- [24] D. Gil and M. Johnsson, "Using support vector machines in diagnoses of urological dysfunctions," *Expert Systems with Applications*, vol. 37, pp. 4713-4718, 2010.
- [25] W. Tao and H. Burkhardt, "Vision-guided flame control using fuzzy logic and neural networks," *Particle and Particle Systems Characterization*, vol. 12, pp. 87-94, 1995.
- [26] A. Cessou, C. Maurey, and D. Stepowski, "Parametric and statistical investigation of the behavior of a lifted flame over a turbulent free-jet structure," *Combustion and Flame*, vol. 137, pp. 458-477, 2004.
- [27] F. Parsinejad, J. C. Keck, and H. Metghalchi, "On the location of flame edge in Shadowgraph pictures of spherical flames: a theoretical and experimental study," *Experiments in Fluids*, vol. 43, pp. 887-894, 2007.
- [28] H. T. Bookey, A. I. Bishop, M. N. Shneider, and P. F. Barker, "Narrow-band coherent Rayleigh scattering," *Journal of Raman Spectroscopy*, vol. 37, pp. 655-662, 2006.
- [29] J. V. Pastor, J. M. García, J. M. Pastor, and J. E. Buitrago, "Analysis of calibration techniques for laser-induced incandescence measurements in flames," *Measurement Science and Technology*, vol. 17, pp. 3279-3288, 2006.
- [30] V. Stamatov and L. Stamatova, "A Mie scattering investigation of the effect of strain rate on soot formation in precessing jet flames," *Flow, Turbulence and Combustion*, vol. 76, pp. 279-289, 2006.
- [31] D.-Y. Zhang and H.-C. Zhou, "Temperature measurement by holographic interferometry for non-premixed ethylene-air flame with a series of state relationships," *Fuel*, vol. 86, pp. 1552-1559, 2007.

- [32] C.-C. Chang and C.-J. Lin, "LIBSVM : a library for support vector machines," *ACM Transactions on Intelligent Systems and Technology*, vol. 2, pp. 1-27, 2011.
- [33] K. Kohse-Höinghaus, R. S. Barlow, M. Aldén, and J. Wolfrum, "Combustion at the focus: laser diagnostics and control," *Proceedings of the Combustion Institute*, vol. 30, pp. 89-123, 2005.
- [34] J. G. Lee and D. A. Santavicca, "Experimental diagnostics for the study of combustion instabilities in lean premixed combustors," *Journal of Propulsion and Power*, vol. 19, pp. 735-750, 2003.
- [35] M. Alden, J. Bood, Z. S. Li, and M. Richter, "Visualization and understanding of combustion processes using spatially and temporally resolved laser diagnostic techniques," *Proceedings of the Combustion Institute*, vol. 33, pp. 69-97, 2011.
- [36] R. S. Barlow, "Laser diagnostics and their interplay with computations to understand turbulent combustion," *Proceedings of the Combustion Institute*, vol. 31, pp. 49-75, 2007.
- [37] S. Y. Lee, S. Seo, J. C. Broda, S. Pal, and R. J. Santoro, "An experimental estimation of mean reaction rate and flame structure during combustion instability in a lean premixed gas turbine combustor," *Proceedings of the Combustion Institute*, vol. 28, pp. 775-782, 2000.
- [38] G. P. Smith, J. Luque, C. Park, J. B. Jeffries, and D. R. Crosley, "Low pressure flame determinations of rate constants for OH(A) and CH(A) chemiluminescence," *Combustion and Flame*, vol. 131, pp. 59-69, 2002.
- [39] W. Meier, P. Weigand, X. R. Duan, and R. Giezendanner-Thoben, "Detailed characterization of the dynamics of thermoacoustic pulsations in a lean premixed swirl flame," *Combustion and Flame*, vol. 150, pp. 2-26, 2007.
- [40] H. Stadler, M. Förster, and R. Kneer, "Experimental investigation of CH\* chemiluminescence in an oxyfuel flame," presented at the Third European Combustion Meeting, 2007.
- [41] H. Zhao and N. Ladommatos, "Optical diagnostics for soot and temperature measurement in diesel engines," *Progress in Energy and Combustion Science*, vol. 24, pp. 221-255, 1998.
- [42] S. Simonini, S. J. Elston, and C. R. Stone, "Soot temperature and concentration measurements from colour charge coupled device camera images using a three-

- colour method," *Proceedings of the Institution of Mechanical Engineers, Part C: Journal of Mechanical Engineering Science*, vol. 215, pp. 1041-1052, 2001.
- [43] T. L. Berry Yelverton and W. L. Roberts, "Soot surface temperature measurements in pure and diluted flames at atmospheric and elevated pressures," *Experimental Thermal and Fluid Science*, vol. 33, pp. 17-22, 2008.
- [44] G. Lu, Y. Yan, G. Riley, and H. C. Bheemul, "Concurrent measurement of temperature and soot concentration of pulverized coal flames," *IEEE Transactions on Instrumentation and Measurement*, vol. 51, pp. 990-995, 2002.
- [45] Y. A. Levendis, K. R. Estrada, and H. C. Hottel, "Development of multicolor pyrometers to monitor the transient response of burning carbonaceous particles," *Review of Scientific Instruments*, vol. 63, pp. 3608-3622, 1992.
- [46] T. Panagiotou, Y. Levendis, and M. Delichatsios, "Measurements of particle flame temperatures using three-color optical pyrometry," *Combustion and Flame*, vol. 104, pp. 272-287, 1996.
- [47] H. Yu and J. F. Macgregor, "Monitoring flames in an industrial boiler using multivariate image analysis," *American Institute of Chemical Engineers*, vol. 50, pp. 1474-1483, 2004.
- [48] G. Szatvanyi, C. Duchesne, and G. Bartolacci, "Multivariate image analysis of flames for product quality and combustion control in rotary kilns," *Industrial and Engineering Chemistry Research*, vol. 45, pp. 4706-4715, Jun 21 2006.
- [49] H. W. Huang and Y. Zhang, "Flame colour characterization in the visible and infrared spectrum using a digital camera and image processing," *Measurement Science and Technology*, vol. 19, p. 9, 2008.
- [50] K. Sujatha, N. Pappa, and A. Kalaivani, "Combustion quality estimation in power station boilers using median threshold clustering algorithms," *International Journal of Engineering Science and Technology*, vol. 2, pp. 2623-2631, 2010.
- [51] F. Wang, X. J. Wang, Z. Y. Ma, J. H. Yan, Y. Chi, C. Y. Wei, M. J. Ni, and K. F. Cen, "The research on the estimation for the NO<sub>x</sub> emissive concentration of the pulverized coal boiler by the flame image processing technique," *Fuel*, vol. 81, pp. 2113-2120, 2002.

- [52] G. Lu, Y. Yan, Y. Huang, and A. Reed, "An intelligent vision system for monitoring and control of combustion flames," *Measurement and Control*, vol. 32, pp. 164-168, 1999.
- [53] Z. W. Jiang, Z. X. Luo, and H. C. Zhou, "A simple measurement method of temperature and emissivity of coal-fired flames from visible radiation image and its application in a CFB boiler furnace," *Fuel*, vol. 88, pp. 980-987, 2009.
- [54] L. Xu and Y. Yan, "A new flame monitor with triple photovoltaic cells," *IEEE Transactions on Instrumentation and Measurement*, vol. 55, pp. 1416-1421, 2006.
- [55] L. Xu, Y. Yan, S. Cornwell, and G. Riley, "On-line fuel identification using digital signal processing and fuzzy inference techniques," *IEEE Transactions on Instrumentation and Measurement*, vol. 53, pp. 1316-1320, Aug 2004.
- [56] L. Xu, Y. Yan, S. Cornwell, and G. Riley, "Online fuel tracking by combining principal component analysis and neural network techniques," *IEEE Transactions on Instrumentation and Measurement*, vol. 54, pp. 1640-1645, 2005.
- [57] S. Su, J. H. Pohl, D. Holcombe, and J. A. Hart, "Techniques to determine ignition, flame stability and burnout of blended coals in p.f. power station boilers," *Progress in Energy and Combustion Science*, vol. 27, pp. 75-98, 2001.
- [58] X. Paubel, A. Cessou, D. Honore, L. Vervisch, and R. Tsiava, "A flame stability diagram for piloted non-premixed oxycombustion of low calorific residual gases," *Proceedings of the Combustion Institute*, vol. 31, pp. 3385-3392, 2007.
- [59] C.-H. Hwang, S. Lee, J.-H. Kim, and C.-E. Lee, "An experimental study on flame stability and pollutant emission in a cyclone jet hybrid combustor," *Applied Energy*, vol. 86, pp. 1154-1161, 2009.
- [60] C.-E. Lee and C.-H. Hwang, "An experimental study on the flame stability of LFG and LFG-mixed fuels," *Fuel*, vol. 86, pp. 649-655, 2007.
- [61] C.-E. Lee, C.-H. Hwang, and S.-C. Hong, "Proposal and validation of a new type of flame stability diagram for partially premixed flames," *Fuel*, vol. 87, pp. 3687-3693, 2008.
- [62] D. Y. Kiran and D. P. Mishra, "Experimental studies of flame stability and emission characteristics of simple LPG jet diffusion flame," *Fuel*, vol. 86, pp. 1545-1551, 2007.

- [63] W. B. Ng, K. J. Syed, and Y. Zhang, "The study of flame dynamics and structures in an industrial-scale gas turbine combustor using digital data processing and computer vision techniques," *Experimental Thermal and Fluid Science*, vol. 29, pp. 715-723, 2005.
- [64] J. F. MacGregor and T. Kourti, "Statistical process control of multivariate processes," *Control Engineering Practice*, vol. 3, pp. 403-414, 1995.
- [65] S. Bersimis, S. Psarakis, and J. Panaretos, "Multivariate statistical process control charts: an overview," *Quality and Reliability Engineering International*, vol. 23, pp. 517-543, 2007.
- [66] J.-M. Lee, C. Yoo, and I.-B. Lee, "Statistical monitoring of dynamic processes based on dynamic independent component analysis," *Chemical Engineering Science*, vol. 59, pp. 2995-3006, 2004.
- [67] M. J. Zuo, J. Lin, and X. Fan, "Feature separation using ICA for a one-dimensional time series and its application in fault detection," *Journal of Sound and Vibration*, vol. 287, pp. 614-624, 2005.
- [68] D. Lieftucht, U. Kruger, and G. W. Irwin, "Improved reliability in diagnosing faults using multivariate statistics," *Computers and Chemical Engineering*, vol. 30, pp. 901-912, 2006.
- [69] S. Joe Qin, "Statistical process monitoring: basics and beyond," *Journal of Chemometrics*, vol. 17, pp. 480-502, 2003.
- [70] T. Kourti, "Application of latent variable methods to process control and multivariate statistical process control in industry," *International Journal of Adaptive Control and Signal Processing*, vol. 19, pp. 213-246, 2005.
- [71] J.-H. Cho, J.-M. Lee, S. W. Choi, D. Lee, and I.-B. Lee, "Fault identification for process monitoring using kernel principal component analysis," *Chemical Engineering Science*, vol. 60, pp. 279-288, 2005.
- [72] A. Simoglou, E. B. Martin, and A. J. Morris, "Multivariate statistical process control of an industrial fluidised-bed reactor," *Control Engineering Practice*, vol. 8, pp. 893-909, 2000.
- [73] J. Zhao, J. Huang, and W. Sun, "On-line early fault detection and diagnosis of municipal solid waste incinerators," *Waste Management*, vol. 28, pp. 2406-2414, 2008.

- [74] G. Tavares, Z. Zsigraiova, V. Semiao, and M. d. G. Carvalho, "Monitoring, fault detection and operation prediction of MSW incinerators using multivariate statistical methods," *Waste Management*, vol. 31, pp. 1635-1644, 2011.
- [75] K. Li, S. Thompson, P. Wieringa, J. Peng, and G. Duan, "Neural networks and genetic algorithms can support human supervisory control to reduce fossil fuel power plant emissions," *Cognition, Technology and Work*, vol. 5, pp. 107-126, 2003.
- [76] M. Shakil, M. Elshafei, M. A. Habib, and F. A. Maleki, "Soft sensor for NO<sub>x</sub> and O<sub>2</sub> using dynamic neural networks," *Computers and Electrical Engineering*, vol. 35, pp. 578-586, 2009.
- [77] S. Tronci, R. Baratti, and A. Servida, "Monitoring pollutant emissions in a 4.8 MW power plant through neural network," *Neurocomputing*, vol. 43, pp. 3-15, 2002.
- [78] A. L. Ahmad, I. A. Azid, A. R. Yusof, and K. N. Seetharamu, "Emission control in palm oil mills using artificial neural network and genetic algorithm," *Computers and Chemical Engineering*, vol. 28, pp. 2709-2715, 2004.
- [79] G. Ferretti and L. Piroddi, "Estimation of NO<sub>x</sub> emissions in thermal power plants using neural networks," *Journal of Engineering for Gas Turbines and Power*, vol. 123, pp. 465-471, 2001.
- [80] R. Hernández and J. Ballester, "Flame imaging as a diagnostic tool for industrial combustion," *Combustion and Flame*, vol. 155, pp. 509-528, 2008.
- [81] M. G. Allen, C. T. Butler, S. A. Johnson, E. Y. Lo, and F. Russo, "An imaging neural network combustion control system for utility boiler applications," *Combustion and Flame*, vol. 94, pp. 205-214, 1993.
- [82] H. Bae, S. Kim, B.-H. Wang, M. H. Lee, and F. Harashima, "Flame detection for the steam boiler using neural networks and image information in the Ulsan steam power generation plant," *IEEE Transactions on Industrial Electronics*, vol. 53, pp. 338-348, 2006.
- [83] H. D. Cheng, X. H. Jiang, Y. Sun, and J. L. Wang, "Color image segmentation: advances and prospects," *Pattern Recognition*, vol. 34, pp. 2259-2281, 2001.
- [84] W. Yizhong, C. Yanhua, C. Shaohui, Z. Ping, H. Huafang, and G. Q. Huang, "Study on HSI color model-based fruit quality evaluation," in *IEEE*

- International Congress on Image and Signal Processing*, Yantai, P. R. China, 2010, pp. 2677-2680.
- [85] R. S. Ledley, M. Buas, and T. J. Golab, "Fundamentals of true-color image processing," in *Proceedings of 10th International Conference on Pattern Recognition*, 1990, pp. 791-795.
- [86] A. Graps, "An introduction to wavelets," *IEEE Computational Science & Engineering*, vol. 2, pp. 50-61, 1995.
- [87] I. Daubechies, "The wavelet transform, time-frequency localization and signal analysis," *IEEE Transactions on Information Theory*, vol. 36, pp. 961-1005, 1990.
- [88] B. Schölkopf, A. Smola, and K. R. Muller, "Nonlinear component analysis as a kernel eigenvalue problem," *Neural Computation*, vol. 10, pp. 1299-1319, 1998.
- [89] J.-M. Lee, C. Yoo, S. W. Choi, P. A. Vanrolleghem, and I.-B. Lee, "Nonlinear process monitoring using kernel principal component analysis," *Chemical Engineering Science*, vol. 59, pp. 223-234, 2004.
- [90] B. E. Boser, I. M. Guyon, and V. N. Vapnik, "A training algorithm for optimal margin classifiers," in *Proceedings of the 5th Annual Workshop on Computational Learning Theory*, Pittsburgh, USA, 1992, pp. 144-152.
- [91] C. J. C. Burges, "A tutorial on support vector machines for pattern recognition," *Data Mining and Knowledge Discovery*, vol. 2, pp. 121-167, 1998.
- [92] H. C. Hottel and F. P. Broughton, "Determination of true temperature and total radiation from luminous gas flames," *Industrial and Engineering Chemistry*, vol. 4, pp. 166-175, 1932.
- [93] ScitecInstruments. *SG01M data sheet*. Available: <http://www.scitec.uk.com>
- [94] EdmundOptics. *InGaAs photodiodes NT62-271*. Available: <http://www.edmundoptics.com>
- [95] Centronic. *General purpose silicon sensors OSD1-5T*. Available: <http://www.centronic.co.uk>
- [96] TexasInstruments. *Designing photodiode amplifier circuits with OPA128*. Available: <http://www.ti.com>
- [97] L. Xu and Y. Yan, "An Improved Algorithm for the Measurement of Flame Oscillation Frequency," *Instrumentation and Measurement, IEEE Transactions on*, vol. 56, pp. 2087-2093, 2007.

- [98] DesignSoft. *TINA*. Available: <http://www.tina.com/>
- [99] P. Stoica and R. L. Moses, *Introduction to Spectral Analysis*: Prentice-Hall, 1997.
- [100] Microchip. *dsPIC33FJ256GP710 data sheet* Available: <http://www.microchip.com>
- [101] IDS. *UI-1640SE datasheet*. Available: <http://www.ids-imaging.com>
- [102] Axiomtek. *PICO820 data sheet*. Available: <http://www.axiomtek.com>
- [103] LandAmetek. *Landcal R1500T manual*. Available: <http://www.landinst.com/products>
- [104] N. P. Laboratory, "Certificate of calibration of tungsten lamp," 1999.
- [105] A. Rebola and M. Costa, "Simultaneous reduction of NO<sub>x</sub> and particulate emissions from heavy fuel oil-fired furnaces," *Proceedings of the Combustion Institute*, vol. 29, pp. 2243-2250, 2002.
- [106] Z. A. Mansurov, "Soot formation in combustion processes (review)," *Combustion, Explosion, and Shock Waves*, vol. 41, pp. 727-744, 2005.
- [107] J. E. Jackson, *A user's guide to principal components*. New York: Wiley, 1991.
- [108] S. A. Kalogirou, "Applications of artificial neural-networks for energy systems," *Applied Energy*, vol. 67, pp. 17-35, 2000.
- [109] G. Q. P. Zhang, "Neural networks for classification: A survey," *IEEE Transactions on Systems Man and Cybernetics Part C-Applications and Reviews*, vol. 30, pp. 451-462, 2000.
- [110] MathWorks. *Neural network toolbox user's guide*. Available: <http://www.mathworks.co.uk>
- [111] T. Lieuwen, H. Torres, C. Johnson, and B. T. Zinn, "A mechanism of combustion instability in lean premixed gas turbine combustors : Internal Combustion Engines," *Journal of engineering for gas turbines and power*, vol. 123, pp. 182-189, 2001.
- [112] K. C. Schadow and E. Gutmark, "Combustion instability related to vortex shedding in dump combustors and their passive control," *Progress in Energy and Combustion Science*, vol. 18, pp. 117-132, 1992.

# Appendix 1:

## Schematic and PCB Layout of the Embedded Photodetector and Signal-Processing Board

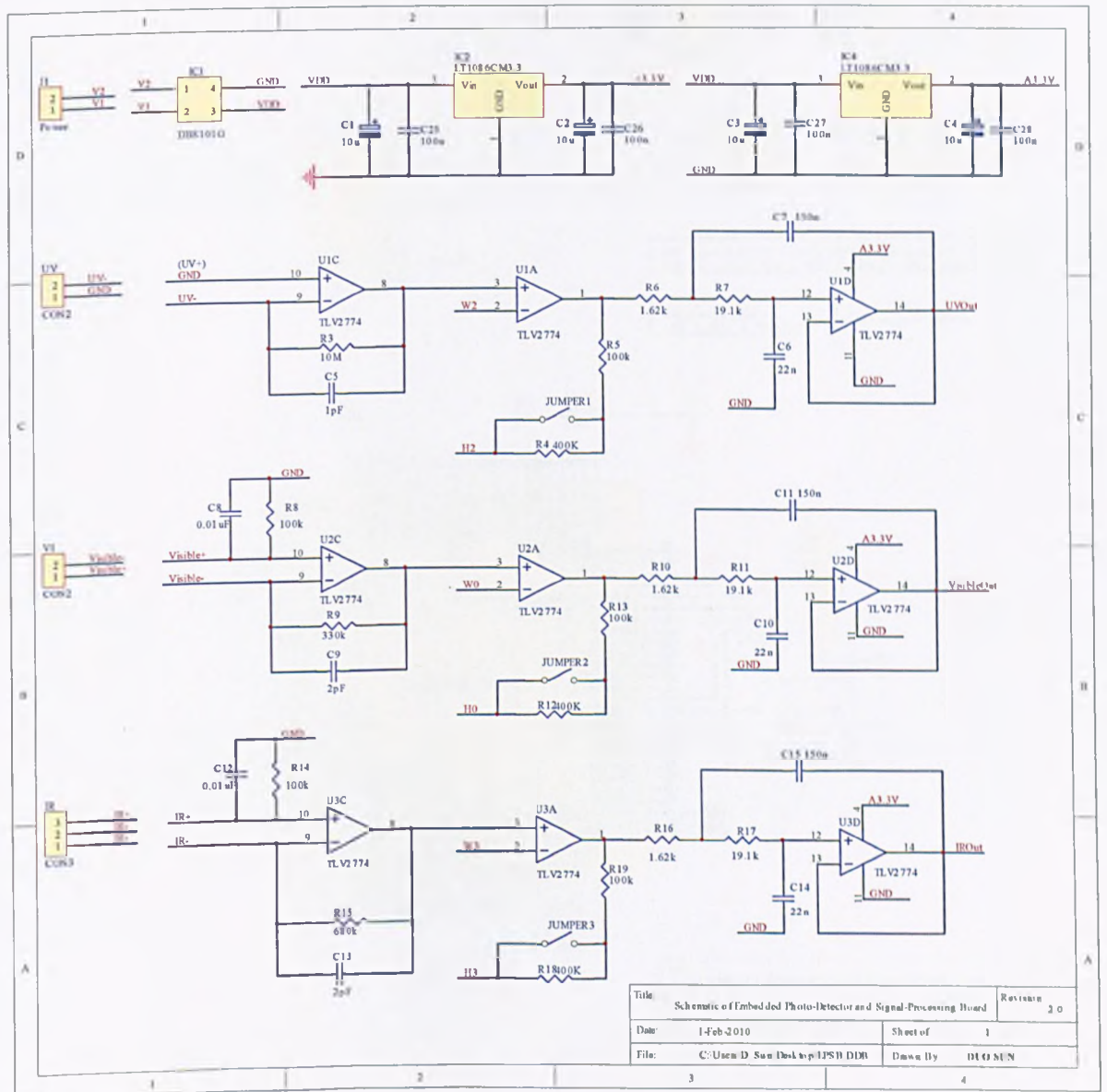


Figure A1.1 Sensor electronics schematic (1/2)

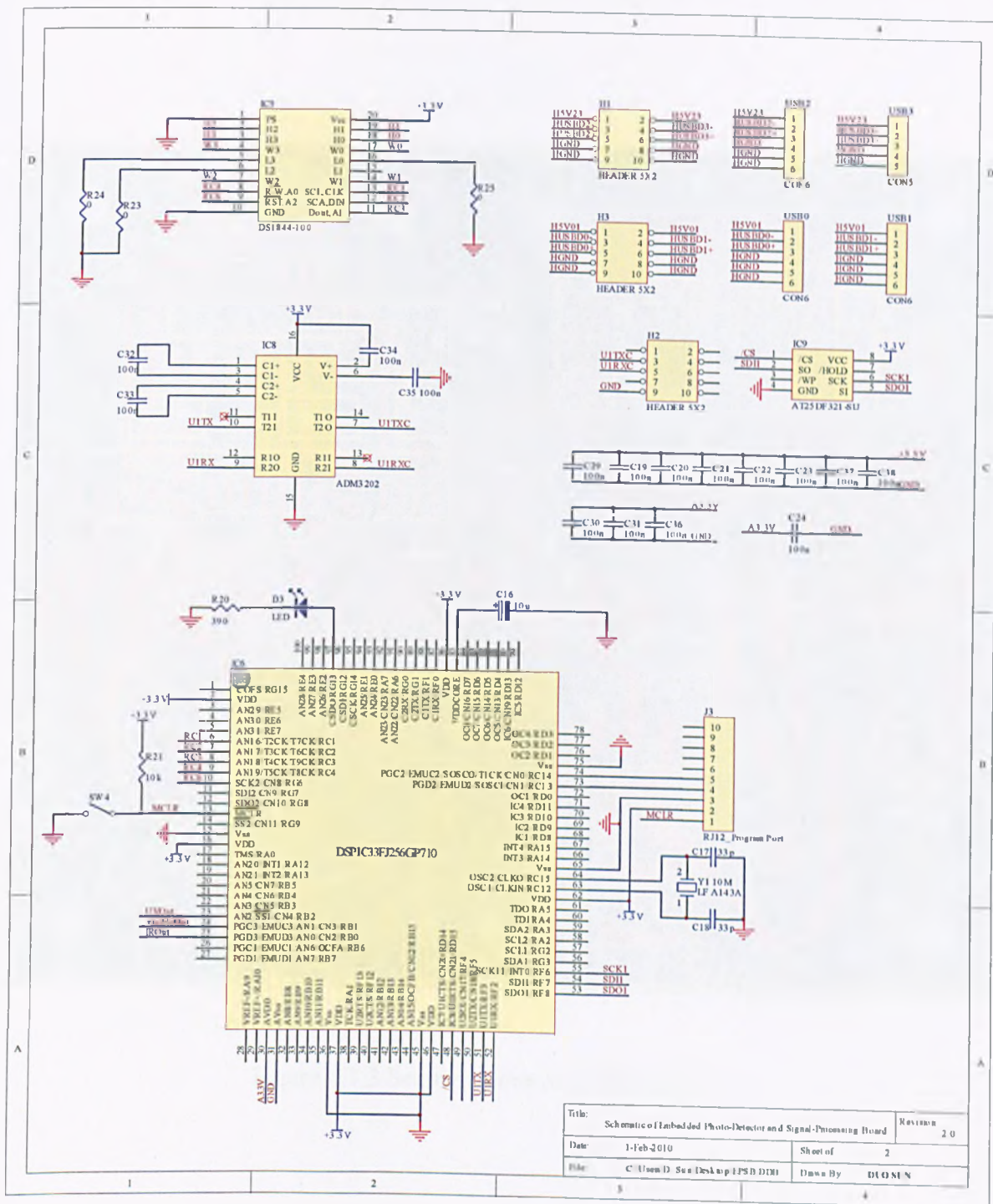


Figure A1.2 Sensor electronics schematic (2/2)

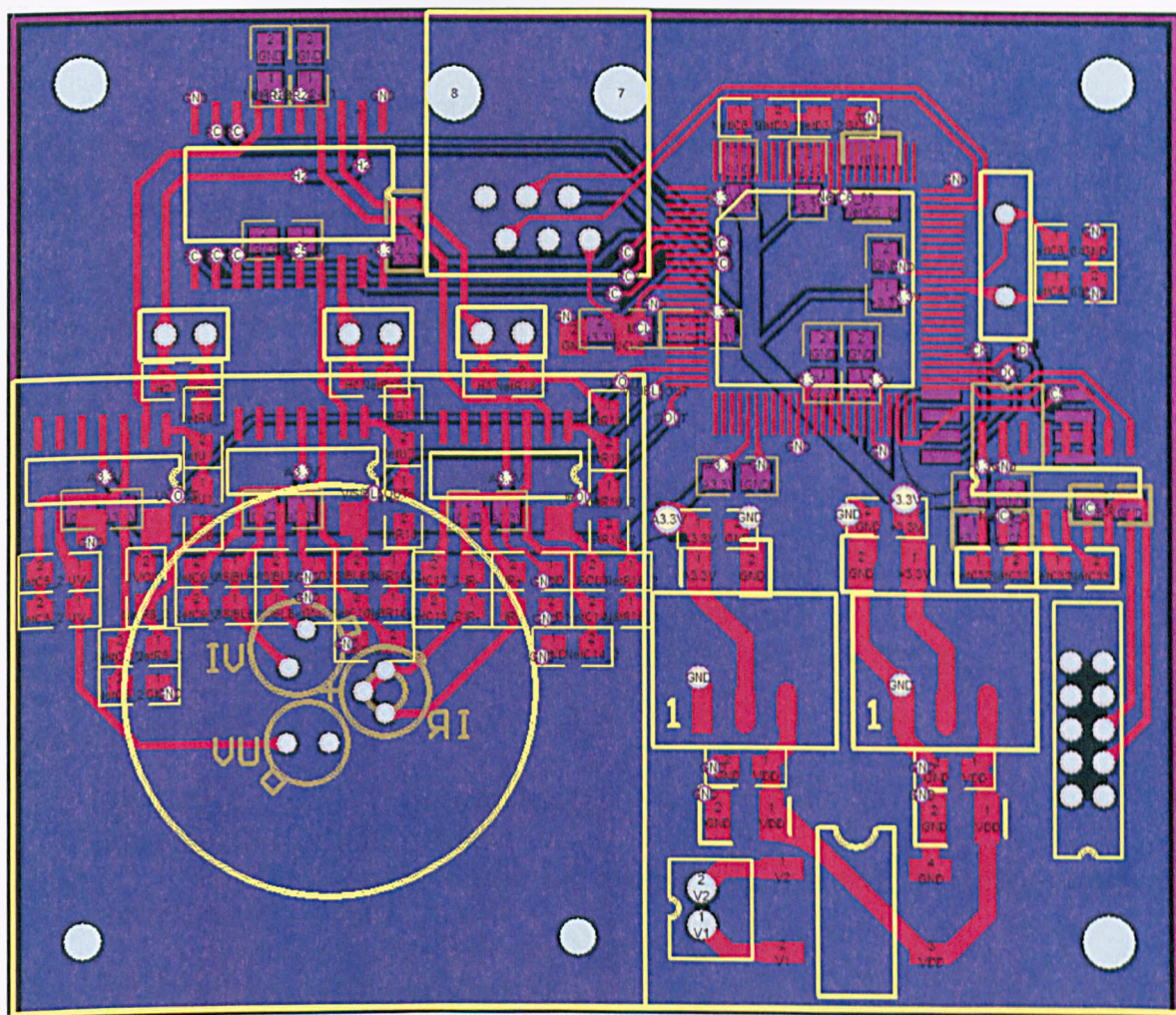


Figure A1.3 Sensor electronics PCB layout

## Appendix 2:

### Program for dsPIC Microcontroller Configuration

```

% *****%
% File name:      dspicConfiguration.c
% Synopses:      1) ADC
%                2) UART
%                3) Digital potentiometer
% Programmer:    Duo Sun, School of Engineering and Digital Arts, University of Kent
% Date:          August 1, 2011
% *****%

//***** ADC *****/

#include "p33FJ256GP710.h"
#include "dsp.h"
#include "def.h"

/* Definition of Global Variables */
fractional dmaBuffer[NUM_CHAN][DMA_BUFF_SIZE]
__attribute__((space(dma),aligned(NUM_CHAN*DMA_BUFF_SIZE*2)));

void InitAdc1(void)
{
    //AD1CON1: ADC1 Control Register1
    AD1CON1bits.ADON = 0x0;
        //setting to 1 turns on the ADC module. Keep off while changing settings
    AD1CON1bits.ADSIDL = 0x0;
        //Continue module operation in idle mode
    AD1CON1bits.ADDMABM = 0x0;
        //DMA buffers are written in Scatter/Gather mode
    AD1CON1bits.AD12B = 0x0;
        //10-bit 4-channel mode
    AD1CON1bits.FORM = 0x2;
        //For 10-bit operation:
        //11 = Signed fractional (DOUT = sddd dddd dd00 0000,s = .NOT.d<9>)
        //10 = Fractional (DOUT = dddd dddd dd00 0000)
        //01 = Signed integer (DOUT = ssss sssd dddd dddd, s = .NOT.d<9>)
        //00 = Integer (DOUT = 0000 00dd dddd dddd)
        //NB: whatever load into the adc buffer in simulation (using register
        injection) gets shifted over to the left by 6 bits when adc buffer is read

    AD1CON1bits.SSRC = 0x2;

```

```

//0x2=GP timer (Timer 3 for ADC1) compare ends sampling and starts
conversion
//0x7=internal counter ends sampling and starts conversion (auto-
convert)
AD1CON1bits.SIMSAM = 0x1;
//samples ch0-ch3 simultaneously (when CHPS=1x)
//setting SIMSAM=0 samples in sequence
AD1CON1bits.ASAM = 0x1;
//1=sampling begins immediately after last conversion is done;
//0=sampling begins when SAMP bit is set
//AD1CON1bits.SAMP = 0x0;
//1=ADC sample/hold amps are sampling,
//0=ADC sample/hold amps are holding
//AD1CON1bits.DONE = 0x0;
//ADC conversion status bit: Write '0' to clear DONE status

//AD1CON2: ADC1 Control Register2
AD1CON2bits.VCFG = 0x0;
//voltage reference is Avdd and Avss
AD1CON2bits.CSCNA = 0x0;
//input scan bit. Do not scan inputs
AD1CON2bits.CHPS = 0x2;
//0x2 converts ch0-ch3. 0x1 converts ch0 and ch1, 0x0 converts only ch0
AD1CON2bits.SMPI = 0x0;
//increments DMA address after every sample/conversion operation
AD1CON2bits.BUFG = 0x0;
//always start filling the buffer from the start address
AD1CON2bits.ALTS = 0x0;
//always uses channel input selects for sample A

//AD1CON3: ADC1 Control Register3
AD1CON3bits.ADRC = 0x0;
//clock derived from system clock
AD1CON3bits.ADCS = 0xFF;
//conversion clock select. Set TAD

//AD1CON4: ADC1 Control Register4
AD1CON4bits.DMABL = 0x6;
//Number of DMA Buffer Locations per Analog Input;
//total words of DMA buffer: 2k
//64 words of buffer to each analog input.

AD1CHS123 = 0x0000;
//ch1 to ch3 positive inputs are AN0, AN1, and AN2 respectively;
//negative input is VREFL
AD1CHS0 = 0x0006;
//ch0 positive input is AN6; negative input is VREFL;
//NB: ch0 is unused in application
AD1CSSH = 0x0000;

```

```

        //select channels for input scan. None selected since don't want scan
        AD1CSSL    = 0x0000;
        //select channels for input scan. None selected since don't want scan
        AD1PCFGH  = 0xFFFF;
        //all pins with possible analog input functions set to digital i/o
        AD1PCFGL  = 0xFFB8;
        //except the ones used for sensor inputs (AN0,AN1,AN2, and AN6)

        IFS0bits.AD1IF  = 0;    //Clear the A/D interrupt flag bit
        IEC0bits.AD1IE  = 0;    //Disable ADC1 interrupt

        AD1CON1bits.ADON = 1; //start adc
    }

void InitTmr3Adc1(void)
{
    T3CONbits.TON    = 0; //Stop timer 3

    T2CONbits.T32    = 0; //Timer2 and 3 act as one 16-bit timer

    T3CONbits.TSIDL  = 0; //continue module operation in idle mode
    T3CONbits.TGATE  = 0; //gated time accumulation disabled
    T3CONbits.TCKPS  = 0; //prescale 1:1
    T3CONbits.TCS    = 0; //internal clock source (Fcy)

    TMR3            = 0x0000;
    PR3             = 39062; //1024 samples per second

    IFS0bits.T3IF   = 0; //Clear Timer 3 interrupt
    IEC0bits.T3IE   = 0; //Disable Timer 3 interrupt

    T3CONbits.TON  = 1; //Start Timer 3
}

void InitDma0Adc1(void)
{
    // DMA0 configuration
    // Direction: Read from peripheral address 0x300 (ADC1BUF0)
    //              and write to DMA RAM
    // IRQ: ADC Interrupt

    DMA0CONbits.CHEN = 0;    // disable dma channel 0
    DMA0CONbits.SIZE = 0;    // word size data (1=byte size data)
    DMA0CONbits.DIR  = 0;    // read from peripheral address
    DMA0CONbits.HALF = 0;    // initiate block transfer complete interrupt
                                // when all of the data has been moved
    DMA0CONbits.NULLW = 0;   // don't null write
}

```

```

DMA0CONbits.AMODE = 0x2; // Peripheral indirect addressing mode
DMA0CONbits.MODE   = 0;   // 0: Continuous Ping-Pong modes disabled

DMA0REQ           = 13;    // select ADC1 as DMA request source
DMA0PAD           = 0x0300; // Point DMA to ADC1BUF0
DMA0CNT           = DMA_BUFF_SIZE*NUM_CHAN - 1;
                  // eg. 256 DMA request (4 buffers, each with 64 words)

DMA0STA = __builtin_dmaoffset(&dmaBuffer);

IFS0bits.DMA0IF   = 0;    // clear the DMA interrupt flag bit
IEC0bits.DMA0IE   = 1;    // enable DMA0 interrupts

DMA0CONbits.CHEN  = 1;
                  // now that everything is set up, enable dma channel 0
}

//***** UART *****/

#include "p33FJ256GP710.h"
#include "dsp.h"
#include "def.h"

fractional dmaUart1TxBuffer[UART1_TX_DMA_BUFF_SIZE]
__attribute__((space(dma),aligned(UART1_TX_DMA_BUFF_SIZE*2)));

void InitUart1(void)
{
    //U1MODE
    U1MODEbits.UARTEN = 0;
        // Bit15 TX, RX DISABLED, ENABLE at end of func
        //U1MODEbits.notimplemented;// Bit14
    U1MODEbits.USIDL  = 0; // Bit13 Continue in Idle
    U1MODEbits.IREN   = 0; // Bit12 No IR translation
    U1MODEbits.RTSMD  = 0;// Bit11 Flow Control Mode.
        //U1MODEbits.notimplemented;// Bit10
    U1MODEbits.UEN    = 0;
        // Bits8,9 TX,RX enabled, CTS, RTS not.
        //CTS,RTS and BCLK pins are controlled by port latches
    U1MODEbits.WAKE   = 0; // Bit7 No Wake up (since we don't sleep here)
    U1MODEbits.LPBACK = 0; // Bit6 No Loop Back
    U1MODEbits.ABAUD  = 0; // Bit5 No Autobaud (would require sending '55')
    U1MODEbits.URXINV = 0; // Bit4 Idle State = 1 (for dsPIC)
    U1MODEbits.BRGH   = 0; // Bit3 16 clocks per bit period
    U1MODEbits.PDSEL  = 0; // Bits1,2 8bit, No Parity
    U1MODEbits.STSEL  = 0; // Bit0 One Stop Bit

```

```

// Load a value into Baud Rate Generator. Example is for 9600.
U1BRG          = 21;      // 40Mhz osc, 115200 Baud
                               // = 259;      // 40Mhz osc, 9600 Baud

//U1STA
U1STAbits.UTXISEL1 = 0;
    //00 = Interrupt generated when at least one location is empty
    //in the transmit buffer
U1STAbits.UTXISEL0 = 0; //Bit13 Other half of Bit15
U1STAbits.UTXINV   = 0; //Bit14 U1TX idle state is '0'
//U1STAbits.notimplemented = 0; //Bit12
U1STAbits.UTXBRK   = 0; //Bit11 Sync break transmission is disabled
U1STAbits.UTXEN    = 0; //Bit10 Transmitter disabled
//U1STAbits.UTXBF   = 0; //Bit9 *Read Only Bit*
//U1STAbits.TRMT    = 0; //Bit8 *Read Only bit*
U1STAbits.URXISEL  = 0; //Bits6,7 Int. on character recieved
U1STAbits.ADDEN    = 0; //Bit5 Address Detect Disabled
//U1STAbits.RIDLE   = 0; //Bit4 *Read Only Bit*
//U1STAbits.PERR    = 0; //Bit3 *Read Only Bit*
//U1STAbits.OERR    = 0; //Bit1 *Read Only Bit*
//U1STAbits.URXDA   = 0; //Bit0 *Read Only Bit*
//U1STAbits.FERR    = 0; //Bit2 *Read Only Bit*

//IPC2bits.U1RXIP   = 7; //Already set in main routine
//IPC3bits.U1TXIP   = 4; //no need

IFS0bits.U1TXIF    = 0; // Clear the Transmit Interrupt Flag
IEC0bits.U1TXIE    = 0; // disable Transmit Interrupts
IFS0bits.U1RXIF    = 0; // Clear the Recieve Interrupt Flag
IEC0bits.U1RXIE    = 1; // Enable Recieve Interrupts

U1MODEbits.UARTEN  = 1; // And turn the peripheral on

U1STAbits.UTXEN    = 1;
    //The UTXEN bit should not be set until the UARTEN bit has been set;
    //otherwise,UART transmissions will not be enabled.
}

void InitDma1Uart1Tx(void)
{
    // Configure DMA Channel 1 to Uart1Tx
    // Transfer data from RAM to UART
    // One-Shot mode
    // Register Indirect with Post-Increment
    // Using single buffer
    // Transfer byte

    DMA1CONbits.CHEN = 0; //disable dma channel 1
    DMA1CONbits.SIZE = 1; //Data transfer size: Byte

```

```

DMA1CONbits.DIR    = 1; //From DPSRAM to peripheral address
DMA1CONbits.HALF  = 0;
    //initiate block transfer complete interrupt
    //when all of the data has been moved
DMA1CONbits.NULLW = 0; //don't null write
DMA1CONbits.AMODE = 0; //Post-Increment
DMA1CONbits.MODE  = 1; //One-Shot, Ping-Pong modes disabled

DMA1REQ = 0x000c    // Select UART1 Transmitter
DMA1STA = __builtin_dmaoffset(dmaUart1TxBuffer);
DMA1PAD = (volatile unsigned int) &U1TXREG;

IFS0bits.DMA1IF = 0;    //Clear DMA1 Interrupt Flag
IEC0bits.DMA1IE = 1;    //Enable DMA1 interrupt
}

void SendDataUart1(fractional* pData, unsigned int lengthWord)
    //lengthWord should not exceed 512 and UART1_TX_DMA_BUFF_SIZE
{
    unsigned int i=0;

    if (lengthWord>UART1_TX_DMA_BUFF_SIZE)
    {
        lengthWord = UART1_TX_DMA_BUFF_SIZE;
    }
    for (i=0; i<lengthWord; i++)
    {
        dmaUart1TxBuffer[i]=*(pData+i);
    }

    DMA1CNT = lengthWord * 2 - 1; //Number of bytes needed to be transmitted

    DMA1CONbits.CHEN = 1;    //Enable dma channel 1
    DMA1REQbits.FORCE = 1;    //Manual start dma transfer

} //Least byte of a word will be sent firstly, then the Most byte.

//***** Digital potentiometer *****//

#include "p33FJ256GP710.h"
#include "def.h"
#include "delay.h"

void WriteDigitalRes(unsigned int rValue, unsigned int rIndex)
    //rValue: 0 to 63; rIndex: 0(Visible), 2(UV) or 3(IR)
{

```

```

if (rValue>63)
    //rValue must be in the range 0 to 63 for the DS1844-100 digital resistor
    {
        rValue = 63;
    }
else if (rValue<0)
    {
        rValue = 0;
    }

rValue = 63 - rValue;
    //Due to the way the resistor is set up in the circuit,
    //lower values producing higher gain,
    //this line makes higher values produce a higher gain.

rIndex = rIndex & 0b11;

RV1CLK    = 0;    //a data bit is latched on a 0 to 1 transition of CLK signal
RV1RST    = 0;    //communication starts with a 0 to 1 transition on this pin.
RV1RW     = 0;    //0 = mode to write resistor value ,
                //1 = mode to read resistor value
                //Must be stable for more than 30ns before 0 to 1
                //transition of RV1RST

Delay_us(1);

RV1RST    = 1;

//Select Potentiometer
if (rIndex & 0b10)
    {
        RV1DIN = 1
    }
else
    {
        RV1DIN = 0;
    }

Delay_us(1);
RV1CLK=1;
Delay_us(1);
RV1CLK=0;

if (rIndex & 0b01)
    {
        RV1DIN = 1;
    }
else
    {
        RV1DIN = 0;
    }

```

```
}
Delay_us(1);
RV1CLK=1;
Delay_us(1);
RV1CLK=0;

//Set Wiper Value
if (rValue & 0b100000)
{
    RV1DIN = 1;
}
else
{
    RV1DIN = 0;
}
Delay_us(1);
RV1CLK=1;
Delay_us(1);
RV1CLK=0;

if (rValue & 0b10000)
{
    RV1DIN = 1;
}
else
{
    RV1DIN = 0;
}
Delay_us(1);
RV1CLK=1;
Delay_us(1);
RV1CLK=0;

if (rValue & 0b1000)
{
    RV1DIN = 1;
}
else
{
    RV1DIN = 0;
}
Delay_us(1);
RV1CLK=1;
Delay_us(1);
RV1CLK=0;

if (rValue & 0b100)
{
    RV1DIN = 1;
```

```

    }
    else
    {
        RV1DIN = 0;
    }
    Delay_us(1);
    RV1CLK=1;
    Delay_us(1);
    RV1CLK=0;

    if (rValue & 0b10)
    {
        RV1DIN = 1;
    }
    else
    {
        RV1DIN = 0;
    }
    Delay_us(1);
    RV1CLK=1;
    Delay_us(1);
    RV1CLK=0;

    if (rValue & 0b1)
    {
        RV1DIN = 1;
    }
    else
    {
        RV1DIN = 0;
    }
    Delay_us(1);
    RV1CLK=1;
    Delay_us(1);
    RV1CLK=0;

    Delay_us(1);
    RV1RST = 0;
}

unsigned int ReadDigitalRes(unsigned int rIndex)
{
    unsigned int rVal[4]={0,0,0,0};
    unsigned int rValIndexed;
    unsigned i, j;

```

```

RV1CLK    = 0;
           //a data bit is valid on the falling edge of cloc pulse after maximum 20ns
RV1RST    = 0;
           //communication starts with a 0 to 1 transition on this pin.
RV1RW     = 1;
           //0 = mode to write resistor value , 1 = mode to read resistor value
           //Must be stable for more than 30ns before 0 to 1 transition of RV1RST
Delay_us(1);

RV1RST    = 1;

Delay_us(1);

for (i=0; i<4; i++)
{
    for (j=7; j>0; j--)
    {
        RV1CLK    = 1;
        Delay_us(1);
        RV1CLK    = 0;
        Delay_us(1);
        rVal[i] = rVal[i]|RV1DOUT;
        rVal[i] = rVal[i]<<1;
    }
    RV1CLK    = 1;
    Delay_us(1);
    RV1CLK    = 0;
    Delay_us(1);
    rVal[i] = rVal[i]|RV1DOUT;
}

RV1RST    = 0;

rValIndexed = rVal[rIndex] & 0b00111111;

return 63-rValIndexed;
}

```

## Appendix 3:

### Program for Computation of Oscillation Frequency

```
% *****%
% File name:      CalculateOscillationFrequency.c
% Synopses:      1) Remove DC
%                2) Perform FFT
%                3) Compute power spectral density
%                4) Derive oscillation frequency
% Programmer:    Duo Sun, School of Engineering and Digital Arts, University of Kent
% Date:          August 1, 2011
% *****%
```

```
#include "p33FJ256GP710.h"
#include "dsp.h"
#include "def.h"
#include "main.h"
#include "twiddlefactors.h"
```

```
fractional ComputeOscillationFrequency(fractional *pBuffer)
```

```
{
    unsigned int i = 0;
    int peakFrequencyBi = 0;    /* Declare post-FFT variables to compute the */
    unsigned long peakFrequency = 0; /* frequency of the largest component */
    unsigned int m = 0;
    unsigned int n = 0;
    fractional flicker          = 0;
    fractional *pFractional;
    unsigned long tempVar1      = 0; // unsigned long : 32bit
    unsigned long sumA          = 0;
    unsigned long sumB          = 0;
    unsigned long sumC          = 0;
    fractional tempDC           = 0;

    // Move data from xbuffer to ymemory, scale it to [0,+0.5]
    for(i=0; i<FFT_BLOCK_LENGTH; i++)
    {
        sigCmpx[i].real = (*pBuffer)>>2;
        sigCmpx[i].real = sigCmpx[i].real&0x3FFF;
        sigCmpx[i].imag = 0;
        pBuffer++;
    }
}
```

```

// Calculate DC
for(i=0; i<FFT_BLOCK_LENGTH; i++)
{
    sumC = sumC + sigCmpx[i].real;
}
tempDC = sumC/FFT_BLOCK_LENGTH;

// Remove DC
for(i=0; i<FFT_BLOCK_LENGTH; i++)
{
    sigCmpx[i].real = sigCmpx[i].real - tempDC;
}

// Perform FFT operation
FFTComplexIP (LOG2_BLOCK_LENGTH, &sigCmpx[0], (fractcomplex *)
__builtin_psvoffset(&twiddleFactors[0]), (int)
__builtin_psvpage(&twiddleFactors[0]));

// Store output samples in bit-reversed order of their addresses
BitReverseComplex (LOG2_BLOCK_LENGTH, &sigCmpx[0]);

// Compute the square magnitude of the complex FFT output array
SquareMagnitudeCplx(FFT_BLOCK_LENGTH, &sigCmpx[0],
&sigCmpx[0].real);

// Remove DC component
sigCmpx[0].real = 0;

// Find the frequency Bin that has the largest energy*/
VectorMax(FFT_BLOCK_LENGTH/2, &sigCmpx[0].real,
&peakFrequencyBin);

// Compute the frequency (in Hz) of the largest spectral component
peakFrequency = peakFrequencyBin;
peakFrequency =
(peakFrequency*SAMPLING_RATE)/FFT_BLOCK_LENGTH;

// Compute the denominator of oscillation frequency computation
// SUMB = SUM(pi)
pFractional = &sigCmpx[0].real;
n = 0;
sumB = 0;

for (i=0; i<FFT_BLOCK_LENGTH/2; i++)
{
    tempVar1 = *pFractional >> n;
    if (sumB&0x80000000) // in case of overflow.
    {
        n++;
    }
}

```

```

        sumB = sumB>>1;
        tempVar1 = tempVar1 >> 1;
        sumB = sumB + tempVar1;
    }
    else
    {
        sumB = sumB + tempVar1;
    }
    pFractional++;
}

// Compute the numerator of flicker computation -- SUMA = SUM(pi*fi)
pFractional = &sigCmpx[0].real;
m = 0;
sumA = 0;

for (i=0; i<FFT_BLOCK_LENGTH/2; i++)
{
    tempVar1 = *pFractional;
    tempVar1 = tempVar1*i*10;
    tempVar1 = tempVar1 >> m;
    if (sumA&0x80000000) // in case of overflow
    {
        m++;
        sumA = sumA>>1;
        tempVar1 = tempVar1 >> 1;
        sumA = sumA + tempVar1;
    }
    else
    {
        sumA = sumA + tempVar1;
    }
    pFractional++;
}

// Compute flicker = numerator/denominator
// SUMA/SUMB = SUM(pi*fi)/SUM(pi);
if (m>=n)
{
    sumB = sumB >> (m - n);
}
else if (m<n)
{
    // when it happens, something must be wrong!!
}

flicker = ((sumA/sumB)*SAMPLING_RATE)/FFT_BLOCK_LENGTH;
return flicker; // The real oscillation frequency equals to 1/10 of variable flicker.
}

```

## Appendix 4:

### Program for Computation of Flame Stability Index

```
% *****%
% File name:      FlameStabilityIndexMeasurement.cpp
% Synopses:      1) Convert RGB into HSI colour space
%                2) Extract flame parameters
%                3) Data fusion
% Programmer:    Duo Sun, School of Engineering and Digital Arts, University of Kent
% Date:          August 1, 2011
% *****%
```

```
void CFlameMonitoringDlg::CalculateFlameStabilityIndex(IplImage *Img)
{
```

```
    int height    = Img->height;
    int width     = Img->width;
    int step      = Img->widthStep/sizeof(uchar);
    int channels   = Img->nChannels;
    uchar* pdata  = (uchar *)Img->imageData;
```

```
    if (m_pImgH != NULL)
    {
        delete []m_pImgH;
        m_pImgH = NULL;
    }
```

```
    if (m_pImgS != NULL)
    {
        delete []m_pImgS;
        m_pImgS = NULL;
    }
```

```
    if (m_pImgI != NULL)
    {
        delete []m_pImgI;
        m_pImgI = NULL;
    }
```

```
    m_pImgH = new float[height*width];
    m_pImgS = new float[height*width];
    m_pImgI = new float[height*width];
```

```
    int jRow,iColumn;
```

```

unsigned char b,g,r;
float m,gn,bn;
float h,s,i;
float hSum,sSum,iSum;

// Convert RGB to HSI colour space
for(jRow=0;jRow<height;jRow++)
{
    for(iColumn=0;iColumn<width;iColumn++) //B,G,R
    {
        b = unsigned char(pdata[jRow*step+iColumn*channels+0]);
        g = unsigned char(pdata[jRow*step+iColumn*channels+1]);
        r = unsigned char(pdata[jRow*step+iColumn*channels+2]);

        if (b<=THRESHOLD)||g<=THRESHOLD)||r<=THRESHOLD)
        {
            pdata[jRow*step+iColumn*channels+0] = 0; //B
            pdata[jRow*step+iColumn*channels+1] = 0; //G
            pdata[jRow*step+iColumn*channels+2] = 0; //R

            b = 0;
            g = 0;
            r = 0;
        }

        if ((b == 0)&&(g == 0)&&(r == 0))
        {
            h = 0;
            s = 0;
            i = 0;
        }
        else
        {
            m = static_cast<float>(r)/static_cast<float>(r + g + b);
            gn = static_cast<float>(g)/static_cast<float>(r + g + b);
            bn = static_cast<float>(b)/static_cast<float>(r + g + b);

            if (bn <= gn)
            {
                h = acos(0.5*((rn-gn)+(rn-bn))/sqrt((rn-gn)*(rn-gn)+(rn-bn)*(gn-bn)));
            }
            else
            {
                h = 2*PI - acos(0.5*((rn-gn)+(rn-bn))/sqrt((rn-gn)*(rn-gn)+(rn-bn)*(gn-bn)));
            }
        }
    }
}

```

```

        h = h/(2*PI);          //[0,1]

        if ((rn<gn)&&(rn<bn))  //[0,1]
        {
            s = 1 - 3*m;
        }
        else if ((gb<rn)&&(gn<bn))
        {
            s = 1 - 3*gn;
        }
        else
        {
            s = 1 - 3*bn;
        }

        i = (r + g + b)/(3*255); //[0,1]
    }

    *(m_pImgH+jRow*width+iColumn) = h;
    *(m_pImgS+jRow*width+iColumn) = s;
    *(m_pImgI+jRow*width+iColumn) = i;
}
}

// Extraction of parameters
hSum = 0;
sSum = 0;
iSum = 0;

for(jRow=0;jRow<height;jRow++)
{
    for(iColumn=0;iColumn<width;iColumn++)
    {
        hSum = *(m_pImgH+jRow*width+iColumn) + hSum;
        sSum = *(m_pImgS+jRow*width+iColumn) + sSum;
        iSum = *(m_pImgI+jRow*width+iColumn) + iSum;
    }
}

m_dblMh = hSum/(height*width);
m_dblMs = sSum/(height*width);
m_dblMi = iSum/(height*width);

hSum = 0;
sSum = 0;
iSum = 0;

for(jRow=0;jRow<height;jRow++)

```

```

    {
        for(iColumn=0;iColumn<width;iColumn++)
        {
            hSum = (*(m_pImgH+jRow*width+iColumn) -
m_dblMh)*(*(m_pImgH+jRow*width+iColumn) - m_dblMh) + hSum;
            sSum = (*(m_pImgS+jRow*width+iColumn) -
m_dblMs)*(*(m_pImgS+jRow*width+iColumn) - m_dblMs) + sSum;
            iSum = (*(m_pImgI+jRow*width+iColumn) -
m_dblMi)*(*(m_pImgI+jRow*width+iColumn) - m_dblMi) + iSum;
        }
    }

    m_dblCh = sqrt(hSum/(height*width));
    m_dblCs = sqrt(sSum/(height*width));
    m_dblCi = sqrt(iSum/(height*width));

    iSum = 0;

    for(jRow=0;jRow<height;jRow++)
    {
        for(iColumn=0;iColumn<width;iColumn++)
        {
            if (*(m_pImgI+jRow*width+iColumn)>iThreshold)
            {
                iSum = iSum + 1;
            }
        }
    }

    m_dblAi = iSum/(height*width);

    // Data fusion
    m_dblMhArray[m_nStabilityCount] = m_dblMh;
    m_dblMsArray[m_nStabilityCount] = m_dblMs;
    m_dblMiArray[m_nStabilityCount] = m_dblMi;
    m_dblChArray[m_nStabilityCount] = m_dblCh;
    m_dblCsArray[m_nStabilityCount] = m_dblCs;
    m_dblCiArray[m_nStabilityCount] = m_dblCi;
    m_dblAiArray[m_nStabilityCount] = m_dblAi;

    m_nStabilityCount = m_nStabilityCount + 1;

    if (m_nStabilityCount >= WINDOW_WIDTH)
    {
        m_nStabilityCount = 0;
        m_bISArrayFull = TRUE;
    }

```

```

if (m_bISArrayFull == TRUE)
{
    m_dblMhStd = CalculateSTD(m_dblMhArray, WINDOW_WIDTH);
    m_dblMsStd = CalculateSTD(m_dblMsArray, WINDOW_WIDTH);
    m_dblMiStd = CalculateSTD(m_dblMiArray, WINDOW_WIDTH);
    m_dblChStd = CalculateSTD(m_dblChArray, WINDOW_WIDTH);
    m_dblCsStd = CalculateSTD(m_dblCsArray, WINDOW_WIDTH);
    m_dblCiStd = CalculateSTD(m_dblCiArray, WINDOW_WIDTH);
    m_dblAiStd = CalculateSTD(m_dblAiArray, WINDOW_WIDTH);
}
else
{
    m_dblMhStd = CalculateSTD(m_dblMhArray, m_nStabilityCount);
    m_dblMsStd = CalculateSTD(m_dblMsArray, m_nStabilityCount);
    m_dblMiStd = CalculateSTD(m_dblMiArray, m_nStabilityCount);
    m_dblChStd = CalculateSTD(m_dblChArray, m_nStabilityCount);
    m_dblCsStd = CalculateSTD(m_dblCsArray, m_nStabilityCount);
    m_dblCiStd = CalculateSTD(m_dblCiArray, m_nStabilityCount);
    m_dblAiStd = CalculateSTD(m_dblAiArray, m_nStabilityCount);
}

m_dblStabilityIndex = pow((1-2*m_dblMhStd)*(1-2*m_dblMsStd)*(1-
2*m_dblMiStd)*(1-4*m_dblChStd)*(1-4*m_dblCsStd)*(1-4*m_dblCiStd)*(1-
2*m_dblAiStd),2);

CString strStabilityIndex;

strStabilityIndex.Format("%.2f",m_dblStabilityIndex);
SetDlgItemText(IDC_EDIT_STABILITY_INDEX, strStabilityIndex);

}

double CFlameMonitoringDlg::CalculateSTD(double * dblArray,int Length)
{
    double sum1 = 0;
    double ave1 = 0;

    double sum2 = 0;
    double std = 0;
    int i;

    if (0 == Length)
    {
        return 0;
    }
}

```

```
for (i = 0; i < Length; i++)
{
    sum1 = sum1 + dblArray[i];
}
ave1 = sum1/Length;

for (i = 0; i < Length; i++)
{
    sum2 = sum2 + pow(dblArray[i]-ave1,2);
}
std = sqrt(sum2/Length);

return std;
}
```

## Appendix 5:

### Program for Computation of Temperature

```

% *****%
% File name:      TemperatureMeasurement.cpp
% Synopses:      1) Calculate temperature distribution
%                2) Display minimum, maximum and average temperature on GUI
%                3) Convert temperature distribution into pseudo colour image
%                4) Display pseudo colour image of temperature distribution on GUI
% Programmer:    Duo Sun, School of Engineering and Digital Arts, University of Kent
% Date:         August 1, 2011
% *****%

#define TEMPERATURE_MAX          2100 // °C
#define TEMPERATURE_MIN          1100 // °C

#define TEMPERATURE_LABEL_MAX    2000 // °C
#define TEMPERATURE_LABEL_MIN    1200 // °C

#define NOISE_LEVEL               2    // Noise level
#define THRESHOLD                 15   // Threshold

#define C1                        1.1911e8 // First Planck's Constant
#define C2                        1.4388e4 // Second Planck's Constant

#define LambdaR                   0.614 // (um)
#define LambdaG                   0.541 // (um)

void CFlameMonitoringDlg::CalculateTemperatureDistribution(IplImage *Img)
//IplImage: OpenCV IPL image header
{
    int height      = Img->height;
    int width       = Img->width;
    int step        = Img->widthStep/sizeof(uchar);
    int channels     = Img->nChannels;
    uchar* pdata    = (uchar *)Img->imageData; // flame image

    int jRow,iColumn;
    float g1,g2,ratio,s,temp;
    float tempNum = 0;
    float tempMin = 10000;
    float tempMax = 0;
    double tempSum = 0;

```

```

if (m_pTemp != NULL)
{
    delete []m_pTemp;
    m_pTemp = NULL;
}

m_pTemp = new float[height*width];

// Calculate temperature distribution

for(jRow=0;jRow<height;jRow++)
{
    for(iColumn=0;iColumn<width;iColumn++) //B,G,R
    {
        // g1 = R channel
        g1 = unsigned char ( pdata[jRow*step+iColumn*channels+2] );
        // g2 = G channel
        g2 = unsigned char ( pdata[jRow*step+iColumn*channels+1] );

        if ( (g1>THRESHOLD) && (g2>THRESHOLD) )
        {
            g1 = g1 - NOISE_LEVEL;
            g2 = g2 - NOISE_LEVEL;
            // intensity ratio
            ratio = static_cast<float>(g1)/static_cast<float>(g2);
            // instrument factor
            s = 0.3557*ratio*ratio - 1.294*ratio + 2.469;
            // temperature
            temp = C2*(1/LambdaG -
            1/LambdaR)/log(ratio*s*pow(LambdaR/LambdaG,5));

            if ( (temp<=TEMPERATURE_MAX) &&
            (temp>=TEMPERATURE_MIN) )
            {
                *(m_pTemp+jRow*width+iColumn) = temp;

                if (tempMin > temp) tempMin = temp;
                if (tempMax < temp) tempMax = temp;

                tempSum = tempSum + temp;
                tempNum = tempNum + 1;
            }
            else
            {
                *(m_pTemp+jRow*width+iColumn) = 0;
            }
        }
    }
}

```

```

        }
        else
        {
            *(m_pTemp+jRow*width+iColumn) = 0;
        }
    }
}

```

// Display minimum, maximum and average temperature on the GUI

```

m_dblTMax = tempMax;    // maximum

```

```

if(tempMin == 10000)    // minimum

```

```

{
    m_dblTMin = 0;
}

```

```

else

```

```

{
    m_dblTMin = tempMin;
}

```

```

if (tempNum != 0)      // average

```

```

{
    m_dblTAve = tempSum/tempNum;
}

```

```

else

```

```

{
    m_dblTAve = 0;
}

```

```

CString strTMax,strTMin,strTAve;

```

```

strTMax.Format("%.0f °C",m_dblTMax);
SetDlgItemText(IDC_EDIT_TMAX, strTMax);

```

```

strTMin.Format("%.0f °C",m_dblTMin);
SetDlgItemText(IDC_EDIT_TMIN, strTMin);

```

```

strTAve.Format("%.0f °C",m_dblTAve);
SetDlgItemText(IDC_EDIT_TAVE, strTAve);

```

// Convert numerical temperature distribution into pseudo color image

```

int k;
BOOL flag;

```

```

if ((height!=m_pCvImgTemperature->height)||width!=m_pCvImgTemperature

```

```

->width)||((channels!=m_pCvImgTemperature->nChannels))
{
    if(NULL!=m_pCvImgTemperature)
    {
        cvReleaseImage(&m_pCvImgTemperature);
    }
    m_pCvImgTemperature =
    cvCreateImage(cvSize(width,height),IPL_DEPTH_8U,channels);
}

// temperature distribution in pseudo color
uchar* pdataT = (uchar *)m_pCvImgTemperature->imageData;
int stepT      = m_pCvImgTemperature->widthStep/sizeof(uchar);

for(jRow=0;jRow<height;jRow++)
{
    for(iColumn=0;iColumn<width;iColumn++)
    {
        temp = *(m_pTemp+jRow*width+iColumn);

        flag = FALSE;

        for (k=0;k<COLOR_NUMBER;k++)
        {
            if(temp > m_nTempScale[k])
            {
                pdataT[jRow*stepT+iColumn*channels+0] =
                m_colorCode[3*k+0]; //B
                pdataT[jRow*stepT+iColumn*channels+1] =
                m_colorCode[3*k+1]; //G
                pdataT[jRow*stepT+iColumn*channels+2] =
                m_colorCode[3*k+2]; //R

                flag = TRUE;

                break;
            }
        }

        if(TRUE != flag) // Black
        {
            pdataT[jRow*stepT+iColumn*channels+0] = 0; //B
            pdataT[jRow*stepT+iColumn*channels+1] = 0; //G
            pdataT[jRow*stepT+iColumn*channels+2] = 0; //R
        }
    }
}

```

```

// Display the pseudo color image of temperature distribution on GUI
CDC *pDC = GetDlgItem(IDC_DISPLAY_TEMPERATURE)->GetDC();
HDC hDC = pDC->GetSafeHdc();

CRect rect;

GetDlgItem(IDC_DISPLAY_TEMPERATURE)->GetClientRect(&rect);

CvImage cimg;

if (m_pCvImgTemperature != NULL)
{
    cimg.CopyOf(m_pCvImgTemperature);

    cimg.DrawToHDC(hDC,&rect);
}

ReleaseDC(pDC);
}

void CFlameMonitoringDlg::InitColorBar()
{
    m_colorCode[0] = 0;           //BGR Red:highest temperature
    m_colorCode[1] = 0;
    m_colorCode[2] = 255;

    m_colorCode[3] = 0;           //BGR
    m_colorCode[4] = 64;
    m_colorCode[5] = 255;

    m_colorCode[6] = 0;           //BGR
    m_colorCode[7] = 143;
    m_colorCode[8] = 255;

    m_colorCode[9] = 0;           //BGR
    m_colorCode[10] = 223;
    m_colorCode[11] = 255;

    m_colorCode[12] = 48;         //BGR
    m_colorCode[13] = 255;
    m_colorCode[14] = 207;

    m_colorCode[15] = 128;        //BGR
    m_colorCode[16] = 255;
    m_colorCode[17] = 128;
}

```

```

m_colorCode[18] = 207;           //BGR
m_colorCode[19] = 255;
m_colorCode[20] = 48;

m_colorCode[21] = 255;           //BGR
m_colorCode[22] = 223;
m_colorCode[23] = 0;

m_colorCode[24] = 255;           //BGR
m_colorCode[25] = 143;
m_colorCode[26] = 0;

m_colorCode[27] = 255;           //BGR
m_colorCode[28] = 64;
m_colorCode[29] = 0;

m_colorCode[30] = 255;           //BGR Blue:lowest temperature
m_colorCode[31] = 0;
m_colorCode[32] = 0;

for (int i=0;i<COLOR_NUMBER;i++)
{
    m_nTempScale[i] = TEMPERATURE_LABEL_MAX -
        (i+0.5)*(TEMPERATURE_LABEL_MAX -
        TEMPERATURE_LABEL_MIN)/(COLOR_NUMBER-1);
}

m_pCvImgColorbar = cvCreateImage( cvSize(4, COLOR_NUMBER),
IPL_DEPTH_8U, 3 );
int height = m_pCvImgColorbar->height;
int width = m_pCvImgColorbar->width;
int step = m_pCvImgColorbar->widthStep/sizeof(uchar);
int channels = m_pCvImgColorbar->nChannels;
uchar* data = (uchar *)m_pCvImgColorbar->imageData;

for (int i=0;i<height;i++)
{
    for(int j=0;j<width;j++)
    {
        data[i*step+j*channels+0] = m_colorCode[i*3+0]; //B
        data[i*step+j*channels+1] = m_colorCode[i*3+1]; //G
        data[i*step+j*channels+2] = m_colorCode[i*3+2]; //R
    }
}
}

```

## Appendix 6:

### Program for of Abnormal Condition Detection in a Combustion Process Using KPCA

```

% *****%
% File name:      abnormalConditionsDetectionKPCA.m
% Synopses:      1) Load data
%                2) Scale the data using the mean and std of training data
%                3) Carry out KPCA
%                4) Compute principal components in kernel feature space
%                5) Compute T2 & SPE limit
%                6) Compute T2, Q statistics of test data
%                7) Display results and draw figures
% Programmer:    Duo Sun, School of Engineering and Digital Arts, University of Kent
% Date:          August 1, 2011
% *****%

clear all;
close all;
clc;

%% Load data
cdir = pwd;
cd ([cdir '\data']);

data_normal = load ('normal.dat');
data_abnormal = load ('abnormal.dat');

cd (cdir);

cvp = cvpartition(size(data_normal,1),'holdout',0.20);

training_data = data_normal(cvp.training,:);
test_data     = vertcat(data_normal(cvp.test,:),data_abnormal);

%% Scale the data using the mean and std of training data
n = size(training_data,1); % number of observations
m = size(training_data,2); % number of variables

Xmean = mean(training_data,1);

```

```

Xstd = std(training_data);

X = bsxfun(@minus,training_data,Xmean);
X = X./repmat(Xstd,n,1);

Xt = bsxfun(@minus,test_data,Xmean);
Xt = Xt./repmat(Xstd,size(Xt,1),1);

training_patterns = X;
test_patterns     = Xt;

%% Carry out KPCA
rbf_var = 1000;
cov_size = size(training_patterns,1);

for i=1:cov_size,
    for j=i:cov_size,
        K(i,j) = exp(-norm(training_patterns(i,:)-training_patterns(j,:))^2/rbf_var);
        K(j,i) = K(i,j);
    end
end
unit = ones(cov_size, cov_size)/cov_size;
K_n = K - unit*K - K*unit + unit*K*unit;

[evects,evals] = eig(K_n);
evals          = real(diag(evals));

[evals IX] = sort(evals,'descend');
evects     = evects(:,IX);

for i=1:cov_size,
    evects(:,i) = evects(:,i)/(sqrt(evals(i)));
end

percent = 0.99;
k=0;
for i = 1:length(evals)
    per(i) = sum(evals(1:i))/sum(evals);
    if per(i) >= percent
        k = i;
        break;
    end
end

%% Compute principal components in kernel feature space
% training data
train_num = size(training_patterns,1);

```

```

for i=1:train_num,
    for j=1:cov_size,
        K_train(i,j) = exp(-norm(training_patterns(i,:)-training_patterns(j,:))^2/rbf_var);
    end
end
unit_train = ones(train_num,cov_size)/cov_size;
K_train_n = K_train - unit_train*K - K_train*unit + unit_train*K*unit;

training_features = K_train_n * evecs(:,1:end);

% test data
test_num = size(test_patterns,1);

for i=1:test_num,
    for j=1:cov_size,
        K_test(i,j) = exp(-norm(test_patterns(i,:)-training_patterns(j,:))^2/rbf_var);
    end
end
unit_test = ones(test_num,cov_size)/cov_size;
K_test_n = K_test - unit_test*K - K_test*unit + unit_test*K*unit;

test_features = K_test_n * evecs(:,1:end);

%% Compute T2 & SPE limit
beta = 0.95;
alpha = 1-beta;

T2knbeta = k*(n-1)/(n-k)*finv(beta,k,n-k)

theta=zeros(3,1);
for i=1:3
    for j=k+1:size(evecs,1)
        theta(i) = theta(i) + evals(j)^i;
    end
end
h0 = 1 - 2/3*theta(1)*theta(3)/(theta(2)^2);
Qbeta = theta(1)*(1 + theta(2)*h0*(h0-1)/(theta(1)^2)...
        + norminv(beta)*(2*theta(2)*h0^2)^0.5/theta(1)...
        )^(1/h0)

%% Compute T2, Q statistics of test data
T2_test = diag(test_features(:,1:k)*diag(1./evals(1:k))*test_features(:,1:k).');

for i=1:size(test_features,1)
    Q_test(i) = test_features(i,k+1:end)*test_features(i,k+1:end).';
end

```

```
%% Display results and draw figures
T2 = [T2_test];
Q = Q_test. ';

figure;
plot(T2,'k');
hold on; plot(T2*beta*ones(1,length(T2)), 'r--');
xlabel('Observations'); ylabel('T^{2}-Statistic');
legend('T^{2}-Statistic', ['T^{2}_{\alpha}, \alpha=' num2str(beta*100) '%']);

figure
plot(Q,'k');
hold on; plot(Q*beta*ones(1,length(Q)), 'r--');
xlabel('Observations'); ylabel('Q-Statistic');
legend('Q-Statistic', ['Q_{\alpha}, \alpha=' num2str(beta*100) '%']);
```

## Appendix 7:

### Program for Flame State Identification Using SVM

```

% *****%
% File name:      flameStateIdentificationSVM.m
% Synopses:      1) Load data (flame characteristics)
%                2) Conduct scaling on the data
%                3) Divide the data randomly into training set 80%, and test set 20%
%                4) Use cross-validation to find the best parameter c and gamma
%                5) Use the best c and gamma to train the whole training set
%                6) Use the trained SVM model to predict test data set
%                7) Display results and draw figures
% Programmer:    Duo Sun, School of Engineering and Digital Arts, University of Kent
% Date:          August 19, 2012
% *****%

clear all;
close all;
clc;

%% Load data
cdir = pwd;
cd ([cdir 'flameCharacteristics']);

class_labels = [1:18];    % 18 different test conditions
attributes    = [];       % input of svm: flame characteristics
target       = [];       % output of svm: flame state

for iClass = 1:length(class_labels)
    iClass_attributes = load(['flameCharacteristicsC' num2str(iClass) '.dat']);
    attributes        = vertcat(attributes,iClass_attributes);

    iClass_target     = iClass*ones(size(iClass_attributes,1),1);
    target            = vertcat(target,iClass_target);
end

cd (cdir);

%% Conduct scaling on the data
attributes=(attributes-
repmat(min(attributes,[],1),size(attributes,1),1))*spdiags(1./(max(attributes,[],1)-
min(attributes,[],1))',0,size(attributes,2),size(attributes,2));

```

```

%% Divide the data randomly into training set 80%, and test set 20%
nTrials = 20; % 20 trials
for iTrial = 1:nTrials
    cvp(iTrial) = cvpartition(target,'holdout',0.2);
end

%% Carry out SVM
for iTrial = 1:nTrials
    disp(['Trial ' num2str(iTrial)]);

    test_target      = target(cvp(iTrial).test);
    test_attributes  = attributes(cvp(iTrial).test,:);

    training_target  = target(cvp(iTrial).training);
    training_attributes = attributes(cvp(iTrial).training,:);

    nTest            = cvp(iTrial).TestSize;
    nTrain           = cvp(iTrial).TrainSize;

    % Use cross-validation to find the best parameter c and gamma
    bestcv = 0;

    for log2c = 3:7
        for log2g = -4:1
            cmd = ['-v 5 -c ', num2str(2^log2c), ' -g ', num2str(2^log2g), ' -q'];
            cv = svmtrain(training_target, training_attributes, cmd);
            if (cv >= bestcv),
                bestcv = cv; bestc = 2^log2c; bestg = 2^log2g;
                bestlog2c = log2c; bestlog2g = log2g;
            end
            fprintf('%g %g %g\n', log2c, log2g, cv);
            fprintf('best log2c=%g, c=%g, log2g=%g, g=%g, rate=%g\n', bestlog2c,
                bestc, bestlog2g, bestg, bestcv);
        end
    end

    % Use the best parameter C and gamma to train the whole training set
    model = svmtrain(training_target, training_attributes, ['-c ' num2str(bestc) ' -g '
        num2str(bestg) ' -q']);

    % Use the trained model to predict training data set
    [training_target_predicted, training_accuracy, prob_estimates] =
        svmpredict(training_target, training_attributes, model);

```

```

% Use the trained model to predict test data set
[test_target_predicted, test_accuracy, prob_estimates] = svmpredict(test_target,
test_attributes, model);

```

```

% Record results

```

```

training_target_array(iTrial,:)      = training_target;
training_target_predicted_array(iTrial,:) = training_target_predicted;
training_accuracy_array(iTrial)      = training_accuracy(1);

```

```

test_target_array(iTrial,:)          = test_target;
test_target_predicted_array(iTrial,:) = test_target_predicted;
test_accuracy_array(iTrial)          = test_accuracy(1);

```

```

disp(['Success rate of predicting training data: ' num2str(training_accuracy(1))]);
disp(['Success rate of predicting test data: '      num2str(test_accuracy(1))]);

```

```

end

```

```

%%% Draw figures

```

```

figure;
plot(training_accuracy_array,'Marker','o','LineStyle',':','Color',[0 0 0]);
xlabel('Trial number');
ylabel('Success rate of classification of training data (%)');
axis([1 20 85 100]);

```

```

figure;
plot(test_accuracy_array,'Marker','o','LineStyle',':','Color',[0 0 0]);
xlabel('Trial number');
ylabel('Success rate of classification of test data (%)');
axis([1 20 85 100]);

```

## Appendix 8:

### Program for NO<sub>x</sub> Emission Prediction Using SVM

```

% *****%
% File name:      NOxPredictionSVM.m
% Synopses:      1) Load data (flame characteristics)
%                2) Conduct scaling on the data
%                3) Divide the data randomly into training set 80%, and test set 20%
%                4) Use cross-validation to find the best parameter c and gamma
%                5) Use the best c and gamma to train the whole training set
%                6) Use the trained SVM model to predict test data set
%                7) Display results and draw figures
% Programmer:    Duo Sun, School of Engineering and Digital Arts, University of Kent
% Date:         August 19, 2012
% *****%

clear all;
close all;
clc;

%% Load data
cdir = pwd;
cd ([cdir 'flameCharacteristics']);

class_labels = [1:18];      % 18 different test conditions
attributes    = [];         % input of svm: flame characteristics
target       = [];         % output of svm: flame state

for iClass = 1:length(class_labels)
    iClass_attributes = load(['flameCharacteristicsC' num2str(iClass) '.dat']);
    attributes        = vertcat(attributes,iClass_attributes);

    iClass_target     = load(['NOxC' num2str(iClass) '.dat']);
    target            = vertcat(target,iClass_target);
end

cd (cdir);

%% Conduct scaling on the data
attributes=(attributes-
repmat(min(attributes,[],1),size(attributes,1),1))*spdiags(1./(max(attributes,[],1)-
min(attributes,[],1)),0,size(attributes,2),size(attributes,2));

```

```

%% Divide the data randomly into training set 80%, and test set 20%
nTrials = 20; % 20 trials
for iTrial = 1:nTrials
    cvp(iTrial) = cvpartition(target,'holdout',0.2);
end

%% Carry out SVM
for iTrial = 1:nTrials
    disp(['Trial ' num2str(iTrial)]);

    test_target      = target(cvp(iTrial).test);
    test_attributes  = attributes(cvp(iTrial).test,:);

    training_target  = target(cvp(iTrial).training);
    training_attributes = attributes(cvp(iTrial).training,:);

    nTest            = cvp(iTrial).TestSize;
    nTrain           = cvp(iTrial).TrainSize;

    % Use cross-validation to find the best parameter c and gamma
    bestmse = inf;

    for log2c = 3:7
        for log2g = -2:3
            cmd = ['-s 3 '-v 5 -c ', num2str(2^log2c), '-g ', num2str(2^log2g), '-q'];
            svm_mse = svmtrain(training_target, training_attributes, cmd);
            if (svm_mse <= bestmse),
                bestmse = svm_mse; bestc = 2^log2c; bestg = 2^log2g;
                bestlog2c = log2c; bestlog2g = log2g;
            end
            fprintf('%g %g %g\n', log2c, log2g, svm_mse);
            fprintf('best log2c=%g, c=%g, log2g=%g, g=%g, mse=%g\n', bestlog2c,
                bestc, bestlog2g, bestg, bestmse);
        end
    end

    % Use the best parameter C and gamma to train the whole training set
    model = svmtrain(training_target, training_attributes, ['-s 3 '-c ' num2str(bestc) '-g '
        num2str(bestg) '-q']);

    % Use the trained model to predict training data set
    [training_target_predicted, training_accuracy, prob_estimates] =
        svmpredict(training_target, training_attributes, model);

    % Use the trained model to predict test data set

```

```
[test_target_predicted, test_accuracy, prob_estimates] = svmpredict(test_target,
test_attributes, model);
```

```
% Record results
```

```
training_target_array(iTrial,:) = training_target;
training_target_predicted_array(iTrial,:) = training_target_predicted;
training_accuracy_array(iTrial) = training_accuracy;
```

```
test_target_array(iTrial,:) = test_target;
test_target_predicted_array(iTrial,:) = test_target_predicted;
test_accuracy_array(iTrial) = test_accuracy;
```

```
end
```

```
%% Draw figure: predicted value vs. measured value
iTrial = 1;
```

```
figure;
plot(test_target_array(iTrial,:),
test_target_predicted_array(iTrial,:), 'k', 'Marker', '.', 'LineStyle', 'none');
ylabel('Predicted NOx (ppm)');
xlabel('Measured NOx (ppm)');
```

```
x = [160:345]; y = x;
hold on; plot(x(2:end-8), y(2:end-8)*1.03, 'k', 'LineStyle', ':');
hold on; plot(x(1:end-5), y(1:end-5), 'k', 'LineStyle', '--');
hold on; plot(x(5:end-4), y(5:end-4)*0.97, 'k', 'LineStyle', ':');
axis([150 350 150 350])
```

```
%% Draw figure: variation of mse with trial number
figure;
plot(test_accuracy_array, 'k', 'Marker', '.', 'LineStyle', ':');
ylabel('Mean squared error');
xlabel('Trial number');
```

## Publications and Dissemination

The following publications were produced during the course of the work leading to the preparation of this thesis.

1. **D. Sun**, G. Lu, H. Zhou, and Y. Yan, "Flame stability monitoring and characterization through digital imaging and spectral analysis," *Measurement Science and Technology*, vol. 22, p. 114007, 2011.

(The article has been selected by the editors of *Measurement Science and Technology* for inclusion in the 'Highlights of 2011–2012' collection, a special collection of some of the best articles published in the journal in the last 18 months.)

2. Md. M. Hossain, Gang Lu, **D. Sun**, and Y. Yan "Three-dimensional reconstruction of flame temperature and emissivity distribution using optical tomographic and two-colour pyrometric techniques," *Measurement Science and Technology*, 2012. (accepted for publication)
3. **D. Sun**, G. Lu, H. Zhou, and Y. Yan, "Condition monitoring of combustion processes through flame imaging and kernel principal component analysis," *Combustion Science and Technology*, 2012. (accepted for publication)
4. X. Li, **D. Sun**, G. Lu, J. Krabicka, and Y. Yan, "Prediction of NO<sub>x</sub> emissions through flame radical imaging and neural network based soft computing," *Proceedings of IEEE International Conference on Imaging Systems and Techniques*, Manchester, UK, pp. 502-505, 13-17 July 2012.
5. X. Li, **D. Sun**, G. Lu, J. Krabicka, and Y. Yan, "Emission prediction of a combustion process through flame radical imaging and application of support vector machine techniques," *The 17<sup>th</sup> IFRF Members Conference*, Maffliers, France, 11-13 June 2012.

6. **D. Sun**, G. Lu, H. Zhou, and Y. Yan, "Measurement of soot temperature, emissivity and concentration of a heavy-oil flame through pyrometric imaging," *Proceedings of IEEE International Instrumentation and Measurement Technology Conference*, Graz, Austria, pp. 1865 – 1869, 13-16 May 2012.
7. **D. Sun**, G. Lu, and Y. Yan, "An embedded imaging and signal processing system for flame stability monitoring and characterisation," *Proceedings of IEEE International Conference on Imaging Systems and Techniques*, Thessaloniki, Greece, pp. 210-213, 1-2 July 2010.
8. Y. Yan, **D. Sun**, S. J. Rodrigues, and G. Lu, "Monitoring and Characterisation of Biomass and Coal Fired Flames on a Full-Scale Power Station," *The 9<sup>th</sup> European Conference on Coal Research and its Applications*, Nottingham, UK, 10-12 September 2012.
9. **D. Sun**, G. Lu, and Y. Yan, "Flame stability monitoring through digital imaging and spectral analysis," *The 2<sup>nd</sup> School Research Conference*, University of Kent, UK, 13 January 2012.
10. **D. Sun**, G. Lu, and Y. Yan, "Flame stability and burner condition monitoring through spectral analysis and digital imaging," *The 8<sup>th</sup> European Conference on Coal Research and its Applications*, Leeds, UK, 6-8 September 2010.
11. **D. Sun**, G. Lu, and Y. Yan, "Digital imaging based flame stability and burner condition monitoring," *IOP Conference on Current Research in Combustion*, Loughborough University, UK, 22 September 2009.
12. **D. Sun**, G. Lu, and Y. Yan, "Flame stability and burner condition monitoring through spectral analysis and digital imaging," *The 1<sup>st</sup> School Research Conference*, University of Kent, UK, 15 January 2010.

# Flame stability monitoring and characterization through digital imaging and spectral analysis

Duo Sun<sup>1</sup>, Gang Lu<sup>1,3</sup>, Hao Zhou<sup>2</sup> and Yong Yan<sup>1</sup>

<sup>1</sup> Instrumentation, Control and Embedded Systems Research Group, School of Engineering and Digital Arts, University of Kent, Canterbury, Kent CT2 7NT, UK

<sup>2</sup> State Key Laboratory of Clean Energy Utilization, Institute for Thermal Power Engineering, Zhejiang University, Hangzhou 310027, People's Republic of China

E-mail: ds322@kent.ac.uk, g.lu@kent.ac.uk, y.yan@kent.ac.uk and zhouhao@cme.zju.edu.cn

Received 9 January 2011, in final form 7 April 2011

Published 14 October 2011

Online at stacks.iop.org/MST/22/114007

## Abstract

This paper presents the design, implementation and evaluation of an instrumentation system for the stability monitoring and characterization of combustion flames. The system, incorporating optical sensing, image processing and spectral analysis techniques, is designed to monitor a range of flame characteristic parameters. The stability of the flame is assessed through statistical analysis of the flame parameters obtained. Embedded computer techniques are employed to ensure the compactness and robustness of the system. Experiments were conducted on a gas-fired combustion test rig to evaluate the system. The impact of equivalence ratio on the stability of the gaseous flame is investigated. Further trials were carried out on a 9 MW<sub>th</sub> heavy-oil-fired combustion test facility. The impact of the swirl vane angle of tertiary air on the oil-fired flames is studied. The results demonstrate the effectiveness of the system for the monitoring and characterization of the flame stability.

**Keywords:** flame monitoring, flame stability, photo-detector, CMOS camera, image processing, embedded systems, spectral analysis

(Some figures in this article are in colour only in the electronic version)

## 1. Introduction

Unstable flames are a recognized problem in fossil-fuel-fired combustion processes, particularly where low-quality fuel, fuel blends and co-firing of biomass with fossil fuels are applied. The unstable flame can result in many combustion problems such as low combustion efficiency, high NO<sub>x</sub> emissions and unburnt carbon in flue gas. It may also cause non-uniform thermal distribution in flue gas and increase the wall thermal stress and vibration of the furnace [1]. The stability of flame should therefore be monitored and maintained continuously for the improved overall performance of the furnace. However, flame monitoring techniques currently available to the power generation industry can only provide basic information such as flame presence or absence

for furnace safety purposes. They cannot give quantitative information on the stability of the flame.

The flame stability depends on many factors, including the ignitability of fuel or a blend, equivalence ratio, inlet fuel distribution, inlet swirl, burner type and boiler structure [2, 3]. A number of studies have been devoted to such issues theoretically and experimentally [4–13]. Various techniques for flame monitoring and characterization have been proposed, but digital imaging has been identified as one of the most effective approaches for use in practical furnaces in terms of system functionality, portability and cost-effectiveness [5]. Significant efforts have been made in the last decade to develop two-dimensional (2D) and three-dimensional (3D) techniques for the visualization and characterization of flames. However, only a few works focused on the quantitative assessment of the flame stability. Furthermore, practical issues such as optical

<sup>3</sup> Author to whom any correspondence should be addressed.

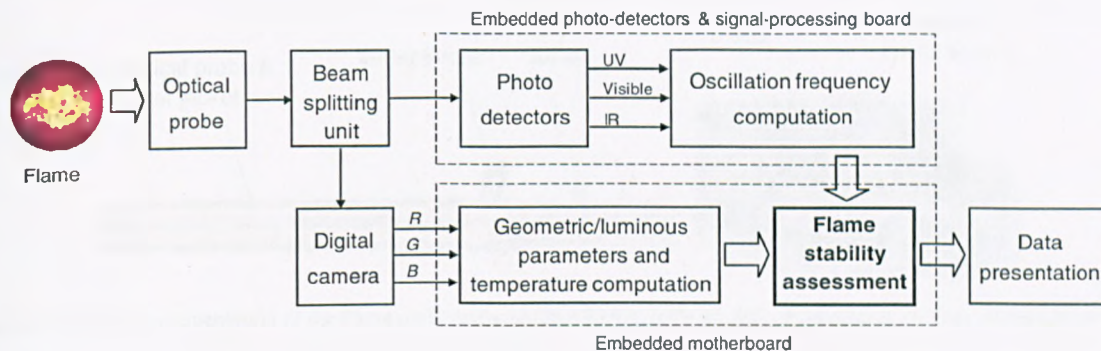


Figure 1. Block diagram of the flame monitoring system.

access requirement, lack of ruggedness and high capital cost limit their application to industrial furnaces. Paubel *et al* [6] used a CCD camera to record chemiluminescence images of excited CH radicals in a non-premixed flame of low calorific residual gases and employed topology analysis techniques to study the stability diagram of the flame. Kiran and Mshira [7] studied the stability characteristics of a jet diffusion LPG (liquefied petroleum gas) flame in terms of its lift-off height, length and emission levels, which were derived from images obtained by a CCD camera. Mansour [8] investigated the stability of a partially premixed turbulent lifted methane flame using the combined technique of Rayleigh scattering, LIPF (laser-induced predissociation fluorescence) and LIF (laser-induced fluorescence). Several prototype systems have also been developed using direct imaging techniques for 2D and 3D flame monitoring and characterization on both laboratory- and industrial-scale combustion test facilities [9–13]. The systems are designed for measuring and quantifying the characteristic parameters of a flame such as size, shape, brightness, oscillation frequency and temperature. Information obtained has laid a foundation for advancing the imaging technology for the quantitative assessment of the flame stability.

This research focuses on the development of an embedded instrumentation system for the monitoring and characterization of the flame stability in industrial furnaces. The system, operating on optical sensing, digital imaging, signal processing and embedded computing techniques, is capable of measuring a number of flame parameters such as ignition point, brightness, oscillation frequency and temperature distribution on an online continuous basis. The stability of the flame is then assessed through the statistical analysis of the characteristic parameters obtained. Technical issues including design considerations, computer algorithms and system implementation are described. Experimental results on a laboratory-scale combustion test rig and on a 9 MW<sub>th</sub> industrial-scale heavy-oil combustion test facility are reported and discussed.

## 2. System description

### 2.1. Design and implementation

Figure 1 shows a block diagram of the prototype flame monitoring system. The system consists of an optical

probe, a beam-splitting unit, an embedded photo-detector and signal-processing board, a digital camera and an embedded motherboard with associated application software. The optical probe, which has a 90° viewing-angle objective lens protected by purging air flow, is used to penetrate the furnace and transmit the light of flame to the imaging system. The beam splitter divides the light of flame into two beams. The first beam is captured by the camera for the measurement of flame geometric and luminous parameters and temperature distribution. The second beam is received by the photo-detectors on the signal-processing board for the measurement of flame oscillation frequency.

**2.1.1. Digital camera.** It is an industrial CMOS RGB camera with resolution up to 1280(H) × 1024(V) at 25 frames s<sup>-1</sup>. It also features a partial scan mode which allows the camera to capture images up to 265 frames s<sup>-1</sup> with a resolution of 320 × 256, making it ideal for imaging a fast-changing object such as a combustion flame.

**2.1.2. Embedded photo-detectors and signal-processing board.** The board has three separate photo-detectors, covering ultraviolet (UV), visible and infrared (IR) spectral bands. The detectors convert the incoming flame light intensity into current signals corresponding to the three spectral bands. A signal conditioning unit is used to ensure that the signals are adequately amplified and filtered prior to digital signal processing. A digital signal microcontroller (dsPIC) digitizes the three signals simultaneously with a processing speed of 40 MHz. Embedded system techniques are employed for on-board signal processing to ensure robustness, compactness and fast response of the system.

**2.1.3. Embedded motherboard.** It is a high-performance embedded motherboard which acquires and processes images from the camera. It also performs as the master board for controlling and receiving data from the embedded photo-detectors and signal-processing board so as to achieve parallel and real-time signal processing and transmission (via Ethernet).

The optical probe and all optical and electronic parts are integrated as a single unit, offering the system excellent portability and robustness. Dedicated application software is

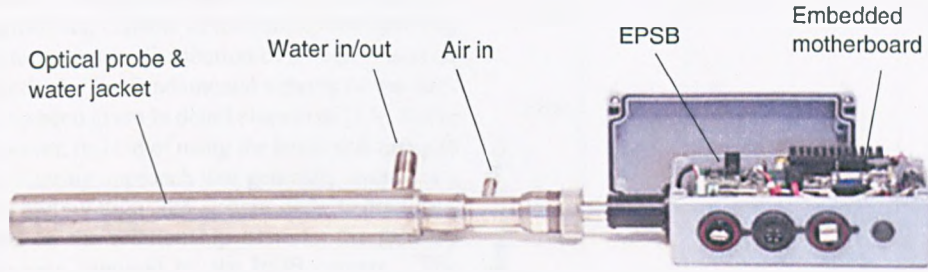


Figure 2. Physical implementation of the flame monitoring system (EPSB: embedded photo-detectors and signal-processing board).

also developed as an integral part of the system. Figure 2 is the physical implementation of the system.

### 2.2. Measurement principles

**2.2.1. Geometric and luminous parameters.** These are determined by processing flame images using digital image processing techniques. The number of parameters that are measured can vary, depending upon the nature of the flame and the purpose of the measurement. In the case of this study, the parameters computed include *ignition points (maximum, minimum and mean)*, *luminous region, brightness and non-uniformity*. The detailed definition and determination of these parameters were given elsewhere [10]. Note that the absolute determination of these parameters is dependent on the specific installation of the system (i.e. the distance between the flame and the image sensor) and the camera settings (i.e. iris and shutter speed, etc). In the case of the present study, the relative values are used as only the variations of these parameters are of interest. The instability of a flame parameter ( $\delta_x$ ) is defined as the standard deviation normalized to its mean value, i.e.

$$\delta_x = \frac{\sigma_x}{\bar{x}} \times 100\%, \quad (1)$$

where  $\bar{x}$  and  $\sigma_x$  are the mean value and the standard deviation of the parameter  $x$ , respectively.

**2.2.2. Geometric and luminous instability.** The geometric and luminous stability of a flame can be evaluated based on the statistical analysis of its geometric and luminous parameters. To quantify the flame geometric and luminous stability, a parameter,  $\delta$ , is defined as the sum of weighted instabilities of the flame parameters, i.e.

$$\delta = \sqrt{\sum_{i=1}^m (w_i \delta_{x_i})^2}, \quad (2)$$

with

$$\sum_{i=1}^m w_i^2 = 1,$$

where  $m$  is the number of flame parameters considered and  $w_i$  is the weight for the corresponding parameter  $x_i$ . A larger weight is given to an estimate with a larger variance of the parameter whilst a smaller weight to an estimate with a smaller variance. The greater the  $\delta$ , the more unstable the flame in its geometry and luminosity.

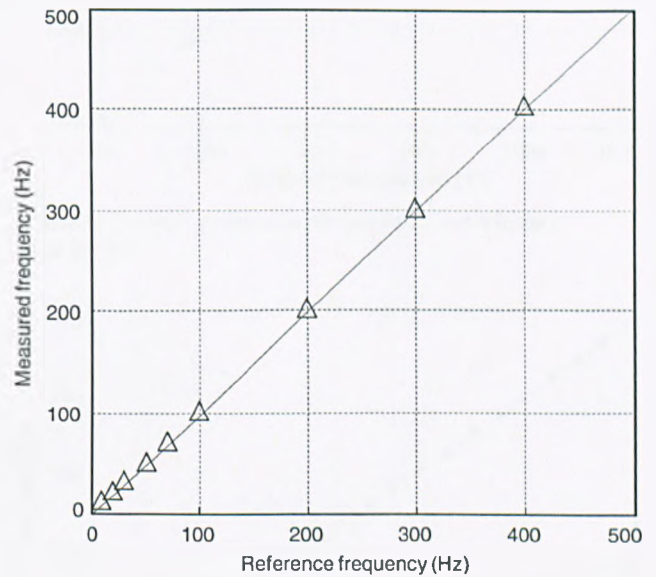


Figure 3. Comparison between the measured and reference frequencies.

**2.2.3. Oscillation frequency.** The oscillation frequency of the flame is one of the most important properties closely linked to flame stability [9]. It is derived from the flame intensity signals captured by the photo-detectors through frequency spectral analysis. A quantitative frequency is determined as the power-density weighted average frequency over the entire frequency range [9], i.e.

$$F = \frac{\sum_{i=1}^n p_i f_i}{\sum_{i=1}^n p_i}, \quad (3)$$

where  $F$  is the oscillation frequency,  $f_i$  is the  $i$ th frequency,  $p_i$  is the power density of the  $i$ th frequency component and  $n$  is the number of frequency components.

A standard frequency-varying light source with a resolution of  $1 \mu\text{Hz}$  was used as an idealized flame light to evaluate the accuracy of the oscillation frequency measurement. Figure 3 shows a comparison between the measured and reference frequencies. Each data point is an average of ten instantaneous values. It was found that the relative error of the frequency measurement is no greater than 2% over the frequency range from 0 to 500 Hz.

**2.2.4. Temperature.** The system developed can be used as a vision-based pyrometer, capable of measuring continuously two-dimensional temperature distribution of a flame based on the two-colour method. The fundamental aspects of the two-colour method have been given in detail elsewhere [13]. In the present study, however, instead of using the beam splitting and narrow-bandpass filtering approach that generally results in a complex system configuration, the system derives the flame temperature based on the relationship between the primary colours of the images captured by the RGB camera. The RGB camera used in the system has three separate channels corresponding to primary colours red (R), green (G) and blue (B). In other words, each image produced can be disintegrated into three principal images R, G and B. Combinations of the colour-banded images can thus be used for the determination of the flame temperature distribution using the two-colour technique. In this study, the R and G images have been chosen, i.e.

$$T = \frac{C_2 \cdot \left(\frac{1}{\lambda_R} - \frac{1}{\lambda_G}\right)}{\ln \frac{G(\lambda_R, T)}{G(\lambda_G, T)} + \ln \frac{S_{\lambda_G}}{S_{\lambda_R}} + \ln \left(\frac{\lambda_R}{\lambda_G}\right)^5}, \quad (4)$$

where  $C_2$  is the second Planck's constant,  $G(\lambda_R, T)$  and  $G(\lambda_G, T)$  are the grey levels of images from the red and green channels of the camera, respectively.  $\lambda_R$  and  $\lambda_G$  are the peak wavelengths of the spectral ranges corresponding to the red and green channels, and are 540 and 615 nm, respectively.  $S_{\lambda_R}$  and  $S_{\lambda_G}$  are the spectral sensitivities of the system for  $\lambda_R$  and  $\lambda_G$ , respectively. The ratio  $S_{\lambda_R}/S_{\lambda_G}$  is the instrument factor and can be determined through a calibration procedure using a pre-calibrated tungsten lamp. In this study, the apparent temperature of the tungsten lamp varied from 900 to 1500 °C with an interval of 50 °C, by controlling the current of the power supply. The instrument factor,  $S = S_{\lambda_R}/S_{\lambda_G}$ , is then determined by

$$S = \frac{e^{C_2 \cdot (1/\lambda_G - 1/\lambda_R)/T}}{\frac{G(\lambda_R, T)}{G(\lambda_G, T)} \cdot \frac{\varepsilon_{\lambda_G}}{\varepsilon_{\lambda_R}} \cdot \left(\frac{\lambda_R}{\lambda_G}\right)^5}, \quad (5)$$

where  $\varepsilon_{\lambda_R}$  and  $\varepsilon_{\lambda_G}$  are the emissivity of the tungsten lamp at  $\lambda_R$  and  $\lambda_G$ , respectively, and can be estimated using the method proposed in [14].

The accuracy of the temperature measurement was verified by applying the system to measure the true temperature of the tungsten lamp, and the results are shown in figure 4. Each data point is an average of ten instantaneous values. The maximum error of 8.5 °C occurs at the true temperature of 1070 °C and is equivalent to a relative error of 0.8%.

**2.3. Evaluation of the imaging system**

Since a tungsten lamp has very stable irradiance for a given temperature, it was used to evaluate the characteristics of the system for different camera settings including exposure time, aperture and viewing distance.

**2.3.1. System linearity.** This was assessed by taking images of the filament of the tungsten lamp for different camera exposure durations at a fixed temperature setting. Figure 5 illustrates the relationship between the averaged grey levels

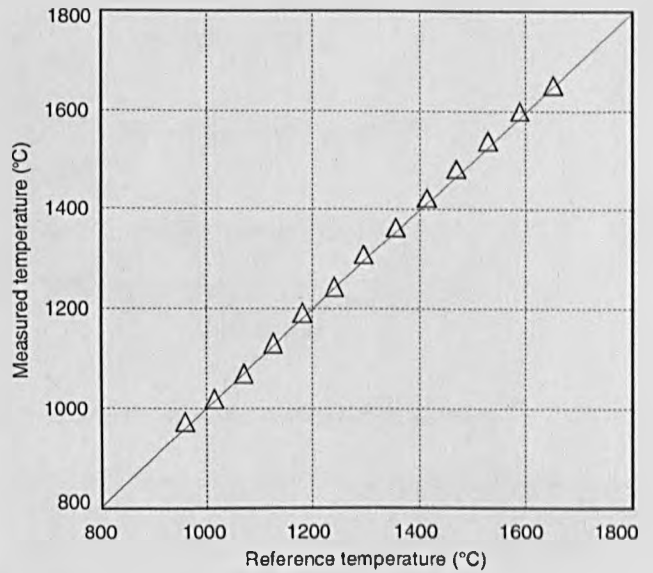


Figure 4. Comparison between the measured and reference temperatures.

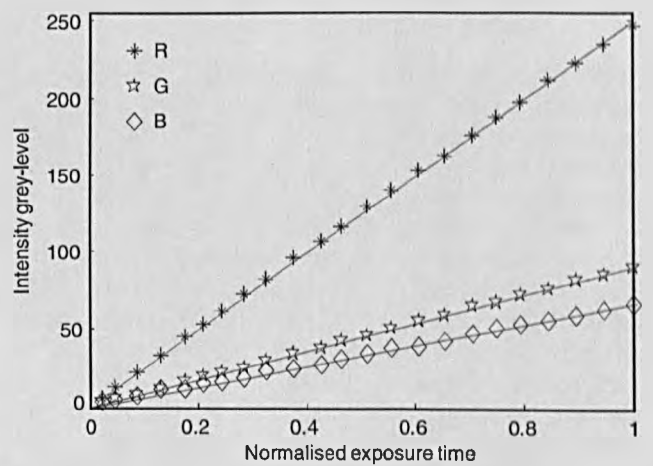


Figure 5. Relationship between the averaged grey levels of the filament images of the tungsten lamp and the camera exposure time for the R, G and B channels of the camera.

of the filament images and the camera exposure time for the R, G and B channels at the true temperature of 1070 °C. The exposure time is normalized to the maximum exposure time at which the image is approaching saturation. As can be seen, the system exhibits high linearity for different camera exposure times. This suggests that the accuracy of the temperature measurement will not be affected by the variation in exposure time, and therefore it is unnecessary to calibrate the system for different camera exposure times. This is particularly important when applying the system to industrial furnaces where the flame irradiance can vary for different operation conditions, and thus the camera exposure time has to be adjusted to avoid under- or over-exposure of images.

It can also be seen from figure 5 that the R channel gives a much stronger intensity grey level than the other

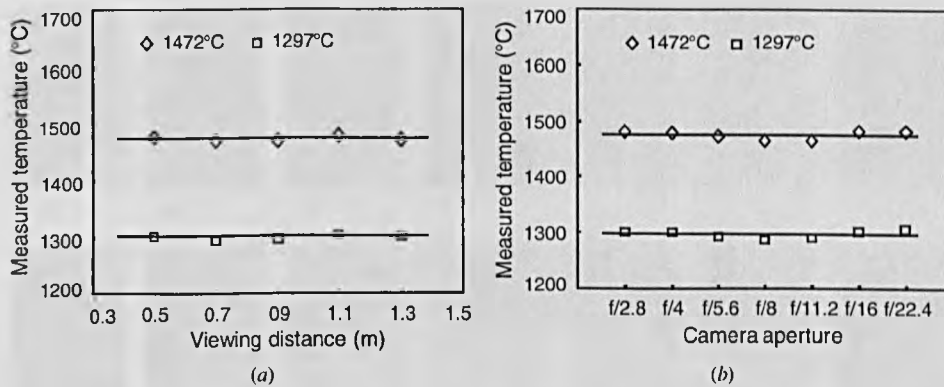


Figure 6. Measured temperatures of the tungsten lamp for different viewing distances and camera apertures.

two. This could result in over-exposure on images produced by the R channel and under-exposure on images by the G and B channels. Although adjusting the hardware gain of the R channel to a relative low level or using the white balance function of the camera may avoid the problem, the resulting image may not reflect the true colour profile of the flame. In practice, the intensity grey level of the R channel is continuously monitored, and the exposure time is then adjusted accordingly to avoid the possible saturation.

**2.3.2. Effect of viewing distance.** The imaging system may be installed on furnaces with different structures and dimensions. It is therefore important to ensure that different viewing distances (i.e. the distance between the flame and the objective lens of the optical probe) do not affect the sensitivity and accuracy of the temperature measurement. The effect of viewing distance on the measurements was evaluated using the tungsten lamp. Figure 6(a) shows the variations of the measured temperature with viewing distance for two given temperature settings. Each data point is an average of 60 instantaneous values, and the maximum standard deviation of each point is approximately 3 °C. It has been found that the maximum temperature difference is no greater than 9 °C for the temperatures tested over the distance ranging from 0.5 to 1.3 m. This relative independence of the temperature measurement from the viewing distance stems from the principle of the two-colour method where the temperature is computed from the grey-level ratio of two-banded images, thus reducing the dependence on the geometrical or optical settings of the imaging system.

**2.3.3. Effect of camera aperture.** Another important factor that should be considered is the aperture of the camera, which controls the depth of field as well as the amount of light that reaches the imaging sensor. The diameter of the camera aperture is measured in f-stops. A lower f-stop number opens the aperture, admitting more light onto the imaging sensor but narrowing the depth of field, whilst a higher f-stop number reduces the aperture and admits less light onto the sensor but deepens the depth of field. Figure 6(b) shows the measured temperatures for different aperture values for the two given temperature settings of the tungsten

lamp. Again, each data point is an average of 60 instantaneous values with a standard deviation less than 4 °C. The maximum relative error of measurements is about 1.4% over the aperture range.

### 3. Experimental results and discussions

#### 3.1. Experiments on a gas-fired combustion test rig

To evaluate the imaging system as well as the methodology developed, experiments were carried out on a laboratory-scale combustion test rig. A Bunsen-type burner with an outlet diameter of 11 mm was used to generate premixed air-propane flames in an enclosed cylindrical chamber with an inner diameter of 150 mm and a height of 300 mm. A mesh screen was mounted across the outlet of the burner to stabilize the flame. Fuel and air flows to the burner were metered during the experiments. A total of 14 test conditions were created by varying air supplies at a fixed fuel flowrate of 0.3 l min<sup>-1</sup>. Each combustion condition is identified by the equivalence ratio which has been recognized to be one of the most important factors relating to fuel conversion, pollutant emissions, heat losses and flame stability [15]. The equivalence ratio,  $\Phi$ , is defined as the ratio of fuel to air supplied for combustion divided by the stoichiometric fuel to air ratio (the chemically correct fuel to air ratio necessary to achieve complete combustion of the fuel. For propane, the stoichiometric ratio is 1:23.9 by volume), i.e.

$$\Phi = \frac{(\text{fuel-to-air ratio})_{\text{actual}}}{(\text{fuel-to-air ratio})_{\text{stoichiometric}}} \quad (6)$$

The equivalence ratio created in the tests ranges between approximately 0.74 and 1.28, where  $\Phi$  less than 1 represents a fuel-lean condition whilst greater than 1 indicates a fuel-rich condition.

Figure 7 shows the flame images captured by the camera for 14 different equivalence ratios. Each image is an average of ten successive images taken in 1 s. It is evident that the physical appearance (size, brightness, etc) of the flame varies with the equivalence ratio.

Figure 8(a) illustrates the instabilities of the flame parameters including the maximum ignition point, luminous region, brightness and non-uniformity for different

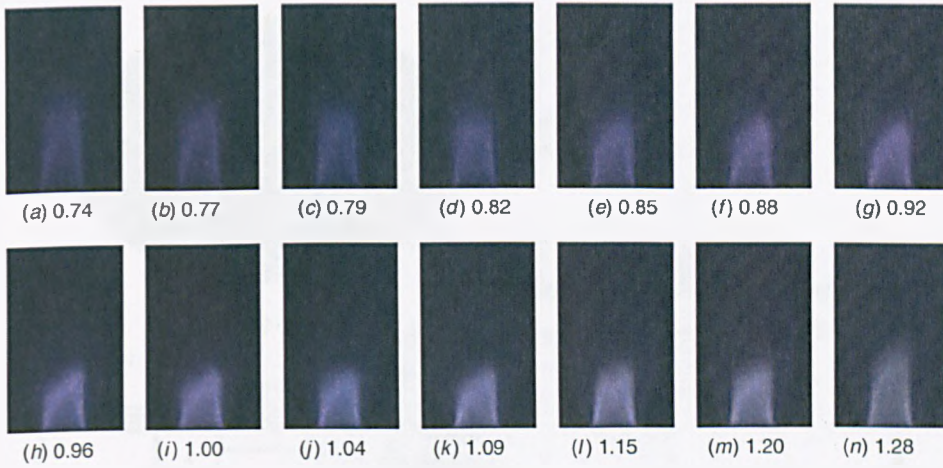


Figure 7. Flame images for different equivalence ratios.

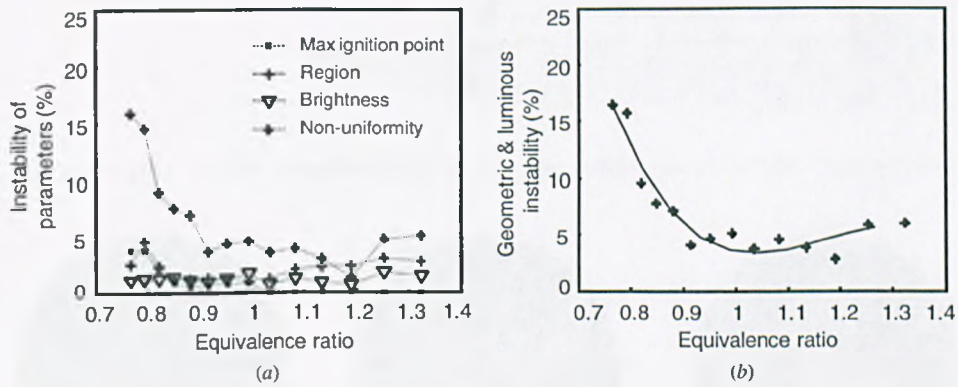


Figure 8. Instabilities of flame parameters for different equivalence ratios.

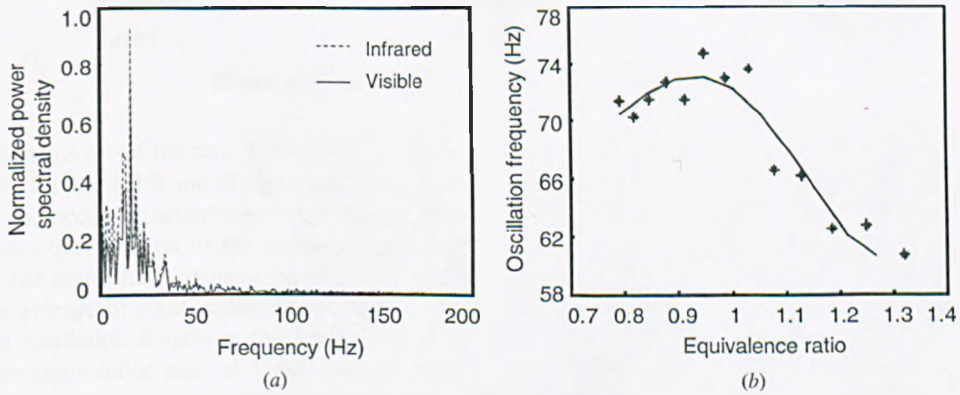


Figure 9. PSD estimates of flame signals (visible and IR bands) and the weighted oscillation frequency (IR band).

equivalence ratios. As can be seen, the instabilities of parameters are relatively small above the stoichiometric conditions ( $\Phi = 1$ ). As the equivalence ratio decreases (i.e. fuel-lean conditions), a significant variation in the non-uniformity is observed. Such variations are the main causes of the geometric and luminous instability of the flame, as shown in figure 8(b). It was observed during the experiments that the flame was extremely unstable under the fuel-lean conditions

( $\Phi < 1$ ) and eventually blown off at an equivalence ratio of 0.74.

Figure 9(a) depicts a typical example of the power spectral density (PSD) estimates of the flame radiation signals taken at the visible and IR spectral ranges for the equivalence ratio of 1.28 (the UV signal was too weak to be detected in the case studied). The sampling rate of the signals was 1024 Hz. The dc components of the signals were removed as dynamic

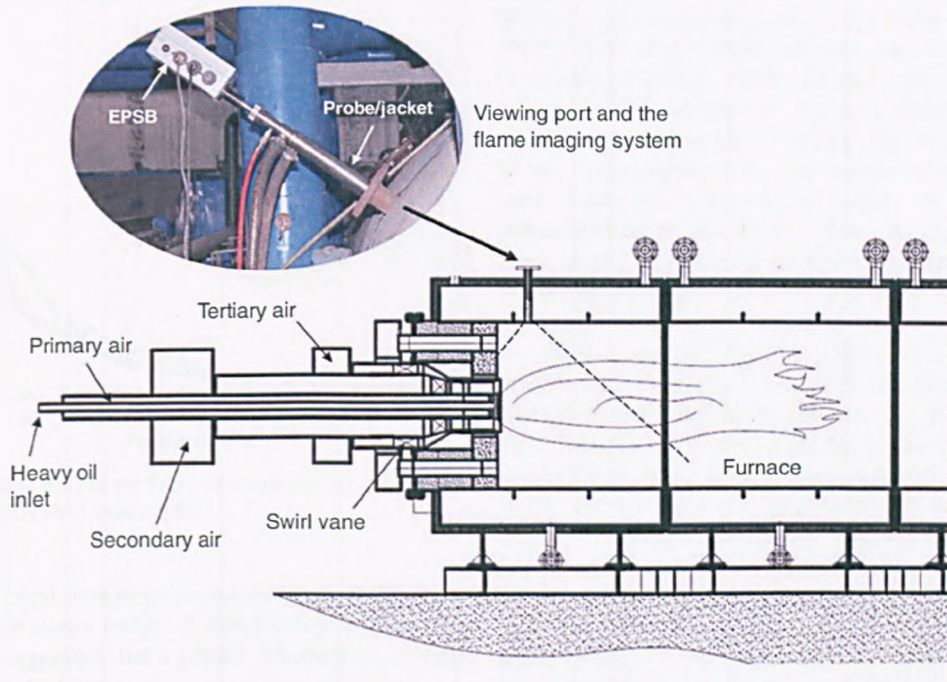


Figure 10. Schematic diagram of the test furnace and the location of the flame imaging system. EPSB—imaging and data processing unit.

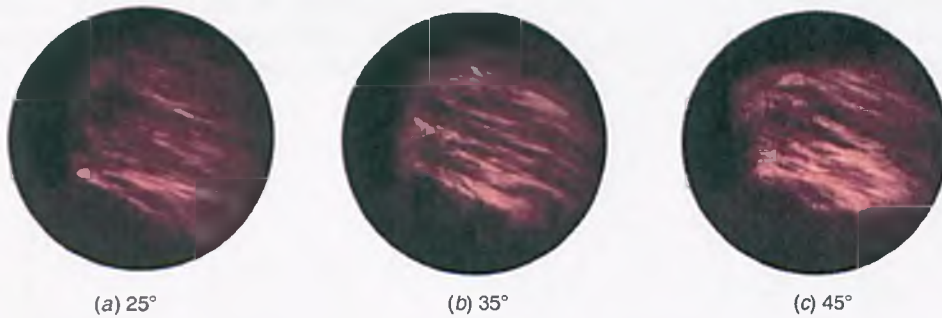


Figure 11. Flame images for different TA swirl vane angles.

frequency components are of interest. It has been found that the PSD estimates for the visible and IR signals are very similar with the peak value occurring around the frequency of 18 Hz. Figure 9(b) shows the variation of the weighted oscillation frequency with the equivalence ratio in the IR band. Each data point is an average of eight instantaneous values. It is evident that the oscillation frequency reaches its maximum value around the equivalence ratio of 1 and then decreased with equivalence ratio, indicating increased flame stability in such combustion conditions.

### 3.2. Experiments on an industrial combustion test facility

Further experimental work was undertaken on a 9 MW<sub>th</sub> industrial-scale heavy-oil-fired combustion test facility. The test rig has an 11 m long horizontal cylindrical combustion chamber with an internal cross-section of 1.3 m in diameter. Heavy oil was atomized by steam and injected into the combustion chamber through an oil gun, and then mixed

with surrounding primary air (PA), secondary air (SA), and tertiary air (TA) successively. The overall air flowrate was kept constant of 9100 N m<sup>3</sup> h<sup>-1</sup> (PA: 17%, SA: 43% and TA: 40%). The imaging system was installed at the side of furnace close to the front wall, as illustrated in figure 10. The resulting field of view of the imaging system was about 1.3 m in diameter along the burner axis. The root region of the flame, which is regarded as the primary reaction zone of the combustion process in terms of energy conversion and emission formation, was fully observed.

In the experiments, the impact of the TA swirl vane angle on the flame stability was investigated. Previous studies suggested that the TA swirl vane angle affects significantly the aerodynamics of the entering air flow and its mixture level with fuel thus the structure and stability of the flame [16, 17]. The TA swirl vane angle can be varied from 0° to 90° with 0° representing the air inlet fully closed and 90° the air inlet fully open without any swirl. In the tests, three different TA swirl vane angles, i.e. 25°, 35° and 45°, were created. Figure 11

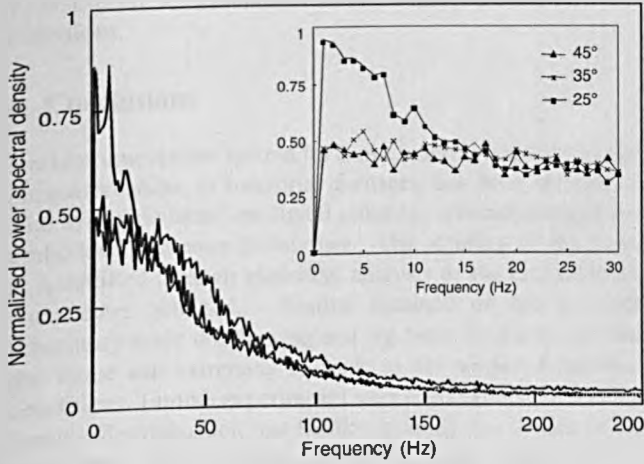


**Figure 12.** Averaged PSD of the flame radiation signals in visible band for different TA swirl vane angles.

illustrates the typical images of the heavy-oil-fired flame for the TA swirl vane angles tested. A direct comparison among the images has suggested that a greater TA swirl vane angle resulted in a stretched flame.

Figure 12 illustrates typical examples of the PSD estimates of the flame radiation signals taken in the visible band for the three test conditions. It is evident that the amplitude of the low-frequency components for 25° is much higher than that for 35° and 45°, whilst the high-frequency components are

very similar in all cases. Previous studies have revealed that the low-frequency components in the flame signal are mainly attributed to its geometrical fluctuations due to aerodynamic or convective effects, whilst the high-frequency components reflect kinetic variations in the heat release rate or energy transitions in intermediate radicals [9]. The PSD estimates of the flame signals have thus suggested that the TA swirl vane angle has a significant impact on the geometrical characteristics of the flame. This has been demonstrated more clearly in figure 13(a) where the weighted oscillation frequency has shown an increased trend with the TA swirl vane angle, indicating increased flame stability in terms of the flame geometric characteristics. This result is in line with the data obtained through the statistical analysis of the geometric and luminous parameters, as illustrated in figure 13(b) which clearly shows greater geometric and luminous instability at 25°. Figure 13(c) suggests a slight increase in the averaged flame temperature with the TA swirl vane angle. An increased standard deviation of the temperature (as shown as error bars in the figure, computed for 250 instantaneous images) has been observed at 25°, indicating a greater fluctuation of the flame temperature under such a vane angle setting. It can therefore be concluded that, under TA swirl vane angles 35° and 45°, the flame is more stable in terms of its geometric, luminous and fluid-dynamic characteristics. This finding is also consistent with the emission analysis of the flue gas, which was taken simultaneously during the test. As shown in figure 13(d), the volume of NO<sub>x</sub> in the flue gas decreases with the vane angle, suggesting that

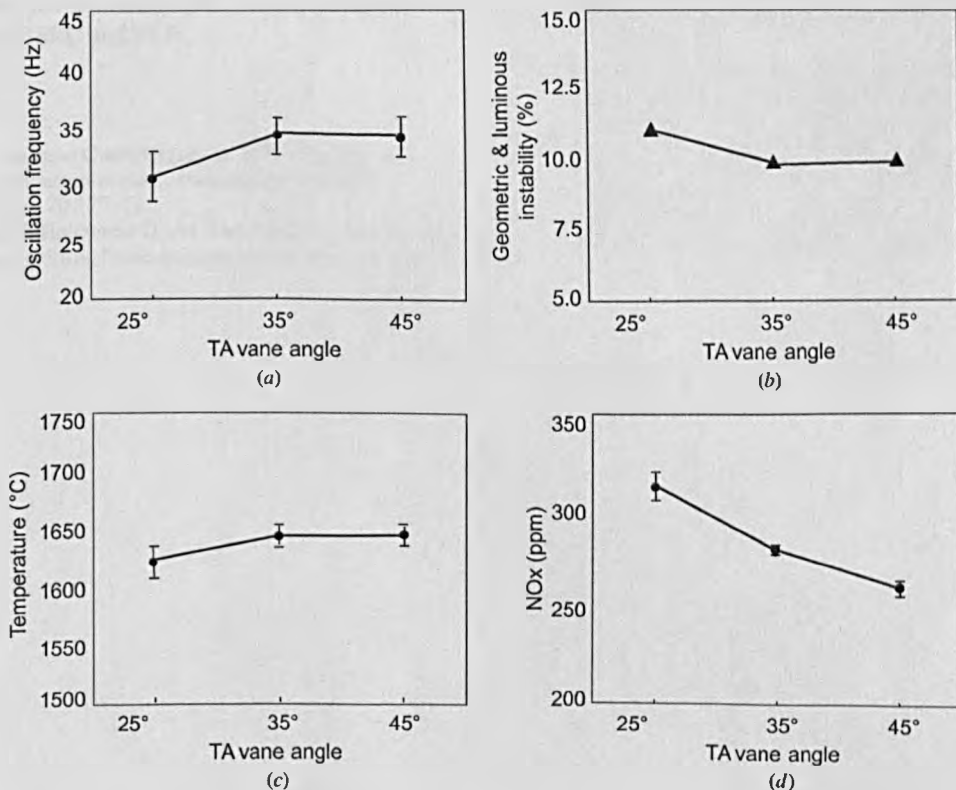


**Figure 13.** Variation of flame parameters and NO<sub>x</sub> in flue gas with TA swirl vane angle.

it is crucial to maintain a stable flame for reduced NO<sub>x</sub> emissions.

#### 4. Conclusions

An instrumentation system for flame stability monitoring and characterization in industrial furnaces has been developed. The system is based on digital imaging, spectral analysis and embedded computer techniques. The stability of the flame is quantified through statistical analysis of the characteristic parameters obtained. Results obtained on the gas-fired laboratory-scale combustion test rig have demonstrated that the flame was extremely unstable at the premixed fuel-lean conditions. Further experiments were carried out on a 9 MW<sub>th</sub> heavy-oil combustion test facility to study the impact of the swirl vane angle of tertiary air on the flame stability. It has been found that a decreased swirl angle gives rise to poorer flame stability in terms of its geometric, luminous and fluid-dynamic characteristics. The test results have thus suggested that the prototype system has provided an effective means for monitoring and characterizing the flame stability under both laboratory and industry conditions.

#### Acknowledgments

The authors wish to acknowledge the Research Councils UK (RCUK) for providing financial support for this research as part of The Energy Programme managed by the Engineering Physical Sciences Research Council (EPSRC, EP/F061307/1). The Energy Programme is an RCUK cross-council initiative led by the EPSRC and contributed to by ESRC, NERC, BBSRC and STFC.

#### References

- [1] Fichera A, Losenno C and Pagano A 2001 Experimental analysis of thermo-acoustic combustion instability *Appl. Energy* **70** 179–91
- [2] Su S, Pohl J H, Holcombe D and Hart J A 2001 Techniques to determine ignition, flame stability and burnout of blended coals in p.f. power station boilers *Prog. Energy Combust.* **27** 75–98
- [3] Venkataraman K K, Preston L H, Simons D W, Lee B J, Lee J G and Santavicca D A 1999 Mechanism of combustion instability in a lean premixed dump combustor *J. Propul. Power* **15** 909–18
- [4] Kadowaki S and Hasegawa T 2005 Numerical simulation of dynamics of premixed flames: flame instability and vortex-flame interaction *Prog. Energy Combust.* **31** 193–241
- [5] Hernández R and Ballester J 2008 Flame imaging as a diagnostic tool for industrial combustion *Combust. Flame* **155** 509–28
- [6] Paubel X, Cessou A, Honore D, Vervisch L and Tsiava R 2007 A flame stability diagram for piloted non-premixed oxycombustion of low calorific residual gases *Proc. Combust. Inst.* **31** 3385–92
- [7] Kiran D Y and Mishra D P 2007 Experimental studies of flame stability and emission characteristics of simple LPG jet diffusion flame *Fuel* **86** 1545–51
- [8] Mansour M S 2003 Stability characteristics of lifted turbulent partially premixed jet flames *Combust. Flame* **133** 263–74
- [9] Huang Y, Yan Y, Lu G and Reed A 1999 On-line flicker measurement of gaseous flames by images processing and spectral analysis *Meas. Sci. Technol.* **10** 726–33
- [10] Lu G, Yan Y and Colechin M 2004 A digital imaging based multifunctional flame monitoring system *IEEE Trans. Instrum. Meas.* **53** 1152–8
- [11] Smart J, Lu G, Yan Y and Riley G 2009 Characterisation of an oxy-coal flame through digital imaging *Combust. Flame* **157** 1132–9
- [12] Gilbert G, Lu G and Yan Y 2007 Tomographic reconstruction of the luminosity distribution of a combustion flame *IEEE Trans. Instrum. Meas.* **56** 1300–6
- [13] Lu G, Yan Y, Riley G and Bheemul H C 2002 Concurrent measurement of temperature and soot concentration of pulverized coal flames *IEEE Trans. Instrum. Meas.* **51** 990–5
- [14] Larrabee R D 1959 Spectral emissivity of tungsten *J. Opt. Soc. Am.* **49** 619–25
- [15] Ballester J and García-Armingol T 2010 Diagnostic techniques for the monitoring and control of practical flames *Prog. Energy Combust.* **36** 375–411
- [16] Huang Y and Yang V 2009 Dynamics and stability of lean-premixed swirl-stabilized combustion *Prog. Energy Combust.* **35** 293–364
- [17] Nettleton M A 2004 The influence of swirl angles on flame stability in pilot-scale plant *Fuel* **83** 253–6

# Measurement of Soot Temperature, Emissivity and Concentration of a Heavy-Oil Flame through Pyrometric Imaging

Duo Sun<sup>1</sup>, Gang Lu<sup>1</sup>, Hao Zhou<sup>2</sup>, Yong Yan<sup>1</sup>

<sup>1</sup>Instrumentation, Control and Embedded Systems Research Group  
School of Engineering and Digital Arts, University of Kent, Canterbury, Kent CT2 7NT, UK

<sup>2</sup>State Key Laboratory of Clean Energy Utilization  
Institute for Thermal Power Engineering, Zhejiang University, Hangzhou 310027, China

**Abstract**—This paper presents the monitoring and characterization of emissive properties of soot particles in heavy oil flames based on pyrometric imaging techniques. The soot temperature is derived from the relationship between the primary colors of flame images captured by a RGB camera. The emissivity of soot particles is then estimated by using the gray-level ratio of a primary color of the image to that of a blackbody source at the same temperature. The soot concentration is represented and estimated by *KL* factor, which is derived from the Hottel and Broughton's model once the emissivity is determined. The imaging system is calibrated using a blackbody furnace as a standard temperature source. The measurement accuracy is verified by applying the system to measure the true temperature of a tungsten lamp. The maximum relative error is about 0.9%. Experiments were conducted on a 9MW<sub>th</sub> industrial-scale combustion test facility to investigate the impact of the ratio of overfire air to total air, and the location of overfire air ports on the soot temperature, emissivity and concentration of a heavy oil flame.

**Keywords**—temperature; emissivity; soot concentration; digital imaging; heavy oil flame; overfire air

## I. INTRODUCTION

Soot temperature, emissivity and concentration of flames in fossil fuel fired furnaces, particularly where heavy-oil fuel is used, are important parameters in the analysis of combustion processes. The temperature of a flame, generally referring to the temperature of solid particles such as soot and fly-ash in the flame zone, plays a key role in every part of the combustion process such as ignition, burnout and formation of pollutant emissions (NO<sub>x</sub>, SO<sub>x</sub>, etc) [1]. Soot contributes significant fraction to radiative heat transfer in luminous flames [2], and its concentration and emissivity are important thermal properties required for heat transfer calculations in furnace operation and CFD (Computational Fluid Dynamics) modeling. Thus, online and continuous measurement of soot temperature, emissivity and concentration is essential for the in-depth understanding and subsequent optimization of combustion processes.

The techniques available for the temperature measurement of a flame can be intrusive or non-intrusive. The intrusive techniques mainly include thermocouples and gas-sampling probes, which are simple, low cost, but only give a single-

point gas temperature measurement [3]. Non-intrusive techniques operate on optical principles, including laser, optical fiber, and direct imaging techniques [3-7]. Laser-based optical methods such as laser-induced fluorescence and laser scattering of molecules are commonly used in laboratories but they are unsuitable for routine operation in industry due to the complexity and high cost of the system. Direct imaging has been identified as one of the most effective approaches for use in practical furnaces in terms of system functionality, portability and cost-effectiveness. It has been widely used not only for the temperature but also for the soot concentration measurement in both fossil fuel fired furnaces and internal combustion engines [4, 5]. Berry et al. [6] utilized a monochrome CCD (charge-coupled device) camera with two near infrared filters in combination with neutral density filters to measure the temperature of laminar jet diffusion flames under atmospheric and elevated pressures. Huang et al. [3] adopted a single CCD camera with optical filters mounted on a rotatable holder to acquire alternatively the radiation images at two different wavelengths to measure the temperature of a coal flame in a 500kW model furnace. Lu et al. [7] constructed an imaging system for on-line measurement of temperature distribution and soot concentration of pulverized coal flames. The system incorporated a monochrome CCD camera with a beam splitting unit and two band-pass filters centered at 650nm and 700nm to capture the flame images at two wavelengths. However, these systems involve a complex system configuration. There are some techniques which have been developed for the measurement of soot emissivity of a flame such as spectral radiometer and pyroelectric detector [8]. The direct imaging technique has also been adopted for measuring soot emissivity. Lou et al. [9] used color imaging detectors to measure the emissivity and the radiative properties of the particulate media in pulverized-coal-fired boilers.

This paper describes a pyrometric imaging technique for the simultaneous and two-dimensional measurement of soot temperature, emissivity and concentration of heavy oil flames. The measurement principles, technical and operational considerations are included. Experimental results obtained on a 9MW<sub>th</sub> heavy oil combustion test facility are also presented and discussed.

This work is supported by the Research Council UK (RCUK)'s Energy Programme (EP/F061307/1). The Energy Programme is an RCUK cross-council initiative led by EPSRC and contributed to by ESRC, NERC, BBSRC and STFC.

## II. METHODOLOGY

### A. System Description

The measurement of the soot temperature, emissivity and concentration of a flame is an integral part of the flame imaging system [10]. The system consists of a 90° viewing-angle optical probe protected by a water-cooled jacket, a 1/3-inch CMOS (Complementary Metal Oxide Semiconductor) RGB camera with a resolution of 1280H×1024V pixels, and an embedded motherboard with dedicated application software. The optical probe penetrates the furnace wall and transmits the light of flame to the camera. The camera features a partial scan mode which allows the camera to capture images at an adjustable frame rate from 25 frames per second to 265 frames per second (with a resolution of 320H×256V), making it ideal for imaging a fast-changing object such as flames. The embedded motherboard ensures all the measurements can be conducted on an on-line basis. The detailed structure and description of the system can be found elsewhere [10].

### B. Measurement Principles

1) *Soot temperature*- The measurement principle of the soot temperature is based on the two-color method. The two-color pyrometric technique has been widely accepted in the determination of the radiative temperature of solid particles (e.g., soot, flying ash) in the flame where the emissivity of the medium is unknown. The fundamental aspects of the two-color method can be found elsewhere [3, 4]. In the present study, instead of using the complex beam splitting and narrow-bandpass filtering approach, the system derives flame temperature from the relationship between the primary colors of the images captured by the RGB camera. The camera has three separate channels corresponding to primary colors Red (R), Green (G) and Blue (B). Each image frame produced can be disintegrated into three principal images R, G and B. A combination of the color-banded images can thus be used for the determination of the flame temperature distribution based on the two-color principle. In this study, the red and green images have been chosen, i.e.,

$$T = \frac{C_2 \left( \frac{1}{\lambda_G} - \frac{1}{\lambda_R} \right)}{\ln \frac{G(\lambda_R, T)}{G(\lambda_G, T)} + \ln \frac{S_{\lambda_R}}{S_{\lambda_G}} + \ln \left( \frac{\lambda_R}{\lambda_G} \right)^5}, \quad (1)$$

where  $T$  is the soot temperature,  $C_2$  is the second Planck's constant,  $G(\lambda_R, T)$  and  $G(\lambda_G, T)$  are the gray-level intensities of images from the red and green channels, respectively.  $\lambda_R$  and  $\lambda_G$  are the peak wavelengths of the spectral ranges corresponding to the red and green channels, and are 540 nm and 615 nm, respectively.  $S_{\lambda_R}$  and  $S_{\lambda_G}$  are the spectral sensitivities of the system for  $\lambda_R$  and  $\lambda_G$ , respectively. Ratio  $S_{\lambda_R}/S_{\lambda_G}$  is the instrument factor which can be determined through a calibration procedure using a standard temperature source [section II C].

The choice of red and green images for the temperature calculation instead of other combinations is because the CMOS sensor of the camera gives higher spectral sensitivities for the red and green channels than that for the blue channel and thus a better signal-to-noise ratio can be achieved. It must also be stressed that the use of primary color images for

temperature measurement offers advantages in simplicities in system design, calibration and operation. It would, however, result in some errors in the temperature calculation due to the fact that each primary color covers not only one single wavelength but a certain range of wavelengths. But it will not affect the general trend of the temperature distribution of the flame. In fact, experimental results show that the system has a very good measurement accuracy when applied to measure a reference temperature [section II C].

2) *Soot emissivity and concentration*- Once the soot temperature is determined from (1), the emissivity of soot particles in the flame at wavelength  $\lambda_R$  for temperature  $T$ ,  $\epsilon_{\lambda_R}(T)$ , can be estimated by its definition, i.e.,

$$\epsilon_{\lambda_R}(T) = \frac{M(\lambda_R, T)}{M_b(\lambda_R, T)}, \quad (2)$$

where  $M(\lambda_R, T)$  and  $M_b(\lambda_R, T)$  are the monochromatic emissive power of a non-blackbody (e.g., soot particles) and that of a blackbody, respectively. For the given imaging system, the relationship of the gray-level intensity of images and the monochromatic emissive power of the non-blackbody and the blackbody can be expressed by,

$$G(\lambda_R, T) = AS_{\lambda_R} M(\lambda_R, T), \text{ and} \quad (3)$$

$$G_b(\lambda_R, T) = AS_{\lambda_R} M_b(\lambda_R, T), \quad (4)$$

where  $G(\lambda_R, T)$  and  $G_b(\lambda_R, T)$  are the gray-level intensities of the red images of the non-blackbody and the blackbody captured by the imaging system for temperature  $T$ , respectively. The relationship between  $G_b$  and  $T$  can be determined through the calibration by using a blackbody source [section II C].  $A$  is an instrument constant which is independent of wavelength and reflects the effect of various factors including the radiation attenuation due to the optical system, atmosphere, observation distance, lens properties and signal conversion. Substitute (3) and (4) into (2), we get,

$$\epsilon_{\lambda_R}(T) = \frac{G(\lambda_R, T)}{G_b(\lambda_R, T)}. \quad (5)$$

In practice, the emissivity of soot particles can also be estimated from the widely used empirical equation proposed by Hottel and Broughton [11],

$$\epsilon_{\lambda}(T) = 1 - e^{-KL/\lambda^\alpha}, \quad (6)$$

where  $K$  is the absorption coefficient,  $L$  is the geometrical thickness of the flame along the optical axis of the imaging system, and  $\alpha$  is an empirical parameter depending upon  $\lambda$ . For visible spectral range,  $\alpha$  is considered to be a fixed value of 1.39 [11] for a steady luminous flame. Rearranging (6) yields,

$$KL = -\lambda^\alpha \ln(1 - \epsilon_{\lambda}), \quad (7)$$

thus

$$KL = -\lambda_R^\alpha \ln \left( 1 - \frac{G(\lambda_R, T)}{G_b(\lambda_R, T)} \right). \quad (8)$$

Previous studies have revealed that  $KL$  is proportional to the concentration of soot particles in the flame [4]. Although an estimate of the volumetric and gravimetric density of soot can be obtained if some assumptions are made, the  $KL$  factor

is used in the present study to investigate the soot concentration of a flame.

### C. System Calibration

The system was calibrated by using a pre-calibrated blackbody furnace (Landcal R1500T). The furnace has a blackbody cavity of 45mm in inner diameter and 100mm in length with an emissivity of approximately 0.99. The furnace was calibrated for a temperature range from 500°C to 1500°C with a resolution of  $\pm 1^\circ\text{C}/2^\circ\text{F}$ .

The calibration for the instrument factor  $S_{\lambda_R}/S_{\lambda_G}$  [refer to (1)] and the blackbody gray-level intensity  $G_b(\lambda_R, T)$  [refer to (5)] was carried out by reproducing the geometrical relationship between the imaging system and the flame to be measured in the temperature range from 900°C to 1500°C with an interval of 50°C. The obtained relationship between the instrument factor and the gray-level ratio is given in Fig. 1. A polynomial function, as in (9), is used to fit the relationship,

$$S = 0.3557 * \left(\frac{G(\lambda_R, T)}{G(\lambda_G, T)}\right)^2 - 1.294 * \left(\frac{G(\lambda_R, T)}{G(\lambda_G, T)}\right) + 2.469. \quad (9)$$

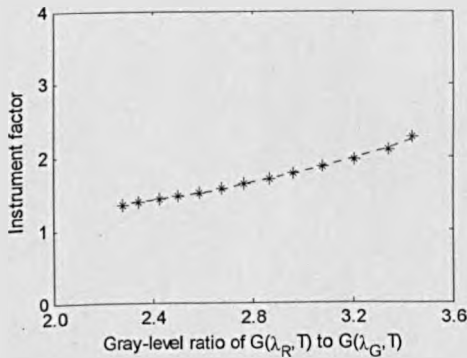


Fig. 1. Variation of instrument factor with gray-level ratio.

Fig. 2 shows the variation of the gray-level intensity of the red channel image with the blackbody temperature at an exposure time of 1ms. It has been found that the variation is satisfied by a Gaussian function, i.e.,

$$G_b(\lambda_R, T) = 1965 * e^{-\left(\frac{T-2214}{443}\right)^2}. \quad (10)$$

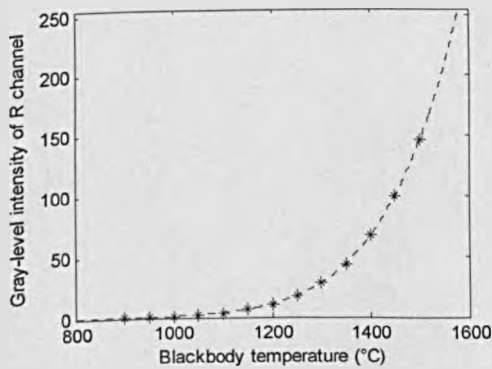


Fig. 2. Variation of the gray-level intensity of the red channel with the blackbody temperature.

It has been proven that the system exhibits a linear characteristic for different camera exposure times [10]. This suggests that the accuracy of the temperature measurement will not be affected by the variation in exposure time. This is particularly important when applying the system to industrial furnaces where the flame irradiance can vary with operation conditions and thus the camera exposure time has to be adjusted to avoid under- or over-exposure of images.

The measurement accuracy was verified by applying the system to measure the true temperature of a standard tungsten lamp. The apparent temperature of the tungsten lamp varied from 900°C to 1500°C with an interval of 50°C by controlling the current of the power supply. The corresponding true temperatures of the tungsten lamp, which can be derived from its apparent temperature by using the method given in [12], varied from 958°C to 1650°C. Fig. 3 shows the comparison between measured and reference temperatures. It was found that the maximum error of 14.8°C occurs at a true temperature of 1650°C and is equivalent to a relative error of 0.9%.

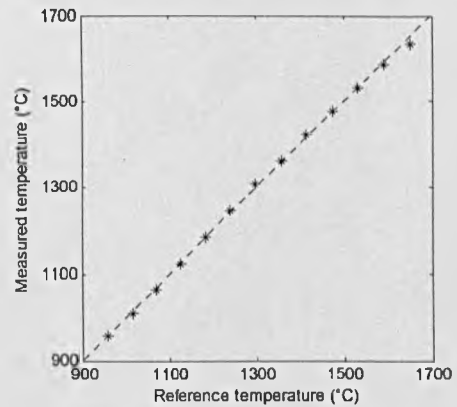


Fig. 3. Comparison between the measured and reference temperatures.

### III. RESULTS AND DISCUSSIONS

Experimental work was undertaken on a 9MW<sub>th</sub> heavy-oil-fired industrial-scale combustion test facility. The facility has an 11-meter long horizontal cylindrical combustion chamber with an internal cross-section of 1.3 meters in diameter. A low-NO<sub>x</sub> burner was fitted horizontally. Heavy oil was atomized by steam and injected into the combustion chamber through an oil gun, and then mixed with surrounding PA (Primary Air), SA (Secondary Air), and TA (Tertiary Air) successively. The imaging system was installed on the side wall of the furnace close to the front wall. Fig. 4 shows a schematic diagram of the combustion test facility and system installation.

The experiments were undertaken for different OFA (Overfire Air) operations. The OFA is an effective technology for reducing NO<sub>x</sub> emissions from a combustion process. Combustion air is reduced from the burner to create a fuel rich condition in the primary combustion zone. Fuel-bound nitrogen conversion to NO is reduced in the furnace. The peak temperature of the flame is then restrained to limit thermal NO<sub>x</sub> formation. A large amount of air is fed and intersected the combustion gases in the downstream of the furnace to complete the combustion. During the experiments, a series of

tests were conducted to reveal the impact of the ratio of the OFA to total air, and the position of OFA port on the emissive characteristics of the heavy oil fired flame. Two OFA injection positions, assigned OFA-A and OFA-B, were tested, as illustrated in Fig. 4. The distances from the burner outlet to the two OFA ports are 4.5m and 6.6m, respectively. For each OFA position, four different OFA ratios were created, i.e., 0%, 15.0%, 17.5% and 20.0%, whilst the total air (the sum of PA, SA, TA and OFA) was kept constant during the tests. The detailed test programme is summarized in Table I.

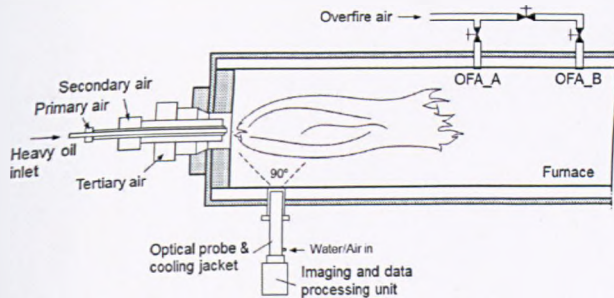


Fig. 4. The combustion test facility and the system installation.

TABLE I. TEST PROGRAMME.

OFA (%)	PA (%)	SA (%)	TA (%)
0	17.0	43.0	40.0
15.0	14.5	36.5	34.0
17.5	14.0	35.5	33.0
20.0	13.6	34.4	32.0

Fig. 5 (a) illustrates a typical averaged image of the heavy oil fired flame, which is derived from 20 instantaneous images taken at the non-OFA condition (0% OFA). The corresponding distributions of temperature, emissivity and KL factor are shown in pseudo-color in Fig. 5(b), (c) and (d), respectively.

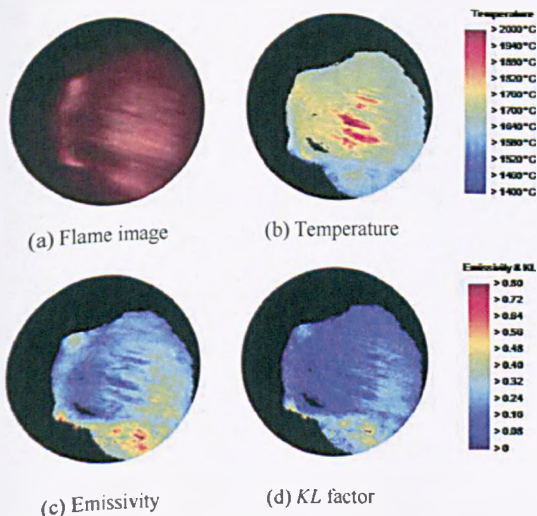


Fig. 5. Averaged image of the heavy oil flame and the corresponding distributions of soot temperature, emissivity and concentration.

Fig. 6 shows the variation of the measured average temperature of the flame with the ratio and nozzle position of

the OFA. Each data point is an average of sixty instantaneous values and the standard deviation is given as an error bar. The decreased temperature can be explained by the fact that the higher the OFA, the less the air (PA, SA and TA) in the primary combustion zone, which reduces the combustion intensity and hence the temperature. The decline in the temperature suppresses the thermal- $\text{NO}_x$  formation. On the other hand, the reduction of the oxygen concentration in the primary zone of the flame leads to less fuel-N conversion to  $\text{NO}_x$  [13]. This is evidenced by the emission analysis data where  $\text{NO}_x$  in flue gas has shown an almost linearly decreasing trend as the flame temperature, as shown in Fig. 7. Furthermore, under the same OFA ratio, the OFA-B results in a lower flame temperature and  $\text{NO}_x$  emission than the OFA-A. This is due to a longer delay, associated to the location of the OFA-B port, in the mixing between the combustion gases from the primary zone and the OFA. The longer delay increases the residence time of the combustion gases in the zones with low oxygen concentrations, resulting in the reduced concentration of nitrogen radicals reaching the secondary zone (OFA zone) and, thus, the reduced conversion of these radicals to  $\text{NO}_x$  [13].

Figs. 8 and 9 depict the average emissivity and concentration of soot particles within the flame, respectively, under the tested conditions. Increased soot emissivity and concentration (KL factor) are observed for an increased OFA. This may be due to the fact that the reduction of oxygen concentration in the primary combustion zone could promote the formation process of soot [14]. It is also noted that the bottom part of the flame exhibits a higher emissivity and soot concentration, as shown in Fig. 5(c) and (d). This phenomenon is to be studied in the near future.

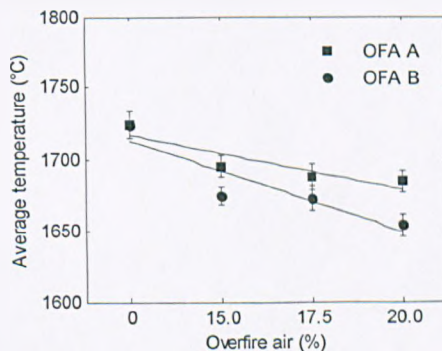


Fig. 6. Variations of soot temperature with the OFA ratio and position.

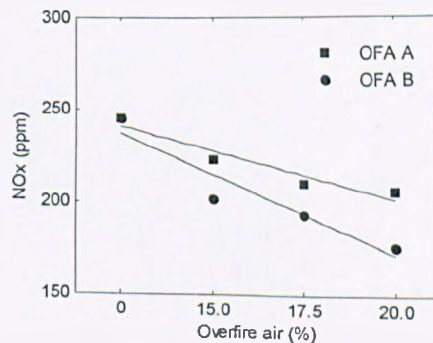


Fig. 7. Variations of  $\text{NO}_x$  emissions with the OFA ratio and position.

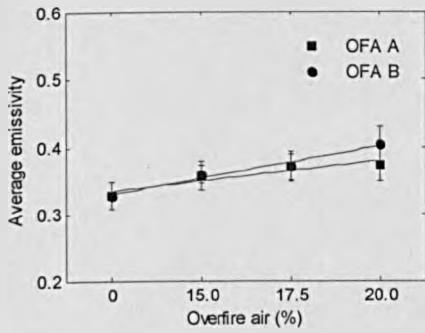


Fig. 8. Variations of average emissivity with the OFA ratio and position.

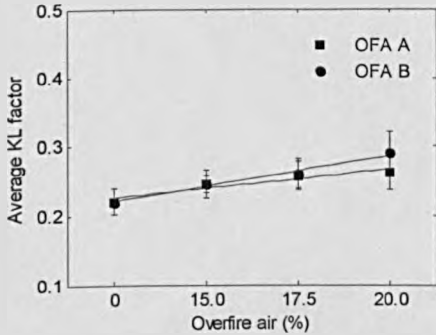


Fig. 9. Variations of average KL factor with the OFA ratio and position.

#### IV. CONCLUSION

The monitoring and characterization of emissive properties of heavy oil flames has been carried out using pyrometric imaging techniques. The characteristic parameters including soot temperature, emissivity and concentration of the flame are measured using a RGB digital imaging system based on the two-color pyrometric principle. The soot emissivity and concentration can be calculated once the temperature is determined. The imaging system has been calibrated using a blackbody furnace as a standard temperature source. The measurement accuracy has been verified by applying the system to measure the true temperature of a tungsten lamp. The maximum relative error of the temperature measurement is about 0.9%. The technique developed has been applied to investigate the impact of the overfire air operation on the emissive characteristics of heavy oil flames on a 9MW<sub>th</sub> combustion test facility. The results have demonstrated that the developed technique is capable of providing instantaneous and two-dimensional measurement of the soot temperature, emissivity and concentration (KL factor) of the flame under different furnace conditions.

#### REFERENCES

- [1] R. Khatami and Y. A. Levendis, "On the deduction of single coal particle combustion temperature from three-color optical pyrometry," *Combustion and Flame*, vol. 158, pp. 1822-1836, 2011.
- [2] S. Distasio and P. Massoli, "Influence of the soot property uncertainties in temperature and volume-fraction measurements by two-colour pyrometry," *Measurement Science and Technology*, vol. 5, pp. 1453-1465, 1994.
- [3] Y. Huang, Y. Yan, and G. Riley, "Vision-based measurement of temperature distribution in a 500-kW model furnace using the two-colour method," *Measurement*, vol. 28, pp. 175-183, 2000.
- [4] H. Zhao and N. Ladommatos, "Optical diagnostics for soot and temperature measurement in diesel engines," *Progress in Energy and Combustion Science*, vol. 24, pp. 221-255, 1998.
- [5] S. Simonini, S. J. Elston, and C. R. Stone, "Soot temperature and concentration measurements from colour charge coupled device camera images using a three-colour method," *Proceedings of the Institution of Mechanical Engineers, Part C: Journal of Mechanical Engineering Science*, vol. 215, pp. 1041-1052, 2001.
- [6] T. L. Berry Yelvert and W. L. Roberts, "Soot surface temperature measurements in pure and diluted flames at atmospheric and elevated pressures," *Experimental Thermal and Fluid Science*, vol. 33, pp. 17-22, 2008.
- [7] G. Lu, Y. Yan, G. Riley, and H. C. Bheemul, "Concurrent measurement of temperature and soot concentration of pulverized coal flames," *IEEE Transactions on Instrumentation and Measurement*, vol. 51, pp. 990-995, 2002.
- [8] R.-B. Salvador, S. Rebecca, M. Reza, E.-B. Samch, and J. T. Murray, "Real time, non-intrusive measurement of particle emissivity and gas temperature in coal-fired power plants," *Measurement Science and Technology*, vol. 18, pp. 3479-3488, 2007.
- [9] C. Lou, H. C. Zhou, P. F. Yu, and Z. W. Jiang, "Measurements of the flame emissivity and radiative properties of particulate medium in pulverized-coal-fired boiler furnaces by image processing of visible radiation," *Proceedings of the Combustion Institute*, vol. 31, pp. 2771-2778, 2007.
- [10] D. Sun, G. Lu, H. Zhou, and Y. Yan, "Flame stability monitoring and characterization through digital imaging and spectral analysis," *Measurement Science and Technology*, vol. 22, p. 114007, 2011.
- [11] H. C. Hottel and F. P. Broughton, "Determination of true temperature and total radiation from luminous gas flames," *Industrial and Engineering Chemistry*, vol. 4, pp. 166-175, 1932.
- [12] G. Lu and Y. Yan, "Temperature profiling of pulverized coal flames using multicolor pyrometric and digital imaging techniques," *IEEE Transactions on Instrumentation and Measurement*, vol. 55, pp. 1303-1308, 2006.
- [13] A. Rebola and M. Costa, "Simultaneous reduction of NO<sub>x</sub> and particulate emissions from heavy fuel oil-fired furnaces," *Proceedings of the Combustion Institute*, vol. 29, pp. 2243-2250, 2002.
- [14] Z. A. Mansurov, "Soot formation in combustion processes (review)," *Combustion, Explosion, and Shock Waves*, vol. 41, pp. 727-744, 2005.

# An Embedded Imaging and Signal Processing System for Flame Stability Monitoring and Characterisation

Duo Sun, Gang Lu\*, Yong Yan

Instrumentation, Control and Embedded Systems Research Group  
School of Engineering and Digital Arts, University of Kent, Canterbury, Kent CT2 7NT, UK  
ds322@kent.ac.uk, g.lu@kent.ac.uk, y.yan@kent.ac.uk

**Abstract** - This paper presents the design, implementation and evaluation of an instrumentation system for flame stability monitoring and characterisation on industrial furnaces. The system, incorporating digital imaging and spectral analysis techniques, is designed to monitor a range of flame characteristic parameters. The stability of the flame is then assessed through statistical analysis of the flame parameters obtained. Embedded computer techniques are employed to ensure the system is compact and robust. Experiments were conducted on a laboratory-scale combustion test rig to evaluate the system. The impact of the air-to-fuel ratios on the stability of a gaseous flame is investigated. The results demonstrate that the system is capable of monitoring flame stability in a statistical way.

**Keywords** - flame monitoring; flame stability; photodetector; CMOS camera; embedded technology

## I. INTRODUCTION

Flame stability in pulverized coal combustion is a good indication of plant safety, combustion efficiency and pollutant emissions. It is becoming increasingly an area of concern because of the trends of extending the use of low-quality coal, coal blends, and coal-biomass co-firing in existing power plants. Variations in coal diet and biomass addition can have a significant impact on the combustion stability and efficiency. Flame characteristics should therefore be continuously monitored to maintain constant combustion stability. However, the current flame monitoring techniques available to the power generation industry can only provide very basic information such as flame on or out. They cannot give quantitative information of the flame. An advanced technique for flame stability monitoring is therefore desirable.

The stability of a flame depends on a number of factors including the ignitability of fuel or a blend, fluid-dynamic pattern, mixing, thermal energy release and loss, burner type and boiler structure [1]. Many theoretical and experimental studies have been devoted to such issues [2-10]. Various techniques for flame monitoring and characterization have been proposed, but digital imaging has been identified as one of the most effective approaches for use in practical furnaces in terms of system functionality, portability and cost-effectiveness [3]. Significant efforts have been made in the last decade to develop two-dimensional (2-D) and three-dimensional (3-D) techniques for flame visualization and characterization. However, few of the techniques can monitor

flame stability. Paubel et al. [4] used a CCD camera to record chemiluminescence images of excited CH radicals in a non-premixed flame of low calorific residual gases and employed topology analysis techniques to study the stability diagram of the flame. Kiran and Mshira [5] studied the stability characteristics of a jet diffusion LPG (liquefied petroleum gas) flame in terms of its lift-off height, length, and emission levels which were derived from images obtained using a CCD camera. Mansour [6] investigated the stability characteristics of a partially premixed turbulent lifted methane flame using a combined 2-D technique based on Rayleigh scattering, LIPF (Laser Induced Predissociation Fluorescence) and LIF (Laser Induced Fluorescence). Several prototype systems have also been developed using direct imaging techniques for 2-D and 3-D flame monitoring and characterization on both laboratory and industrial scale combustion test facilities [7-10]. The systems are designed for measuring and quantifying the characteristic parameters of a flame such as size, shape, temperature, and oscillation frequency. Information obtained from the earlier systems has laid a foundation for developing a technology for the quantitative assessment of flame stability.

The present research is focused on the development of a miniaturized instrumentation system for flame stability monitoring. The system, operating on optical sensing, digital imaging, signal processing and embedded computing techniques, is designed to measure a number of flame parameters such as ignition point, brightness, oscillation frequency and temperature distribution on an online continuous basis. The flame stability can then be assessed through the statistical analysis of the characteristic parameters obtained. This paper describes the design considerations and implementation aspects of the prototype system. Experimental results on a laboratory-scale combustion test rig are reported. The impact of the air-to-fuel ratios on the stability of a gaseous flame is investigated and discussed.

## II. SYSTEM DESCRIPTION

### A. Design and Implementation

Fig.1 shows a schematic diagram of the instrumentation system. The system consists of an optical probe, a beam-splitting unit, an Embedded Photodetectors and Signal-processing Board (EPSB), a digital camera, and an embedded motherboard with associated application software. The optical

\* Corresponding author

probe, which has a 90° view-angle objective lens protected by purging air, is used to penetrate the furnace and transmit the light of flame to the imaging system. The beam splitter divides the light of flame into two identical beams. The first beam is

captured by the camera for the measurement of flame geometric/luminous parameters and temperature distribution. The second beam is received by the EPSB for the measurement of oscillation frequency.

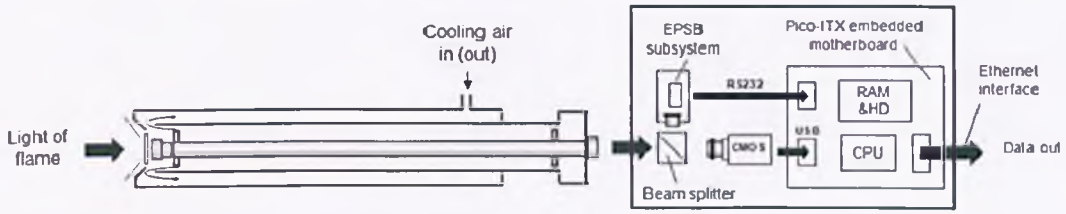


Fig. 1. Schematic diagram of flame monitoring system.

- **Digital camera** - It is an industrial CMOS RGB camera with a resolution up to 1280(H)×1024(V) at 25 frames per second. It also features a partial scan mode which allows the camera to capture images at a frame rate up to 265 frames per second with a resolution of 320×256, making it ideal for imaging a fast-changing object such as combustion flame.

- **EPSB** - The EPSB has three separate photodetectors, covering ultraviolet (UV), visible and infrared (IR) spectral bands, respectively. The detectors convert flame light intensity into current signals corresponding to three spectral bands. A signal conditioning unit is used to ensure the three signals are adequately amplified and filtered prior to digital signal processing. A digital signal microcontroller (dsPIC) digitizes the three signals simultaneously with a processing speed of 40MHz. Embedded system techniques are employed for on-board signal processing to ensure robustness, compactness and fast response of the board. The processed data is transmitted to the motherboard via a RS232 interface.

- **Embedded motherboard** - A high-performance Pico-ITX embedded motherboard acquires and processes the images from the camera. It also performs as the masterboard for controlling and receiving data from the EPSB so as to achieve parallel and real time signal processing and transmission (via Ethernet).

The optical probe and all optical and electronic parts are integrated as a single unit, offering the system excellent portability and robustness. Dedicated application software is also developed as an integral part of the system.

## B. Measurement Principles

- **Geometrical and luminous parameters** - The geometrical and luminous parameters of the flame are determined by processing flame images using digital image processing techniques. The number of the parameters that are measured can vary, depending upon the nature of the flame and purpose of measurement. In the case of the present study, the parameters computed include *Ignition points (maximum, minimum and mean)*, *Length*, *Luminous region*, *Brightness*, and *Non-uniformity*. The detailed definition and determination of these parameters were given in [9]. The instability of a flame parameter is defined as the standard deviation normalized to its mean value, i.e.,

$$\delta_x = \frac{\sigma_x}{\bar{x}} \times 100\% \quad (1)$$

where  $\delta_x$  is the instability of flame parameter  $x$ ,  $\bar{x}$  and  $\sigma_x$  are the mean value and standard deviation of  $x$ , respectively.

- **Flame instability** - The stability of a flame can be evaluated based on the statistical analysis of its geometrical and luminous parameters. To quantify the flame stability, a parameter,  $\delta$  is defined as the sum of weighted instabilities of the flame parameters, i.e.,

$$\delta = \sqrt{\sum_{i=1}^m (w_i \delta_{x_i})^2} \quad (2)$$

$$\text{with } \sum_{i=1}^m w_i^2 = 1,$$

where  $m$  is the number of flame parameters considered,  $w_i$  is the weight for the corresponding parameter  $x_i$ . A larger weight is given to an estimate with a larger variance of the parameter whilst a smaller weight to an estimate with a smaller variance.

- **Oscillation frequency** - The oscillation frequency of the flame is one of the most important properties closely linked to flame stability. It is derived from the flame intensity signals captured by the photodetectors through frequency spectral analysis. A quantitative frequency is determined as the power-density weighted average frequency over the entire frequency range [7], i.e.,

$$F = \frac{\sum_{i=1}^n p_i f_i}{\sum_{i=1}^n p_i} \quad (3)$$

where  $F$  is the oscillation frequency,  $f_i$  is the  $i_{th}$  frequency,  $p_i$  is the power density of the  $i_{th}$  frequency component, and  $n$  is the number of frequency components.

A standard frequency-varying light source has been used as an idealized flame light to evaluate the accuracy of the oscillation frequency measurement. Fig.2 shows a comparison between the measured values against the reference frequencies. The relative error of the frequency measurement is no greater than 2% over the frequency range from 0 to 500Hz.

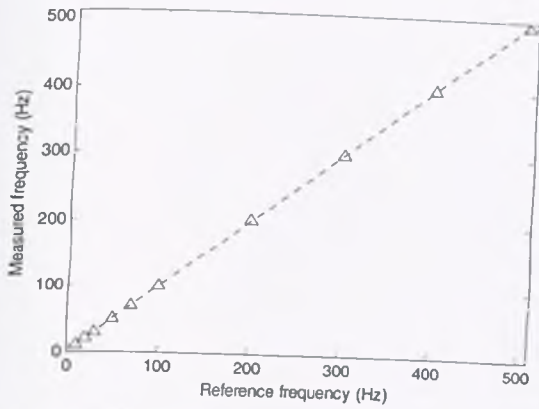


Fig. 2. Comparison between the measured and reference frequencies.

### III. RESULTS AND DISCUSSION

Experiments were carried out on a laboratory-scale combustion test rig to evaluate the imaging system as well as the methodology developed. A Bunsen type burner was used to generate a flame by combusting commercial grade propane in an enclosed combustion environment. Different test conditions were created by varying air supplies for a fixed fuel flow rate of 0.3 liter per minute. Each condition is identified by the equivalence ratio which is defined as the ratio of air to fuel supplied for combustion divided by the stoichiometric ratio of air to fuel. Therefore, an equivalence ratio less than 1 represents an air-lean condition whilst greater than 1 indicates an air-rich condition.

Fig. 3 shows the flame images captured by the camera for different equivalence ratios. Each image is an average of 10 successive images taken in one second. As can be directly observed, the flame physical appearance (size, brightness, etc) varies with the equivalence ratio. Fig. 4 illustrates corresponding binary images of the flame obtained through edge detection and segmentation techniques. These images provide evidence on the changes of flame characteristics and thus form the basis for the determination of flame parameters.

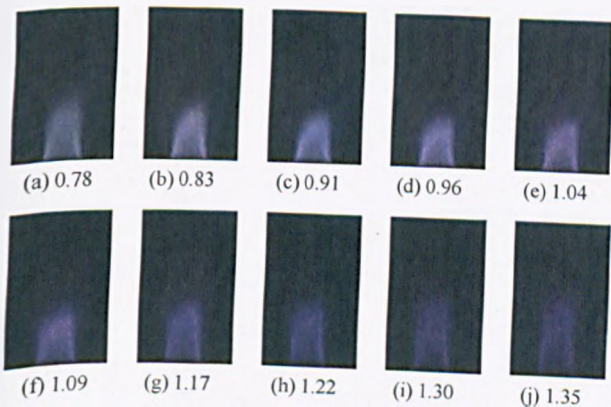


Fig. 3. Flame images for different equivalence ratios.

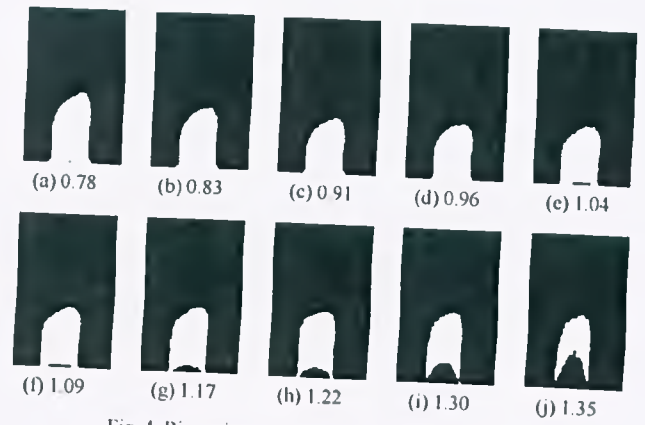


Fig. 4. Binary images of the flame shown in Fig. 3.

Fig. 5 illustrates the instabilities of the flame maximum ignition point, luminous region, brightness, and non-uniformity for different equivalence ratios. As can be seen, the variations of the parameters are relatively small under the stoichiometric conditions (equivalence ratio=1). As the equivalence ratio increases (i.e., air-rich conditions), a great variation in the non-uniformity is observed. Those variations are main causes for the flame instability, as shown in Fig. 6. It was observed during the experiments that the flame was extremely unstable at the high equivalence ratios and eventually blown off at an equivalence ratio of 1.35.

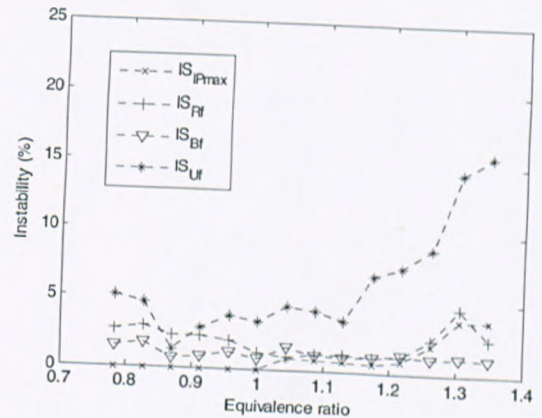


Fig. 5. Instabilities of flame parameters for different equivalence ratios.

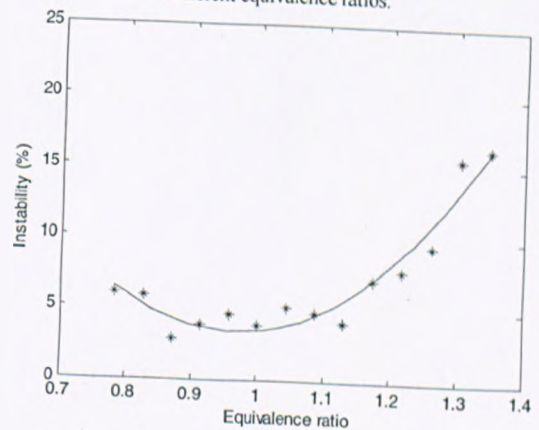


Fig. 6. Flame instability for different equivalence ratios.

Fig. 7 depicts a typical example of the PSD (power spectral density) estimates of the flame signals, which were taken by the EPSB for both the visible and IR spectral ranges for the equivalence ratio of 0.78. The sampling rate of the signals was 1024 Hz. The DC components of the signals were also removed as dynamic frequency components are of interest. It has been found that the PSD estimates for the IR and visible signals are very similar with the peak value occurred around the frequency of 18 Hz. Note that the UV signal was too weak to be detected in the case studied due to chemical properties of the fuel. Fig. 8 shows the variation of the oscillation frequency with the equivalence ratio in the IR spectral range. Each data point is an average of eight instantaneous values. It is evident that the oscillation frequency increases with the equivalence ratio and reaches its max value near equivalence ratio of 1.1, indicating an increased stability in such combustion conditions. It has also been found that a high excess air (equivalence ratio is greater than 1.1) results in a decreased oscillation frequency, and therefore poorer flame stability.

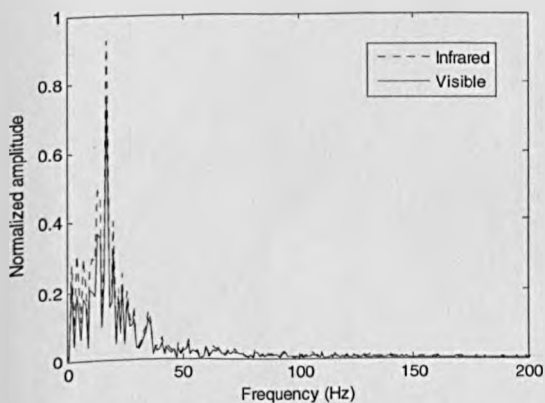


Fig. 7. PSD estimates of flame signals.

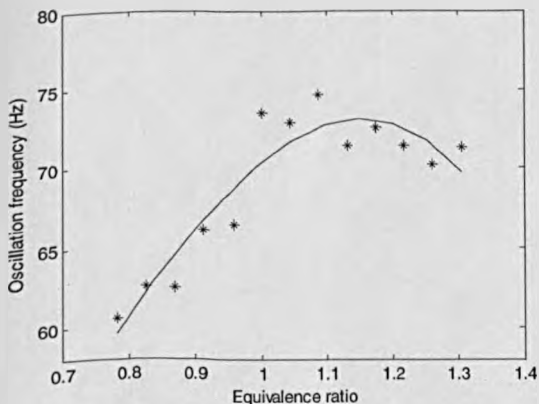


Fig. 8. Oscillation frequency for the IR spectral range.

#### IV. CONCLUSION

An instrumentation system for flame stability monitoring and characterization on industrial furnaces has been developed. The system is based on digital imaging, spectral analysis, and embedded computer techniques. The stability of the flame is quantified through statistical analysis of the characteristic parameters obtained. The system has been tested on a laboratory-scale combustion test rig to investigate the impact of the air-to-fuel ratios on the stability of a gaseous flame. The results have demonstrated that the system is capable of measuring and indicating flame stability in a statistical manner. Future work will be to incorporate the temperature measurement into the system and to undertake more experimental work on industrial scale test facilities.

#### ACKNOWLEDGMENT

The authors wish to acknowledge the UK Engineering Physical Science Research Council (EPSRC, EP/F061307/1) for providing financial support for this research.

#### REFERENCES

- [1] S. Su, J. H. Pohl, D. Holcombe, and J. A. Hart, "Techniques to determine ignition, flame stability and burnout of blended coals in p.f. power station boilers," *Progress in Energy and Combustion Science*, vol. 27, pp. 75-98, 2001.
- [2] S. Kadowaki, and T. Hasegawa, "Numerical simulation of dynamics of premixed flames: flame instability and vortex-flame interaction," *Progress in Energy and Combustion Science*, vol. 31, pp. 193-241, 2005.
- [3] R. Hernández and J. Ballester, "Flame imaging as a diagnostic tool for industrial combustion," *Combustion and Flame*, vol. 155, pp. 509-528, 2008.
- [4] X. Paubel, A. Cessou, D. Honore, L. Vervisch, and R. Tsiava, "A flame stability diagram for piloted non-premixed oxycombustion of low calorific residual gases," *Proceedings of the Combustion Institute*, vol. 31, pp. 3385-3392, 2007.
- [5] M. S. Mansour, "Stability characteristics of lifted turbulent partially premixed jet flames," *Combustion and Flame*, vol. 133, pp. 263-274, 2003.
- [6] D. Y. Kiran, D. P. Mishra, "Experimental studies of flame stability and emission characteristics of simple LPG jet diffusion flame," *Fuel*, vol. 86, pp. 1545-1551, 2007.
- [7] Y. Huang, Y. Yan, G. Lu, and A. Reed, "On-line flicker measurement of gaseous flames by images processing and spectral analysis," *Measurement Science and Technology*, vol. 10, pp. 726-733, 1999.
- [8] G. Lu, Y. Yan, and M. Colechin, "A digital imaging based multifunctional flame monitoring system," *IEEE Transactions on Instrumentation and Measurement*, vol. 53, pp. 1152-1158, 2004.
- [9] J. Smart, G. Lu, Y. Yan, and G. Riley, "characterisation of an oxy-coal flame through digital imaging," *Combustion and Flame*, vol. 157, pp. 1132-1139, 2010.
- [10] G. Gilibert, G. Lu, and Y. Yan, "Tomographic reconstruction of the luminosity distribution of a combustion flame," *IEEE Transactions on Instrumentation and Measurement*, vol. 56, pp. 1300-1306, 2007.